MICROSEISMIC MONITORING: PHYSICAL MODELING AND SOURCE CHARACTERIZATION

A Thesis

Presented to

the Faculty of the Department of Earth and Atmospheric Sciences

University of Houston

In Partial Fulfillment

of the Requirements for the Degree

Master of Science

in Geophysics

by

Omer Akbas

December 2013

MICROSEISMIC MONITORING: PHYSICAL MODELING AND SOURCE CHARACTERIZATION

_____

Omer Akbas

APPROVED:

_____

Dr. Robert R. Stewart, Chairman

_____

Dr. Hua-Wei Zhou

_____

Dr. Erkan Ay

_____

Dean, College of Natural Science and Mathematics

Acknowledgements

It is my pleasure to take this opportunity to thank a number of people who contributed to completion of this thesis.

I would like to express my deepest gratitude to my advisor, Dr. Robert Stewart, for his excellent guidance, patience, and providing me with an excellent atmosphere for doing research at the University of Houston.

Special thanks are given to my committee member, Dr. Erkan Ay from Shell. I am grateful to his generous support and valuable guidance throughout my thesis research.

I would also like to thank Dr. Nikolay Dyaur, who let me experience the research with physical models in the lab. His guidance and ideas on physical modeling experiments enlighten me during the modeling and data acquisition process. Extended special thank to committee member Dr. Hua-Wei Zhou for his valuable advise on this research. Not only have they been invaluable for the development of my master thesis, but it has furthermore always been a great pleasure to work with them.

I would like express my appreciation to my previous advisor in Kocaeli University, Dr. Ertan Peksen, for introducing and teaching MATLAB to me. Without the knowledge of MATLAB, it would not been possible to complete this research. It has always been a pleasure to work with him.

Thanks to all AGL (Allied Geophysical Laboratories) staff and students. Thanks Li Chang, Anoop William, Eray Kocel, and other valuable members of AGL.

I would like to thank Turkish Petroleum Corporation (TPAO) for their financial support during my gradate study.

I would like to extend my personal gratitude to my roommates, Kenan Yazan, Sercan Pisen, Gokhan Alkir, and to all my colleagues in University of Houston. Special thanks are given to Suleyman Coskun, Selin Deniz Akhun Coskun, and Ozbil Yapar for their support in this research.

I also want to express my appreciation for Gozde Ceylan, who stuck with me during the long months of researching and writing this thesis even when I retreated to long days with my computer.

Finally, but most importantly, I would also like to thank my parents, Metin and Emine Akbas, two elder sisters, Ayse and Husniye, and two elder brothers, Cemil and Huseyin. I have extended this personal gratitude to my uncle-in-law, Ahmet Tanir, to my aunts-in-law, Asli and Emine Akbas. They were always supporting and encouraging me with their best wishes. Without their encouragement, the completion of my thesis would not have been possible.

MICROSEISMIC MONITORING: PHYSICAL MODELING AND SOURCE CHARACTERIZATION

An Abstract

of a

Thesis

Presented to

the Faculty of the Department of Earth and Atmospheric Sciences

University of Houston

In Partial Fulfillment

of the Requirements for the Degree

Master of Science

in Geophysics

by

Omer Akbas

December 2013

Abstract

This research investigates some fundamental aspects of microseismic monitoring: location and source mechanism. We developed a ray-tracing and diffraction-stack procedure to determine source locations. The location algorithm uses a grid-search technique to find source coordinates. For every possible point source, three attributes (traveltime residual, stacked energy and energy/residual ratio) in a grid area are calculated. Then the location can be found by either choosing the point that yields a minimum traveltime residual or maximum stacked energy or maximum energy/-traveltime ratio. Further, focal mechanisms and radiation patterns of simulated microseismic events are examined using Focmec (Focal Mechanism Determination), an open-source program. The location algorithm is developed in a MATLAB environment and tested on physical modeling data from the Allied Geophysical Laboratories (AGL) at the University of Houston.

Three different physical modeling experiments have been conducted using ultrasonic source and 3-component receivers. For the first experiment, a single layer Plexiglas model was used; the second experimental model was built by assembling Plexiglas and aluminum blocks. In the third experiment, a real sandstone rock (57.5 x 43.8 x 17.5 cm) was employed. To determine which method (P versus S waves and travel time versus amplitude) and acquisition design (surface or borehole receivers) is most accurate, we have undertaken variety of tests. Locating events using S-waves is as accurate as with P-waves; however, combining both P and S-waves are the most accurate approach among all experiments. Furthermore, location certainty increases when downhole receivers are included for both P and S-waves.

To increase the speed of the algorithm, CPU and GPU computing was implemented. Locating a single microseismic event with 7 different methods takes 11.4 seconds on single core CPU, whereas, this number is decreased to 4.2 seconds using

multi-core CPU computing. Further, implementing GPU computing further decreases the total elapsed time to only 1.9 seconds. There is more than an 80 percent increase in terms of computation time compared to single core CPU.

Table of Contents

List of Figures

List of Tables

Chapter 1. Introduction, objectives and outline

1.1 GENERAL UNDERSTANDING OF HYDRAULIC FRACTURING

The conventional way to recover natural gas and oil is achieved by drilling and extraction out of the traps generally in permeable sandstone and carbonate formations. It is known that hydrocarbons also exist in low-permeability shale formations, which are one of the unconventional reservoirs. Figure 1.1 illustrates the schematic geology of unconventional reservoirs.

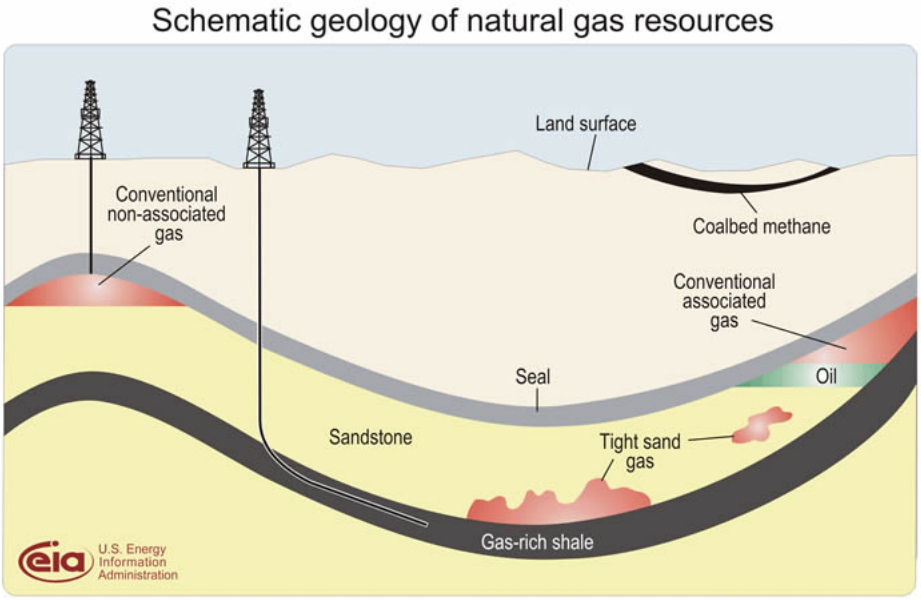

Figure 1.1: United States shale gas plays (U.S. Energy Information Administration; http://www.eia.gov/oil_gas/rpd/shale_gas.pdf)

In North America, there has been a significant interest in unconventional gas reservoirs. Technological advancements of hydraulic fracturing and horizontal drilling have led to development of new sources of shale gas. Figure 1.2 shows the shale gas plays in United States. Increase in new shale play areas is followed by a huge increase in the number of wells drilled in shale reservoirs. Figure 1.3 shows the growth of shale wells in Marcellus shale reservoir, Pennsylvania from January 2007 to September 2010.

The number of drilled wells has increased to 2109 as of September 2010 since January 2007.

"Unconventional gas reservoirs" are generally referred to a low permeability formation that produces mainly natural gas. One way to increase permeability of the reservoir to recover gas at economic rates is hydraulic fracture stimulation. In hydraulic-fracture treatment, once the pressure of the injected fluid exceeds the reservoir pressure, fracturing initiates and propagates throughout the rock (Economides and Nolte, 2000). As a result of that, rock failure due to hydraulic fracturing may generate small earthquakes whose magnitude are between -4 and +2 on Richter scale. These tiny earthquakes are called microseisms, which are too weak to be felt by humans. It is one of the biggest challenges in the industry to distinguish microseismic events from noise due to low signal-to-noise ratio.

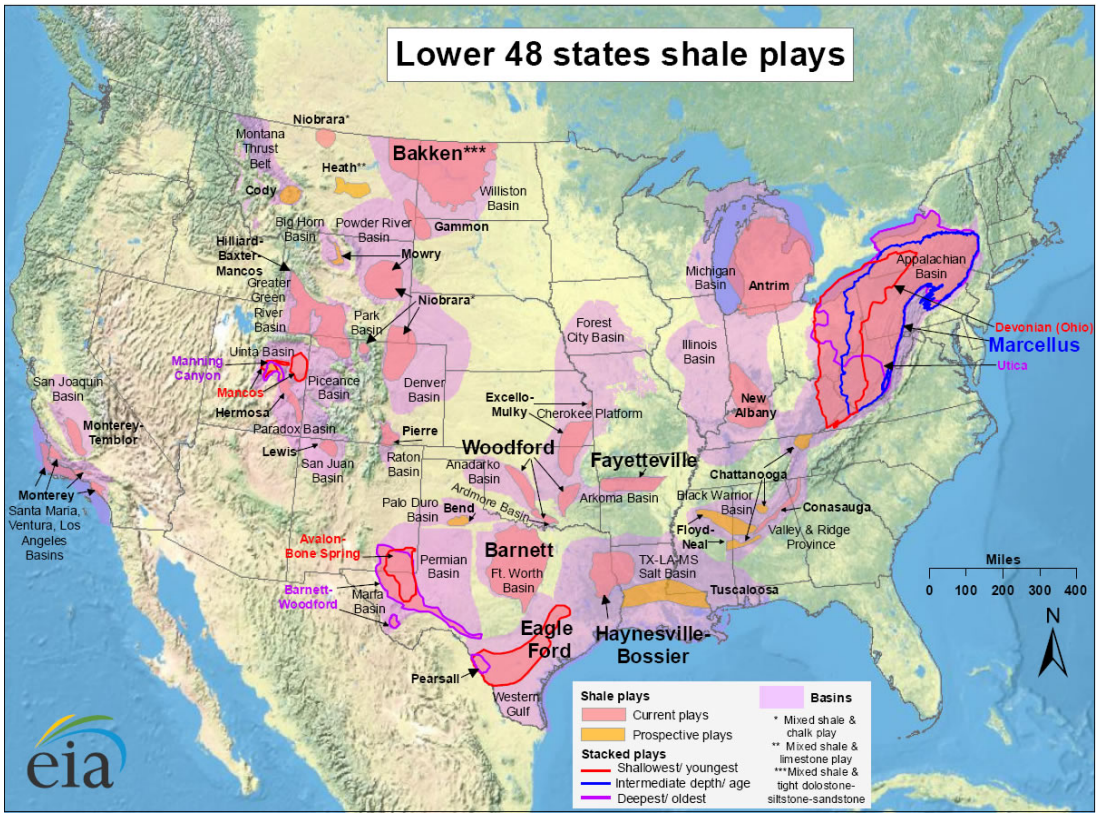

Figure 1.2: United States shale gas plays (U.S. Energy Information Administration; http://www.eia.gov/oil_gas/rpd/shale_gas.pdf)

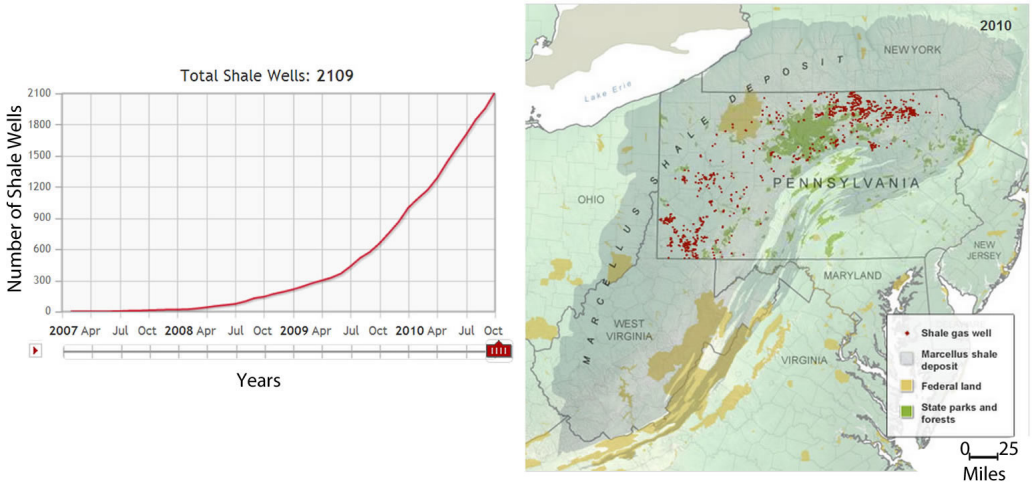

Figure 1.3: Shale wells in Pennsylvania from January 2007 to September 2010 (http://news.nationalgeographic.com/news/2010/10/101022-mapping-a-gas-boom/).

Especially over the past decade, hydraulic rock fracturing has become a much-used technique to increase the permeability and producibility of unconventional petroleum reservoirs. It basically forces the natural gas out of the formation by fractures within the reservoir. Large volumes of fluids are injected into the reservoir, often through deviated or horizontal wells. Fluid pressure changes cause the rock to fail, which then behaves as a seismic source or microseism (Kendall et al., 2011). With the help of proppant and fluids, cracks and new channels are created in the formation so that the hydrocarbons can be recovered from the trapped zones. Injecting high-pressure fluid to the formation may also reactivate pre-existing faults and fractures. Enhancing the subsurface fracture network allows underground resources propagate up to the surface. Figure 1.4 demonstrates the fundamental steps during fracturing process.

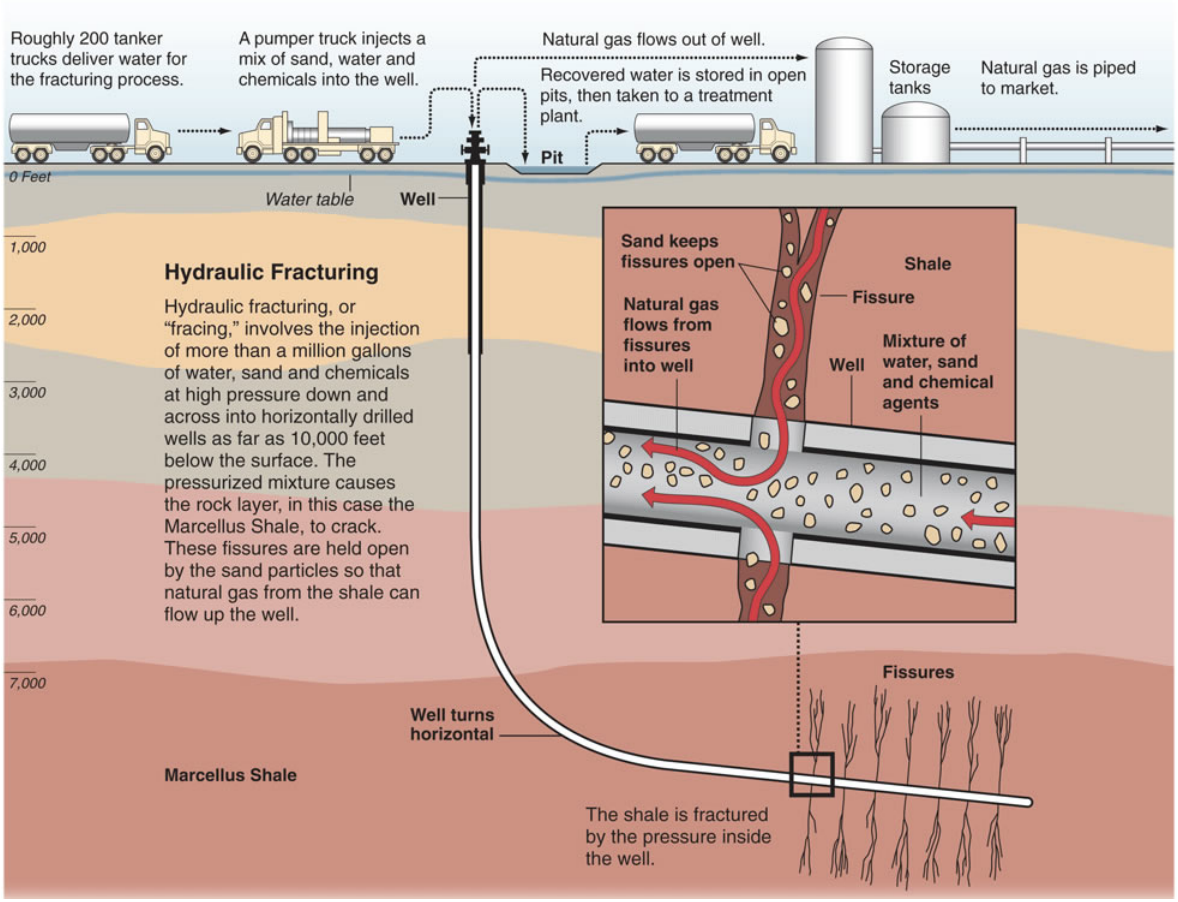

Figure 1.4: Schematic of hydraulic fracturing process (Granberg, 2010).

Microseismic imaging of hydraulic fracturing involves detecting micro-earthquakes associated with the induced fractures (Urbancic et al., 1999). The very small energy from the microseisms is recorded continuously by receivers placed on the surface and/or in the boreholes.

Reservoir dynamics can be mapped by passively listening to the earth and recording the small magnitude earthquakes caused by stress and strain changes in the reservoir. Mapping the event locations and mechanisms both in time and space at different stages can be used to understand how the reservoir rocks response to the stimulations (Eisner et al., 2009). Analyzing microseismicity is also useful for interpreting fracture location, orientation, height, growth, length of the fractured formation (Maxwell, 2012). Additional source parameters such as event magnitude, stress and

energy release, displacement of slip, orientation of fault etc., can be extracted from the microseismic events. Furthermore, moment tensor (beach ball solutions) can be determined by analyzing radiation patterns (Maxwell and Urbancic, 2001).

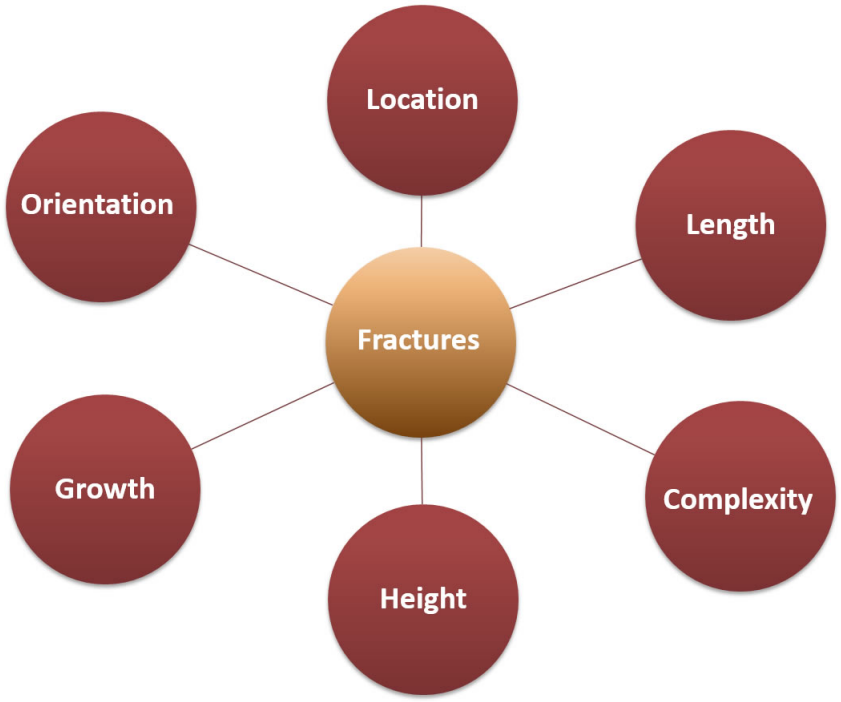

Figure 1.5: Fracture parameters can be extracted by analyzing microseismic events.

Microseismic monitoring is also a commonly used technique in CO_2 geologic sequestration projects. It helps to assess any possible seismic hazards can be caused by injection of CO_2, to map out the CO_2 radiation paths and to monitor fracture network activity (Riding and Rochelle, 2009).

Passive seismic monitoring differs from the active seismic method from various of aspects. Table 1.1 shows a comparison between active and passive seismic techniques (Eisner, 2013).

Table 1.1: Comparison of the passive and active seismic methods.

	Passive Seismic	Active Seismic
Origin time (to)	Unknown	Known and controlled
Seismic source location	Unknown	Known and controlled
Type of seismic source	Unknown	Known (dynamite or vibroseis)
Source Mechanism	Unknown	Uniform seismic source
Fracture type	Unknown	Generally point source assumption

1.2 OBJECTIVES AND CONTRIBUTIONS OF THIS THESIS

This thesis addresses several important aspects of microseismic monitoring:

1. **Experimental physical models;** The microseismic data used in this research are acquired on both physical models and real rocks. This research provides an overview of the physical modeling procedure using ultrasonic sources and receivers, describes and assesses the hypocenter algorithm.

2. **Locating microseismic events in time and space;** we have developed a migration-type location algorithm based on grid searching technique. The algorithm searches for the best location based on the traveltime residual, stacked energy and amplitude/traveltime residual ratio. Our method also uses an algorithm similar to the collapsing grid technique to speed up the location process.

3. **Repeatability of the tests;** In our experiments, we have chosen to test our algorithm and ideas with physical models to find answer for variety of questions: Which location method is more accurate? Should we use P-wave or S-wave or should we combine the two? Should we use traveltime or stacked energy attributes to locate events? Which location techniques are more accurate? How does excluding well-side receivers affect location uncertainty? Which acquisition design is more optimal for microseismic location and source mechanism characterization?

4. **Determination of source mechanism of the microseismic events;** focal

mechanism solutions provide us additional parameters other than just coordinates of microseismic events that helps us to understand the fundamentals of fracturing.

5. **Determining radiation patterns of microseismic events;** we aim to have a further understanding of the microseismic events by determining and analyzing the radiation patterns of the seismic waves.

6. **Studying the fundamentals of microseismic monitoring;** This research also focuses on some fundamental issues related to hydraulic fracturing and microseismic monitoring such as first arrival picking methods, noise attenuation techniques.

7. **Developing algorithms and GUI's;** Another main objective of this thesis is to develop algorithms and scripts related to microseismic monitoring. To this end, more than 30 scripts have been coded; 5 user-friendly GUI's are created, so that, location and focal mechanism algorithms can be used without prior knowledge of coding.

8. **Optimizing the algorithms;** Computation time and cost are vital especially in real-time microseismic monitoring. To increase performance of location algorithm, parallel CPU and GPU computing technologies have been taken advantage of.

1.3 OUTLINE OF THIS THESIS

This thesis composed of six chapters:

- **Chapter 1** introduces hydraulic fracturing and microseismic monitoring techniques. Then objectives and outlines of this research are presented.
- **Chapter 2** reviews the fundamental techniques used in microseismic monitoring.
- **Chapter 3** introduces the location software that is developed throughout this research. Furthermore, location and focal mechanism algorithms are explained in Chapter 3.
- **Chapter 4** explains all the experiments conducted in this research. For each physical modeling experiment, event location, focal mechanism determination, and radiation pattern determination are performed.
- **Chapter 5** summarize major contributions of this thesis.
- **Chapter 6** provides several important recommendations for future work.

Chapter 2. Review of Techniques Used in Microseismic Monitoring

2.1 NOISE-ATTENUATION TECHNIQUES

One of the key problems in geophysics and particularly in microseismic monitoring is to acquire a high quality seismic response of the earth. Geophysicists are trying to obtain seismic signals that have high signal-to-noise ratio (SNR), however, this task is difficult because the seismic signals radiated from the source are weaken by various factors such as attenuation, reflection, diffraction, transmission loss and noise. Sometimes, seismic signals, especially microseismic signals, are completely masked by the noise and it is impossible to detect them. Hence, one of the fundamental goal of the applied seismology is to increase the signal quality by achieving high SNR. Signal-to-noise ratio can be improved at the stage of acquisition and the processing (Bormann and Wielandt, 2013).

In the noise-attenuation process, the first step is to determine the noise characteristics and its cause. Noise characteristics can be divided into two categories regardless of the noise type (Dingus, 2010).

1. Coherent Noise: Ground roll, interbed multiples, powerline noise are some of the examples of the coherent noise. This type of noise can be suppressed or attenuated by applying various techniques such as Predictive Deconvolution, F-K filtering, Radon selection, wavefield extrapolation, etc.

2. Random Noise: Any kind of noise which is not coherent. This type of noise can be removed from the data by averaging, stacking.

In the case of microseismic surveys, having high a signal-to-noise (SNR) ratio is

much more important than in the case of conventional seismic surveys because microseismic events have very weak signals. Seismic waves propagating through the earth continuously lose their energy until they arrive at the receivers. Spherical spreading, attenuation, existence of weathering layer, surface noise decrease seismic energy. Microseismic signals have relatively low magnitude -4 to +2 on Richter scale (Eaton, 2008); therefore, detecting events and first arrivals is a major challenge. Particularly, surface microseismic surveys suffer from this issue more than downhole surveys due to the fact that near surface generally attenuates seismic energy significantly. Since it is very difficult to pick events in seismograms that have low SNR, attenuating noise and increasing SNR is quite desirable especially in the microearthquake case.

2.1.1 Frequency Filtering

In general terms, frequency filtering is the process of separating "the good (wanted)" components from the input signal by eliminating "the bad (unwanted)" frequencies. Filters can be designed and applied in the time domain by taking advantage of convolution; nevertheless, applying filters in frequency domain is more common way. If the filtering is carried out in the time domain, it is called as "Time Domain Filtering" and if it is done in the frequency domain, it is known as "Frequency Domain Filtering".

Digital filters can be characterized by how they handle input raw signals. A high-pass filter passes frequencies higher than the cut-off frequency while attenuating the lower ones. A low-pass filter is the just opposite; attenuates higher frequencies and passes low frequencies. A band-pass filter passes the signals that lie inside of a certain frequency band; whereas it attenuates the signals that lie outside of that frequency band (Press et al., 2007).

The frequency band of a hydraulically fractured microseismic source mainly lies between 80-200 Hz (Han, 2010). In order to attenuate the frequencies outside the

desired frequency band, a band-pass or a low-pass filter may be used to remove the unwanted noise. However, in this thesis, we have acquired data on hand-made physical models and natural rocks, using ultrasonic source and transducers. Ultrasonic transducers transmit signal whose frequency bandwidth is way higher (5 MHz dominant frequency) than the induced microseismic source case. To find out which frequency band is to be suppressed, it is necessary to transform signal to the frequency domain via Fourier transform.

I have developed "Design Filter" tool that allows user to design and apply filter to any kind of signal type. This tool is coded and designed in a MATLAB environment (Figure 2.1). "Design Filter" application has GUI (Graphical User Interface) so that user can interactively design any type of filter.

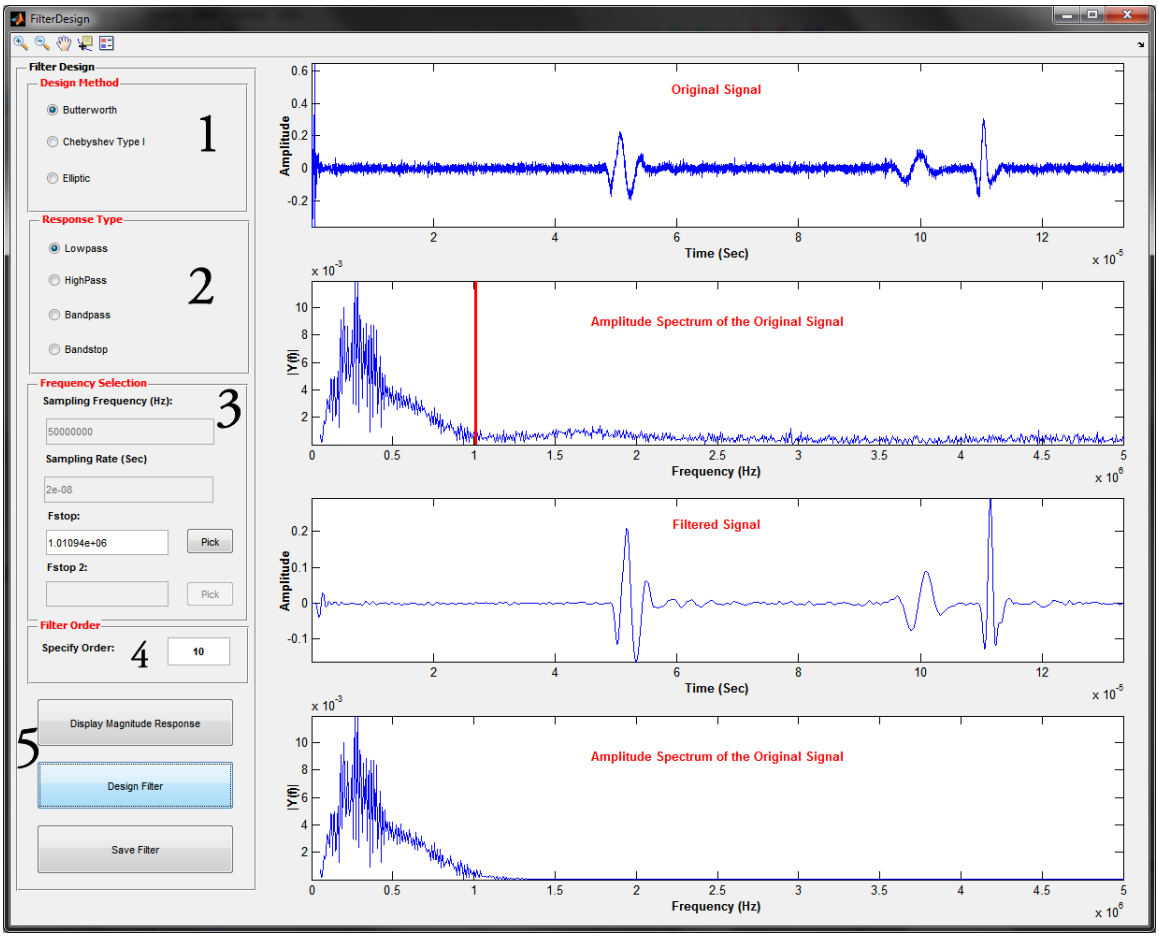

Figure 2.1: An auxiliary tool for designing and applying frequency filters.

From the section "1" on the Figure 2.1, user may choose one of the three types of the filters: Butterworth, Chebyshev filter I and Elliptic.

From the section "2", user may choose the response type of the filter whether it is low-pass, high-pass, band-pass or band-stop.

From the section "3", some parameters (Sampling frequency and sample rate) are shown for the information of user. In this section, user can interactively pick cut-off or corner frequencies after clicking "Pick" button.

From the section "4", it is possible to change the order degree of the filter. Default is 10th order.

At the section "5", user can display Magnitude and Phase response of designed filter. Once "Design Filter" button is clicked, it applies the designed filter to the input signal and shows original and filtered signals along with their Fourier transforms at the right hand side of the figure.

Figure 2.3 shows an individual seismic signal that is acquired on a Plexiglas model. 1-component transducer is used as receiver, and the signal is transmitted with a vertical P-wave source transducer. Due to the fact that the Plexiglas model is isotropic and homogeneous, only P-wave waveform is observed on our signal. Also the signal consists of a primary P-wave reflection from bottom of the Plexiglas model at about 90 microsecond. Sampling frequency and the sampling rate of the signal are 50 MHz and 20 ns (nanosecond), respectively. Nyquist frequency is calculated below in Equation 2.1

$$f_{Nyquist} = \frac{1}{2 * \Delta t} = \frac{1}{2 * 20ns} = 25MHz \tag{2.1}$$

It is important to find out the frequency components of our signal before designing a filter. Figure 2.4 shows the Fourier transform of the original signal. It is thought that the noise is caused by the higher frequencies than 1 MHz. To pass lower frequencies and reject higher ones, a Butterworth low-pass filter is designed. Figure 2.2 illustrates the magnitude and the phase response of the designed filter. Cut-off frequency of the

low-pass filter is chosen as 1 MHz.

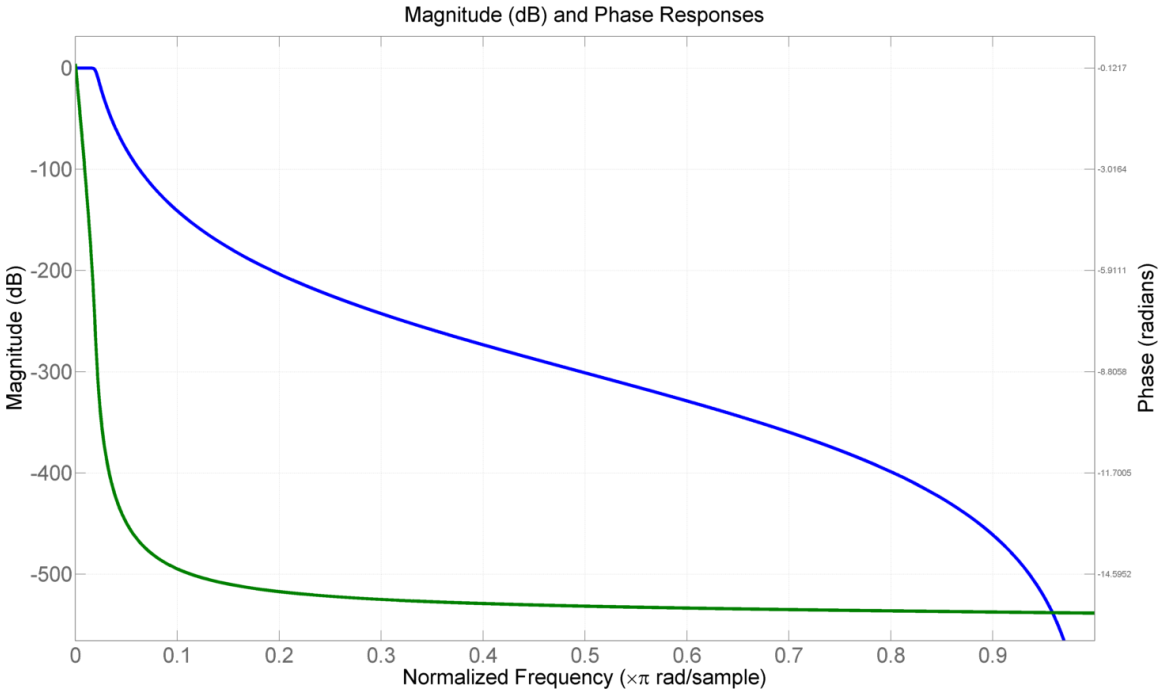

Figure 2.2: Magnitude and Phase Responses of the designed low-pass filter.

After applying the filter to the signal in the frequency domain, data is transformed to the time domain via inverse Fourier transform. Figure 2.5 shows the filtered signal and Figure 2.6 demonstrates the Fourier transform of the filtered signal. It is clear to see that low-pass filter reduces the amount of random noise. Signal-to-Noise ratio (SNR) increased to 36 dB from 17 dB.

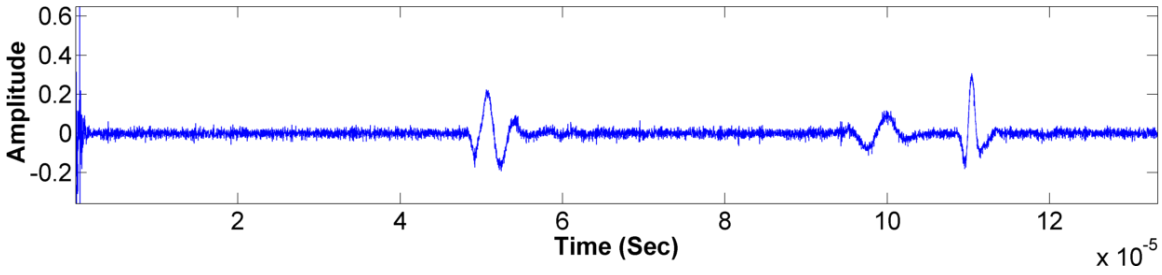

Figure 2.3: Raw seismic data contains only P-wave acquired on Plexiglas model using ultrasonic transducers (SNR=17 dB).

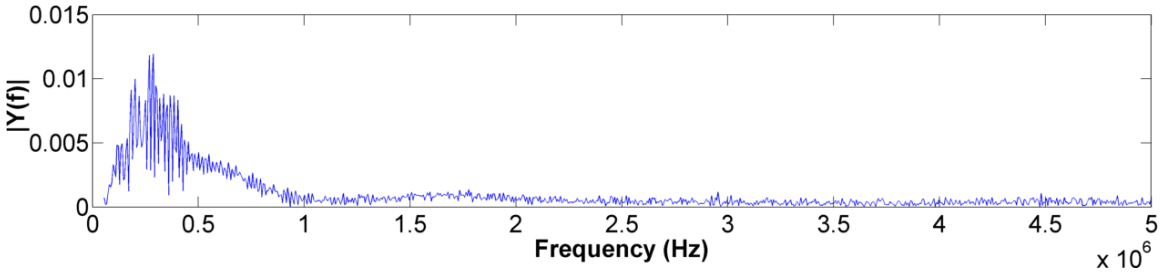

Figure 2.4: Fourier transform of the seismic signal shown in Figure 2.3.

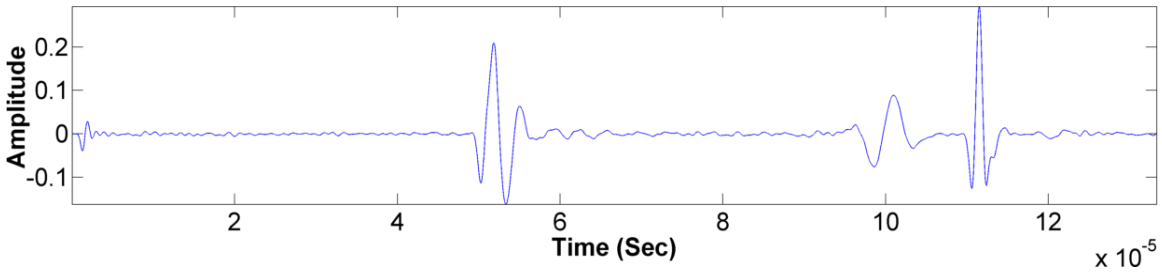

Figure 2.5: Seismic signal after applying low-pass frequency filtering (SNR=36 dB).

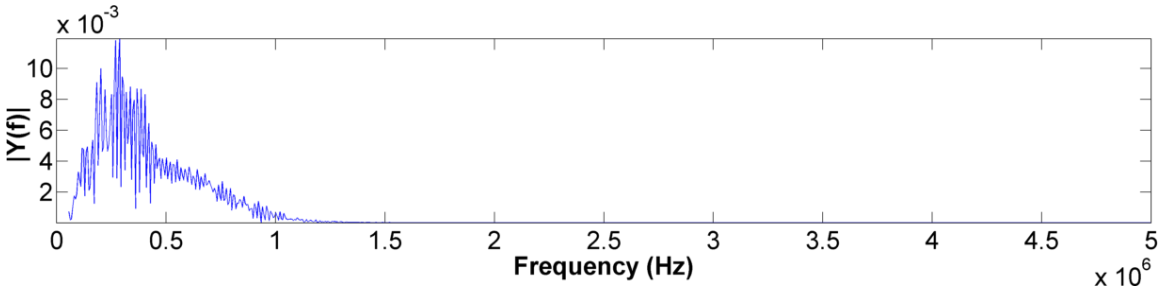

Figure 2.6: Fourier transform of the filtered seismic signal.

Careful selection of cut-off or corner frequencies is fundamental; otherwise, incorrect picking frequencies may cause distortions to the seismic signal. Figure 2.7 shows an example of seismic signal contains of P-wave and random noise with SNR = 17 dB. Figure 2.8 illustrates the Fourier response of the signal. To remove the random noise, a band-pass filter is applied with the following fstop frequencies: 170 kHz and 1 MHz with 10th order filter.

Corner frequencies are selected slightly outside of the target bandwidth intentionally to show the unfavorable effects. Figure 2.7 shows the both original seismic signal and filtered signal with blue and red line, respectively. Signal-to-noise ratio of the seismic signal has increased to 40 dB from 17 dB.

Even though it is observed that the noise is reduced by 23 dB, it is clear to see time shift on the raw data. First arrival of the P-wave is not at the same position anymore. Moreover, waveform of the P-wave is altered. Because of these reasons, careful selection of corner or cut-off frequencies are critical.

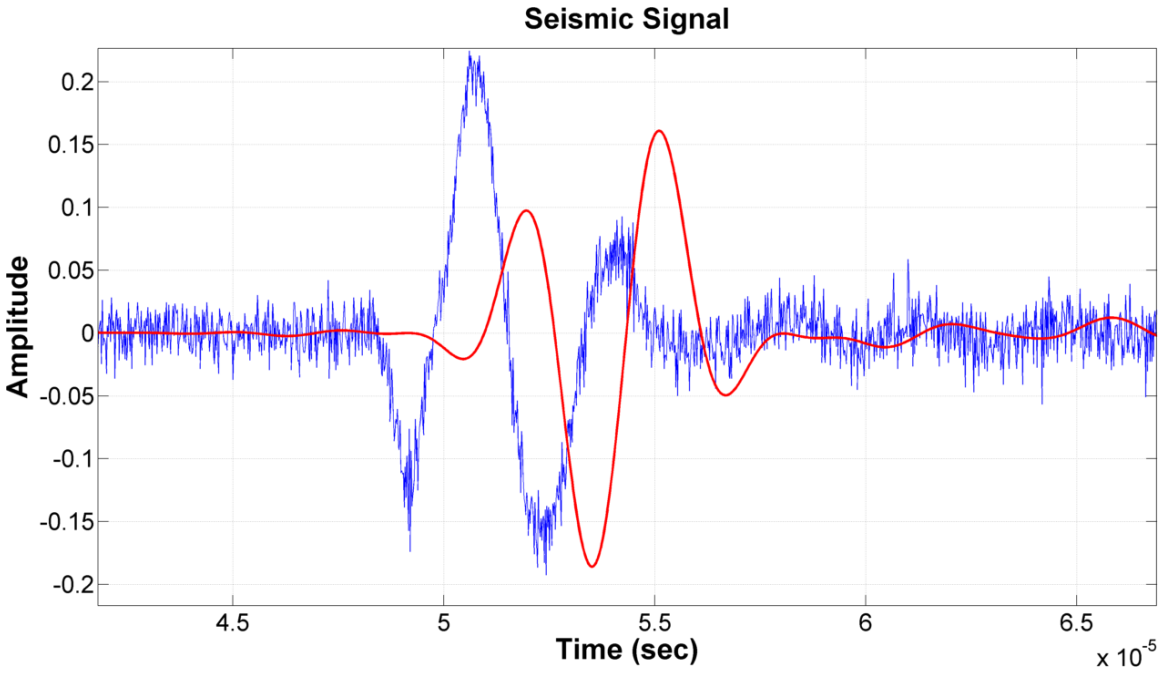

Figure 2.7: Seismic signal with noise (blue line) and the same signal after applying band-pass filter (red line). Picking wrong cut-off or corner frequencies cause time shift on the signal.

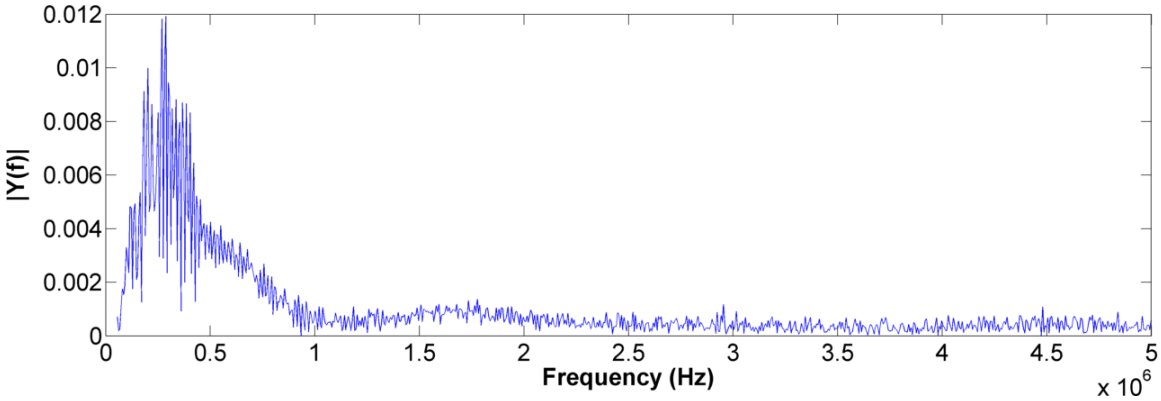

Figure 2.8: Fourier transform of the original seismic signal shown in Figure 2.7.

2.1.2 Trace Stacking

Another applicable and common method to reduce random noise is trace stacking. it is broadly used in seismic processing to sum traces recorded at nearby receivers. Random noise is greatly attenuated by this process, which stacked trace signal-to-noise ratio $\sqrt{n}$ times the original SNR; where n is the number of traces. The major challenge is to properly shift traces in time proportional to the their receiver locations.

In order to illustrate the concept, we have generated a set of synthetic seismograms using the receiver geometry depicted in Figure 2.9. Red and black stars symbolize receiver and source location, respectively. Blue lines represent the ray-paths, assuming it is isotropic and homogeneous medium. The source is set to coordinates of (500,-100) and nine receivers are set to along x-Axis; from 10 meters to 90 meters with 10 meters spacing.

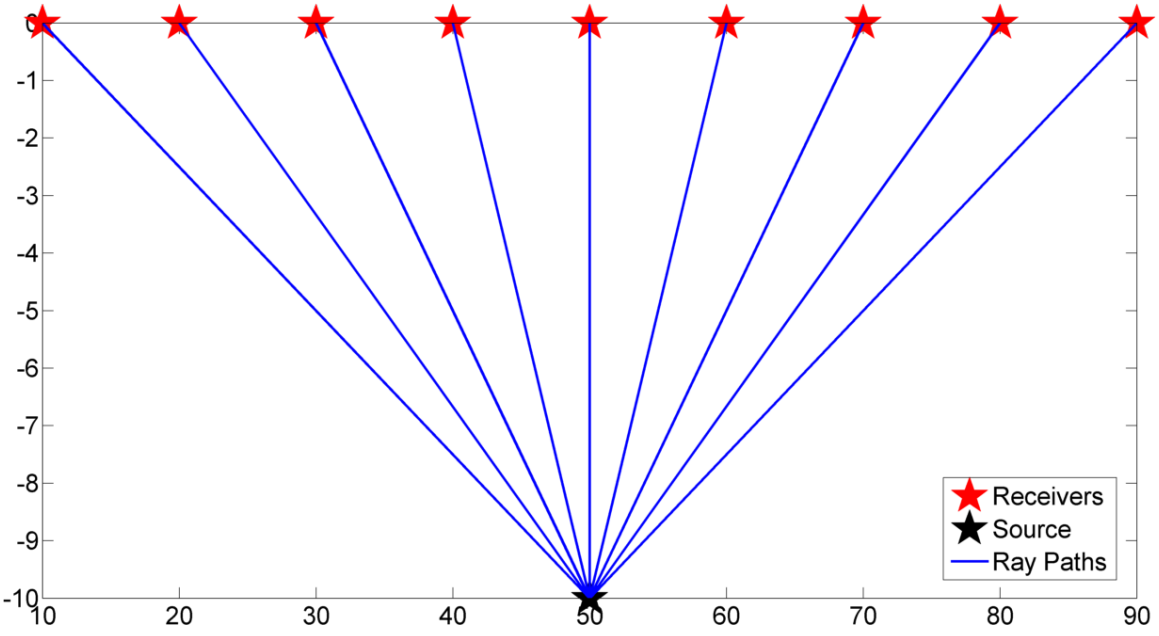

Figure 2.9: Receivers and source location used for generating synthetic seismograms. Red stars shows receiver locations and black star illustrates source location. Blue line is the ray paths from source to receivers.

Synthetic seismograms can be produced by taking a finite difference approach, which takes into account of direct P and S arrivals along with the multiples, refracted,

reflected and converted arrivals based on the velocity-density function. However, in this example, a conventional approach is followed to generate synthetic traces: convolving the wavelet with the reflectivity. Figure 2.11a shows the synthetic traces, note that they are noise free traces.

The synthetic seismogram is created by using the formula shown in 2.2 for each trace.

$$s_i(t) = w(t) * r(t) + n(t) \tag{2.2}$$

where $s_i(t)$ is the i^{th} trace of the t^{th} seismogram, w(t) is the source wavelet, r(t) is the reflectivity series of earth and n(t) is the random noise added to the seismic signal.

Figure 2.10 shows the source wavelet that we used for generating synthetics.

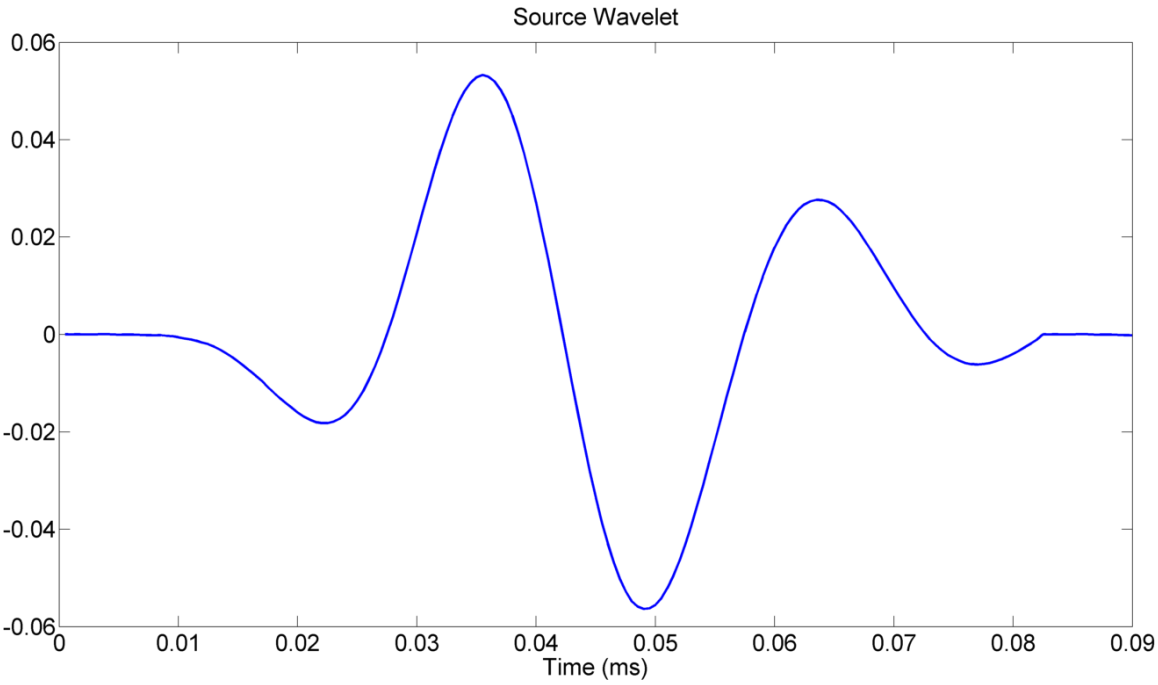

Figure 2.10: Source wavelet is used to correlate with reflectivity of the earth model.

Figure 2.11a illustrates the generated noise-free seismic traces according to acquisition geometry pictured in Figure 2.9. Figure 2.11b shows the seismic traces after

adding a certain amount of Gaussian noise. SNR of the noisy seismic trace is 13 dB.

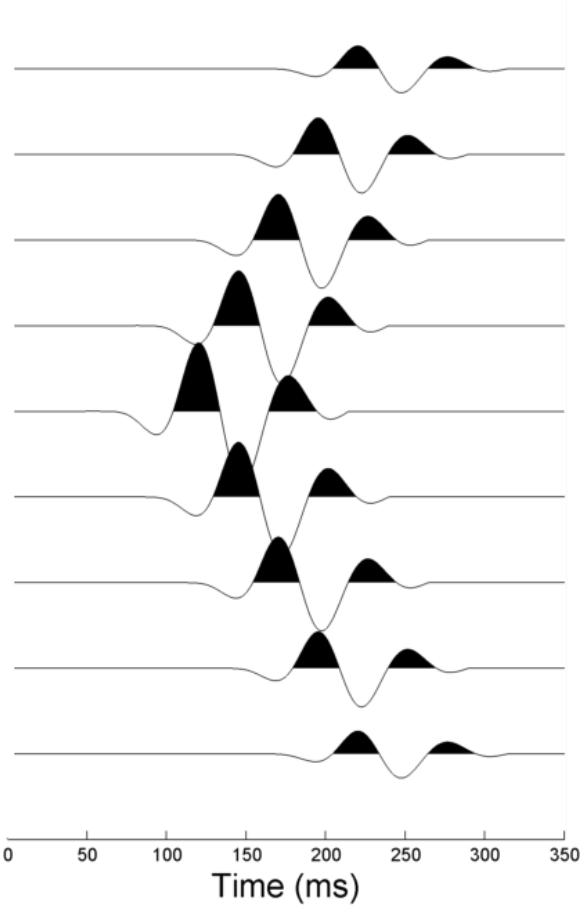

(a) Noise-free synthetic traces.

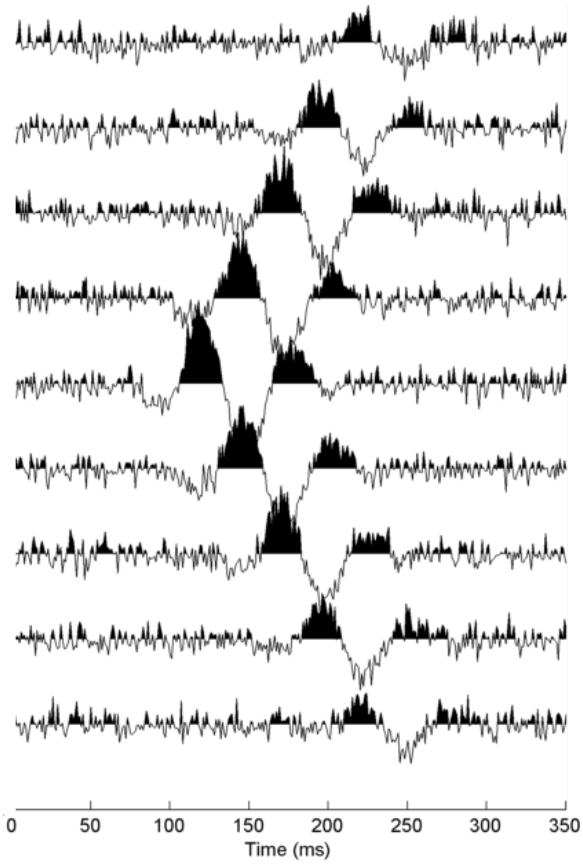

(b) Gaussian noise added to the synthetic traces.

Figure 2.11: (a) Noise-free and (b) noisy synthetic seismograms.

In order to stack the traces, they are all must be aligned by the reference trace. Figure 2.12 displays the aligned traces according to their first arrival time. This process is also called in reflection seismology as *Normal Moveout Correction.* This can be calculated with the formula shown in 2.3.

$$t^2 = t_0^2 + \frac{x^2}{V^2} \tag{2.3}$$

where; V = velocity of the medium, t_0 is the traveltime at zero offset.

After applying NMO correction, the next step is stacking, which is carried out with the equation shown in 2.4. Aligned traces are summed and then divided by the

number of traces.

$$s = \frac{1}{n} \sum_{i=1}^{n} g(i) \tag{2.4}$$

where; s is the stacked trace, $g(t)$ is the i^{th} seismogram and n is the number of seismogram.

Figure 2.12 displays the aligned seismic traces with black lines. At the bottom with red line, stacked trace is shown. It is clear to see that stacking process attenuates random noise greatly, in which SNR of the stacked trace is increased to 33 dB from 13 dB.

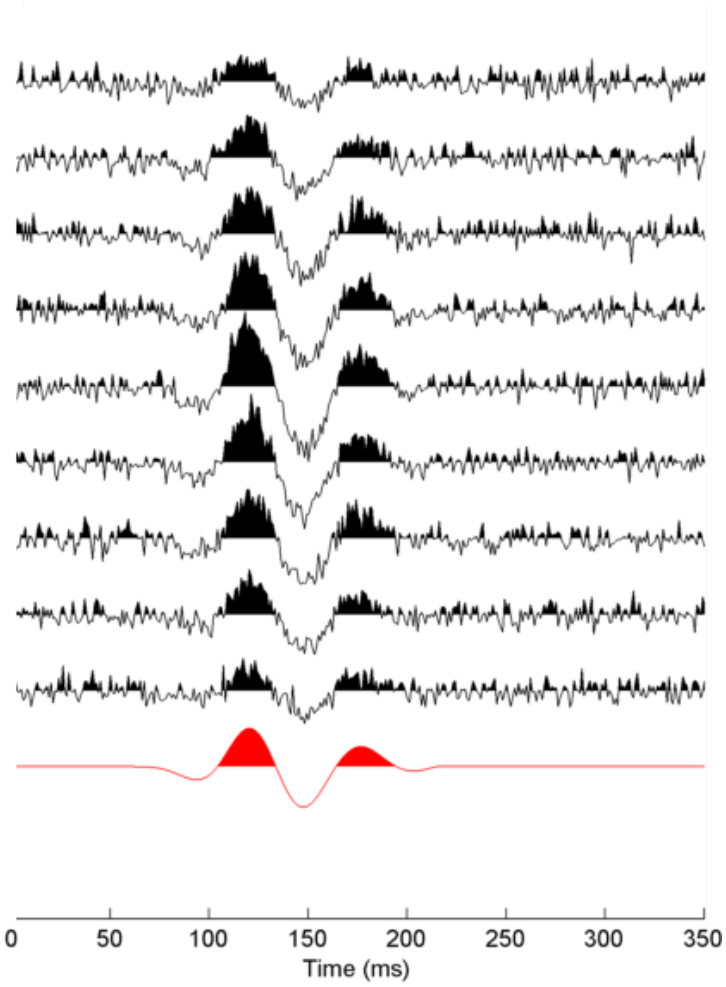

Figure 2.12: Shifted noisy traces (black lines) and stacked trace at the bottom (red line).

In this experiment, we take advantage of a similar concept to stacking during the data acquisition procedure. We acquired data at the same source and receiver location with 64 times and stack all of them, so that signal-to-noise ratio is enhanced remarkably. To further improve the quality of the data, we apply frequency filtering technique that we discussed in Chapter 2.1.1. Figure 2.13(a) displays one of the seismic trace acquired on a Plexiglas physical model along with the stacked and filtered version of the trace. Figure 2.13 shows (a) the raw data recorded on a Plexiglas model (b) same event with 64-fold vertical stacking (averaging) (c) stacked signal plus band-pass filtered data.

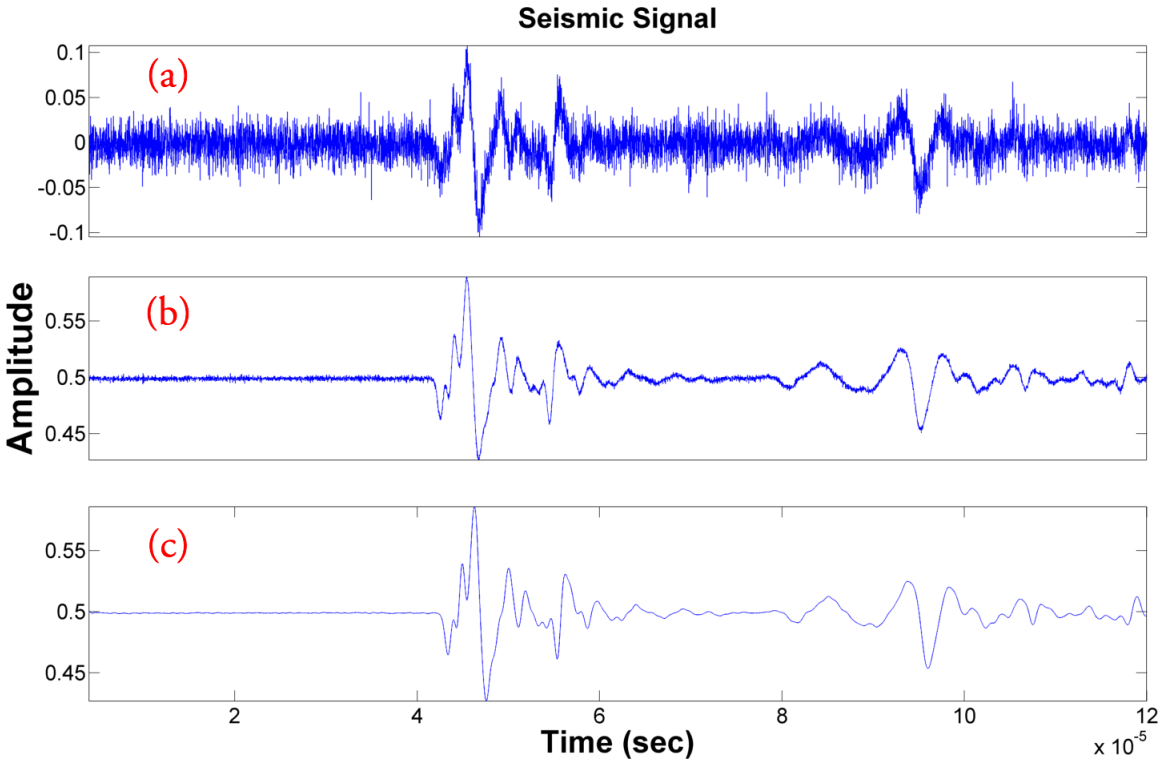

Figure 2.13: (a) Raw seismic signal (b) same signal with 64-fold vertical stack (c) same event with 64-fold vertical stack plus Butterworth band-pass filter applied.

Obtaining the data with 64-fold stack significantly attenuates the random noise, which SNR of the signal is increased to 48 dB from 6 dB. Applying band-pass filter further helps us to have a less noisy data. Signal-to-noise ratio raises to 54 dB from 48 dB. Table 2.1 shows the summary of SNR and peak amplitudes of the three traces.

Table 2.1: Summary of the three different scenarios in terms of their SNR and peak amplitudes.

Event Type	**SNR (dB)**	**Peak Amplitude**
Raw signal	6	0.1074
128-fold vertical stacked signal	48	0.5893
Stacked + bandpass filter applied signal	54	0.5840

2.2 FIRST ARRIVAL PICKING METHODS

In microseismic monitoring process, the first step is accurately locating events in time and space. In order to find the location of the events, it is a must to have accurate first arrival times of P and/or S-waves. Carefully picking first arrivals along with high quality accurate velocity models lead to the less error prone location solutions.

First arrival times of P and S waves can be picked manually if the amount of data is reasonable. However; long-term, live microseismic monitoring generates huge amount of seismic data, which determining first arrivals manually is impractical and time consuming. Having robust, fast, automated first arrival picking algorithms pave the way for real time monitoring of the reservoir dynamics.

Having an automatic-picking algorithm with high accuracy enables to handle huge datasets in seconds. Furthermore, manual picking of phase arrivals can be subjective; onset times may be picked differently by each seismologist. Due to the fact that algorithms depend on the same logic; picking errors are caused by the same picking style and algorithm (Earle and Shearer, 1994; Munro, 2004).

Different type of algorithms have been proposed to find an optimal method to determine first arrivals. Short-term-average over long-term-average (STA/LTA) method (Allen, 1978) is among one of the most popular techniques. Modified Energy function (Wong et al., 2009) is another similar methodology for automatic phase picking. Both of STA/LTA and Modified Energy Ratio (MER) functions use 2 windows that one precedes another. The fundamental difference between STA/LTA and MER is that MER uses windows precedes and follows each step whereas STA/LTA operates over

windows that precede each step (Rodriguez, 2011).

Other than the functions calculate energy of the seismic signal, there have been several other methods that depend upon different criteria: time domain, frequency domain, particle motion processing, or pattern matching (Xiantai et al., 2011). (Saragiotis et al., 2013) developed a method for automatic traveltime picking using instantaneous traveltime, (Montalbetti and Kanasewich, 1970)(Vidale, 1986) make use of polarization analysis tests to pick first breaks automatically, (Song et al., 2010) takes array-based waveform correlation approach, Hafez and Kohda (2009) presents the stationary discrete wavelet transform (SDWT) and Dai and MacBeth (1995) present a completely different alternative that makes use of artificial neural networks.

In my research, we have reviewed STA/LTA and MER methods and implemented them in a MATLAB environment. These first break picking algorithms are tied with the proposed location algorithm to form semi-automatic microseismic monitoring application.

The STA/LTA method uses two sliding energy windows (short and long time windows) with different lengths. This method can be explained in several steps:

First, the absolute amplitudes that lies inside the short and long windows are calculated for each seismic signal. Secondly, average amplitude values of both windows are then computed. At last, the ratio of the short term average and long term average window are calculated. These windows scans through the seismic signal with the user-defined window step value. For each window step, this ratio is compared with the user threshold value. An event is declared when the ratio of STA/LTA exceed a pre-defined threshold value. Selecting a treshold value is critical due to the fact that higher values tend to miss the first breaks whereas lower values may cause false trigger.

Equations 2.5, 2.6, and 2.7 define the energy ratio formulation representing the standard STA/LTA analysis approach:

$$STA(i) = \sum_{j=1}^{l_{sta}} \frac{a(j)^2}{l_{sta}} \tag{2.5}$$

$$LTA(i) = \sum_{j=1}^{l_{lta}} \frac{a(j)^2}{l_{lta}} \tag{2.6}$$

$$ER = \frac{STA(i)}{LTA(i)} \tag{2.7}$$

Where; l_{sta} is the length of the STA energy window, l_{lta} is the length of the LTA energy window under the condition of $l_{lta} > l_{sta}$, a(j) is the time series of seismogram. The LTA window related to the background noise of the seismic trace, wheras the STA window can be more sensitive to abrupt changes in amplitude. (Oye and Roth, 2003). Figure 2.14 shows a schematic diagram of both STA/LTA and MER methods.

The modified energy ratio has similar characteristics with STA/LTA method. In this method, two sliding window lengths are the same but their starting positions are different. Equation 2.8 and 2.9 represent the MER formula; a(j) is the amplitude of seismogram and L is the window length.

$$ER(i) = \frac{\sum_{j=i}^{i+L} a(j)^2}{\sum_{j=i}^{i-L} a(j)^2} \tag{2.8}$$

$$ER3 = [ER(i) * abs(a(i))]^3 \tag{2.9}$$

Figure 2.15 shows the main window of *First Arrival Picking* auxiliary tool implemented in MATLAB. It allows user to choose one of the two pre-coded algorithms and define input parameters (window lengths). After clicking *Plot* button, P and S-wave breaks are determined. Figure 2.16 show the seismic trace acquired on a model that was built by joining both Plexiglas and aluminum blocks. First breaks of P and S-waves are determined with using the Modified Energy function. In figure 2.16, red

and green vertical lines correspond to the P and S-wave arrivals, respectively. Figure 2.17 illustrates the time when the events are declared. First significant increase in the ratio resembles with the P-wave arrival and second significant increase in the ratio corresponds to the S-wave arrival.

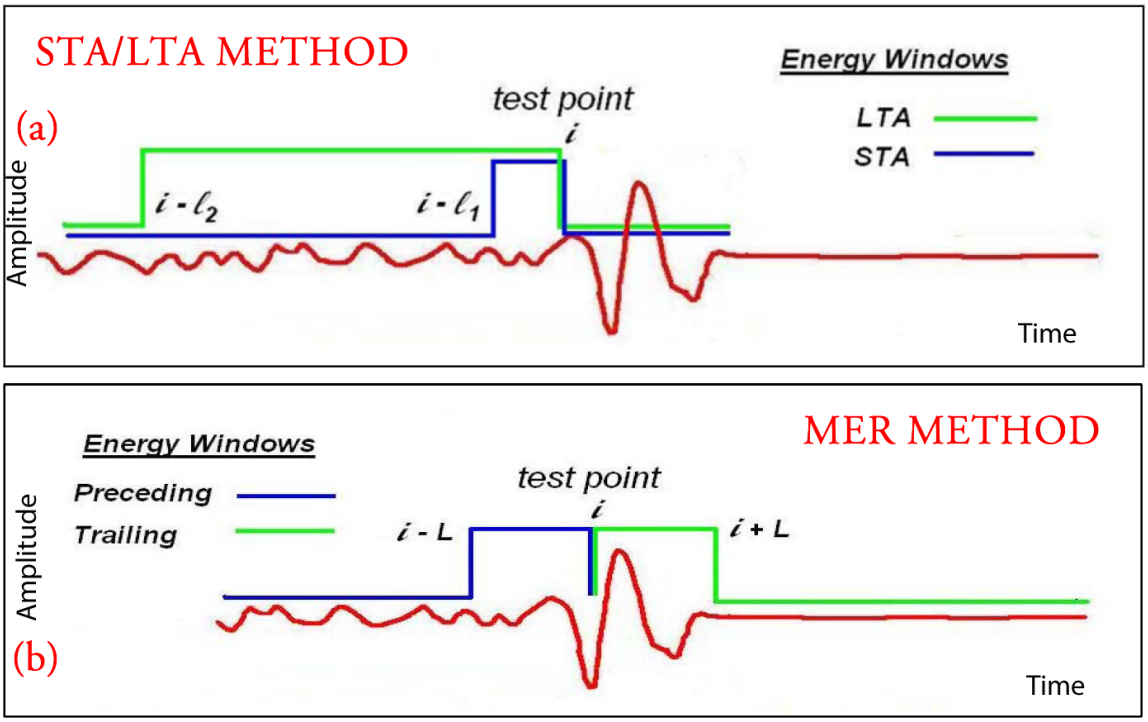

Figure 2.14: Energy windows definitions for (a) STA/LTA method (b) MER method. Adapted from (Han, 2010).

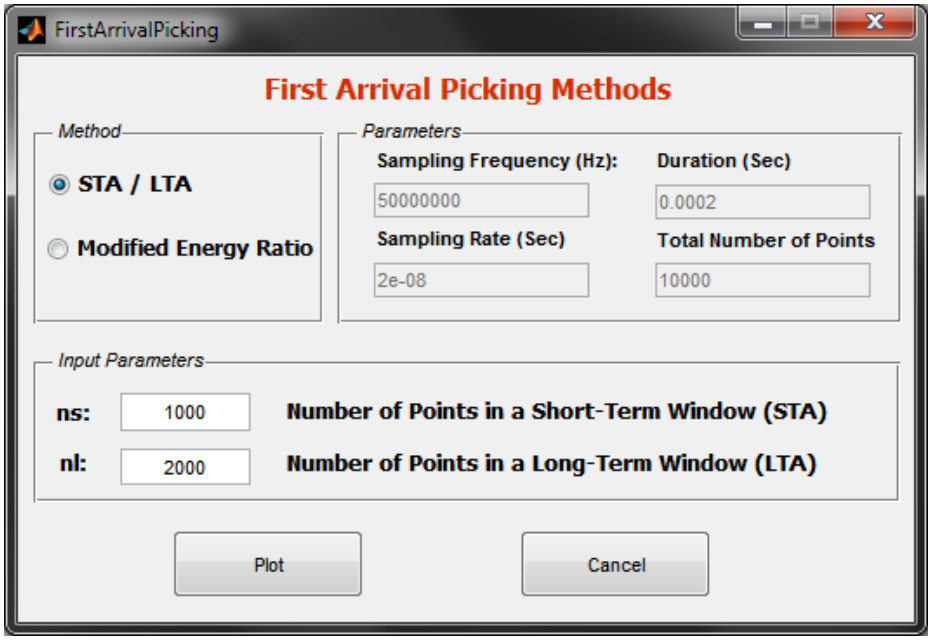

Figure 2.15: Main window of *First Arrival Picking* auxiliary tool implemented in MATLAB

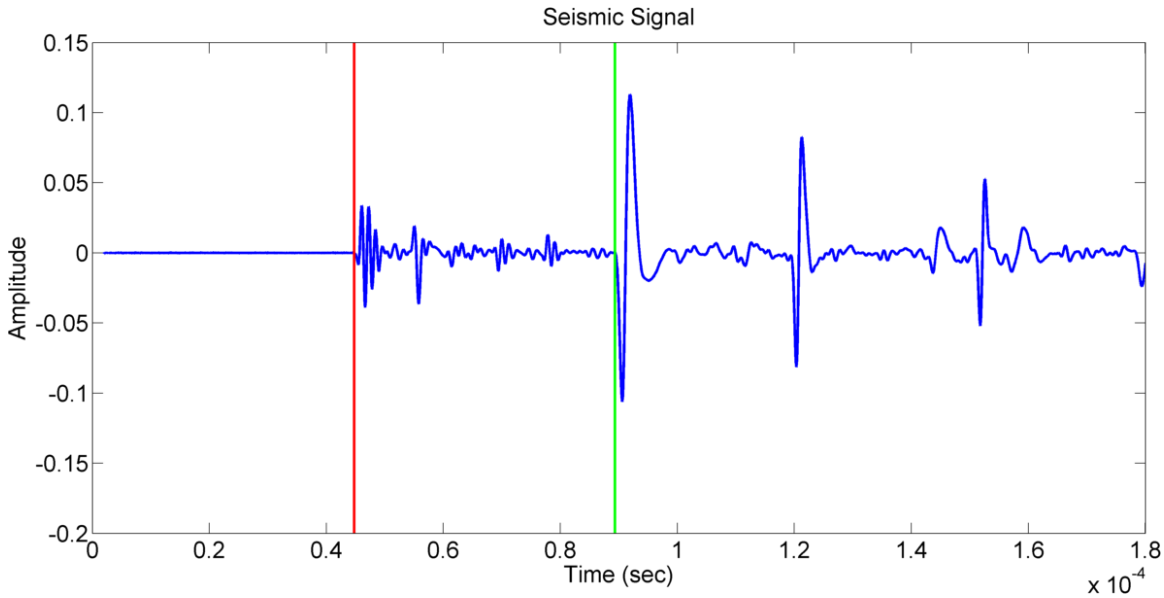

Figure 2.16: Seismic trace acquired on a model that was built by joining both Plexiglas and aluminum blocks. Red and green vertical lines correspond to the P and S-wave arrivals, respectively.

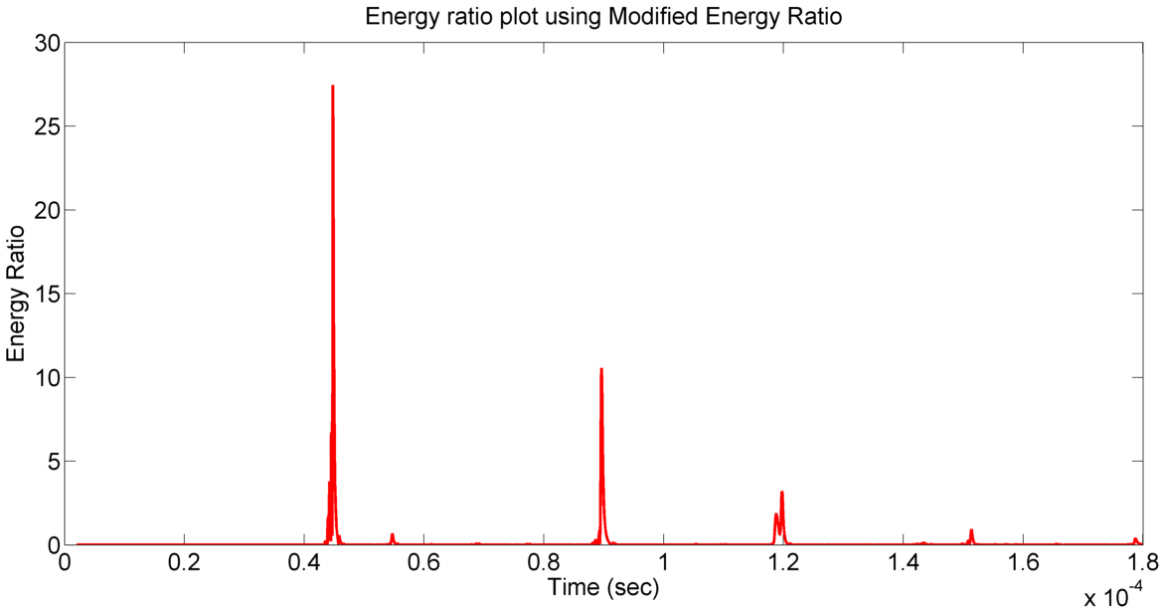

Figure 2.17: First breaks of P and S-waves are determined with using the Modified Energy function. First significant increase in the ratio resembles with the P-wave arrival and second significant increase corresponds to the S-wave arrival.

2.3 POLARIZATION ANALYSIS

In the conventional seismic methods where mostly one-component receivers are used, particle motion and direction of the seismic waves cannot be extracted. One of the fundamental advantages of three-component recordings is that it allows us to compute direction of particle motion of arrived seismic waves. It is well-known that each seismic phase have distinct polarization properties (Aki and Richards, 1980). Obtaining azimuth angle of the compressional and shear waves is vital especially in microseismic monitoring experiments, which they can be used as a constraint to locating events.

Polarization of the seismic waves can be determined both in time and frequency domain (Kanasewich, 1981). Flinn (1965) developed a technique that is based on the eigenproblem solution of covariance matrix as sliding window approach. Another common approach of computing particle motions is called Hodogram analysis. Sheriff (1973) describes "Hodogram" as a plot of the motion of a point as a function of time, that is, a display of a particle path especially with multicomponent detectors. In this research, 2D hodogram analysis method has undertaken and implemented in MATLAB environment.

In the first step of hodogram polarization analysis technique, it is necessary to extract information from the seismic structure that tells us when the P and S-arrival were estimated. This can be done manually or automatically using various types of event detection algorithms. In our research, we have choose to implement STA/LTA event detection algorithm to detect P and S wave time windows. Figure 2.18 illustrates a sample three-component seismogram and selected P and S wave time windows for hodogram analysis. After picking the time windows, the next step is to separate selected portion of the each traces for hodogram analysis.

Each three component (x-y-z) of seismogram can be represented in the form as

follows: $[s_x(t), s_y(t), s_z(t)]$ where; $s_x(t)$ is the x^{th} component, $s_y(t)$ is the y^{th} component, and $s_z(t)$ is the z^{th} component of seismogram "s" at the time index "t". Then the map view of hodogram can be created by cross-plotting $s_x(t)$ versus $s_y(t)$. Likewise, hodogram on the radial section can be generated by cross-plotting $s_z(t)$ versus $s_r(t)$ where, $s_r(t)$ is the radial component of the seismogram (Han, 2010).

Figure 2.19 shows hodogram plots of the three component seismic traces shown in Figure 2.18. Figures at the top with blue lines shows the P-wave particle motion; whereas, figures at the bottom with red lines illustrates S-wave particle motion. P-wave and S-wave polarization azimuth are 87 and -11 degrees, respectively.

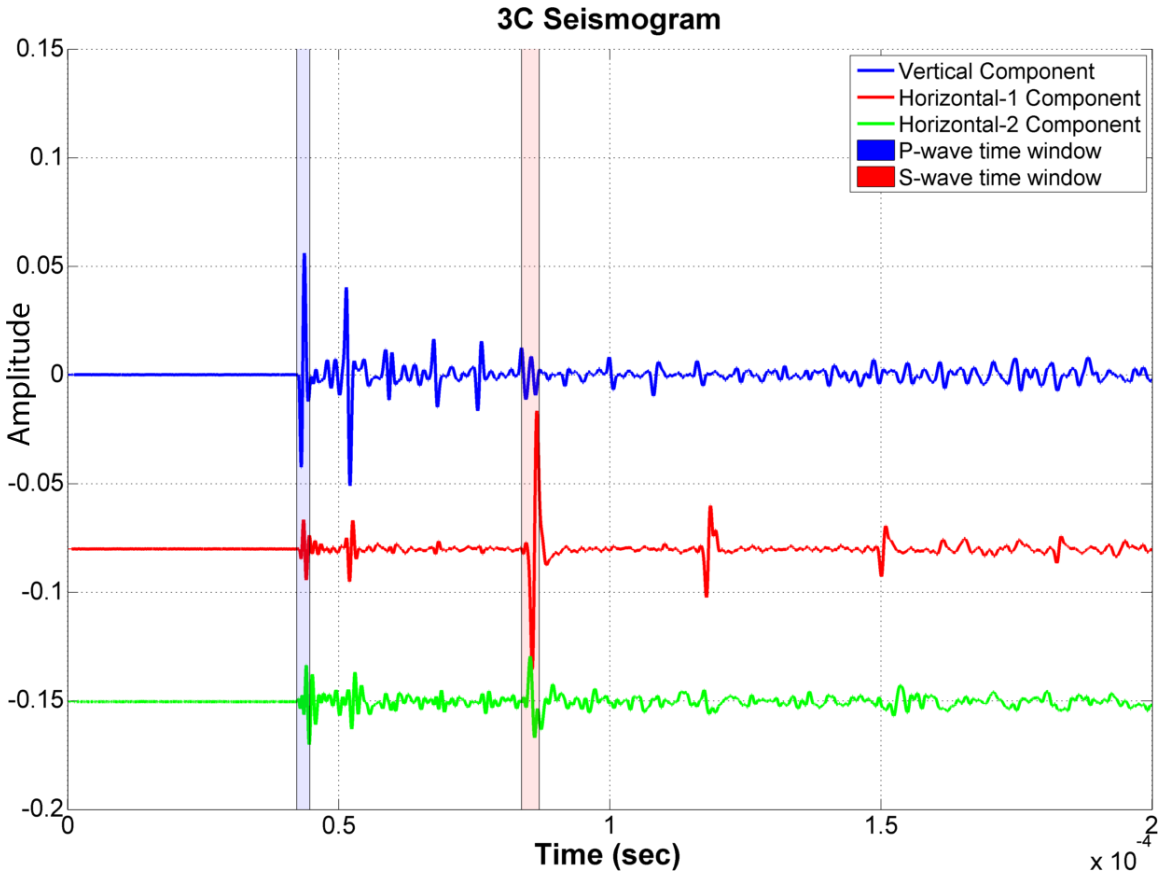

Figure 2.18: Sample 3C seismogram; blue, red and green lines represent vertical, axial and radial components, respectively.

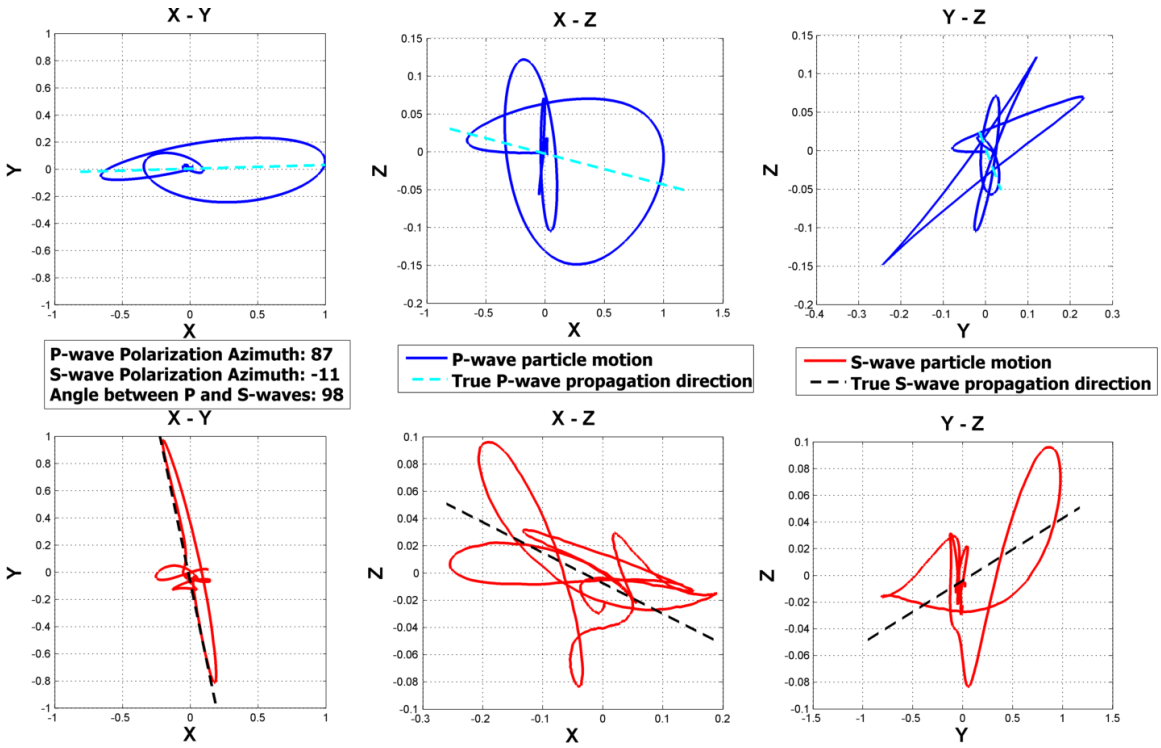

Figure 2.19: Hodogram plots of the three-component seismic signal.

2.4 HYPOCENTER LOCATION METHODS

Finding the spatial coordinates of the seismic sources (induced or tectonic) is one of the fundamental topics in a variety of geophysical applications. Detection of microseismic events caused by hydraulic fracturing applications is similar to the is based on the earthquake seismology. After the introduction of Geiger's method (Geiger, 1912), numerous of techniques has proposed and discussed.

Hypocenter location techniques can be divided into several groups. Location techniques that are based on determining seismic wave onsets and their traveltimes, migration techniques, polarization methods are some of them. Some of widely used methods among the techniques using traveltime are; HYPO71 (Lee and Lahr, 1975), HYPOELLIPSE (Lahr, 1980), and HYPOINVERSE-2000 (Klein, 2002). Another effective method that takes advantage of first arrivals of seismic waves is proposed by Lay and Wallace (1995), which is based on calculating a set of hemispheres of travel

distances using P and S wave arrival time differences. The hypocenter location is then determined at the intersection region of all hemispheres.

All these techniques benefit from the first-arrival determination, which makes precise picking crucial. Taking into consideration that microseismic events have relatively smaller energy than the tectonic earthquakes, more sophisticated methods are proposed to overcome undetectability issue of P and S waves.

Unlike travel-time based location methods, migration based hypocenter location algorithms take advantage of full wavefield of a detected event, which does not require accurate P and S wave picking. Moreover, migration techniques are more suitable when signal-to-noise ratio is low. McMechan (1982) proposed a finite-difference technique to determine hypocenter coordinates. Gajewski and Tessmer (2005) introduced a reverse modeling location technique which does not also depend on any picking of seismic events. Drew et al. (2005) introduced the coalescence microseismic monitoring technique for real-time event localization. Rentsch et al. (2006) proposed a technique inspired by Gaussian-beam migration of three-component data. Oye and Roth (2003) implemented a linearized inversion technique over a directed grid search method as well as the neighborhood algorithm.

In this thesis, we have implemented a grid search algorithm that calculates traveltime residual, stacked energy and amplitude/traveltime residual ratio for each potential point sources in the entire grid area. Localization is carried out in two iteration to increase speed of the algorithm.

In the first stage of the location method, a grid area that contains possible point sources is created. For all possible point sources (Figure 2.20), the following attributes are computed:

- Traveltime residual (difference between observed and calculated traveltimes)
- Stacked amplitudes
- Stacked amplitude/traveltime residual ratio

Synthetic traveltimes for each source and receiver are computed via shortest path ray tracing (Moser, 1991) algorithm. Traveltime residuals are computed by subtracting the calculated and observed traveltimes. Stacked amplitudes are computed by summing all the amplitude values that correspond to the calculated traveltimes at each seismogram. Lastly, the stacked amplitude/traveltime residual ratio is calculated for each source location.

After computing the three parameters mentioned above for all possible point sources, the algorithm picks the location where yields:

- Minimum traveltime residual
- Maximum stacked amplitude
- Maximum amplitude/traveltime ratio

The location algorithm will be introduced in details in Chapter 3.2.

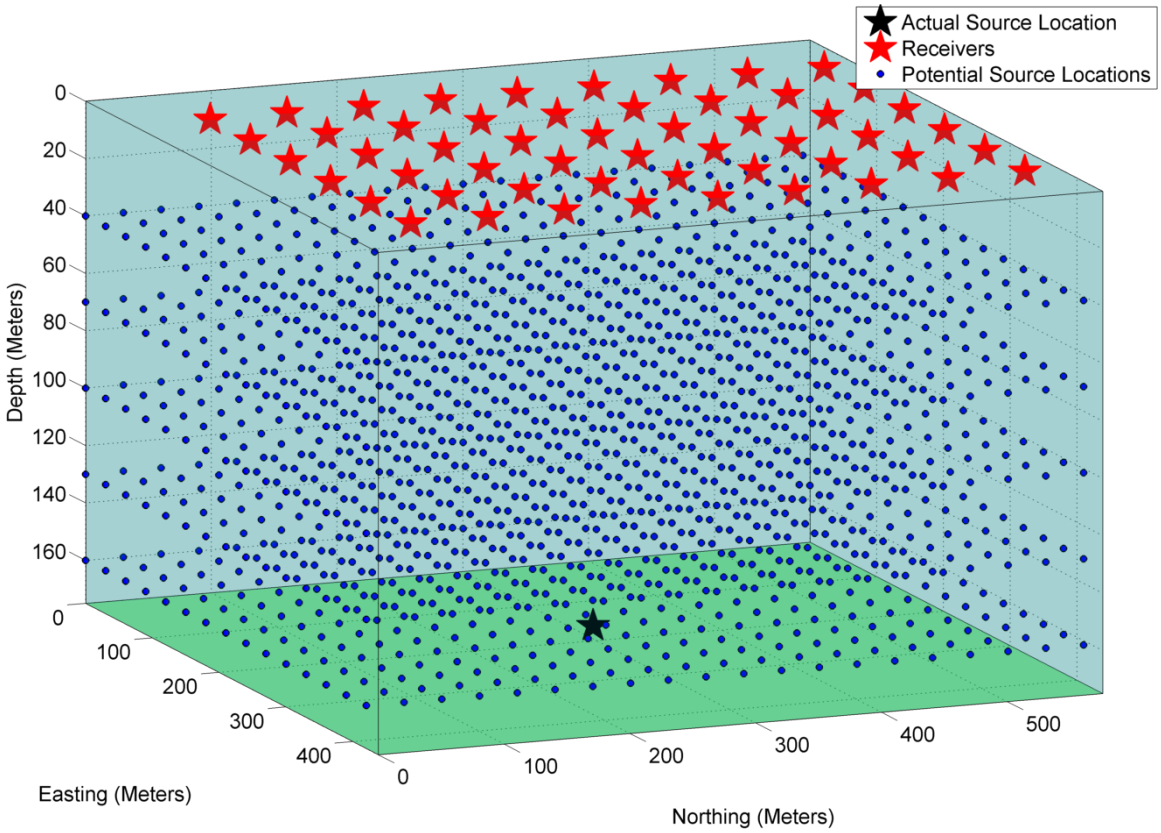

Figure 2.20: 3D view of a model. Red stars are receiver positions; black star is the actual source position and blue dots are potential point sources. The three attributes (traveltime residual, stacked amplitude and their ratio) are computed for each point in the entire grid area.

2.5 FOCAL MECHANISM AND RADIATION PATTERN DETERMINATION

2.5.1 Review of Focal Mechanism

A seismic event, whether tectonic or induced, created by the transformation of the free strain energy to propagating elastic strain energy. Not only seismic waves but also heat and rock displacement are produced as a result of this transformation (Angus, 1999). Understanding the source mechanism of a seismic event allows us to determine reservoir properties. Mapping the event locations and source mechanisms both in time and space at different stages can be used to understand how the reservoir rocks response to the stimulations (Eisner et al., 2009). Recently, extracting source

parameters for microseismic events such as the source type, source radius, slip amount, fault-plane orientation and slip direction, etc. takes more attention than just locating microseisms (Du et al., 2011).

It is desired to characterize source mechanism by associating the observed seismic waves to the source parameters that describe the mechanism best. One way to determine source parameters is to take a forward modeling approach, which requires theoretical displacements are obtained from different source models. In contrast with forward modeling, source parameters are derived from observed seismic waveforms called an inverse problem. In both cases, the first step is to figure out a mechanical model of seismic source (Forouhideh, 2011).

Figure 2.21 illustrates the fault geometry schematics that are commonly used in earthquake studies.

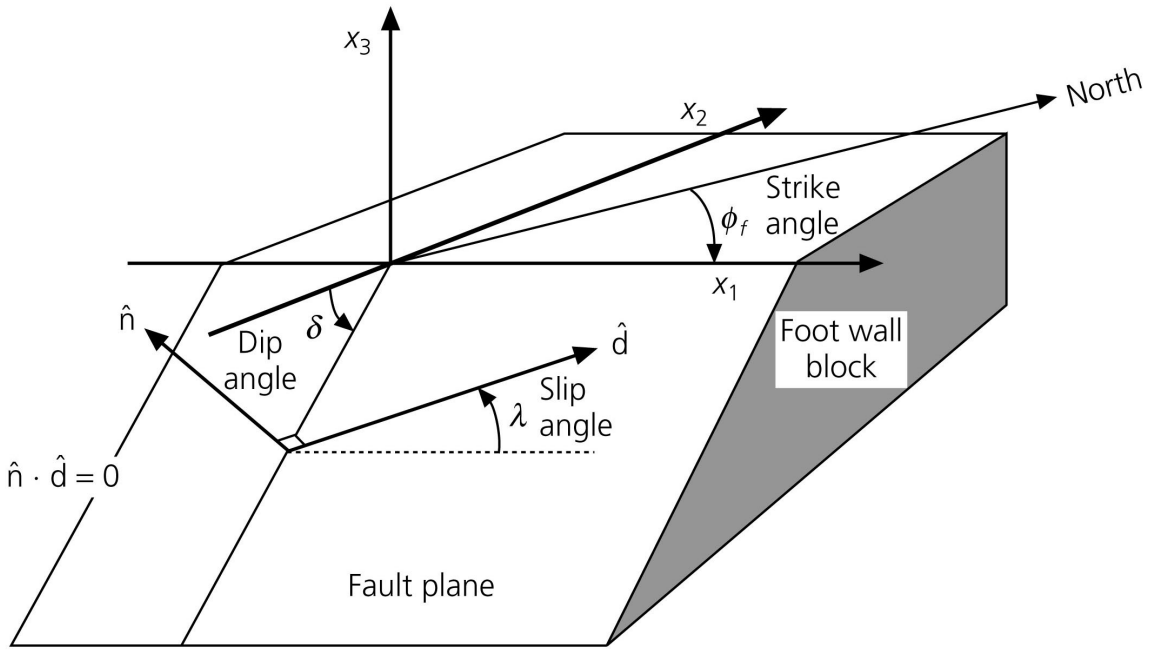

Figure 2.21: Schematics of fault geometry used in earthquake studies. Modified after (Kanamori and Cipar, 1974).

The fault plane is characterized by its normal vector, $\hat{n}$; direction of slip vector is shown with $\hat{d}$. The motion of the hanging wall block with respect to the foot wall

block can be expressed with the slip vector $\hat{d}$. Axis x_3 is chosen as the vertical axis and x_1 is oriented along the fault plane, such that the dip angle δ, is measured from the x_2 axis. Slip angle λ is calculated between x_1 and $\hat{d}$. Strike angle is measured clockwise from north (Stein and Wysession, 2003).

Normal and slip vectors can be mathematically expressed in Equation 2.10 and 2.11.

$$\widehat{n} = \begin{bmatrix} -\sin\delta\sin\phi_f \\ -\sin\delta\cos\phi_f \\ \cos\delta \end{bmatrix} \tag{2.10}$$

$$\widehat{d} = \begin{bmatrix} \cos\lambda\cos\phi_f + \sin\lambda\cos\delta\sin\phi_f \\ -\cos\lambda\sin\phi_f + \sin\lambda\cos\delta\cos\phi_f \\ \sin\lambda\sin\delta \end{bmatrix} \tag{2.11}$$

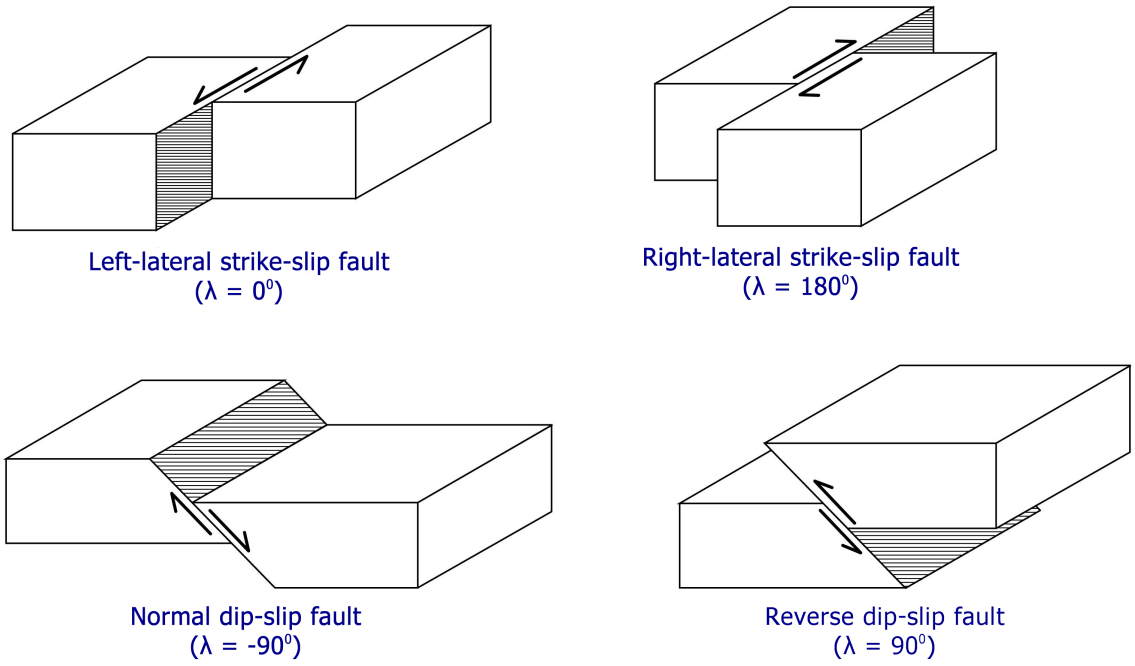

Figure 2.22: Basic types of faulting. Modified after (Stein and Wysession, 2003).

2.5.2 Seismic Moment Tensor

Nakano (1923) was the first to introduce a point-source approximation to the source mechanism literature. This assumption is valid if the distance between source and receivers is larger than the source dimensions (Aki and Richards, 1980).

Nakona defines the source of body forces acting at a point. Because fracturing is as a result of these forces, they are called equivalent forces (Forouhideh, 2011). Various seismic source mechanisms can be modeled by using force couples, which is known as seismic moment tensor. Figure 2.23 shows the variety of force couples that form in nine different source types.

The seismic moment tensor is one of the ways to represent point sources, which is used to differentiate different microseismic source types (Eaton, 2009). Equation 2.12 defines seismic moment tensor mathematically.

$$M = \begin{bmatrix} M_{11} & M_{12} & M_{13} \\ M_{21} & M_{22} & M_{23} \\ M_{31} & M_{32} & M_{33} \end{bmatrix} \tag{2.12}$$

The seismic moment tensor matrix is symmetric as are the stress and strain tensors; therefore, contains only 6 independent components: $M_{12} = M_{21}$; $M_{23} = M_{32}$; and $M_{13} = M_{31}$ Different source mechanisms can be formed with different force couples. Situations where the two couples are oriented in the same direction (M_{11}, M_{22}, or M_{33}), the moment tensor indicates an existence of a volume change at the source. For other source types, where the force couples oriented at the different directions, moment tensor represents deviatoric source mechanism (Aki and Richards, 1980; Angus, 1999).

Combining different couples at different orientations into seismic moment tensor. Figure 2.24 shows general schematics of variety of seismic sources.

By the help of eigenvalues of the moment tensor, it is possible to derive the

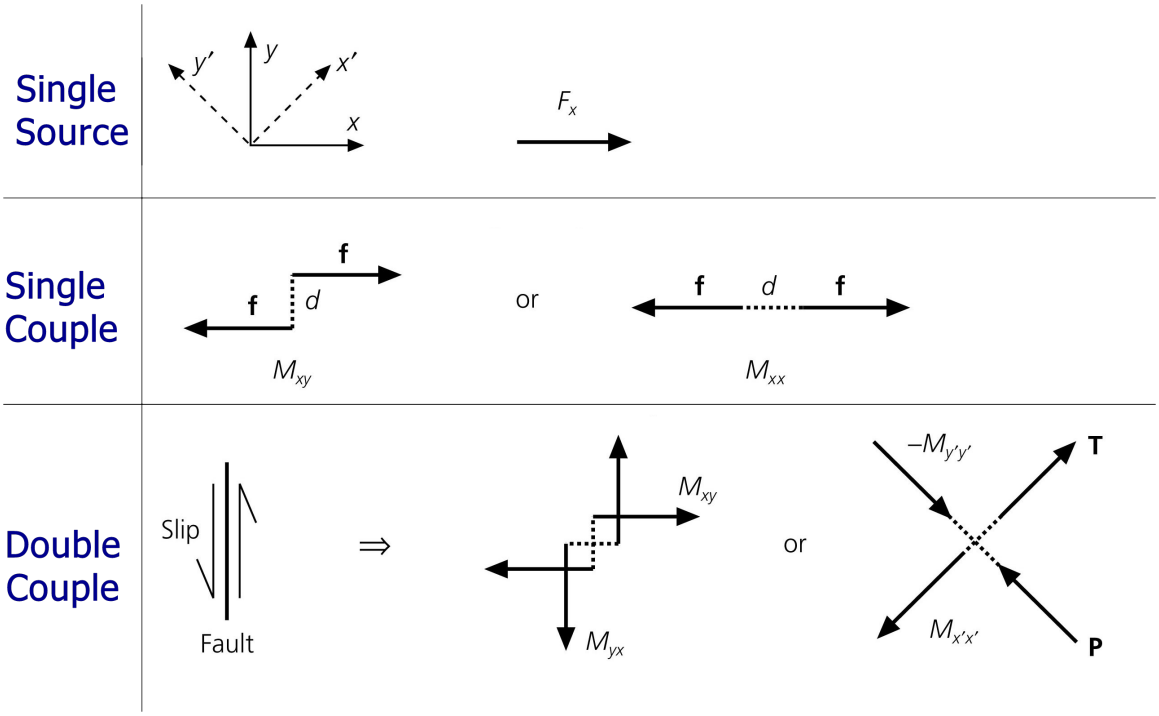

Figure 2.23: Schematic description of equivalent body forces for a single source, single couple and double couple. Modified after (Stein and Wysession, 2003).

equivalent forces. Isotropic component of the moment tensor, in other words a volume change at the source, can be described by the sum of the eigenvalues of the moment tensor. Being negative or positive of the sum of the eigenvalues determines the source type. The source has an explosive component (Figure 2.25) of if the sum is positive. On the other side, if the sum is negative, the isotropic component is due to an implosion (Stein and Wysession, 2003; Jost and Herrmann, 1989).

If the sum of eigenvalues vanishes then the seismic moment tensor has only deviatoric components. If only one eigenvalue is zero, it represents a pure double couple source. Lastly, a CLVD (Compensated Linear Vector Dipole) can be produced in the following conditions: the sum of the eigenvalues are zero and none of the eigenvalues vanishes (Jost and Herrmann, 1989).

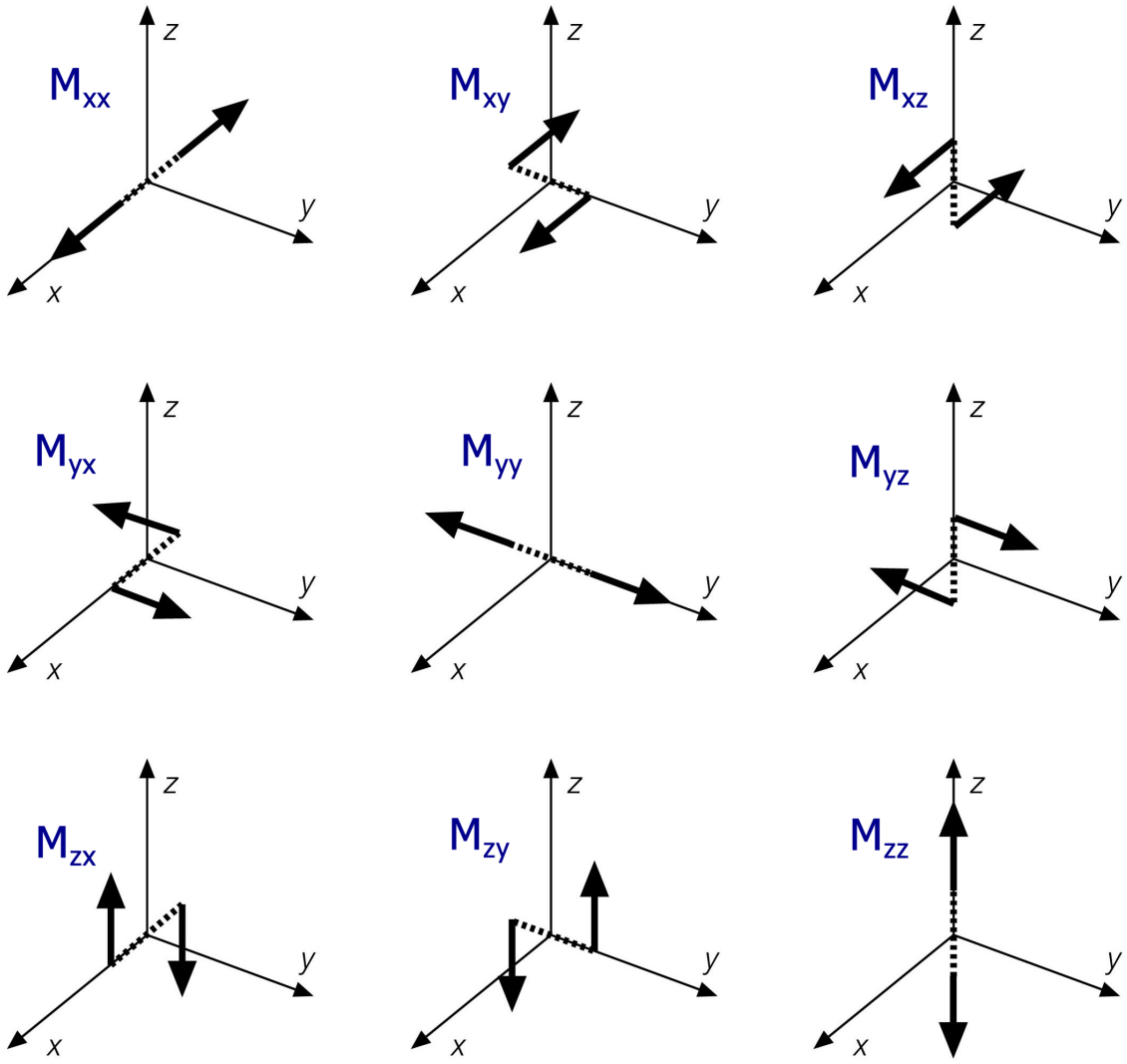

Figure 2.24: Schematics of variety of force couples. Modified after (Aki and Richards, 1980).

In conclusion, seismic moment tensors may be composed of various amounts components, which can be either isotropic, double-couple, or CLVD. Solution and decomposition of moment tensors is unique, which results in variety of interpretations (Forouhideh, 2011; Jost and Herrmann, 1989).

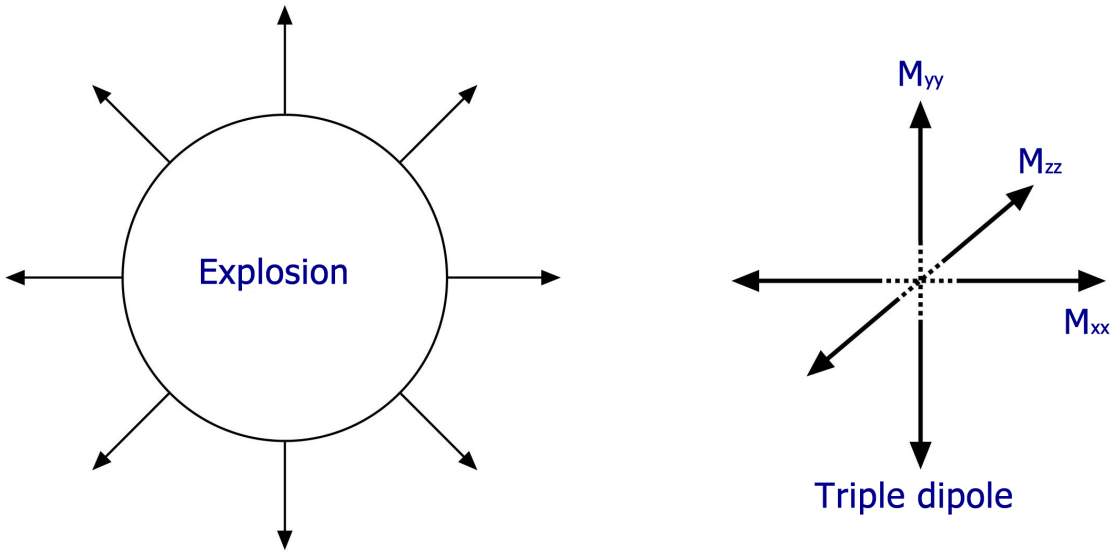

Figure 2.25: Explosion source modeled with triple equal forces. Modified after (Stein and Wysession, 2003).

2.5.3 Moment Tensor Inversion

There are various ways to perform an inversion of the seismic moment tensor. Depending on the type of waves, and available parameters, inversion can be carried out in both time and frequency domain (Jost and Herrmann, 1989). Equation 2.13 can be used to perform an inversion in the time domain (Gilbert, 1971; Strelitz, 1978; Scott and Kanamori, 1985). If the Green's function (source-time function) is not known, the moment tensor can be inverted in the frequency domain (Dziewonski and Gilbert, 1974; Mendiguren, 1977; Romanowicz, 1981) via Equation 2.14.

$$d_n(x,t) = M_{ij}[G_{nk,j} * s(\bar{t})] \tag{2.13}$$

$$d_n(x,f) = M_{kj}(f)G_{nk,j}(f) \tag{2.14}$$

Equation 2.13 and 2.14 can also be expressed in the matrix form:

$$d = G\overline{m} \tag{2.15}$$

Where d is a vector consists of n sampled observed ground displacements. G is a n x 6 matrix composed of the Green's functions and $\overline{m}$ is a vector contains moment tensor elements.

In the frequency domain, Equation 2.15 can be written separately for each frequency, where; d has real and imaginary parts of displacement spectra. G and $\overline{m}$ has also imaginary and real parts if the frequency domain approach is followed (Jost and Herrmann, 1989).

$$\begin{bmatrix} d1 \\ d2 \\ .. \\ dn \end{bmatrix} = \begin{bmatrix} G_{11} & G_{12} & G_{13} & G_{14} & G_{15} & G_{16} \\ .. & .. & .. & .. & .. & .. \\ .. & .. & .. & .. & .. & .. \\ G_{n1} & G_{n2} & G_{n3} & G_{n4} & G_{n5} & G_{n6} \end{bmatrix} \tag{2.16}$$

Solving the matrix equation system shown in Equation 2.16, Green's function (G) has to be inverted. Given that the G is not square matrix, moment tensor inversion can be accomplished via least-squares scheme (Equation 2.17).

$$m = (G^T G)^{-1} G^T u \tag{2.17}$$

2.5.4 Double-couple sources

Earthquakes or microseismic events that are produced as a result of a shear failure may be thought as double-couple source, which, two force couples acting together (Stein and Wysession, 2003). Double-couple source can be expressed in the Equation 2.18.

$$M_{kj} = \mu A(u_k V_j + u_j V_k) \tag{2.18}$$

Where μ is the shear modulus, A is the area of the fault plane, u represents the slip vector, and v is the normal vector to the fault plane (Aki and Richards, 1980).

Double-couple representation as the moment tensor is shown in Equation 2.19.

$$M = \begin{bmatrix} 0 & M_0 & 0 \\ M_0 & 0 & 0 \\ 0 & 0 & 0 \end{bmatrix} = M_0 \begin{bmatrix} 0 & 1 & 0 \\ 1 & 0 & 0 \\ 0 & 0 & 0 \end{bmatrix} \tag{2.19}$$

Fundamental properties of the double-couple source are; one eigenvalue in the matrix is zero, and the trace of the tensor is also zero.

2.5.5 Non-double-couple sources

Non-double couple sources can be divided into two components; isotropic component and CLVD. If the all three diagonal elements of seismic moment tensor is zero and equal, it can be described with the isotropic component of moment tensor such as an explosion or implosion. CLVD can be characterized with the volume change because three sets of force dipoles with one dipole -2 times of the other dipole (Stein and Wysession, 2003; Forouhideh, 2011).

Isotropic and CLVD components can be expressed with the moment tensors shown in Equations 2.20 and 2.21.

$$M_{iso} = \begin{bmatrix} E & 0 & 0 \\ 0 & E & 0 \\ 0 & 0 & E \end{bmatrix} \tag{2.20}$$

$$M_{clvd} = \begin{bmatrix} -\lambda & 0 & 0 \\ 0 & \lambda/2 & 0 \\ 0 & 0 & \lambda/2 \end{bmatrix} \tag{2.21}$$

CLVD mechanism can be explained in two fundamental ways. First is a volcanic eruption event, which may be expressed as a crack opening. Moment tensor of crack opening is as following:

$$M_{clvd} = \begin{bmatrix} \lambda & 0 & 0 \\ 0 & \lambda/2 & 0 \\ 0 & 0 & \lambda + 2\mu \end{bmatrix} \tag{2.22}$$

Where λ and μ are Lame's elastic constants. Seismic moment tensor shown in Equation 2.22 can be decomposed into isotropic components (Forouhideh, 2011) as follows:

$$M_{clvd} = \begin{bmatrix} \lambda & 0 & 0 \\ 0 & \lambda & 0 \\ 0 & 0 & \lambda + 2\mu \end{bmatrix} = \begin{bmatrix} E & 0 & 0 \\ 0 & E & 0 \\ 0 & 0 & E \end{bmatrix} + \begin{bmatrix} -2/3\mu & 0 & 0 \\ 0 & -2/3\mu & 0 \\ 0 & 0 & 4/3\mu \end{bmatrix} \tag{2.23}$$

Furthermore, a CLVD source type can also be composed of two double-couple sources. Equation 2.24 shows the moment tensor of a CLVD source that is decomposed into two double-couple sources.

$$M = \begin{bmatrix} M_0 & 0 & 0 \\ 0 & 0 & 0 \\ 0 & 0 & -M_0 \end{bmatrix} = \begin{bmatrix} 0 & 0 & 0 \\ 0 & -2M_0 & 0 \\ 0 & 0 & 2M_0 \end{bmatrix} + \begin{bmatrix} M_0 & 0 & 0 \\ 0 & -2M_0 & 0 \\ 0 & 0 & M_0 \end{bmatrix} \tag{2.24}$$

2.5.6 Radiation Patterns of Body Waves

Radiation patterns for far-field displacement can be derived by using point-source approximation, which it is valid if the distance between source and receivers is larger than the source dimensions. P and S wave radiation pattern for the far-field displacement from a shear failure in isotropic and homogeneous media can be expressed in Equations 2.25 and 2.26 (Aki and Richards, 2002).

$$A_S^P = (sin2\theta cos\phi)\hat{r} \tag{2.25}$$

$$A_S^S = (cos2\theta cos\phi)\hat{\theta} + (-cos\theta sin\phi)\hat{\phi} \tag{2.26}$$

Where $\hat{r}$, $\hat{\theta}$, and $\hat{\phi}$ represents vectors in spherical-polar coordinate system.

Likewise, far-field radiation patterns of the body waves caused by a tensile dislocation in an isotropic and homogeneous medium can be defined as follows (Shi and Ben-Zion, 2009).

$$A_T^P = (\lambda/\mu + 2cos^2\theta)\hat{r} \tag{2.27}$$

$$A_T^S = (-sin2\theta)\hat{\theta} \tag{2.28}$$

Where A_S^P is the P-wave radiation pattern caused by a shear dislocation, A_S^S is the S-wave radiation pattern caused by a shear failure, A_T^P is the P-wave radiation pattern produced by a tensile failure, and A_T^S represents tensile dislocation causing S-wave radiation pattern.

Radiation pattern is an important topic in the earthquake and microseismic hydraulic fracturing researches because of the fact that radiation patterns of body and surface waves can provide fundamental information about the source mechanism in the prospected reservoir.

Seismic source radiates from its hypocenter to every direction at different amounts and polarity. Figure 2.26 illustrates seismic wave radiation concept due to P-wave of a strike-slip fault. At the left side of the figure, a seismometer records first motion of P-wave as "up" (compressional). The seismometer that is placed to the right side of the fault plane in the figure records the first motion of P-wave as "down" (dilatational)

(Stein and Wysession, 2003).

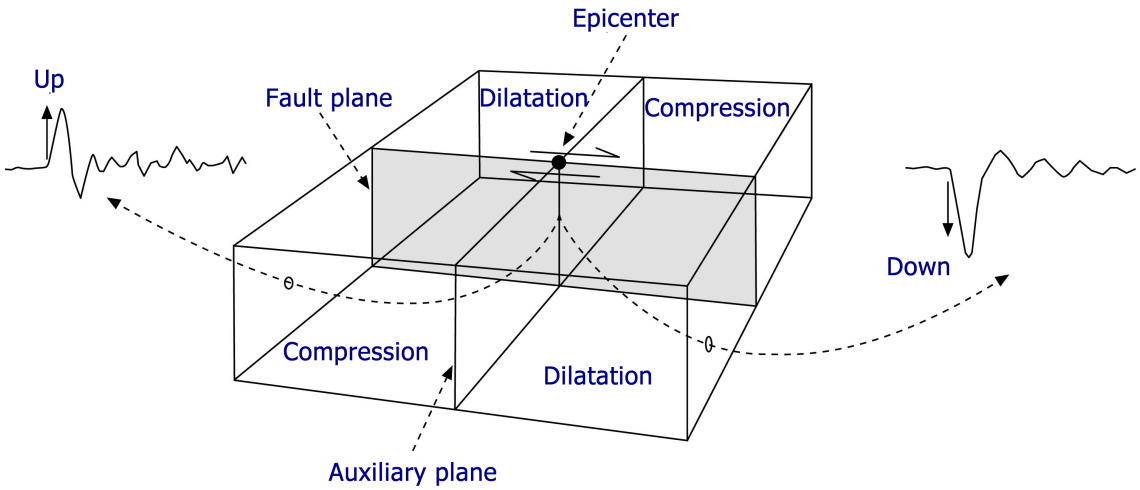

Figure 2.26: First motions of P waves at different seismometer which was located in variety of directions. Two regions can be divided; compressional and dilatational. Modified after (Stein and Wysession, 2003).

Four quadrants are defined by the first motion contrast (two compressional, and two dilatational quadrants). Quadrants are separated along the fault plane and auxiliary plane, which is perpendicular to the fault plane. Considering this fact, analyzing particle motions and polarizations of body waves can provide useful information about the source mechanism. One simple way to derive source parameters is to study the first motion polarities, which are either positive (compressional), or negative (dilatational). Radiation pattern indicates the displacements take place on a sphere with infinitesimal radius on the source (Stein and Wysession, 2003). Figure 2.27 shows the radiation pattern of body waves in $x_1 - x_3$ plane.

We have developed a MATLAB software that allows user to generate theoretical radiation patterns of variety of seismic sources in three-dimensional space. The following formulas (Equation 2.29, 2.30, and 2.31) are used to compute radiation pattern of body waves (Stein and Wysession, 2003):

$$u_r = \frac{1}{4\pi\rho\alpha^3 r} M(t - r/\alpha) sin2\theta cos\phi \tag{2.29}$$

The first term in Equation 2.29, $\frac{1}{4\pi\rho\alpha^3 r}$, called amplitude term showing that amplitude decays as 1/r. The second term, $M(t - r/\beta)$, represents energy pulse radiated from the fault with P-wave velocity α, that arrives at a receiver at the distance r, at a time $(t - r/\alpha)$. The last term, $sin2\theta cos\phi$, describes the P-wave radiation pattern.

$$u_\theta = \frac{1}{4\pi\rho\beta^3 r} M(t - r/\beta) cos2\theta cos\phi \tag{2.30}$$

$$u_\phi = \frac{-1}{4\pi\rho\beta^3 r} M(t - r/\beta) cos\theta sin\phi \tag{2.31}$$

Similarly, for S-wave radiation pattern computation, Equation 2.30 and 2.31 are used. β is the S-wave velocity.

Figure 2.28 shows computed radiation patterns of various source types. Red and blue lobes indicate P-wave and S-wave radiation patterns, respectively.

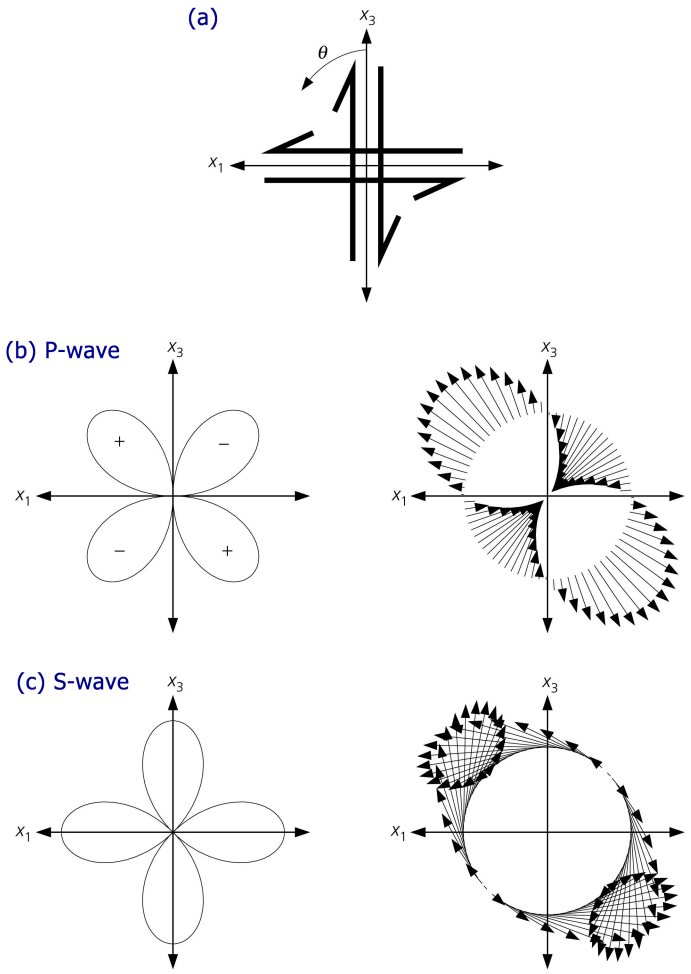

Figure 2.27: Radiation pattern of body waves. (a) depicts fault geometry for double-couple source. (b) shows compressional wave radiation pattern. (c) shows shear-wave radiation pattern. Modified after (Stein and Wysession, 2003).

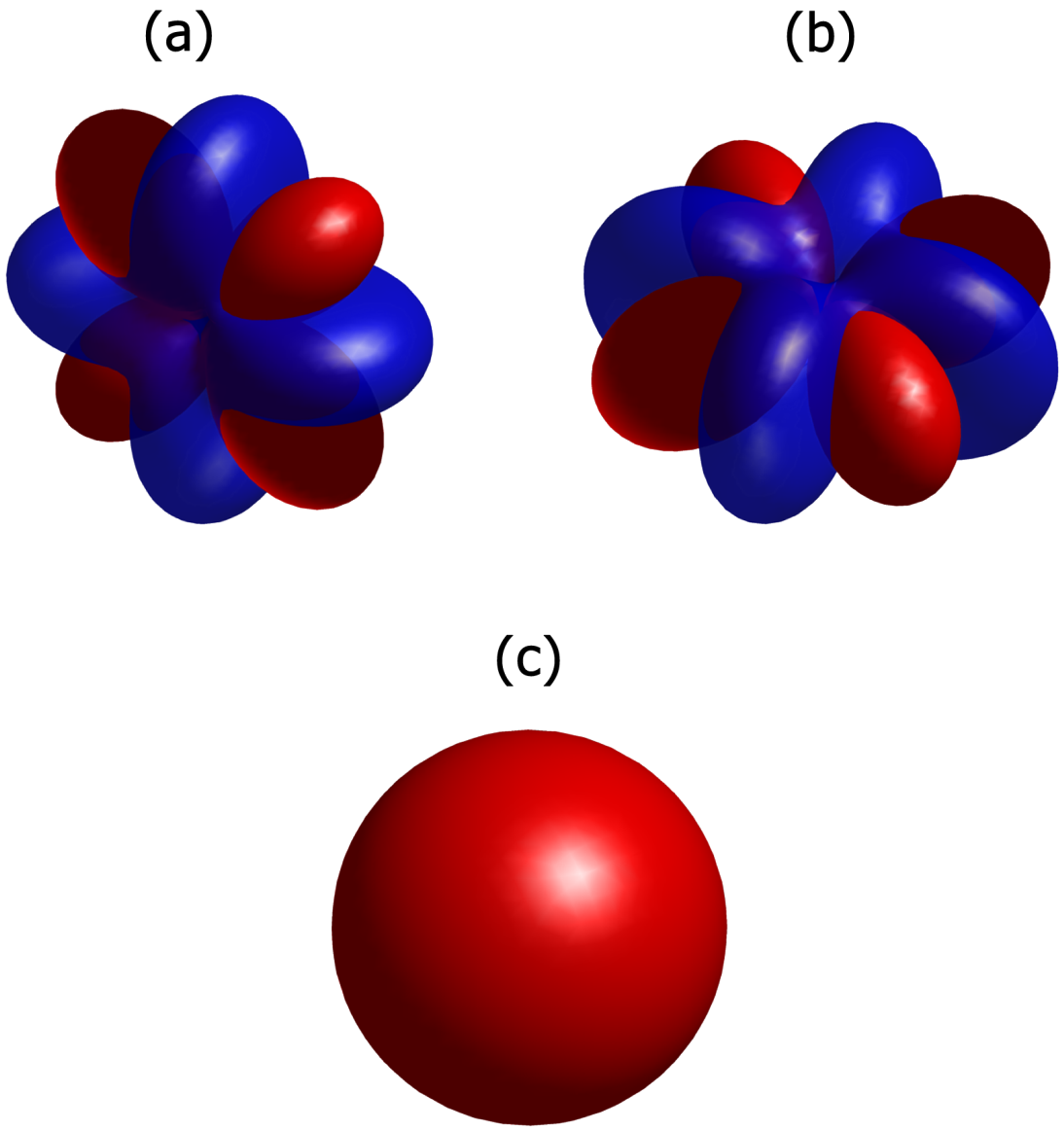

Figure 2.28: Theoretically computed radiation patterns of body waves for three different source types. Red color denotes P-wave and Blue color represents S-wave radiation pattern for cases: (a) Double-couple X-Y (b) Double-couple Y-Z, and (c) Isotropic explosion.

These focal mechanism source parameters can be computed using variety of methods; nevertheless, one common and conventional way is to attempt to search the best fit of first motions of P and S waves at each observed stations. For instance; a shear failure (double-couple source mechanism) should produce seismic wave that is radiated as compression in the tension axis (tension quadrant), and dilatation in the pressure axis (pressure quadrant).

The most widely used way to delineate source mechanism and particle motion is to use of focal mechanism plots or namely, beach-ball diagrams. Beach ball plots are lower-hemisphere projections that characterized by radiated P wave polarization (Shearer, 2009). To generate beach-ball diagrams, apart from the first motion polarities, take-off angles, and azimuths of each station are needed. Take-off angle is the angle between the source and each receiver. Figure 2.29 shows sample beach-ball diagrams for earthquakes that have the same N-S strike plane but varying slip angles. By convention, filled symbols represent the stations whose first motions are up (compressional), and hollow symbols are used for the stations whose polarizations are down (dilatation). In summary, for each station, take-off angles, azimuths and at least P-wave particle motion are needed to generate a beach-ball diagram.

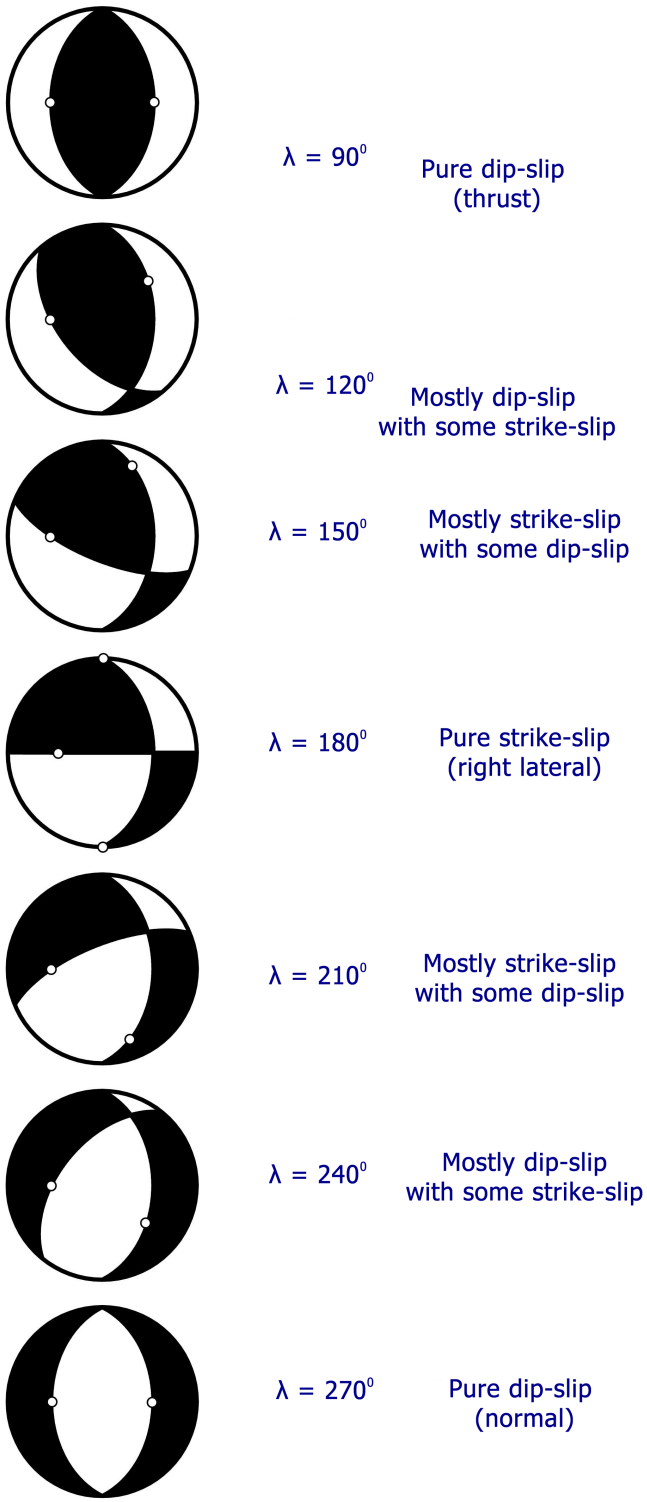

Figure 2.29: Sample beach-ball diagrams for earthquakes that have the same N-S strike plane but varying slip angles. Modified after (Stein and Wysession, 2003).

Chapter 3. Introducing the Software and the Algorithm

3.1 GENERAL INFORMATION ABOUT THE SOFTWARE

Throughout this research, we have tested and implemented variety of algorithms and ideas on a MATLAB environment. For the purpose of developing a user-friendly software, a GUI (graphical-user-interface) based approach has followed. To verify the overall applicability of the codes, we have generated synthetics and acquired data from either various physical models or real rock samples from the Allied Geophysical Laboratories (AGL) at the University of Houston.

All research is undertaken in MATLAB, a scientific programming language that is developed by Mathworks. The reason why we choose MATLAB is because it contains a sizable library which saves us from coding many large and small functions and commands. In addition, MATLAB is one of the most popular software among geologist and geophysicists and it can be used in different platforms such as Mac, Linux, and UNIX. For further information, please visit: http://www.mathworks.com.

Figure 3.1 displays the main window of Locating Events tool. It is used for locating both earthquakes and microseismic events.

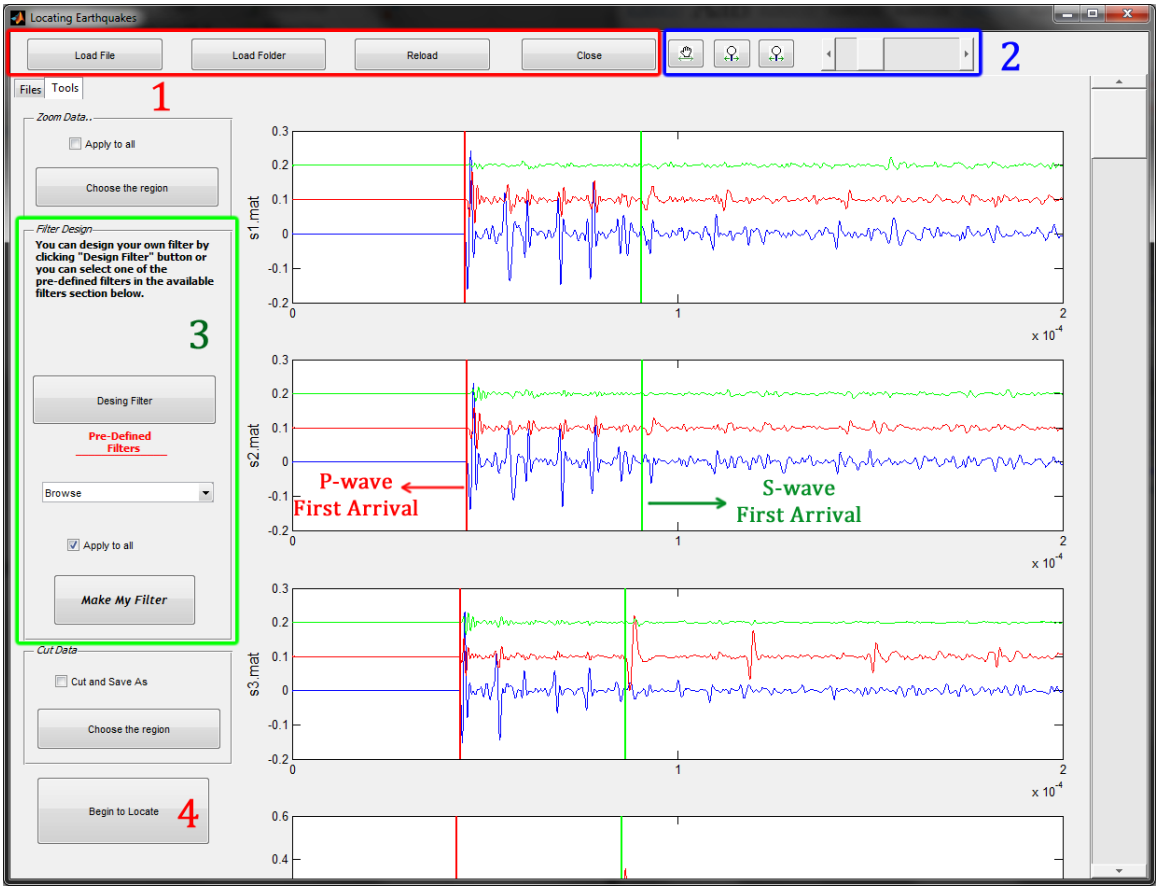

Figure 3.1: Main window of Locating Earthquakes-Microseismic event tool.

In this software, a user may perform simple tasks such as loading data-sets (single files or entire folder), reloading or closing files from the memory.

After loading a data-set, user is prompted to choose one of the two methods (STA/LTA or Modified Energy Ratio) available for determining first arrivals of body waves. Based on the selected method, first breaks are determined for P and S waves and are shown by red and green vertical lines, respectively. If modification is required, vertical lines can be moved by clicking and dragging.

The section illustrated by the number (2) allows user to zoom in/out and/or pan in/out to earthquake records. Also, these features and even more can be performed by using keyboard strokes. The slider at the top can be used to increase/decrease the number of earthquake records listed in the main window.

At left panel of the figure, user may zoom and/or cut data. Additionally, various types of filters can be designed interactively, which is explained in Chapter 2.1.1.

After clicking the *Begin to locate* button, another is script is called to run location algorithm based on grid search technique, which will be explained in the next section.

One of the main objectives of this thesis, rather than just locating microseismic events, is to make a comparison between various types of acquisition geometries and their effects on location uncertainties. To this end, we have developed another GUI based tool allows user to test variety of receiver geometries. Figure 3.2 illustrates the main windows of this tool. In order to use this tool, the model parameters (receiver coordinates, number of well, and etc.) must be inputted by the user.

This tool allows user to interactively enable/disable receivers which are used to locate event in the next step. Left-clicking with the mouse enables and right clicking disables the receiver. Active and inactive receivers are indicated by red and black stars, respectively. This tool also offers user to choose location method, whether using only P-waves, S-waves or both of them.

After clicking *Start to Locate* button, all the information (active receivers, location method, first arrivals) are piped to another script that performs the location. After that, results will be shown in a pop-up window.

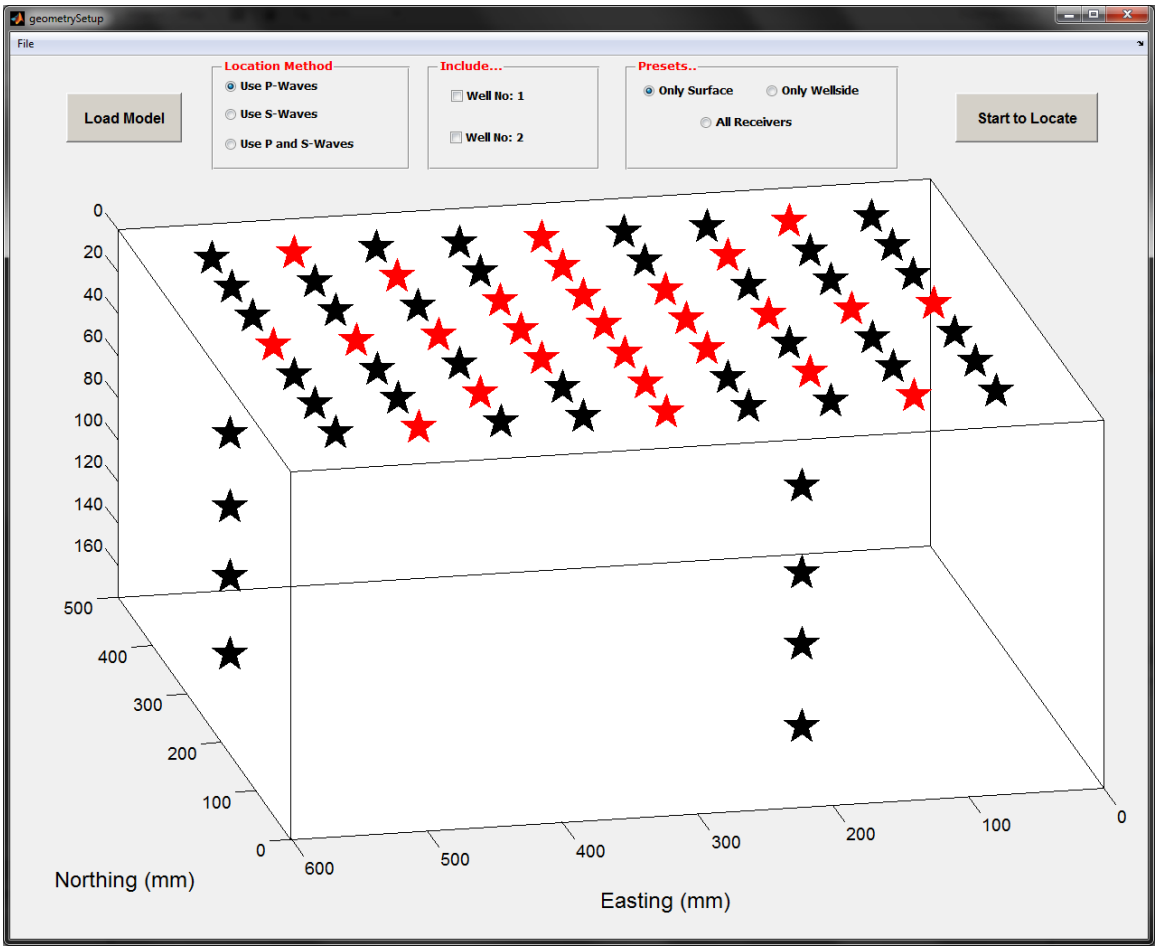

Figure 3.2: Main window of *Test Acquisition Geometry* tool. Star-shape receiver geometry is designed (only red-stars are active).

Another goal of this research is to determine the methods accuracy. To this end, locating a single event is performed simultaneously in seven different ways. When the user prompts a location procedure, all the results of these seven approaches are listed with their relative errors.

1. Using P waves and traveltime residual method
2. Using P waves and stacked energy method
3. Using P waves and energy/traveltime residual ratio
4. Using S waves and traveltime residual method
5. Using S waves and stacked energy method
6. Using S waves and energy/traveltime residual ratio
7. Using P and S waves and traveltime residual method

3.1.1 Complete lists of scripts coded in MATLAB

Table 3.1 summarizes all the scripts that are coded in MATLAB. This list includes codes which are related to location algorithm, focal mechanisms, radiation patterns, and signal processing.

Table 3.1: Complete list of scripts coded throughout this thesis.

File Name	Description
locate.m	Main file of location algorithm
receiverGeometry.m	Allows user to test different receiver geometries for locating events
traceRay2DFermat.m	Performs 2D ray tracing via Fermat's principle
traceRay2DSnell.m	Performs 2D ray tracing via Snell's law
traceRay3DFermat.m	Performs 2D ray tracing via Fermat's principle
traceRay3DSnell.m	Performs 2D ray tracing via Snell's law
computeAmplitudes.m	Compute stacked energy of each possible source location
computeAmpRatio.m	Compute Energy/Traveltime ratio of each possible source location
computeResiduals.m	Compute traveltime residual of each possible source location
createModel.m	Creates 3D model according to input model parameters
focalMechanism.m	Calculates source parameters (strike, dip, rake) for given data-set and its parameters
beachball.m	Generates beach-ball plots for inputted source parameters
radPatternTheory.m	Theoretically generates radiation patterns of body waves for different source types
radPatternObs.m	Generate radiation pattern of body waves for given data-set
calculateSNR.m	Interactive tool for calculating SNR of input seismc data
filterDesign.m	Interactive tool for designing filter to any digital signal
firstArrivalPicking.m	Compiled version of first arrival picking methods
LtaSta.m	Finds first breaks of a seismic data via STA/LTA method
mEnergy.m	Finds first breaks of a seismic data via Modified Energy method
genSynthetics.m	Generate synthetic seismic data
genNoise.m	Generate random noise for seismic signals
genContourMaps.m	Allows user to generate variety of 2D or 3D contour plots
hodogramAnalysis.m	Interactive tool for generating hodogram plots and calculating polarization

3.2 THE LOCATION ALGORITHM: HOW DOES IT WORK?

One key problem in seismology is to efficiently locate seismic events. There are variety of algorithms available based on different techniques. Most location methods are based on phase picking of body waves. Methods relying on traveltime try to minimize observed and calculated arrival times iteratively and pick the location where the difference is minimal. Traveltime based location methods are strongly dependent on the precise first arrival picking, which can be challenging in case of low signal-to-noise ratio. However, there are other methods that do not require precise first arrival pickings such as migration methods which make use of full-wave field around the detected signal. One disadvantage of these migration methods is that they demand higher computational costs.

The main objective of this research is to implement different algorithm and ideas to compare between them. To this end, we have undertaken novel microseismic experiments and we propose location algorithms based on grid searching technique, in which all potential source locations are searched in a grid area until one of the criteria is reached. We developed a ray tracing and diffraction stack procedure along with conventional traveltime based method to undertake locations and their evaluation.

This research also investigates some fundamental aspects of microseismic event location: surface versus borehole receivers, P versus S waves and travel time versus amplitude. The algorithm is developed in a MATLAB environment and tested on physical modeling data from the Allied Geophysical Laboratories (AGL) at the University of Houston.

Figure 3.3 shows a flow chart of our location method.

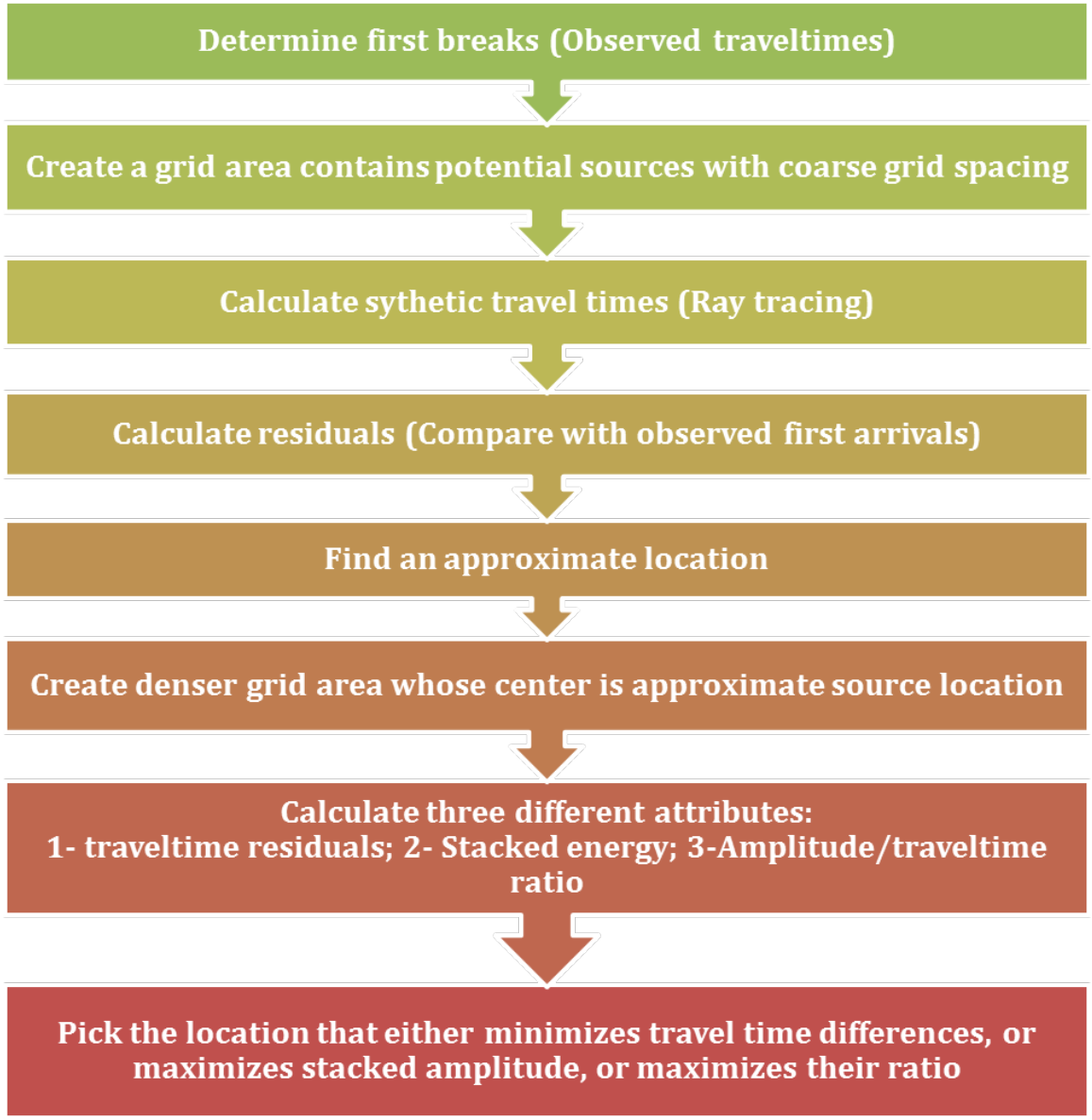

Figure 3.3: Flow chart of the hypocenter location algorithm based on grid searching technique.

We have proposed three different location procedures to determine hypocenter coordinates of simulated microseismic events.

- Traveltime residual method
- Stacked energy method
- Energy/traveltime residual method

Traveltime residual attribute is highly dependent on precise picking first arrivals and velocity model; whereas, migration-type (stacked energy) approach does not depend on accurate picking. These three methods will be explained in the following sections.

3.2.1 Traveltime Residual Method

The traveltime residual method has implemented in such a way that it simultaneously locates events based on the following approaches; P-wave only, S-wave only, and a combined P and S wave approach.

Figure 3.4 illustrates the 3D view of a model. The black star is the true source location, red stars are the receivers. Our main objective is to detect the location of black star. In physical modeling experiments, we generally scale the dimensions of the models by a factor of 10,000 to make the ultrasonic measurements (at 1 MHz) look similar to the seismic band at 100 Hz. All the figures and results in this research reflects scaled dimensions.

The very first step of any type of location technique is to detect an event within a data-set. There are variety of algorithms can be used to find an event, STA/LTA algorithm is just one of them. After determining the event, next step is to pick first arrival of P and possibly S-waves. For each receiver, first arrival times are determined and stored using STA/LTA method. This method has explained in detail in Chapter 2.2.

After determining phase arrivals, the next step is to create a grid area inside the model, where every single grid point in the subsurface/model is presumed to be a potential point source location, $P(x, y, z)$. We make an assumption that microseismic signal radiates from a point source, which is acceptable as the source dimensions are relatively small (source transducer diameter is 10 mm).

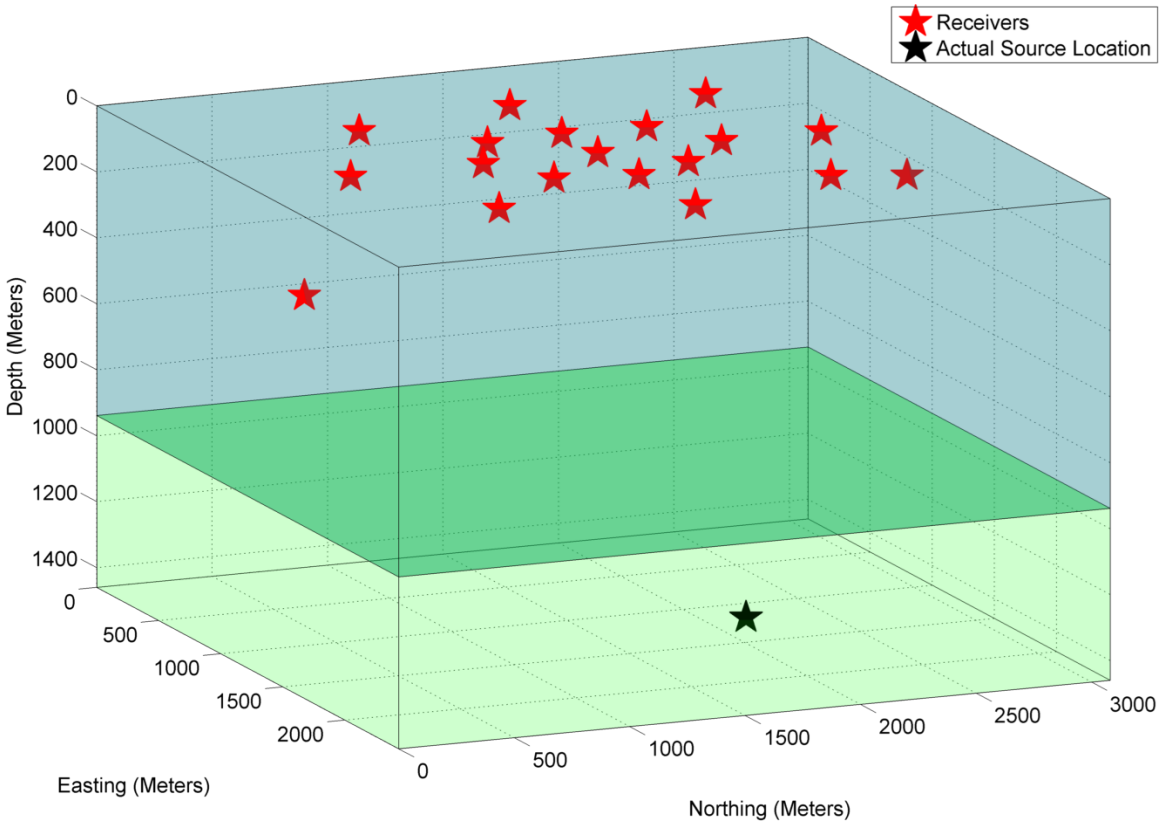

Figure 3.4: 3D view of a model. Black star is the true source location, red stars are the receivers.

In this grid searching technique, the selection of a grid interval is essential. Using a dense grid interval will be more accurate, but slow; whereas using coarse grid interval will be faster, but less accurate. Given that the model dimensions are 3070 x 2425 x 540 meters, using dense grid spacing (10 meters) would create $\sim$ 3.8 million potential point sources. It requires huge amount of computation time, but it will be accurate. If we choose coarse grid interval (200 meters), it would create only 624 potential point sources. Computation will be so much faster, nevertheless location will not be as accurate as we wanted.

Considering the accuracy and the speed of the method mainly depend on the grid interval, we have followed a location procedure, where an event is located in two-iterations. In the first iteration, a coarse grid interval (20 mm or 200 meters with scaled dimension) is used to create grid area, which provides a rough and quick

estimate about the location coordinates. In the second iteration, smaller grid area whose center is the rough event coordinates is created with dense grid interval (1 mm or 10 meters) to locate event more accurately. By the help of this technique, computational time is significantly decreased.

The first iteration of the directed search routine begins with a coarse grid interval. Figure 3.5 shows 3D view of the model and all possible point sources that are created with a coarse grid spacing.

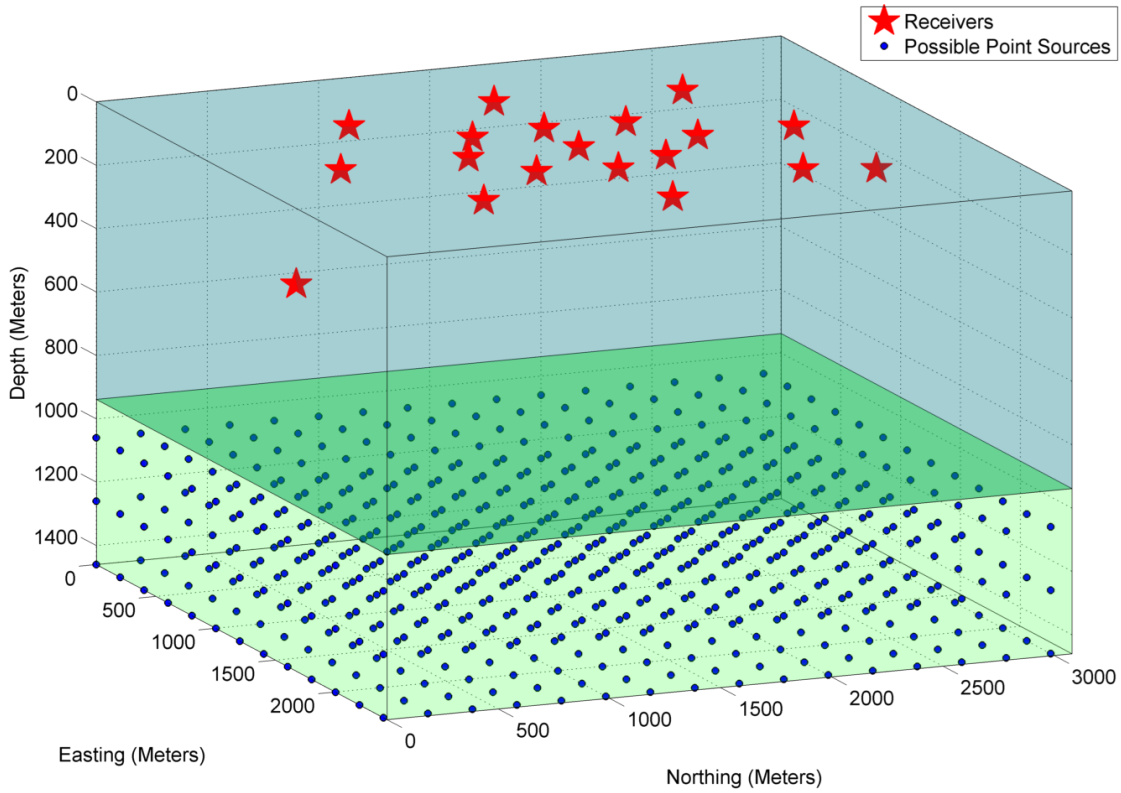

Figure 3.5: To increase computational speed, a grid area is created with a coarse grid spacing in the first iteration, in this case, 200 meters.

In the next step, the algorithm calculates synthetic traveltimes and seismic ray paths for each possible point source locations. In situations where medium is one-layered and isotropic, seismic rays paths and synthetic traveltimes from a source location, $P(x, y, z)$ to a receiver, $R(x', y', z')$ can be determined by simple formulas as follows:

$$r = \sqrt{(x - x')^2 + (y - y')^2 + (z - z')^2} \tag{3.1}$$

$$t_{synthetic} = \frac{r}{v} \tag{3.2}$$

Where; r is the total distance traveled, v is the velocity of the medium and $t_{synthetic}$ is the synthetic traveltime for source-receiver couple.

In case of layered medium or anisotropy, a ray tracing algorithm is needed to compute more accurate synthetic traveltimes and ray paths. To this end, we have implemented a ray tracing algorithm based on shortest path method (Moser, 1991). The method is based on calculating every possible ray paths for a given earth model, and then it picks the ray paths couples or triplets that satisfy Fermat's principle; the ray path travels along a path that minimizes total travel time. Further discussion about ray tracing algorithms are available in Appendix A.

Moreover, this method requires huge amount of computation so that we have optimized our algorithm implementing CPU and GPU computing, which are explained in details in the section 3.4.

Figure 3.6 makes an illustration of seismic ray paths in both 1-layer and 2-layered models.

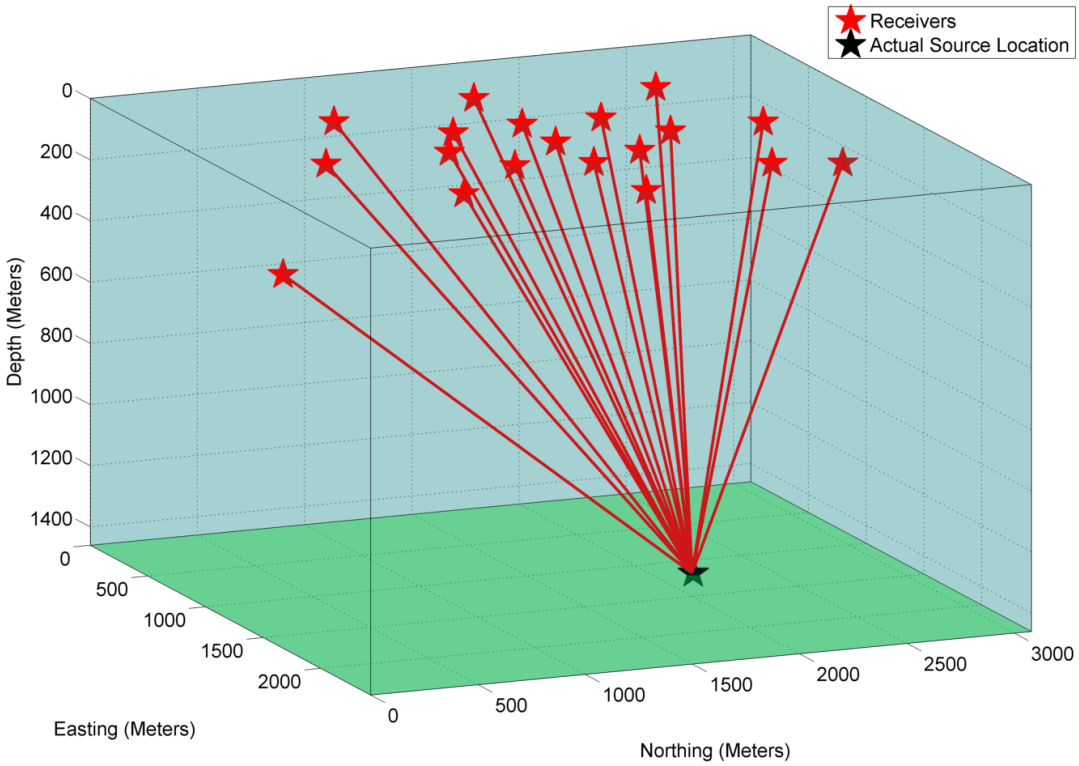

(a) Seismic ray paths are straight lines in an isotropic and homogeneous medium.

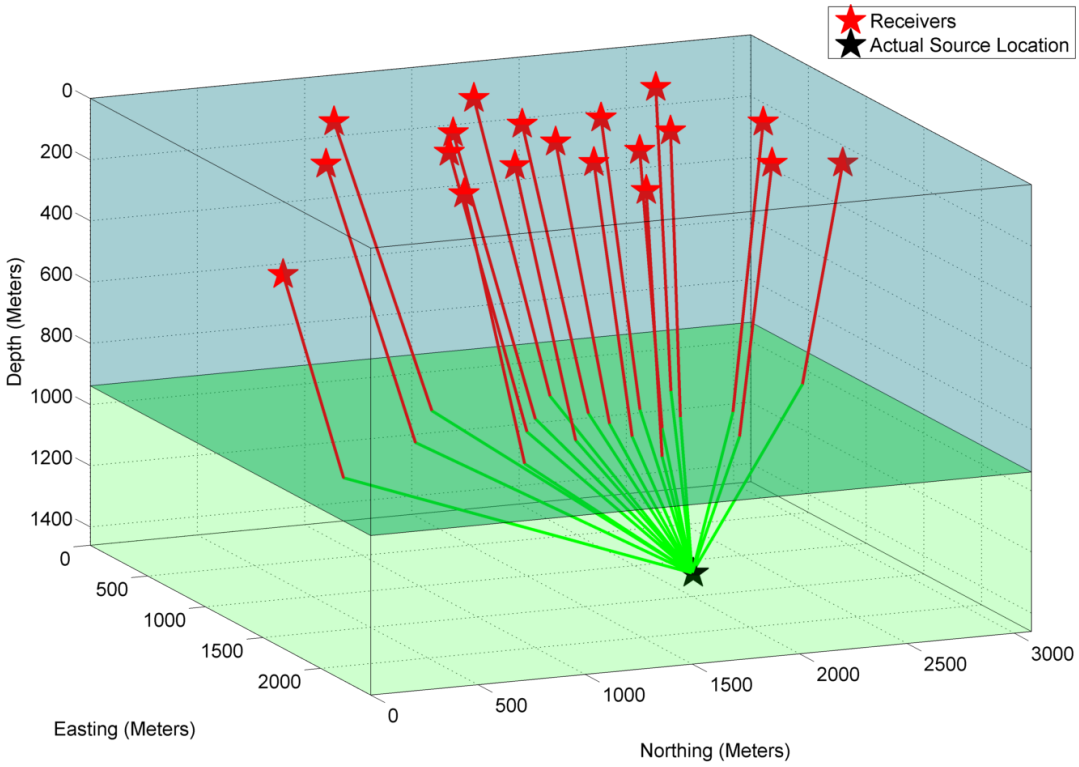

(b) Seismic rays obey Snell's law; hence, transmitted wave bent over the layer boundary depending on the velocity model.

Figure 3.6: Illustration of seismic ray path's in (a) 1-layer isotropic model, (b) 2-layered model.

Further, the algorithm begins ray-tracing for each point in the grid area. Figure 3.7 illustrates a snapshot from directed-search scheme. Red stars are receiver positions; black star is the actual source position, blue dots are potential point sources, and red-green lines show the ray-paths. Blue dots only plotted at the bottom of the model for clarity, however, every single potential point source in the entire grid area is searched.

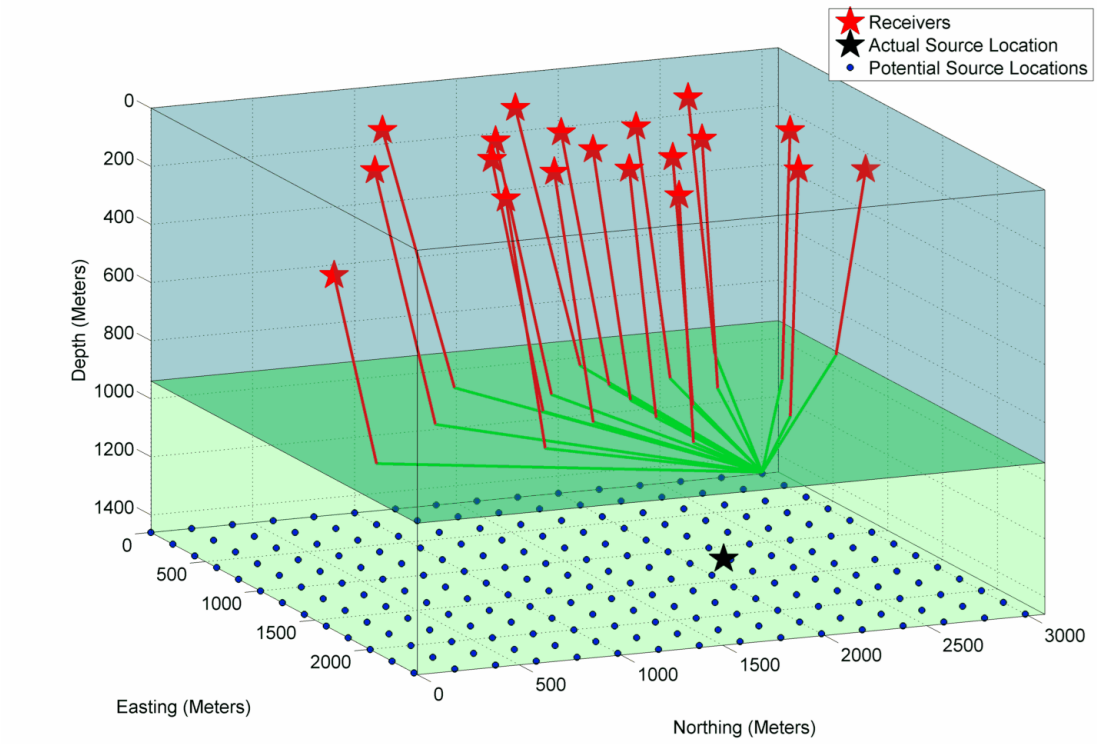

Figure 3.7: 3D view of an experimental physical model. Red stars are receiver positions; black star is the actual source position, blue dots are potential point sources, and red-green lines show the ray-paths. Blue dots only plotted at the bottom of the model for clarity. The algorithm searches for every single potential point source in the entire grid area. An initial ray tracing is performed from each grid point to each receiver.

After calculating synthetic travel-times for each point, the following step is to compute traveltime residuals for entire grid area. This can be done by subtracting the observed traveltimes from the calculated synthetic traveltimes. The grid point yields minimum traveltime residual can be considered as the source location. Figure 3.8

shows the coordinates of a rough estimated source position, denoted as red dot. Actual and approximate source coordinates are (2160,1200,1450) and (2050,1250,1350), respectively. Nevertheless, the rough event position will not be accurate enough due to coarse grid spacing. To this end, a second grid area whose center is the rough source coordinates is generated. The second grid area is smaller but denser in contrast to the first one. Figure 3.9 illustrates the second smaller and denser grid area. Afterwards, we continue to search for a location with minimum traveltime residual.

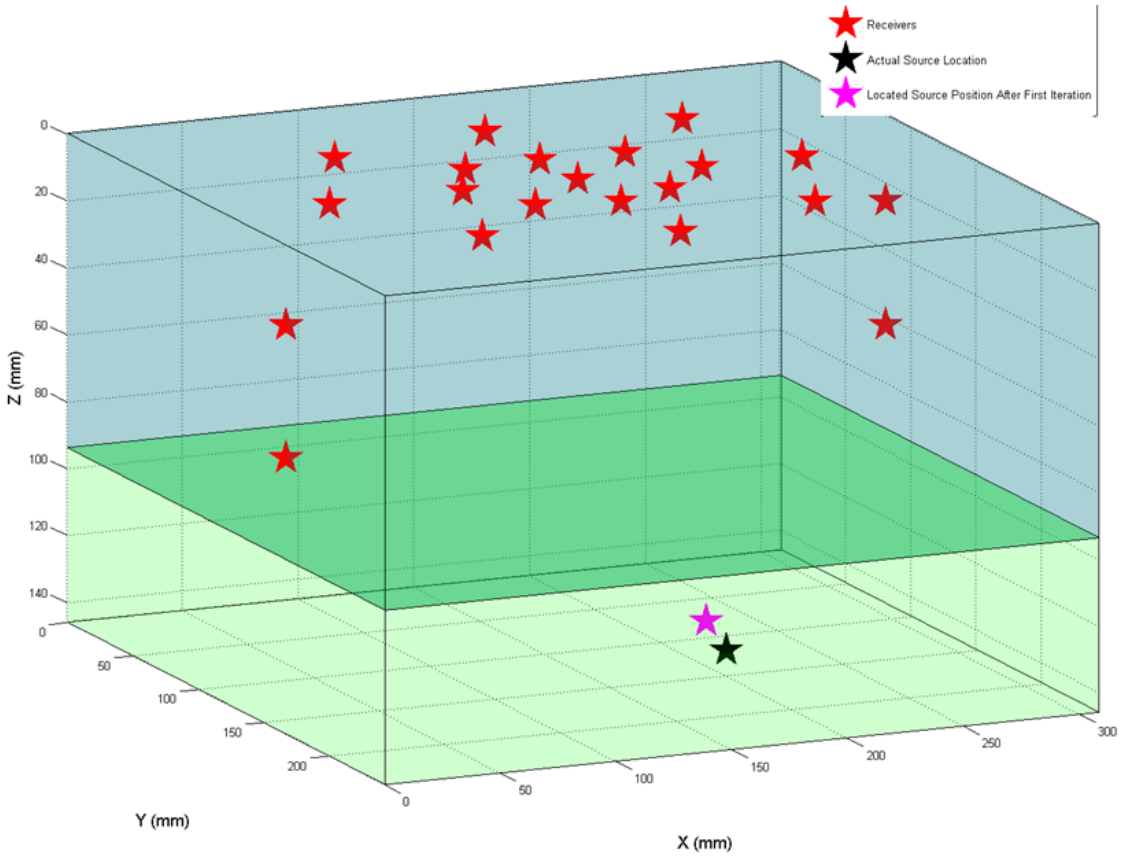

Figure 3.8: Magenta star represents the coordinates of approximate source location that is determined after the first iteration with coarse grid spacing.

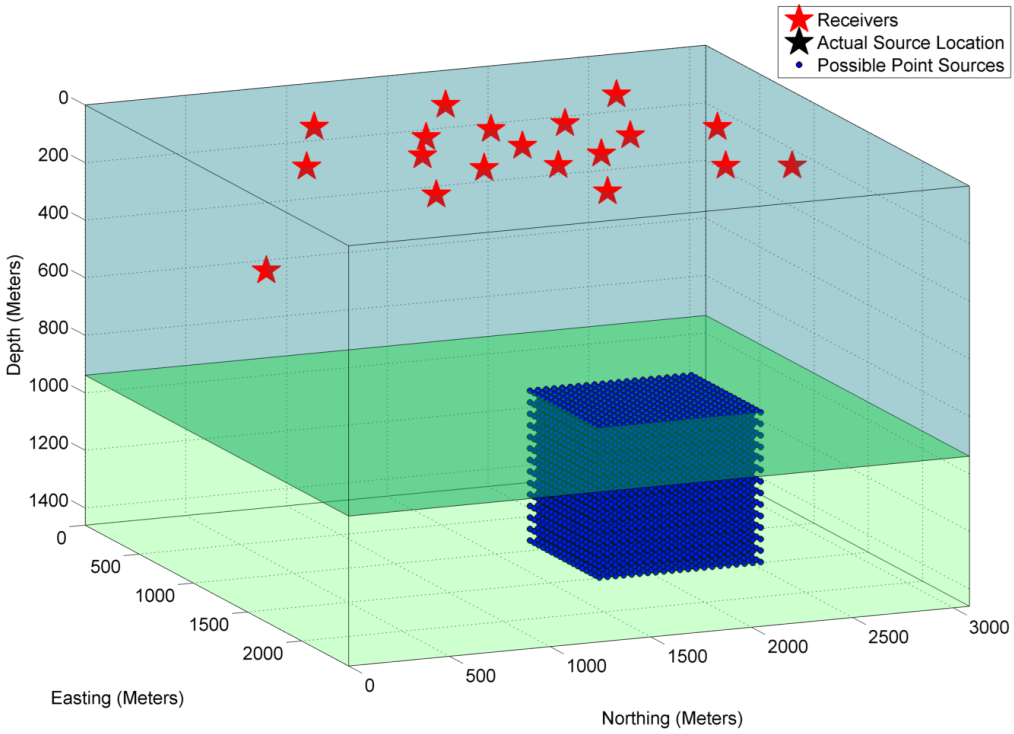

Figure 3.9: After finding an approximate source location, another grid area whose center is the approximate source location is generated. This time grid area is smaller but denser (10 meters).

After performing a second ray tracing and calculating traveltime residuals for a grid area with denser spacing, the last step is to find the location where yields minimum travel-time residual. Figure 3.10 demonstrates travel-time residual contour map, where blue color represent small residual values.

Alternatively, event coordinates can be found based on the Probability Density Function (PDF) using observed and calculated traveltimes. PDF can be calculated by the following formula (Eisner, 2013). The potential point source which yields maximum PDF is declared as the event coordinates.

$$pdf = e^{-(t_p - TP - T_0)^2/\sigma p^2} \tag{3.3}$$

$$pdf = e^{-(t_s - TS - T_0)^2/\sigma s^2} \tag{3.4}$$

Equations 3.3 and 3.4 can be used to compute probability density function using P and S waves, individually. If a combined P and S wave approach is followed, a more generalized version of this equation can be written as follows:

$$pdf = e^{-(t_p - TP - T_0)^2/\sigma p^2 - t_s - TS - T_0)^2/\sigma s^2} \tag{3.5}$$

- t_p and t_s are the measured observed first arrival times of P and S waves.
- TP and TS are the calculated traveltimes for each grid point
- T_0 is grid search over origin times
- Standard deviation of P and S wave observed traveltimes

According to Figure 3.10, event location is marked where yields minimum traveltime residual. Figure 3.11 shows the coordinates of located and true event source coordinates. Magenta and black star represent located and true event locations, respectively. Figure 3.12 illustrates a zoomed-view of the located and true event coordinates. Red circle in the figure corresponds to area of source transducer, which has about 10 mm diameter. The physical meaning of this circle is that the seismic signal may radiate from anywhere inside that circle.

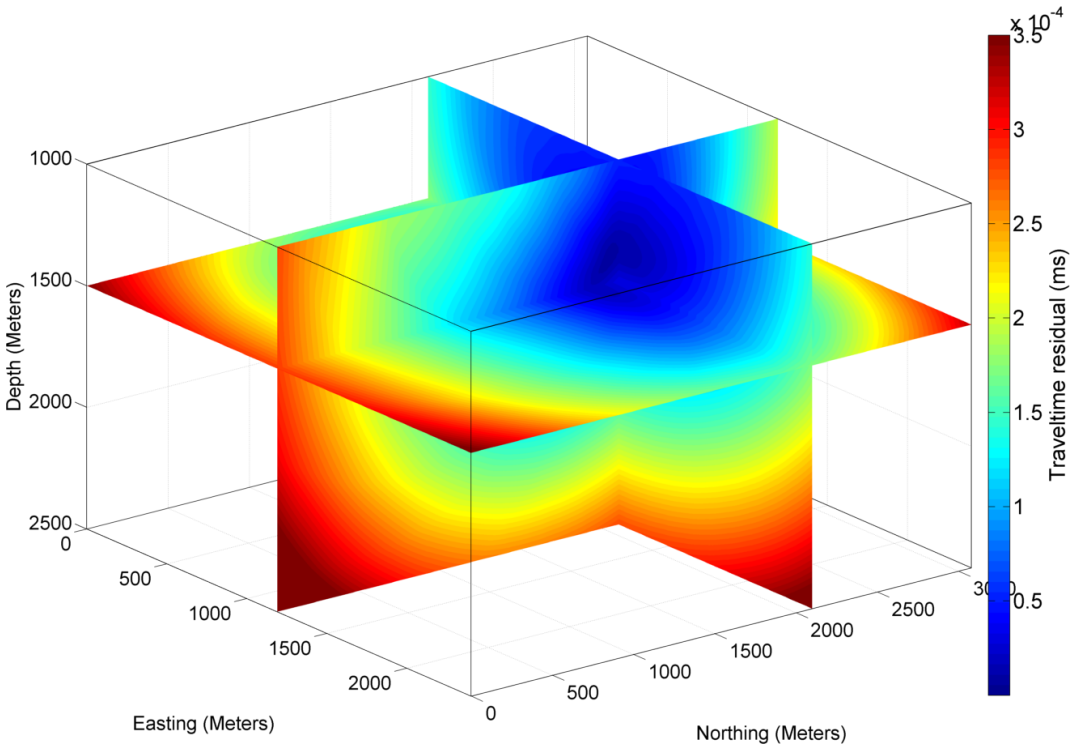

(a) Traveltime residual slices at $x = 2160$ m, $y = 1200$ m, and $z = 1550$ m.

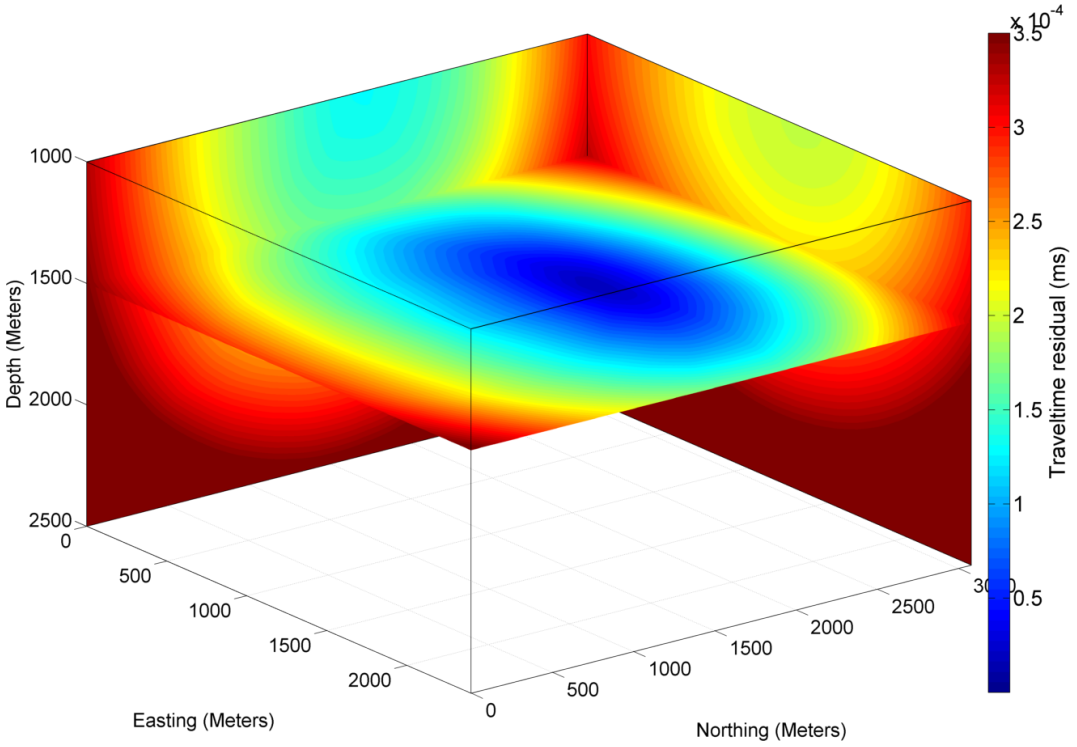

(b) Traveltime residual slices at $x = 3000$ m, $y = 0$ m, and $z = 1550$ m.

Figure 3.10: Variety of traveltime residual contour map slices. Blue colors denotes small residual values, whereas, red color represent high residual. Coordinates of a simulated microseismic event can be marked at the location where minimum traveltime residual is produced.

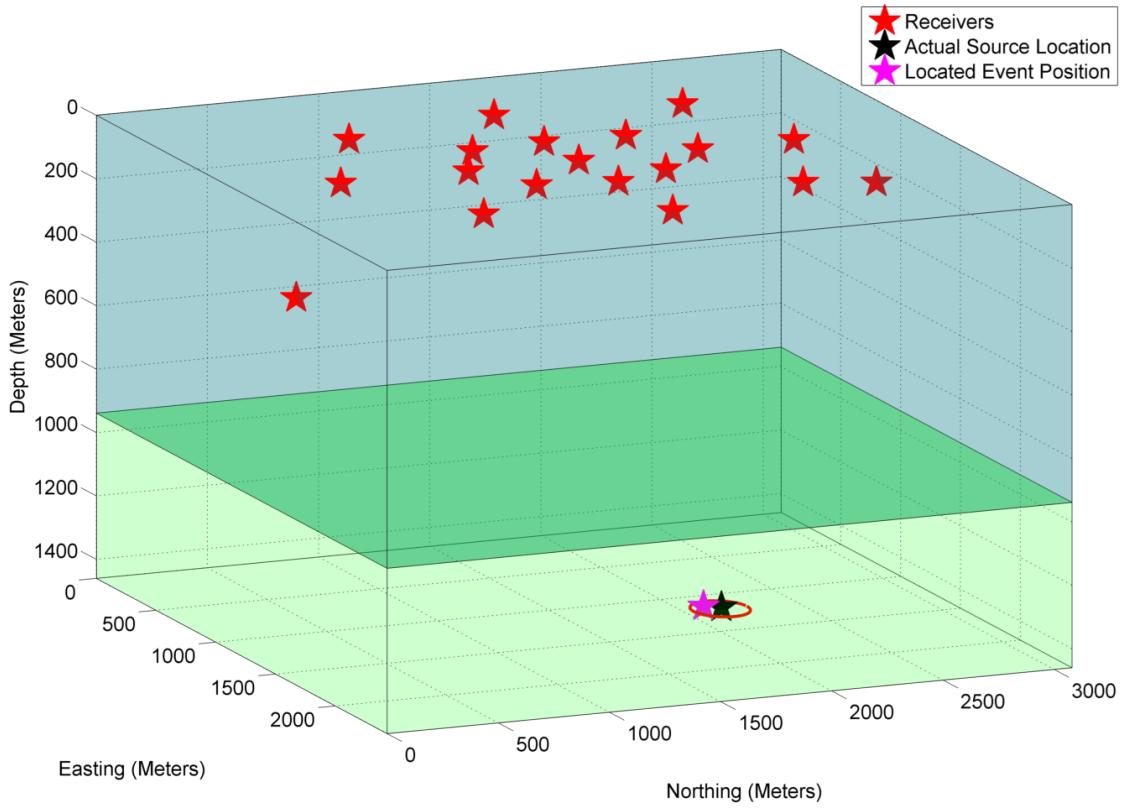

Figure 3.11: Shows the coordinates of located and true event source coordinates. Magenta and black star represent located and true event locations, respectively.

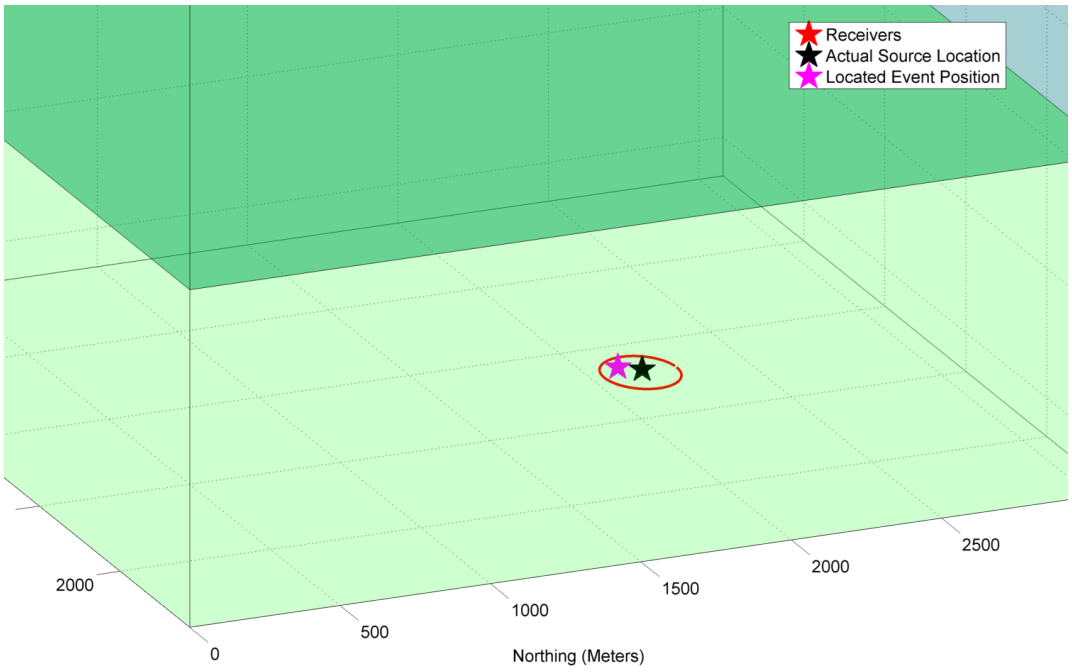

Figure 3.12: Zoomed view of the located and true event coordinates. Red circle corresponds to area of source transducer, which its diameter is about 10 mm diameter.

In situations where only one receiver is available, it is not possible to find an exact source location. Located event would lie on a perfect/bend circle depending on medium properties (isotropic or anisotropic, homogeneous or heterogeneous). The width of the circle is directly related to velocity model. At least three receivers are needed to run the algorithm.

3.2.2 Stacked Energy Method

Travel-time based location methods are beneficial in situations where seismic data has high signal-to-noise ratio and first arrival picking is accurate. In situations where phase picking is troublesome due to noise, migration location methods are preferred to remove dependency of precise first arrival picking. In this research, a migration-type diffraction stacking approach is implemented in MATLAB. This technique requires for computation of stacked amplitudes for each potential source location. Computing stacked energy is similar to computing travel-time residuals. The main difference between traveltime and stacked energy method is that first arrival picking is unessential. To calculate stacked energy, we have taken advantage of a directed grid searching algorithm as we used it in the travel-time method.

The first step for computing stacked energy is to generate equally spaced potential point sources in a grid area, where every single point in the grid area is considered a potential source location. Secondly, initial ray tracing is performed for each image point.

Afterwards, amplitudes from all receivers are stacked along a calculated synthetic travel-time window $[t_1, t_2]$. This time window is defined between t_1 and t_2 arrival times, where t_1 represents the synthetic first arrival time for corresponding potential source location, and t_2 is the time which is just a few cycles after t_1. For each image point, stacked energy is computed by the following formula 3.6:

$$E(x,y,z) = \sum_{n=1}^{m} \sum_{t=t_1}^{t_2} (S_n(t))^2 \tag{3.6}$$

Where; $E(x,y,z)$ is the stacked energy value on the image point at coordinates of x,y,z. $S_n(t)$ is the seismic signal at n^{th} receiver station, and at the t^{th} time sample. t_1 is the first arrival time of traced ray, t_2 is the a few cycle after the first arrival, and m denotes the number of receivers.

This computation is executed for each point sources in the grid area to generate a stacked energy coherency contour map. Summing amplitudes over all receivers produce distinct stacked energy regions. Ideally, incorrect source locations yields low stacked amplitude values, whereas, true source location should produce a maximum stacked energy.

For each potential source location in our grid area, we will have the following; $E(x,y,z)$, stacked amplitude value for each potential source location x,y,z. Using those parameters, it is possible create a 3D volume of stacked energy. Figure 3.13 displays several slices over stacked energy volume. Maximum amplitude value indicates the located event coordinates. Figure 3.14 illustrates 4 different contour slices of stacked energy at different depths; z=1350 meters, z=1400 meters, z=1450 meters, and z=1500 meters. As we expected, maximum stacked energy decreases rapidly as the slice depth moves away from the actual source location.

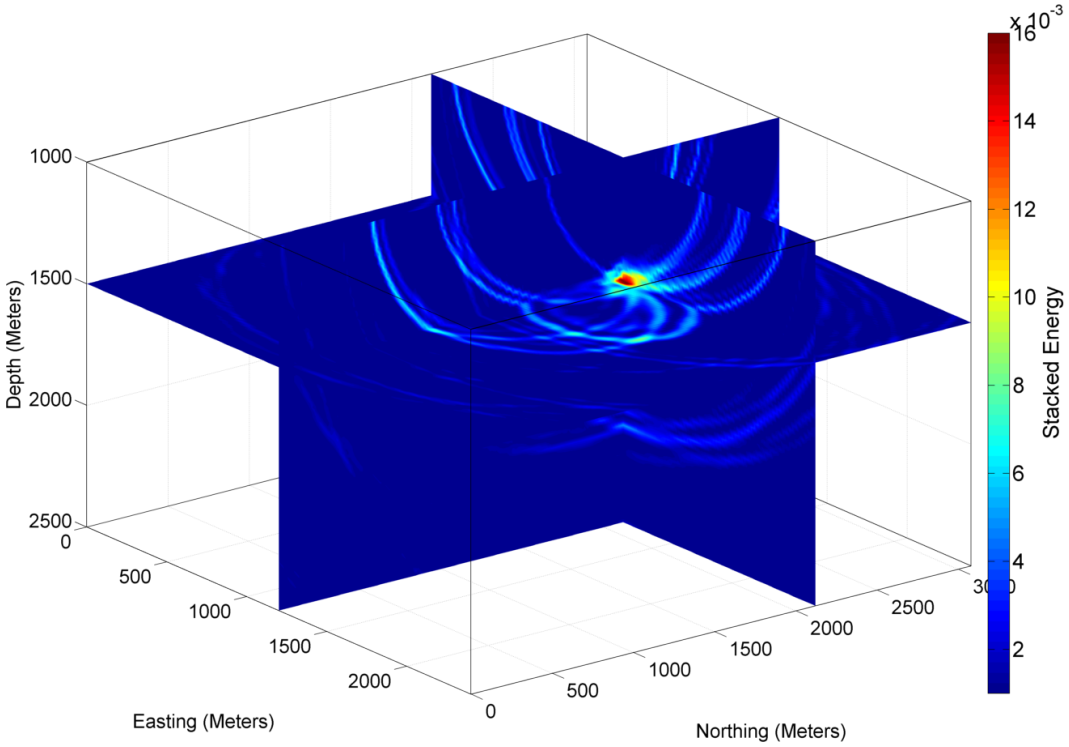

(a) Traveltime residual slices at $x = 2160$ m, $y = 1200$ m, and $z = 1550$ m.

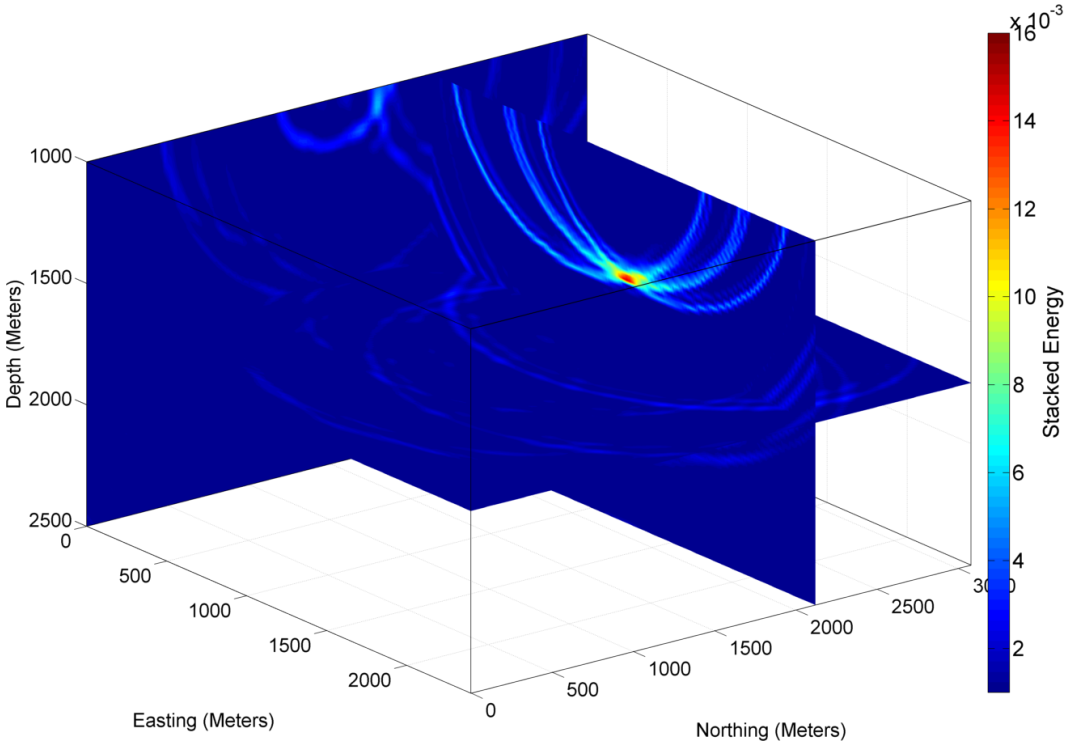

(b) Traveltime residual slices at $x = 3000$ m, $y = 0$ m, and $z = 1550$ m.

Figure 3.13: Variety of traveltime residual contour map slices. Blue colors denotes small residual values, whereas, red color represent high residual. Coordinates of a simulated microseismic event can be marked at the location where minimum traveltime residual is produced.

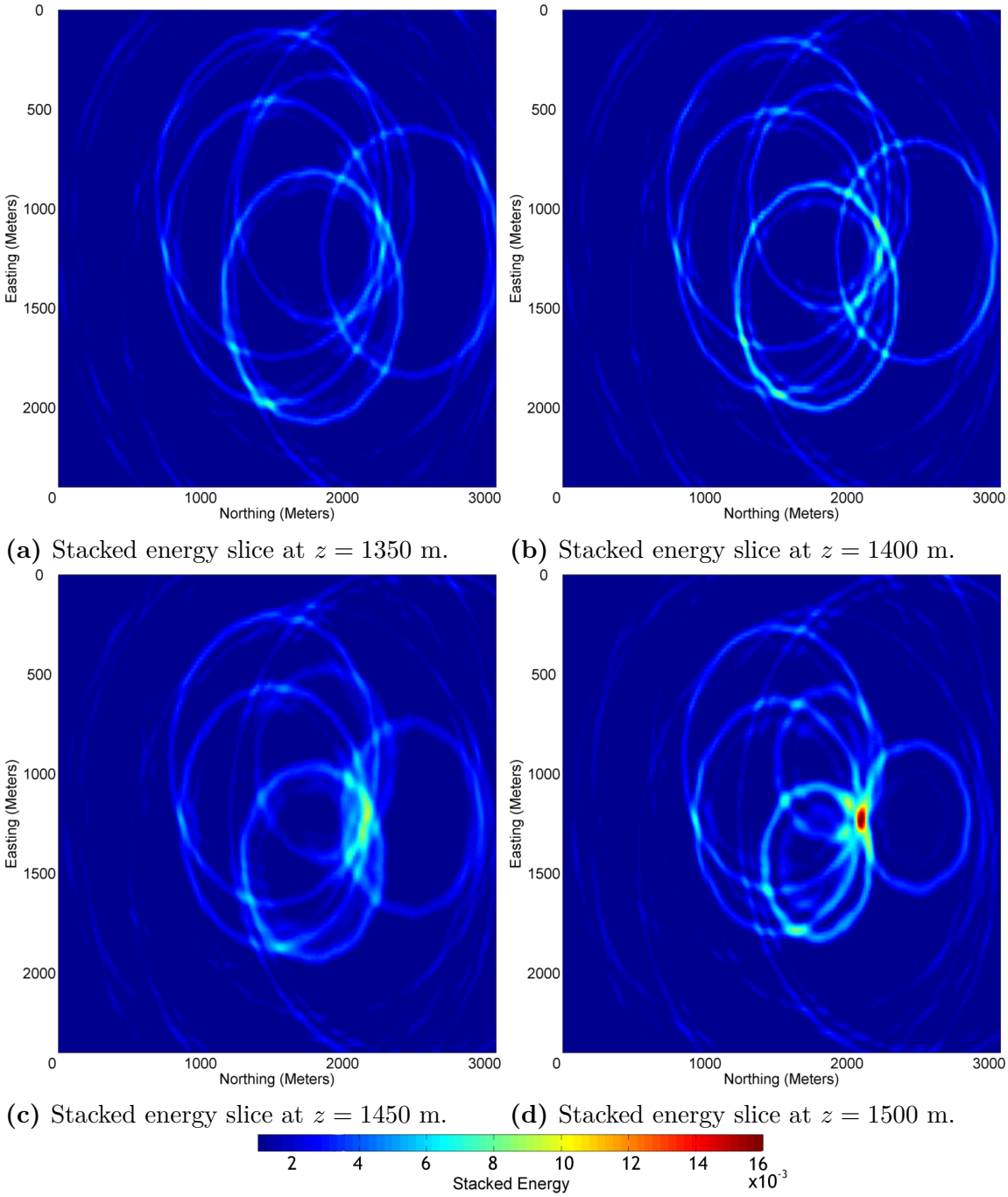

(a) Stacked energy slice at $z = 1350$ m.

(b) Stacked energy slice at $z = 1400$ m.

(c) Stacked energy slice at $z = 1450$ m.

(d) Stacked energy slice at $z = 1500$ m.

Figure 3.14: Stacked energy contour maps of different depth slices: (a) z=1350 meters, (b) z=1400 meters, (c) z=1450 meters, and (d) z=1500 meters. Stacked energy decreases as slice moves away from the actual source depth (z=1500 meters).

3.2.3 Energy/Traveltime Residual Ratio Method

The third attribute that we have been using to locate events is the energy/-traveltime residual ratio. This attribute is the combination of stacked energy and traveltime residual parameters. The ratio is computed during the location algorithm by simply dividing traveltime residuals to amplitude (stacked energy) values for each potential source location. Figure 3.15 displays the surface plot of energy/traveltime residual ratio for the same model discussed in the previous section at slice z=1500 meters. Peak value of this ratio is more likely to be the actual source location.

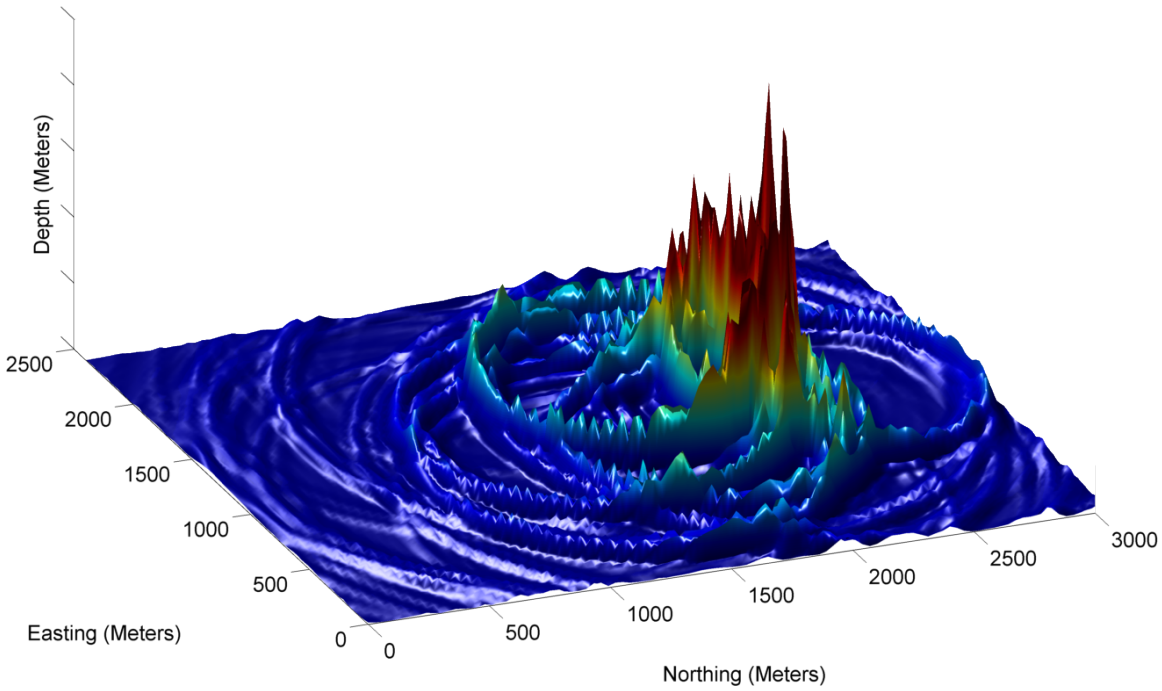

Figure 3.15: Surface plot of energy/traveltime residual ratio at slice z=1500 meters.

Figure 3.16 demonstrates the four different slices of energy/traveltime ratio. As slice depth gets closer to the true source depth, values of the ratio increases. Maximum value indicates the located event coordinates. One major difference between stacked energy and energy/traveltime ratio is that the contour maps of the ratio attribute contains less noise.

From Figure 3.17, it can be seen that both stacked energy and amplitude ratio

attributes accurately pinpoint the source location. Nevertheless, combining both amplitude and traveltime residual parameters forms clearer contour map that it has less artifacts than any other two attributes. Another conclusion is that energy/traveltime residual ratio is less affected by the velocity variations and the noise level.

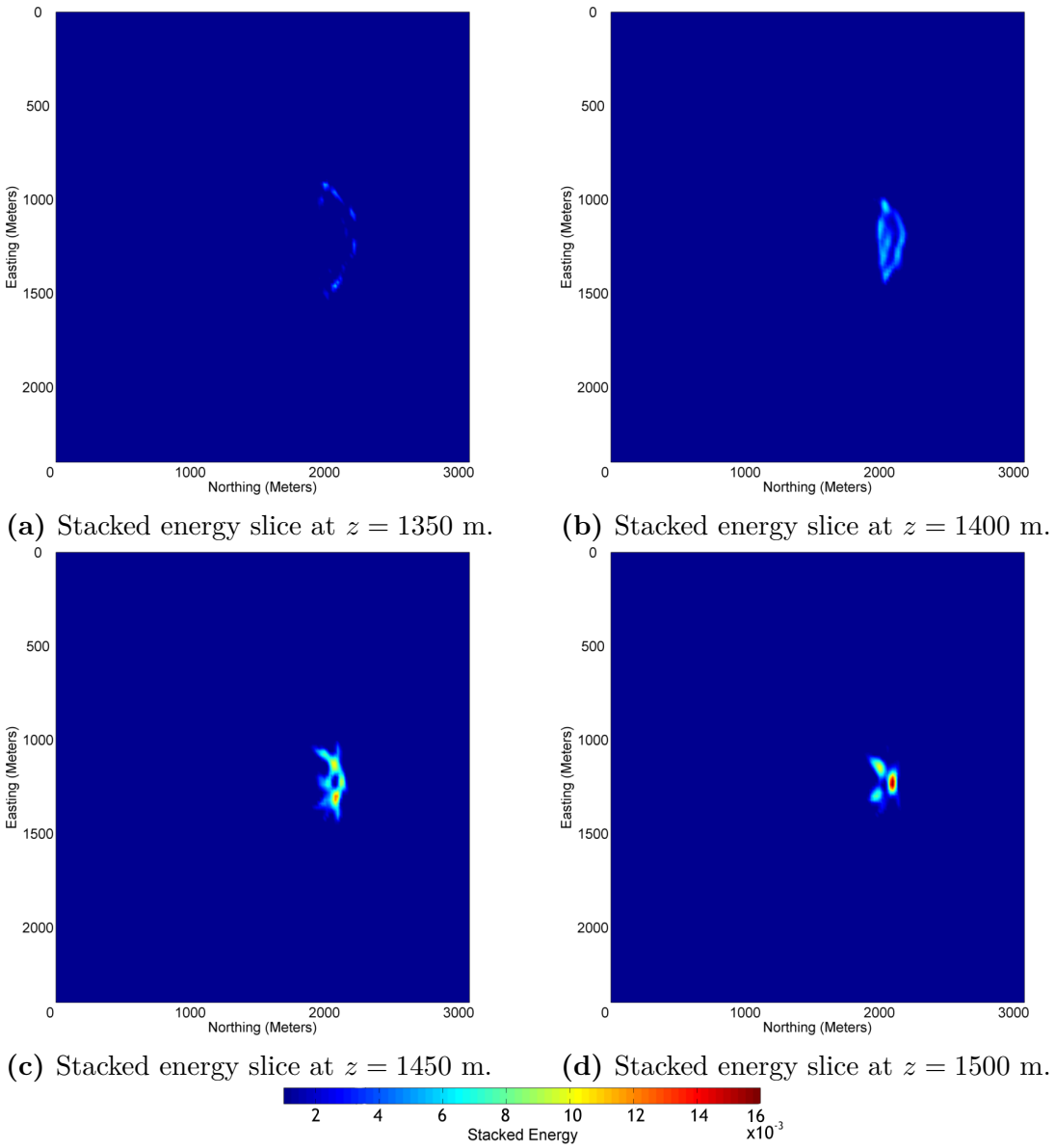

(a) Stacked energy slice at $z = 1350$ m.

(b) Stacked energy slice at $z = 1400$ m.

(c) Stacked energy slice at $z = 1450$ m.

(d) Stacked energy slice at $z = 1500$ m.

Figure 3.16: Energy/Traveltime residual ratio contour maps of different depth slices: (a) z=1350 meters, (b) z=1400 meters, (c) z=1450 meters, and (d) z=1500 meters. Stacked energy decreases as slice moves away from the actual source depth (z=1500 meters).

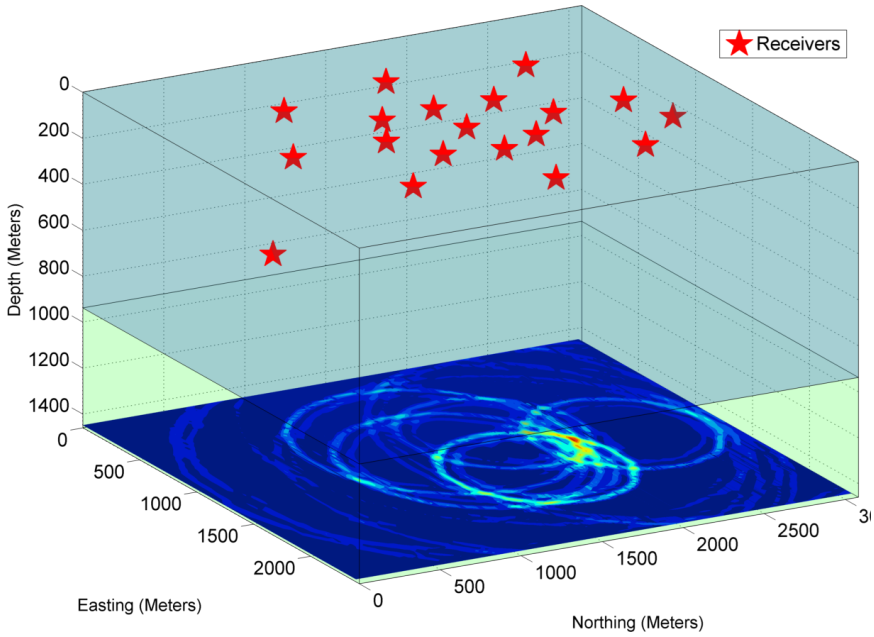

(a) Stacked energy contour map at slice z = 1500 meters.

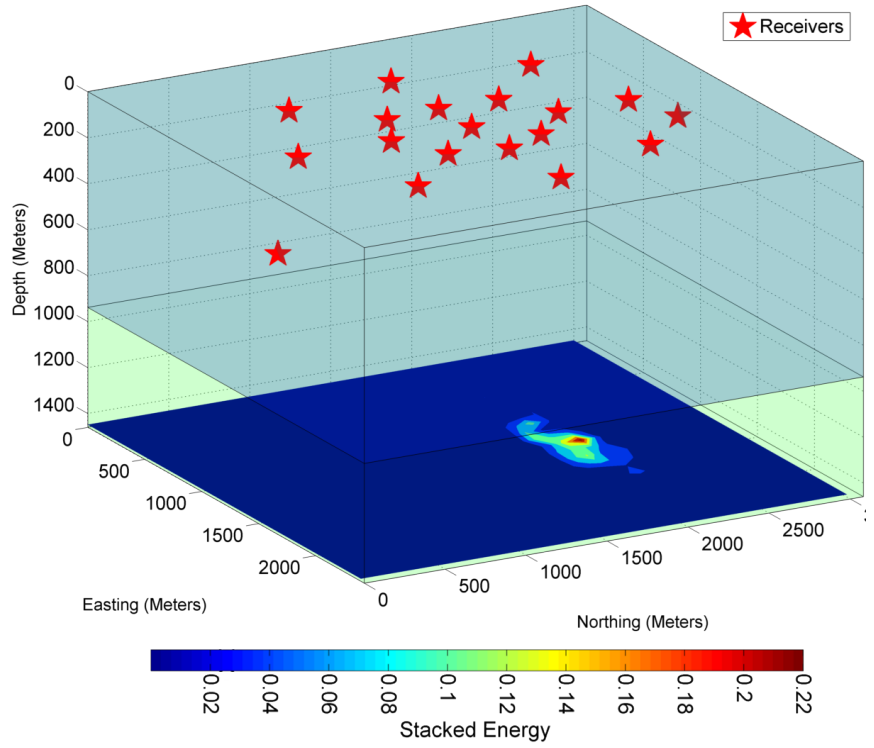

(b) Energy/traveltime residual ratio contour map at slice z = 1500 meters.

Figure 3.17: Comparison of the two methods used in location events. High values of stacked energy and energy/traveltime ratio corresponds to the event location. (a) Stacked energy contour map at slice z = 1500 meters. (b)Energy/traveltime residual ratio contour map at slice z = 1500 meters.

3.3 FOCAL MECHANISM DETERMINATION

Extracting the source mechanism of a microseismic event rather than just locating is essential. It allows interpreter to have a better understanding of reservoir dynamics. To this end, we have integrated a focal mechanism determination package with our location algorithm. The software package we have used is called "FOCMEC", which stands for "FOCal MEChanism Determinations". It is an open-source, Unix-based Fortran code, developed by the Virginia Tech University (Snoke, 2003).

Focmec performs an efficient, systematic search of focal sphere according to parameters inputted. Input may include polarities of P, SV and SH waves, and their amplitude ratios. It is not required to input all body wave amplitude ratios and polarities; nevertheless, it constrains the number of acceptable solutions. Number of polarity errors and errors in amplitude ratio are user-defined.

Focmec reads a data file consists of station information, azimuths, take-off angles, polarities- and/or amplitude ratios of P, SH, SV waves. Then it starts searching all possible focal mechanism solutions and lists optimal solutions based on the criteria inputted by the user. All solutions and their parameters (strike, dip, rake, polarity errors, and/or amplitude ratio errors) are saved to an external file. Listing 3.1 shows a sample data file that is used as an input file for Focmec.

One may think that the fundamental disadvantage of this software is that it is platform-dependent, which means that it is working only on certain platforms. As part of this research, we have complied the source code written in Fortran77, which enables it to run on almost every platforms including 64-bit Windows. Furthermore, complied version of Focmec is integrated with our location software coded in MATLAB. Hence, it becomes possible to do simultaneous location and source mechanism inversion. All necessary parameters (azimuths, take-off angles, polarities) are directly piped to the complied version of Focmec. Found solutions are retrieved and beach-ball diagrams can be generated.

Listing 3.1: Sample input file for Focmec.

```
Comment & Description
ST01   140.00    44.00C                P
ST02    67.00    58.00C               eP
ST03    82.00    77.00D                P
ST04   122.00    79.00D                P
ST05   270.00    60.00C               eP
ST06   158.00    45.00C                P
ST07    47.00    36.00D                P
ST08   103.00    29.00C               eP
ST09    74.00    24.00C                P
ST10    66.00    43.00D                P
```

Listing 3.1 displays sample file that is used in Focmec as an input file. First line of the file has no function in the focal mechanism algorithm. It is reserved for user comments and description. First column of the file should include station ID's or names, e.g. ST01, ST02. Second column contains azimuth degrees for each station. Third column includes take-off angles of seismic waves at each station. Right next to take-off angles, first motions of P or S-waves should be indicated whether they are compressional (up-going) or dilatational (down-going) by C or D symbols. Last column defines that if P wave or S wave polarities are used. The character "e" just before "P" indicates that it is an emergent P-wave arrival.

Azimuth and take-off angles are vital for an accurate source mechanism solution. Assuming seismic waves are traveling from the source location $S(x, y, z)$ to a certain station, $R(x', y', z')$, azimuth angle can be calculated by the following formula:

$$\alpha = arctan(\frac{x - x'}{y - y'}) \tag{3.7}$$

Where, r is the distance between source $S(x, y, z)$ and receiver $R(x', y', z')$

In order to calculate take-off angle, firstly, ray paths need to be determined. Assuming source coordinates is $S(x, y, z)$ and the first reflected point in 3D medium $P(x, y, z)$. Then, angle between two points (vector) in three dimension can be calculated by the Formula 3.8.

$$cos(\theta) = \frac{\vec{a} \cdot \vec{b}}{|\vec{a}| \left|\vec{b}\right|} \tag{3.8}$$

If an angle between S and P is θ; then, cos θ is division of dot product of S and P by product of magnitudes of S and P.

$$\vec{a} \cdot \vec{b} = a_x b_x + a_y b_y + a_z b_z \tag{3.9}$$

$$|\vec{a}| = \sqrt{a_x^2 + a_y^2 + a_z^2} \tag{3.10}$$

$$\left|\vec{b}\right| = \sqrt{b_x^2 + b_y^2 + b_z^2} \tag{3.11}$$

For the purpose of having user-friendly design, we have implemented a Focal Mechanism GUI tool so that user interactively load the Focmec data and input variety of parameters that are required for the algorithm.

Figure 3.18 illustrates the main window of Focal Mechanism GUI tool. After loading station data with clicking "Load Data" button, various parameters can be changed. The user may modify the minimum, the maximum, and the increment value of B-Plunge, B-Trend, and A-Angle parameters. Clicking "BEGIN" button starts the focal mechanism determination algorithm externally. Found solutions are listed after the process is done. To plot beachball diagrams of focal mechanism solutions, "Display Results" button needs to be clicked.

Figure 3.19 demonstrates the sample results that are obtained through Focmec algorithm.

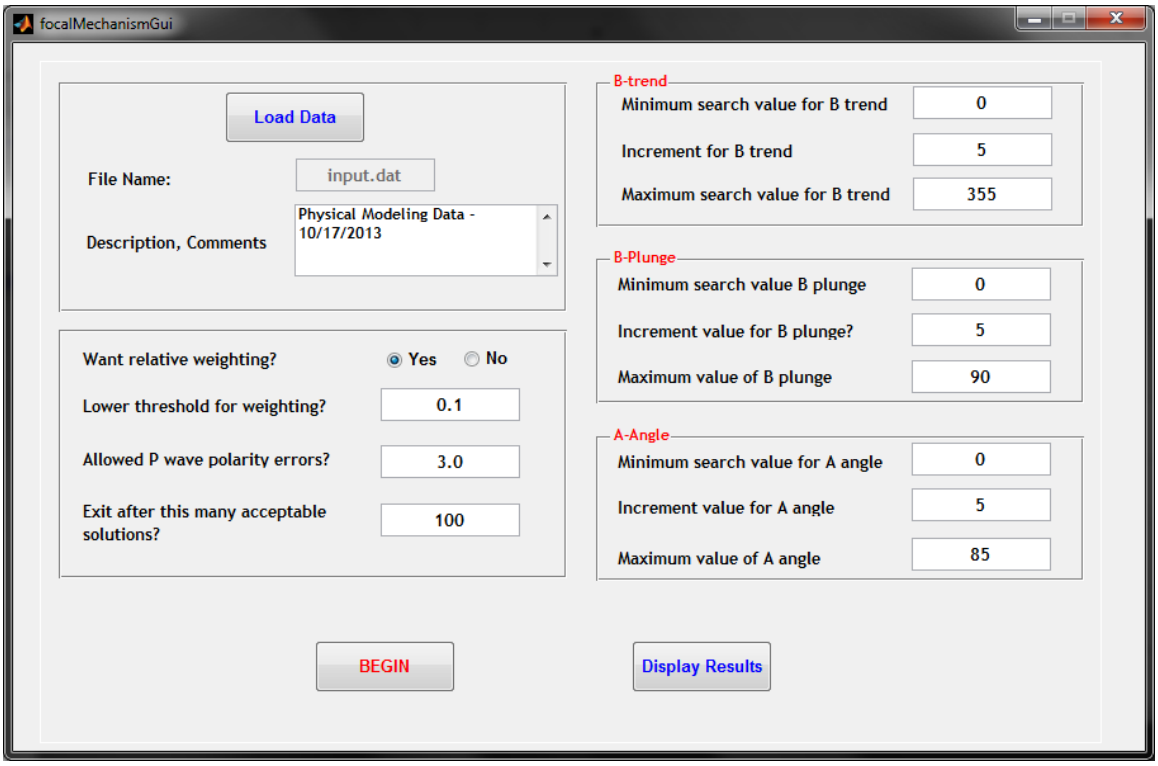

Figure 3.18: Main window of Focal Mechanism determination tool. User may load station data, change parameters, and display results interactively.

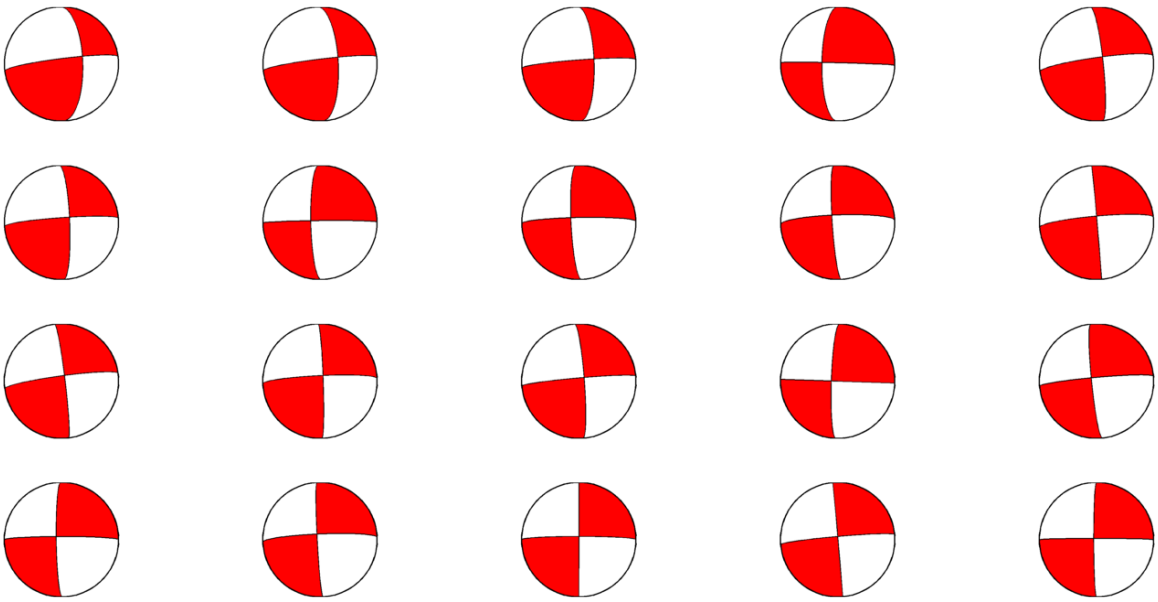

Figure 3.19: Sample beach-ball diagrams of 20 found solutions.

3.4 OPTIMIZATION OF THE ALGORITHM

Searching true event location among millions of potential sources requires enormous amount of computation. With the advancement of technology; increasing the number of FLOPS (floating-point operations per second), memory and storage; computation cost is decreasing dramatically.

Computational time can also be significantly decreased by taking advantage of recent advancements in technology such as parallel computing of CPUs (Central Processing Unit). Even more advance, there is relatively new technology available called GPU (Graphics Processing Unit). Basically, it is the use of a GPU together with a CPU to accelerate general-purpose scientific and engineering applications (Dongarra, 2012).

However, there are some misconceptions about the GPUs. It is thought that GPU is only responsible for rendering visual textures and is limited to only graphics operations like processing cutting-edge graphics. That was partially correct; graphics chips started, as its name reflects the original intention, for the purpose of controlling graphical application; nevertheless, after 2000's, developers and engineers adapt the processing power to accelerate a broad range of both graphical and non-graphical scientific applications. This is called GPGPU or General-Purpose computation of GPU.

GPU is the graphics chip in the video cards in computer and in game consoles. GPU is a massively parallel device so that it renders billions of pixels per second and it does this by taking advantage of parallelism. As opposed to multi-core CPUs, which usually consists of several cores, a GPU contains hundreds of processor cores (Figure 3.20).

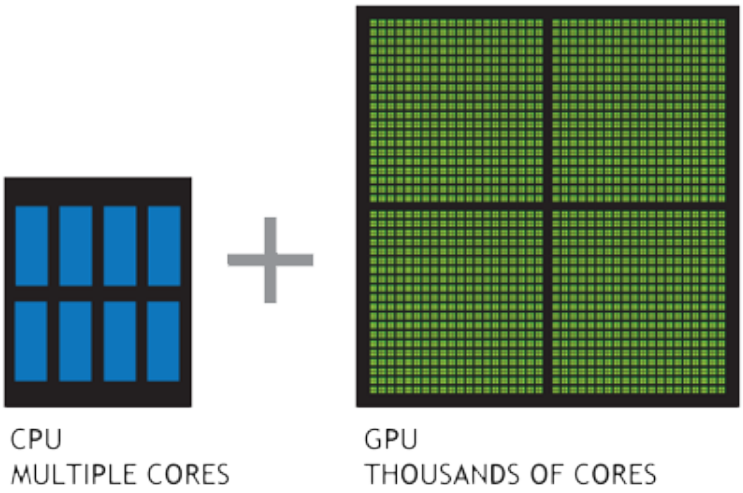

Figure 3.20: Comparison of CPU and GPU. While CPU consists of a few cores, a GPU contains thousands of smaller, efficient cores (Retrieved from: http://www.nvidia.com/object/what-is-gpu-computing.html)

The fundamental reason why GPU computing is much more efficient than the CPU computing is due to the fact that CPU consists of several cores while GPU has hundreds, thousands of small cores that make parallel computing much faster and efficient. GPUs are intentionally designed with highly parallel structure that large datasets can be handled at faster rate. However, GPUs are not suitable for handling relatively small data-sets. Because of the communication time between CPU and GPU, computation time might increase as oppose to speeding up.

One major drawback of GPU computing was that the difficulty in programming in devices. However, with the introduction of CUDA or "Compute Unified Device Architecture" by Nvidia, users can pipe C, C++, Fortran, or MATLAB code straight to GPU without the need of knowing assembly language.

MATLAB offers parallel CPU and GPU computing toolbox for the NVidia users. Taking advantage of this technology, the location algorithm was modified for parallel GPU computing.

We have done several benchmark tests to demonstrate the algorithm performance at different ways; single core CPU, multi-core CPU, and GPU computing. Figure

3.21 illustrates the benchmark results and comparison for the computational times for CPU and GPU computing for the case of two-layered model.

Specifications of the tested desktop computer are as follows:

- AMD Phenom X6 1055T 3.3GHz CPU
- NVidia GeForce GTX 460 1GB Graphic Processing Unit
- 8 GB RAM @1066 MHz

While using simultaneously all the six cores of CPU accelerate computation speed, using GPU together with CPU speeds up computation time significantly. Combining CPU with GPU is a powerful way to accelerate applications and algorithms for the reason that GPU consists of thousands of parallelly designed small, efficient cores; whereas, CPU consists of a few cores optimized especially for serial processing. CPU can run the serial portion of the code, while GPU handles the parallel part of the code.

A single event is located with seven different ways; using only P-wave and only S-wave separately traveltime residual, stacked energy, and energy/traveltime residual ratio as well as using both P and S waves with traveltime residual attribute. This benchmark results show the time that it takes for Ray tracing, locating events, and total elapsed time, individually.

Using single core CPU takes 11.4 seconds to locate a single event with seven different ways. Implementing multi-core CPU computing provides considerable amount of increase in performance such that the total elapsed time decreased to 4.2 seconds. Above all, taking advantage of GPU computing, total elapsed time reduced down to only 1.9 seconds. It is more than %80 increase in terms of computation time compared to single core CPU. When we compare with the multi-core CPU computing, the total increase is 54 percent.

The most significant acceleration we have seen is the Ray Tracing part. Calculating of millions of possible ray paths in parallel requires substantial amount of computation. From the Figure 3.21, it can be seen that elapsed time for Ray Tracing is reduced to 6.5 seconds to 1.3 seconds using multi-core CPU. Further, implementing GPU computing decreases the CPU time, 1.3 seconds, to only 0.6 seconds, which is 53 percent over multi-CPU computing, and 90 percent increase in performance over single core CPU computing.

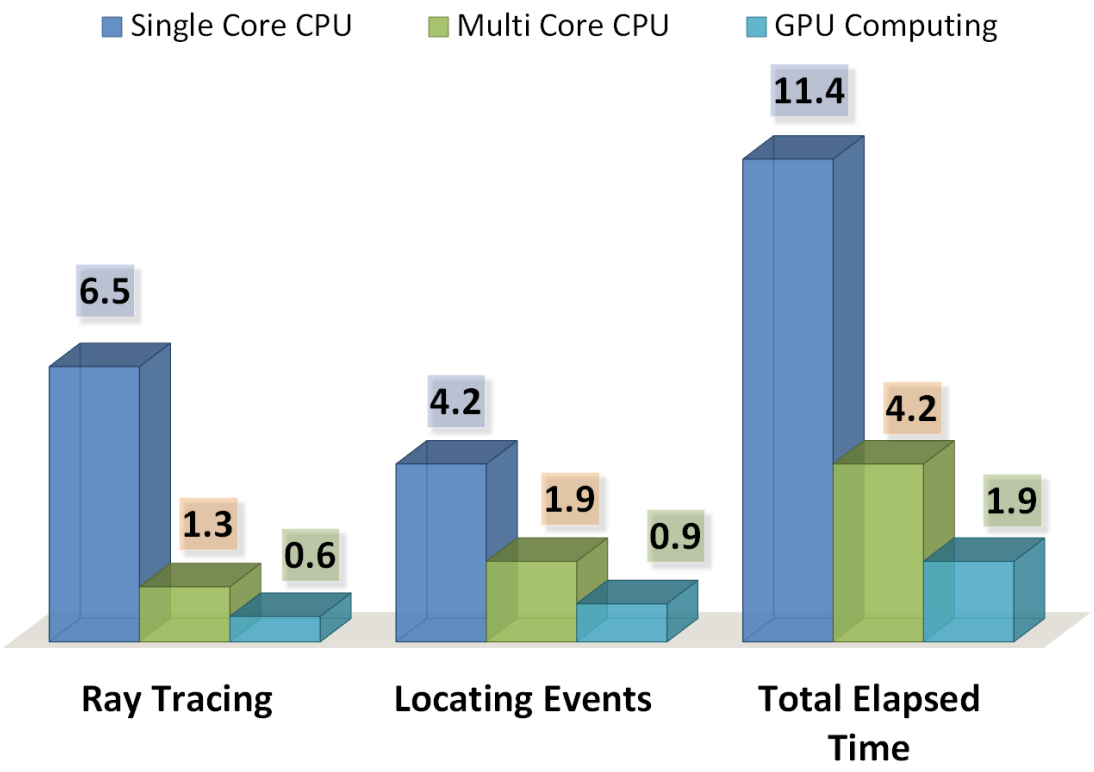

Figure 3.21: Benchmark results of single core, multi core CPU and GPU computing for two layered model case. Significant increase in performance is observed with the implementation of GPU computing. Numbers are shown in this figure is in seconds.

Chapter 4. Physical Modeling Experiments

4.1 INTRODUCTION

In this research, I use three-component simulated microseismic data acquired over various physical models at the Allied Geophysical Laboratories (AGL) at the University of Houston.

Compared to purely numerical, synthetic experiments, physical models produce a more realistic study of the acoustic wave propagation including reflected and refracted events as well as multiples. Physical models may produce distortions that can be generated in the real world. Further, using real rocks in our experiments allows us to understand the behavior of a rock in real world.

Experimenting with physical models and natural rocks have many advantages. Some of them are as follows:

- **Affordable:** Building physical models and/or obtaining a real rock sample is relatively affordable.

- **Faster and easier to acquire data:** Acquiring data on physical models are much faster and easier than acquiring data on field. Data can be acquired semi-automatically once the acquisition parameters are set.

- **Reflects a more realistic data:** Physical models and even better real rocks produce a more realistic data than the synthetic case due to the fact that the use of real vibrations in actual materials.

- **Repeatability:** Acquiring data on the same model over different receiver configurations is possible and easy. Further, physical modeling experiments is more controllable than in the field.

- **Material properties:** Material properties such as anisotropy and elastic modules can be investigated better with laboratory measurements.
- **Answer is known in advance:** Especially in the case of microseismic experiments, knowing the answer (source location, velocity of the medium) in advance allows us to test our algorithms applicability and reliability.

Throughout this research, I have conducted three different experiments with ultrasonic source and receivers. Each experiment will be explained in detail at their section. These experiments are as follows:

1. Single layer physical modeling experiment using Plexiglas model.
2. Two layered model created by joining two different physical models: Aluminum and Plexiglas.
3. Single layer microseismic experiment using sandstone real rock.

In physical modeling experiments, we generally scale the dimensions of the models by a factor of 10,000 to make the ultrasonic measurements (at 1 MHz) look similar to the seismic band at 100 Hz. For instance, a model dimension of 10 mm becomes 100 meters. Throughout this research, all the figures and results will be annotated with the associated scaled dimensions.

4.2 SINGLE LAYER PHYSICAL MODELING EXPERIMENT (PLEXIGLAS)

In the first experiment, I have chosen to study on the simplest physical model; one layered, isotropic, and homogeneous Plexiglas. The actual model dimensions are 307.7 x 242.4 x 93.9 mm, resulting in, after scaling, 3077 meters in X, 2424 meters in Y directions, and 939 meters in Z direction.

4.2.1 Data Acquisition Procedure

Data acquisition is performed with the bench-top ultrasonic system at the AGL. This system includes a pulser/receiver, HS-4 oscilloscope, preamplifier, and P & S-wave ultrasonic transducers.

The data on Plexiglas model was acquired using ultrasonic source and receivers. At the surface of the Plexiglas model, eight ultrasonic, one component transducers were used as receivers in the acquisition procedure.

Before starting data acquisition, we make sure that the Plexiglas block is in good condition for coupling, which is important for acquiring good signal. Sandpaper is used to flatten the surfaces of Plexiglas in order to increase coupling between model surface and transducers.

In the first stage of data acquisition, we have generate signal using 1 MHz ultrasonic source transducer and the signal is recorded at known source-receiver locations and distances to determine both P and S-wave velocities. According to our measurements, P and S-wave average velocities are 2743±5 and 1382±5 meters/second. The estimated Vp/Vs ratio is ~ 1.98 for Plexiglas block. For more accurate measurements, delay time between transducers needs to be taken into account, in our case it is 178.26 nanosecond.

After determining acoustic wave velocities, we have begun to simulate microseismic events. In this part of data acquisition, a vertical source transducer is placed underneath the block at the coordinates of (75.0, 121.2, 93.9 mm) to generate signal. To record the signal, 8 receivers are placed on the surface.

Figure 4.1 shows the picture of the model used in the first experiment. On one surface of the block, receivers are placed; on the other surface, the microseismic signal is simulated. Figure 4.2 shows the back side of the Plexiglas model where source transducers are placed. Data acquisition parameters are listed in Table 4.1.

Table 4.1: List of data acquisition parameters for the first experiment.

Acquisition Parameters	**Value**
P-Wave Velocity	2743 m/s
S-Wave Velocity	1382 m/s
Central Frequency of Transducers	1 MHz
Delay Time between Transducers	178.26 nanosecond
Number of Samples	20k
Total Length of a Recorded Signal	400 microsecond
Sampling Frequency	5 MHz
Sampling Rate	0.02 microsecond

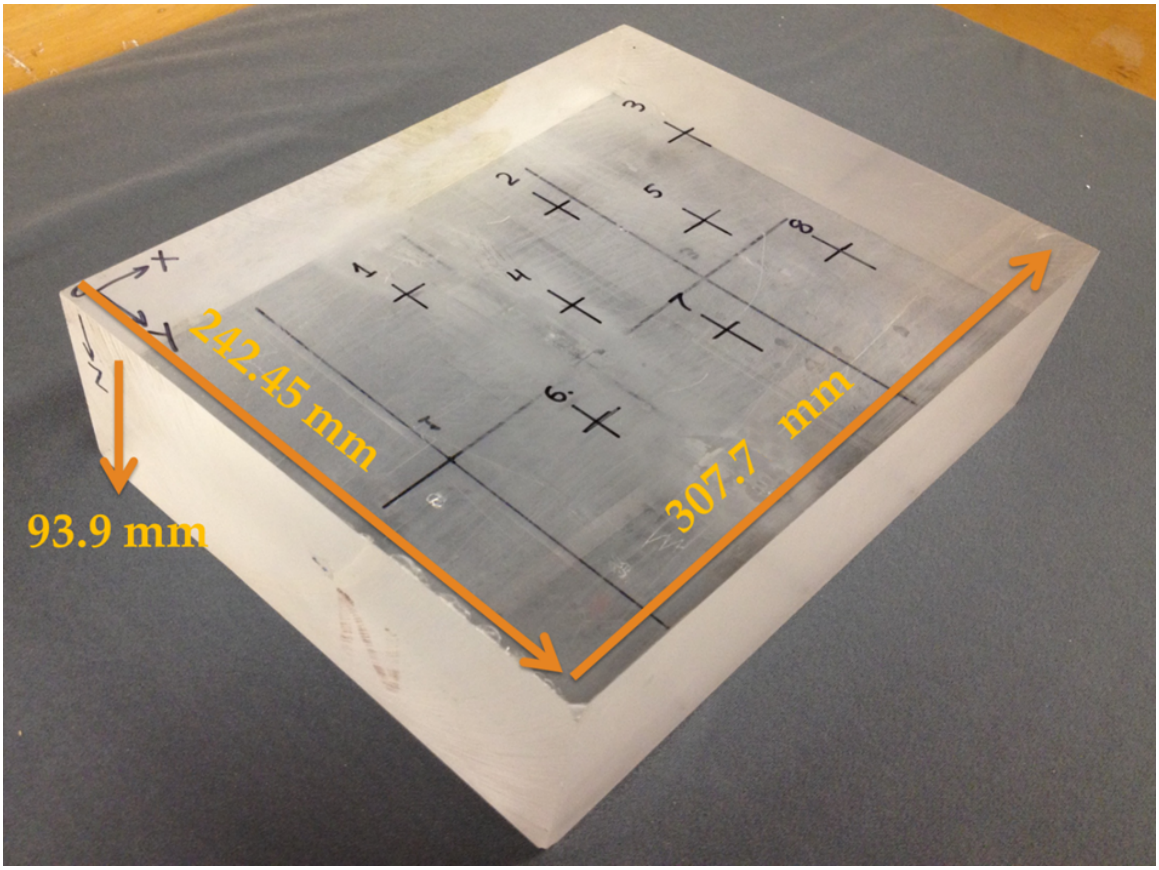

Figure 4.1: Plexiglas model used in the first experiment. 8 receiver positions are on the model's upper surface. Source transducer is placed underneath the block.

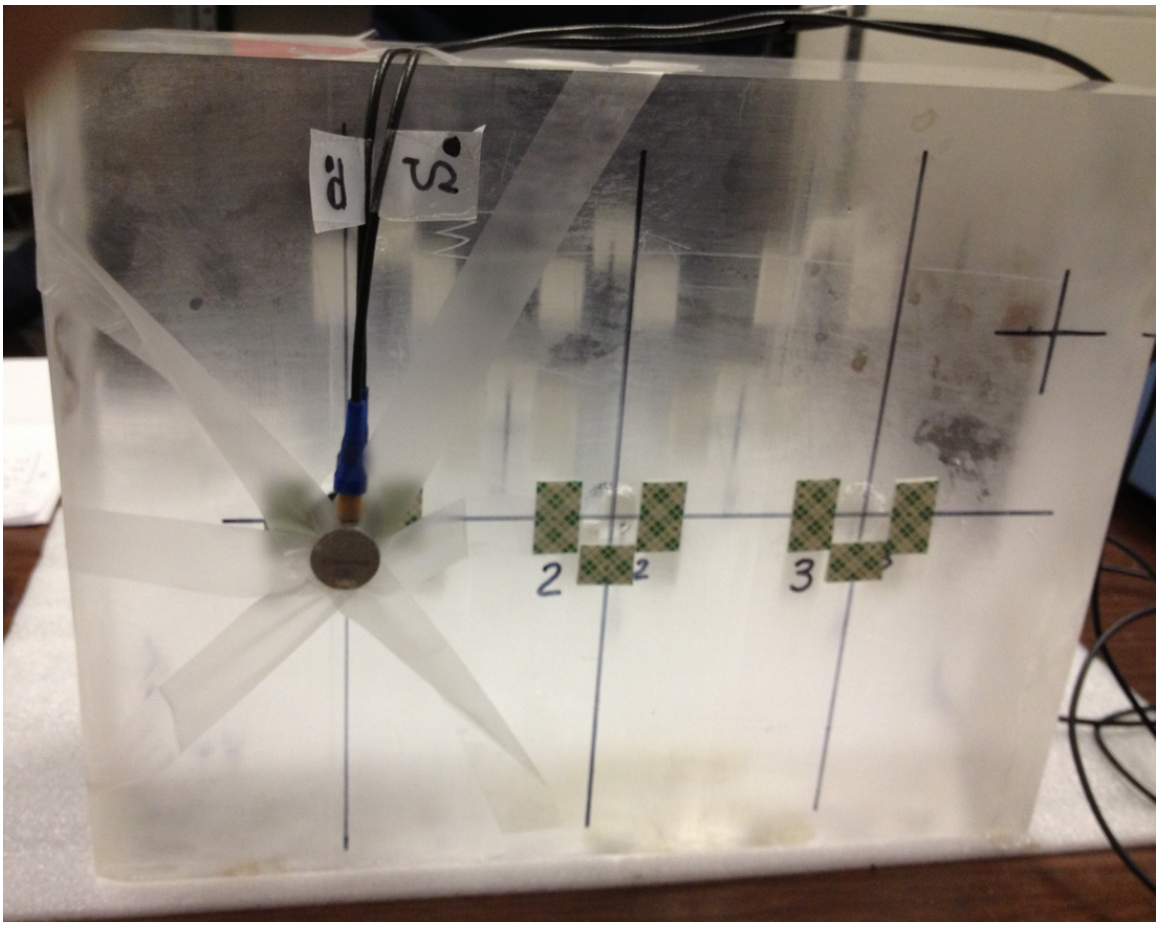

Figure 4.2: Back side of the Plexiglas model where source transducer is positioned.

Figure 4.3 displays the signals that are acquired at the same source-receiver locations but the acquisition approach is different. The signal at the top of the Figure is acquired without stacking technique; however, the signal at the bottom of the Figure is acquired with 128-fold vertical stack. Acquiring data with stacking significantly increases SNR of signal. Therefore, the stacked signal has relatively high signal-to-noise ratio. Frequency filtering is applied to all data to further reduce random noise.

Figure 4.4 displays all 8 traces acquired on the Plexiglas model. Since we have used vertical source to simulate seismic signal, S-waves are weak at the most of the stations. However, we are seeing a very clear P-wave arrivals at every receiver.

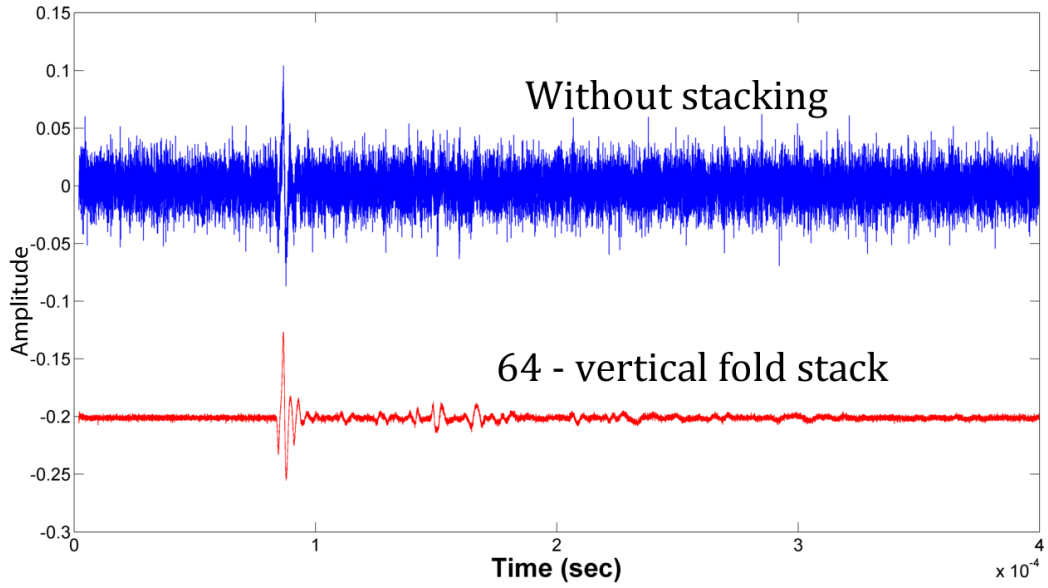

Figure 4.3: Comparison of the same station data obtained with different way. Signal at the top is acquired without stacking; the signal with red color is obtained with 128-vertical fold.

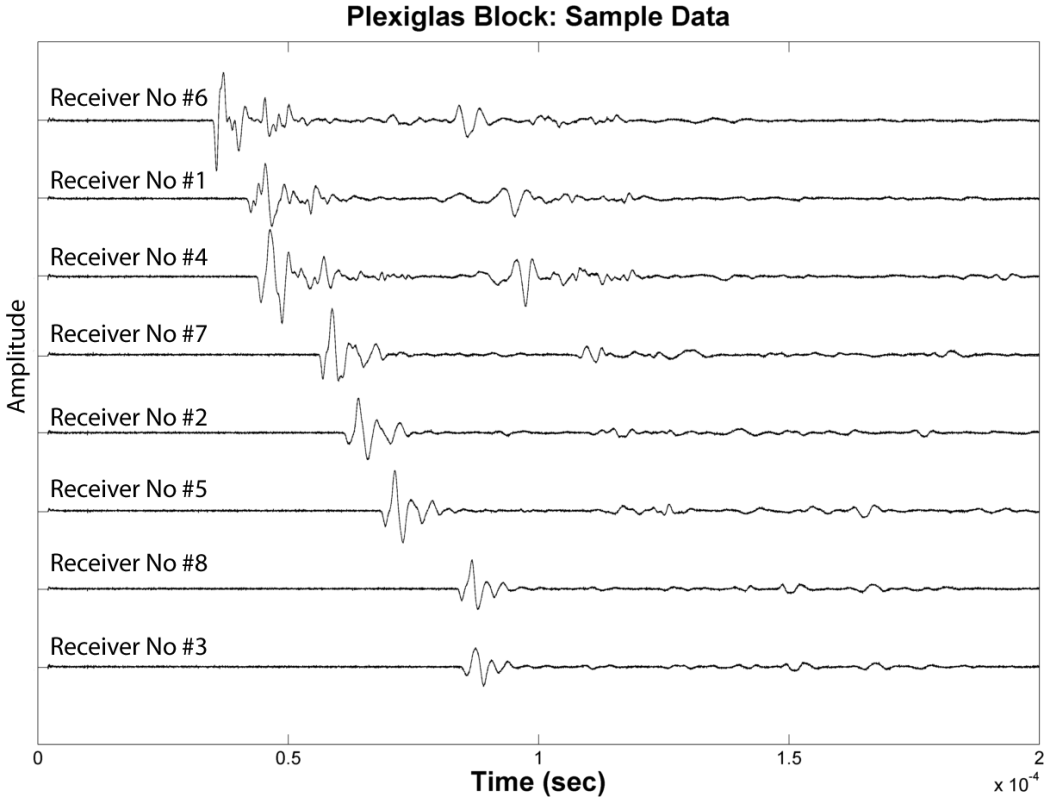

Figure 4.4: Acquired 8 traces at different positions on the Plexiglas model. Using vertical source transducer limits the seismic waves to only P-wave. S-waves do not observed at the most of the stations.

Absence of three component data and not having S-wave signal directed us to conduct the second experiment using 3-C transducers and horizontal (S-wave type) source. In the second experiment, the same Plexiglas model was used; however, data was acquired with different type of receiver geometry. Totally, 21 cylindrical 3-C receivers are used in the experiment; 17 receiver positions are on the model's upper surface and four of them are positioned at the side of the model (borehole equivalent).

Figure 4.5 shows the picture of the model with star-shape receiver geometry used in the second experiment. In this experiment, we have used 3-C transducer as a receiver as shown in Figure 4.6.

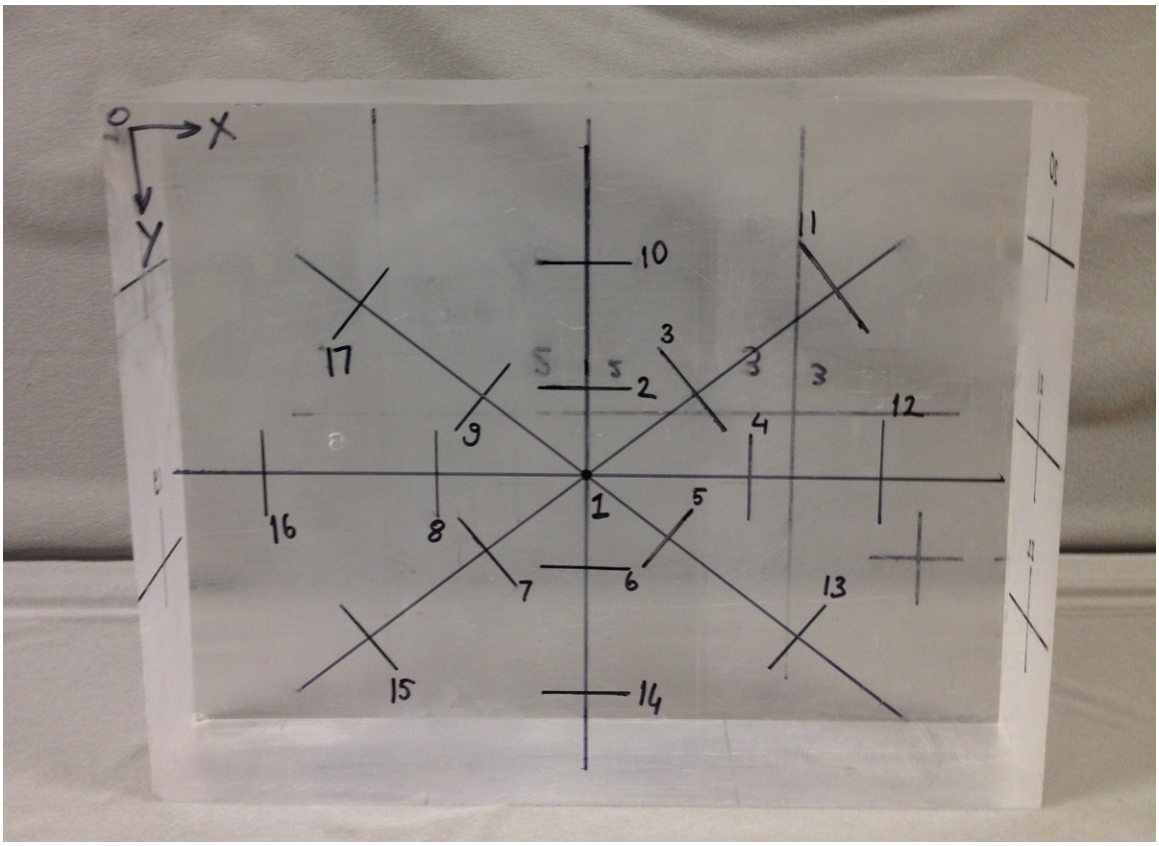

Figure 4.5: Picture of the Plexiglas model used in the second experiment. Star-shape receiver geometry is used in the second experiment. 17 receiver positions are on the model's upper surface. 4 receivers positioned at the side of the model (borehole equivalent). Source transducer is placed on the other surface of the block.

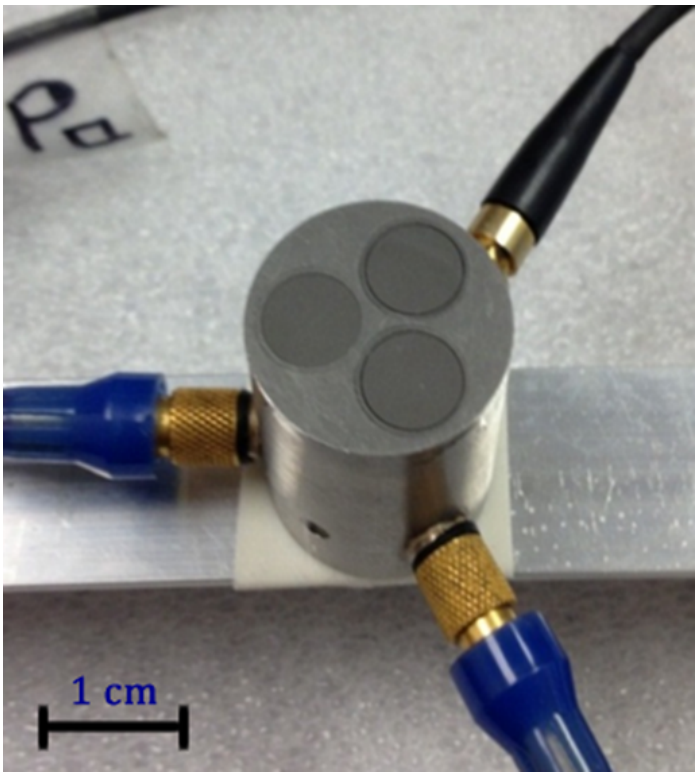

Figure 4.6: Three-component transducer used as a receiver.

The signal was recorded at 21 stations including surface and well-side positions. Figure 4.7 shows a single 3C seismogram at station #1. Unlike the previous experiment, we are observing distinct P and S-wave arrivals. Acquiring data with 128-vertical fold significantly increases the SNR.

Star-shape receiver geometry consists of four lines, two diagonal, one vertical (parallel to y-Axis), and one horizontal (parallel to x-Axis). Figure 4.8 displays one line of vertical sensor data. All the five traces on this line exhibits very clear P and S-wave arrivals, therefore, picking first break has become relatively easy.

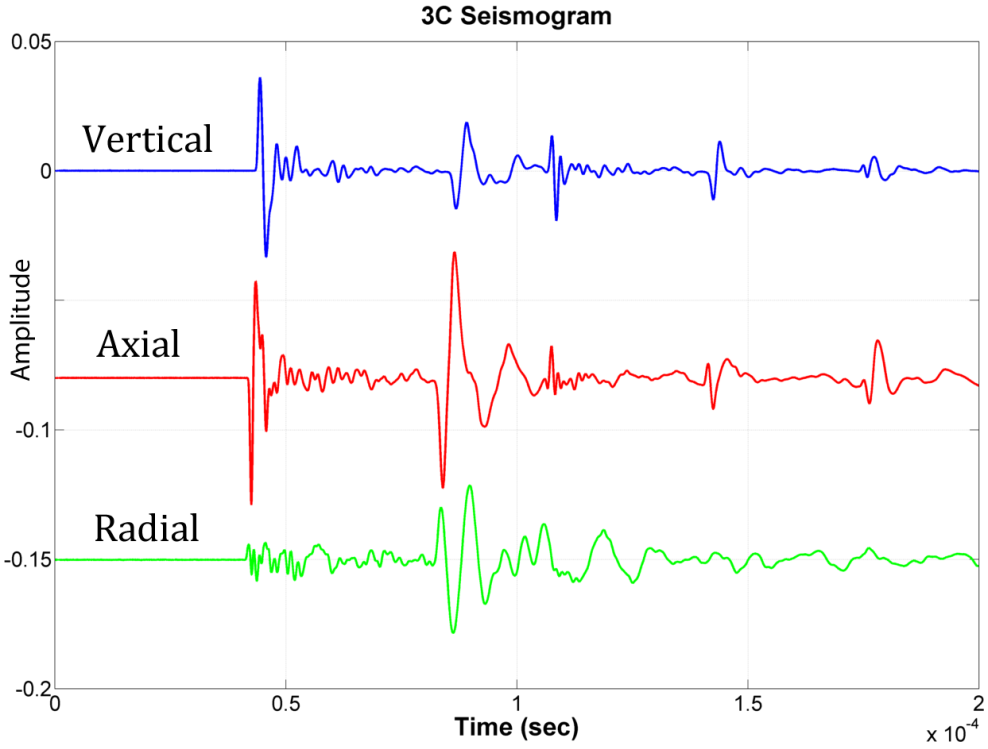

Figure 4.7: Sample 3C seismogram recorded at receiver #1. Distinct P and S-wave arrivals are observed.

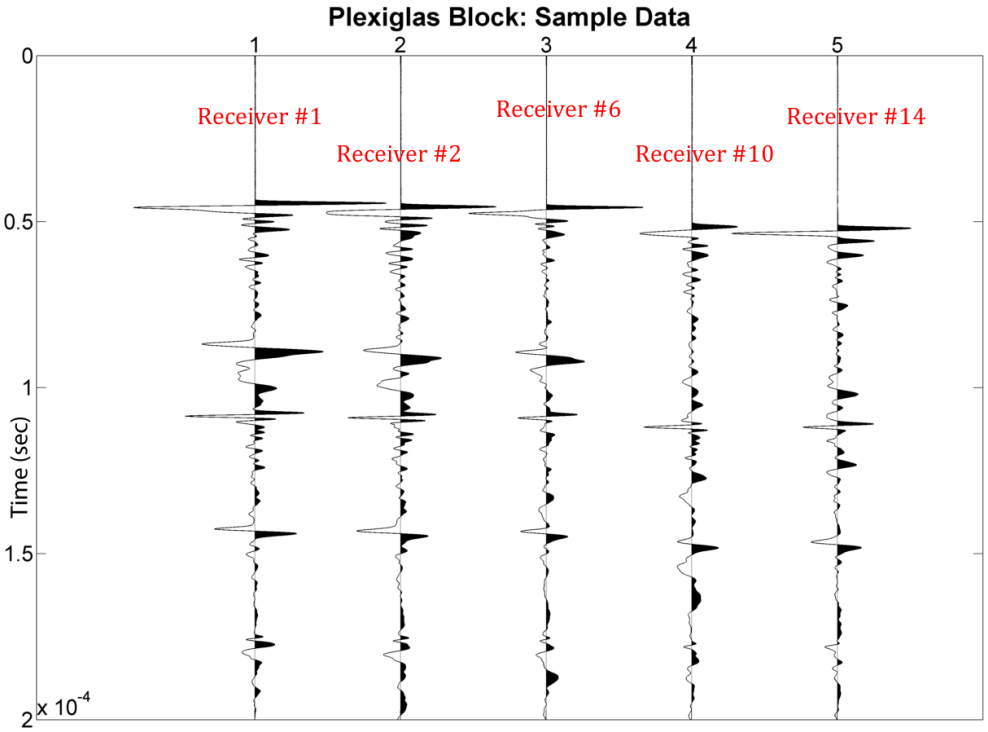

Figure 4.8: One line (parallel to Y-axis) of vertical sensor data from Plexiglas block.

4.2.2 Locating Events

After acquiring the data next step is to test our location algorithm in terms of its accuracy. To this end, frequency filtering is applied to acquired Plexiglas data to reduce random noise. Afterwards, first arrival picking is performed using STA/LTA algorithm. Then the input parameters are piped to the location algorithm. Figure 4.9 shows the 3D view of the model as well as source and receiver positions. In this experiments, four data-set are acquired at four different source location. Black starts represent the source positions, and red stars denote the receiver locations.

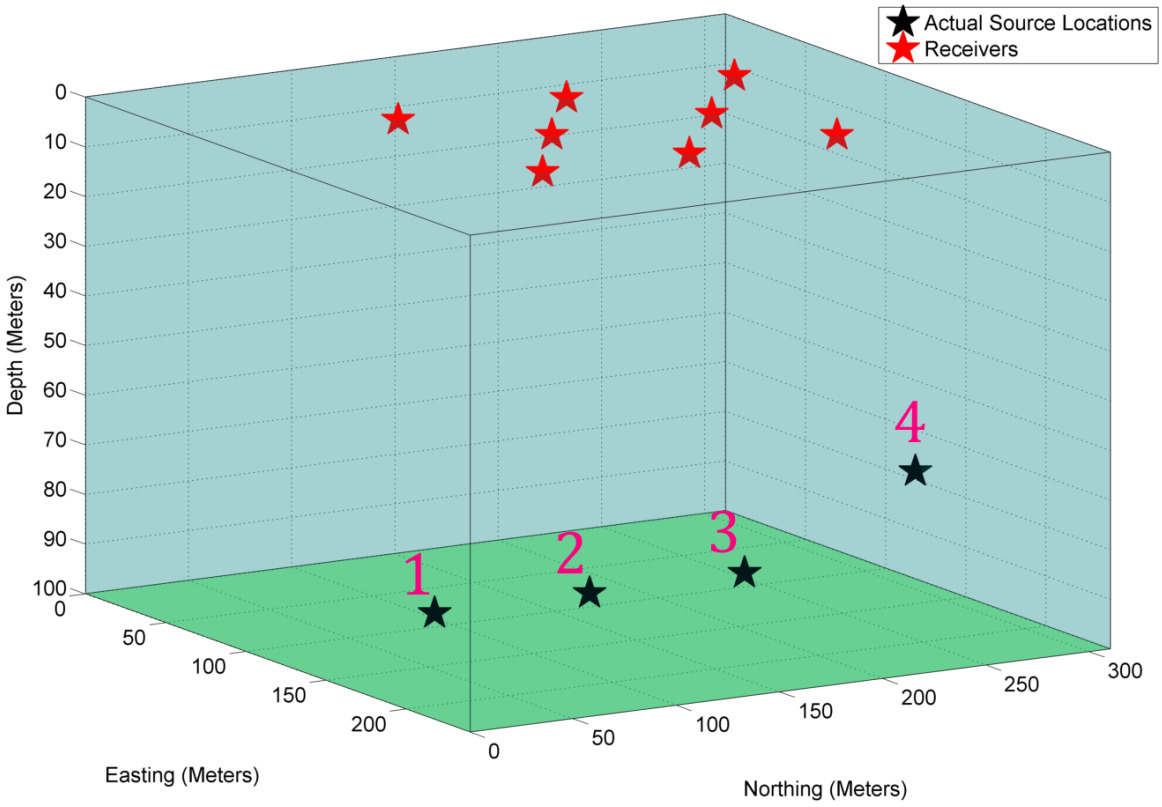

Figure 4.9: 3D view of the model showing receiver and source locations. Black stars denote the true source locations, whereas red stars indicates receiver coordinates.

Because of using vertically polarized source transducer, we observed weak S-wave arrivals; therefore, we could only locate events using P-waves. Figure 4.10 demonstrates the actual source location along with the located event coordinates.

Magenta stars correspond to the found event location. Side view of the 3D model is shown in Figure 4.11.

Table 4.2 compares true source and calculated source locations of these simulated microseismic events. True source location, calculated event coordinates, absolute error, and relative error for each four data-sets are listed. The absolute error is defined as the distance between true and calculated source location; whereas, the relative error is defined as the ration of the absolute error to the distance between two diagonal corners of the model.

Table 4.2: Comparison of actual and calculated source locations in terms of absolute and relative error.

Source ID	**Actual Source Locations (mm)**	**Calculated Source Locations (mm)**	**Absolute Error (mm)**	**Relative Error (%)**
#1	(75.0, 121.2, 93.9)	(80.0, 128.0, 91.0)	8.80	2
#2	(150.0, 121.2, 93.9)	(155.0, 126.0, 95.0)	6.98	1.7
#3	(225.0, 121.2, 93.9)	(220.0, 120.0, 92.0)	5.49	1.3
#4	(307.7, 121.2, 77.9)	(310.0, 117.0, 74.0)	6.20	1.5

According to Table 4.2, all four simulated microseismic events are located within 2 percent of relative error. These locations are found by traveltime residual method using only P-waves.

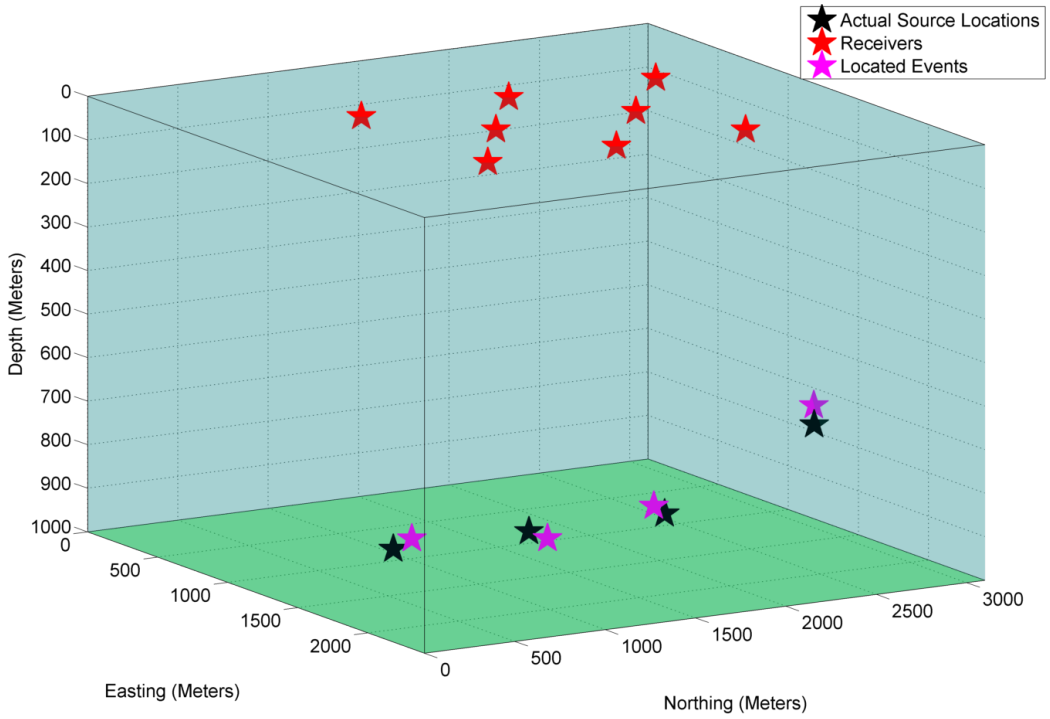

Figure 4.10: Events coordinates are found with traveltime residual method. Located source positions along with actual source locations are plotted with red, black, and magenta stars, that represent receiver, actual source, and located source coordinates, respectively.

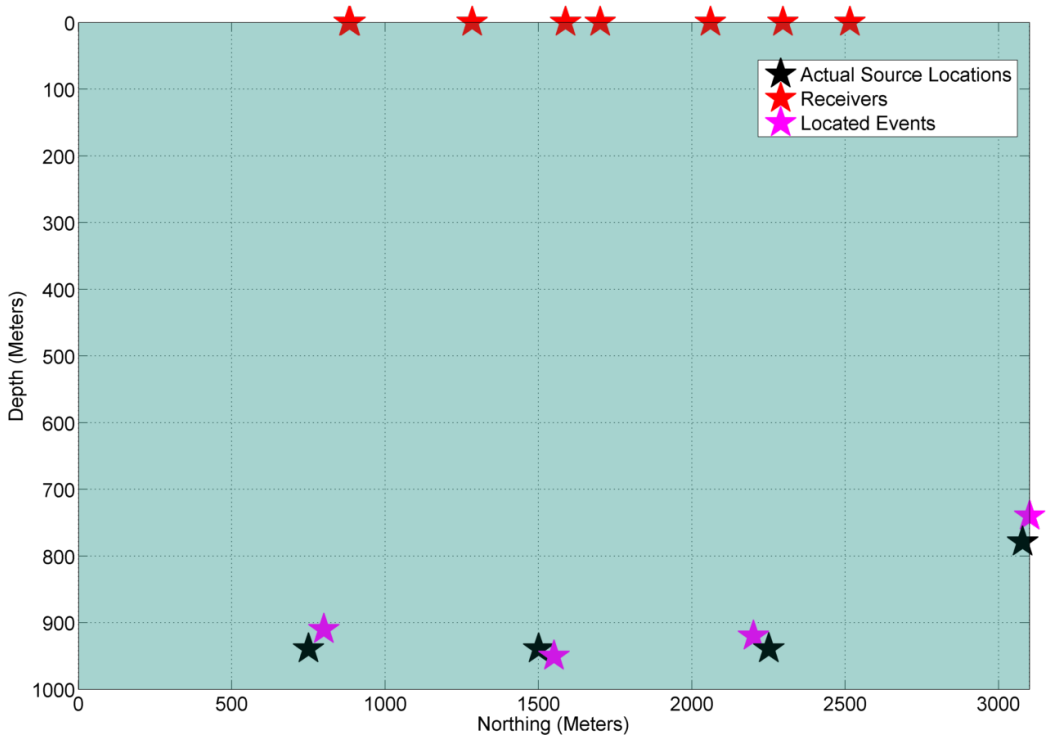

Figure 4.11: Side (X-Z) view of the located events. Not having well-side receivers decreases vertical resolution.

Another effective way to locate events is computing Energy/traveltime residual ratio and picking the location where yields maximum ratio value, which does not mainly depend on first break picking. Figure 4.12 demonstrates three slices of this ratio, which was generated for source #4.

Table 4.3 makes a comparison between the two methods for the 4^{th} source location: Traveltime residual versus energy/traveltime ratio. Latter approach provides a better vertical resolution compared to traveltime residual. Further, absolute error is reduced to 2.35 mm from 8.8 mm. The relative error is also decreased to 0.2 percent from 1.5 percent.

Table 4.3: Comparison of traveltime residual and energy/traveltime residual ratio method.

Approach	**Actual Source Locations (mm)**	**Absolute Error (mm)**	**Relative Error (%)**
True source location	**(307.7, 121.2, 77.9)**	**-**	**-**
Traveltime residual	(310.0, 117.0, 74.0)	8.80	1.5
Amp./Traveltime Ratio	(309.0, 123.0, 77.0)	2.35	0.2

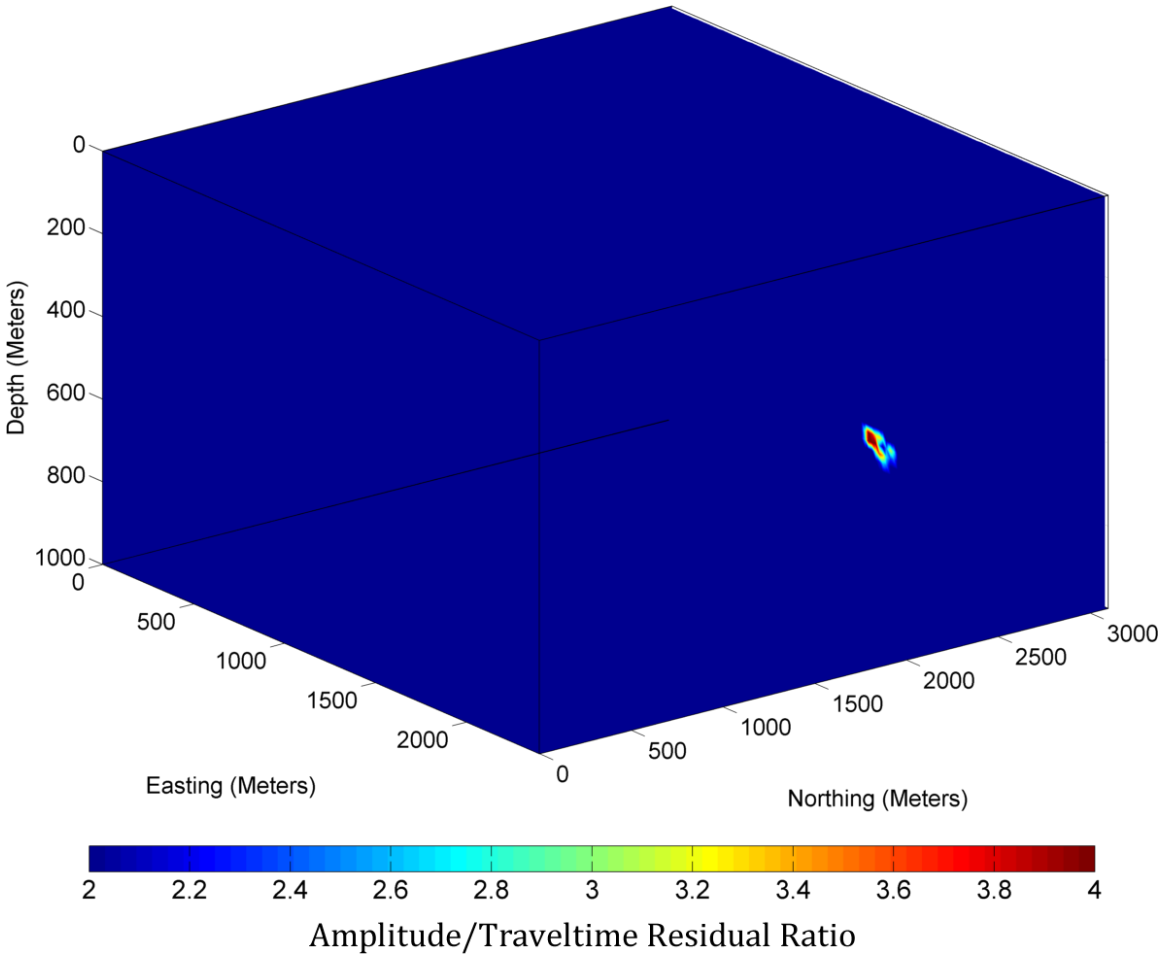

Figure 4.12: Three slices of Energy/traveltime residual ratio at x = 3100 meters, y = 0 m., and z=1000 meters. Maximum of the ratio corresponds to the source location.

The second experiment on Plexiglas block was conduced with a different receiver geometry. A star-shape station configuration is preferred to obtain data with high azimuth coverage. This time four well-side receivers are placed on each side of the Plexiglas block. Figure 4.13 displays receiver, source configuration, and the 3D view of the model. The source transducer is positioned at (75.0, 121.2, 93.9 mm) or with scaled dimensions; (750, 1212, 939 meters).

Another major difference between the two experiments, this time, horizontally polarized source is used, allowing strong S-wave data to be measured. After first break picking is performed for both P and S waves, event coordinates is located in seven different approaches. Moreover, locating is also performed in two different receiver

configurations. First, we include all receivers (surface plus borehole), then we exclude well-side receivers and locate event.

Figure 4.14 and 4.15 illustrates the contour maps of stacked energy, and energy/traveltime residual ratio. Both attributes are accurately locate event position; however, energy/traveltime residual ratio produces a less noisy result.

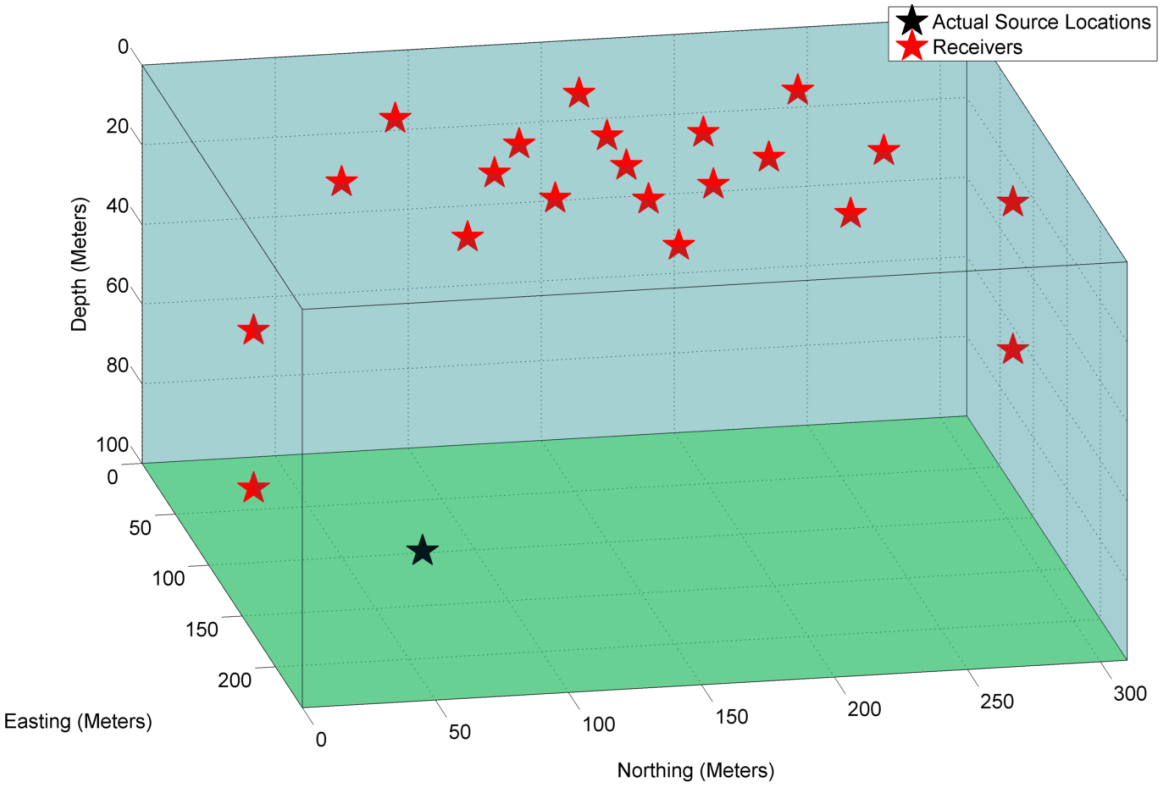

Figure 4.13: Displaying receiver and source configuration. Additional to star-shape receiver geometry, four well-side receiver are placed on each side of the block.

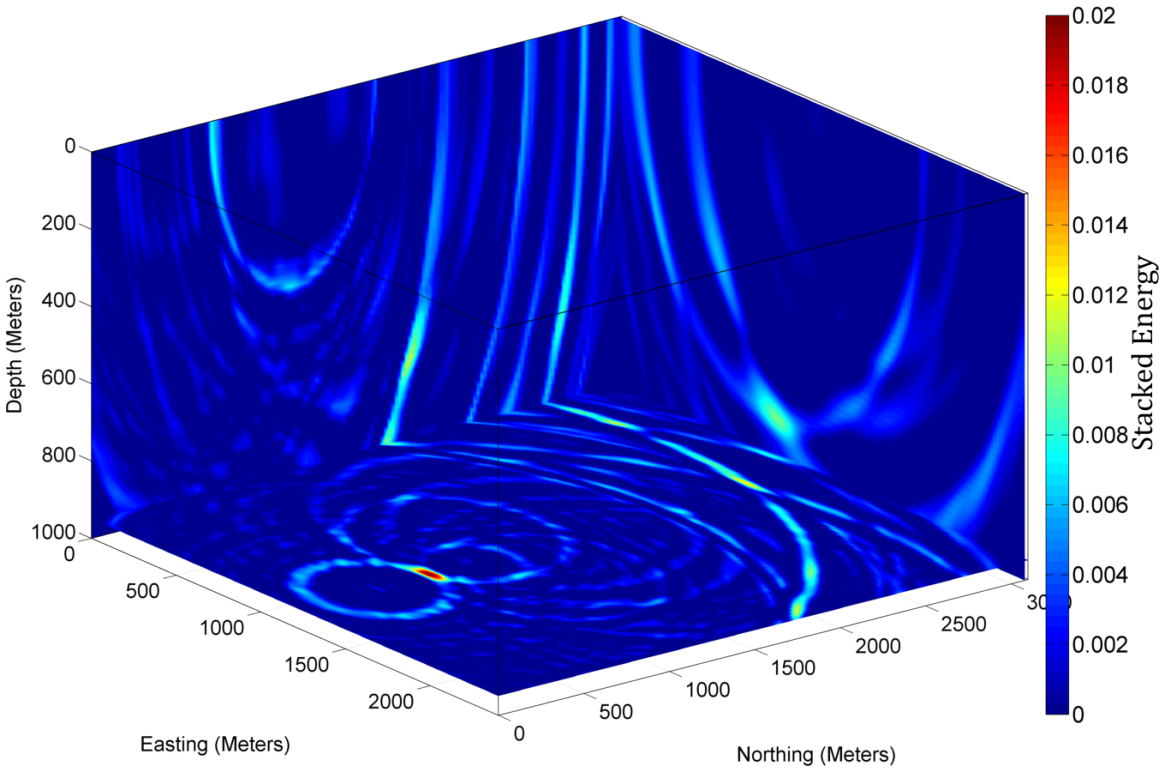

Figure 4.14: Stacked energy contour slices at different position. Simulated event coordinate is found at z = 94 mm or 940 meters.

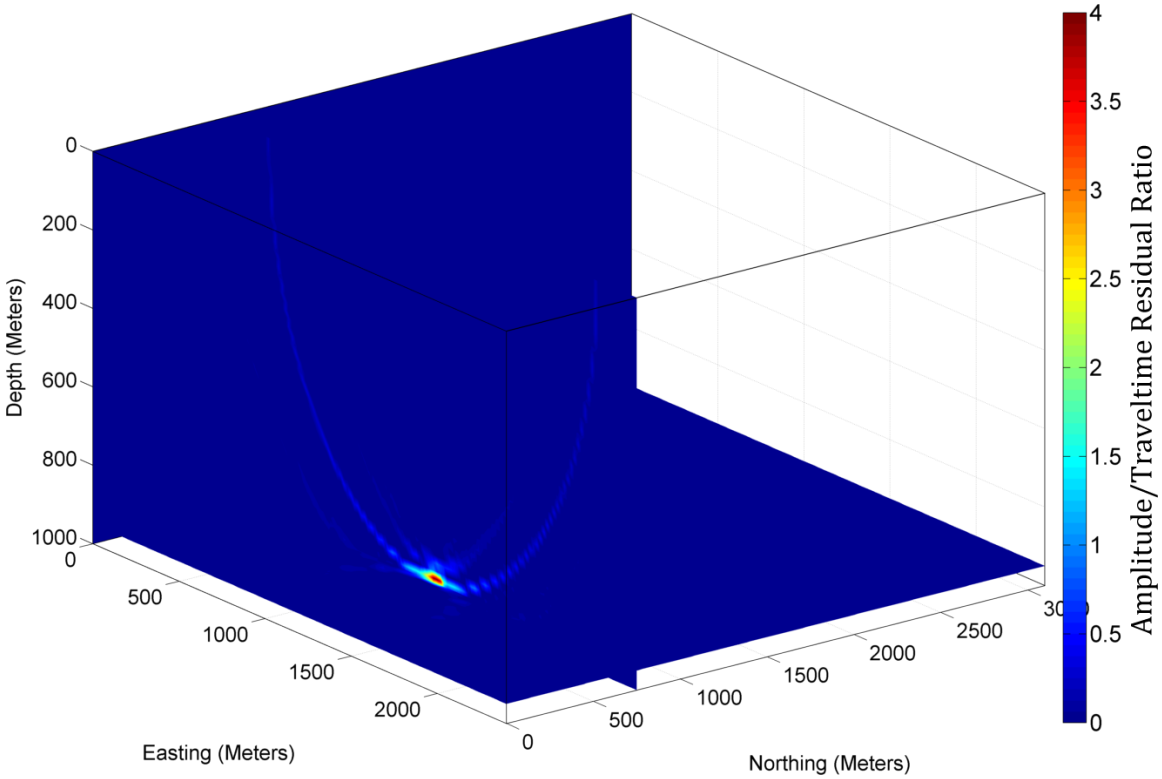

Figure 4.15: Energy/traveltime residual ratio contour map slice at x = 750 meters.

Table 4.4 and Table 4.5 make comparisons of the traveltime residual, stacked energy and energy/traveltime residual ratio methods using only P-waves, only S-waves, and using P and S-waves. Table 4.4 shows the results including all receivers; whereas, Table 4.5 displays the results for using only surface receivers.

We have used three different attributes to locate source locations: traveltime residual, stacked amplitude and energy/traveltime residual ratio. One important conclusion we obtain from the Table 4.4 is that for each cases (P-wave only, S-wave only, and P-S wave), Energy/traveltime residual ratio yields better location accuracy even though using individually all of the three attributes allows us to pinpoint source coordinates with confidence.

Using only P-waves is more accurate approach to locate events in this case compared to using only S-waves, and using P & S-waves. The relative error of P-wave and amplitude-ratio case is 0.43 percent; whereas, the relative error for only S-wave, and P & S-wave case are 1.1 percent and 1.7 percent, respectively.

Location uncertainty increases when downhole receivers are left out for all cases (P-wave only, S-wave only, and P-S wave). The seven approaches are able to locate event with confidence; however, taking the first approach (P waves and all receivers) gives less location error. Surprisingly, combining P and S-waves does not produce as accurate location as in only P or only S-wave case. Including well-side receivers increases location accuracy for P & S-wave approach; however, its accuracy still less than using only P-wave approach.

Table 4.4: Comparison of the traveltime residual, stacked energy and energy/traveltime residual ratio methods using only P-waves, only S-waves, and using P and S-waves. All receivers (surface plus well-side) are included for location.

Approach (All receivers)	**Absolute Error (mm)**	**Relative Error (%)**
Using only P-waves		
Traveltime residual	1.98	0.48
Stacked Energy	2.20	0.55
Energy/traveltime ratio	1.74	0.43
Using only S-waves		
Traveltime residual	8.9	2.4
Stacked Energy	4.45	1.1
Energy/traveltime ratio	4.45	1.1
Using P and S-waves		
Traveltime residual	2.8	0.7

Table 4.5: Comparison of the traveltime residual, stacked energy and energy/traveltime residual ratio methods using only P-waves, only S-waves, and using P and S-waves. Only surface receivers are taken into account to locate events.

Approach (Only surface)	**Absolute Error (mm)**	**Relative Error (%)**
Using only P-waves		
Traveltime residual	3.30	0.82
Stacked Energy	3.30	0.82
Energy/traveltime ratio	2.25	0.55
Using only S-waves		
Traveltime residual	11.3	3.1
Stacked Energy	6.06	1.5
Energy/traveltime ratio	4.45	1.1
Using P and S-waves		
Traveltime residual	3.8	0.94

4.2.3 Focal Mechanism and Radiation Pattern Determination

After locating events, we further continue characterizing source mechanism. First we have determined first arrival polarities of both P an S-waves. Figure 4.17 and Figure 4.16 demonstrates the polarization contour maps for P and S-waves. Since Plexiglas is isotropic and homogeneous, we have not observed any polarity changes across receivers. For all receiver locations, negative amplitudes are observed.

From the Figure 4.16 we are observing typical S-wave radiation pattern (Figure 4.18), where directly above of the source, there is maximum amplitude. As the angle of incidence increase, the first arrival amplitude is decreasing.

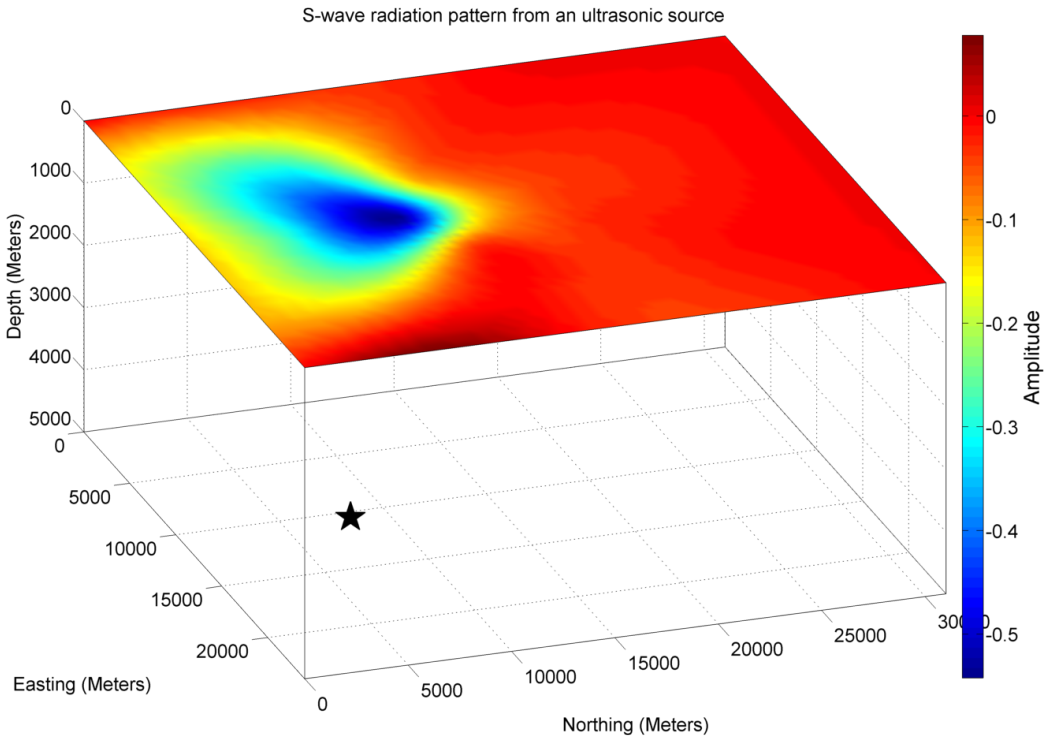

Figure 4.16: S-wave radiation pattern of an ultrasonic source on the Plexiglas model.

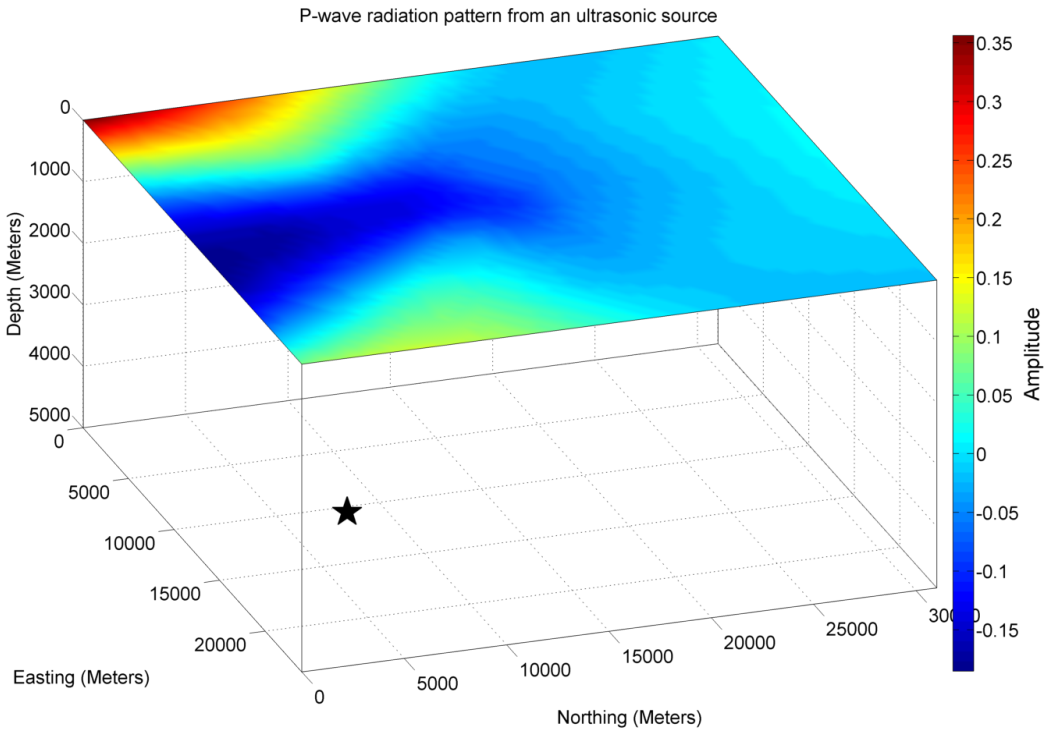

Figure 4.17: P-wave radiation pattern of an ultrasonic source on the Plexiglas model.

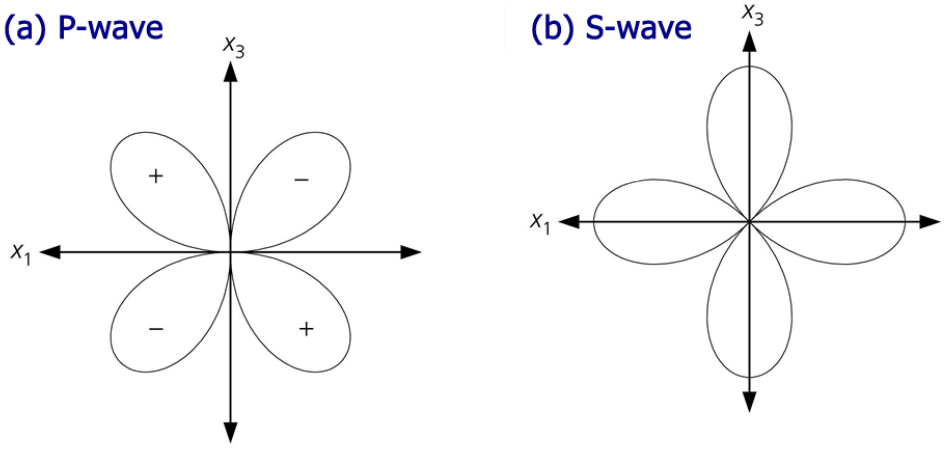

Figure 4.18: Theoretical radiation patterns of double-couple source for (a) P-wave (b) S-wave. Modified after (Stein and Wysession, 2003).

4.3 MULTI LAYER PHYSICAL MODELING EXPERIMENT (ALUMINUM AND PLEXIGLAS)

In the first experiment, we acquire data on 1-layer model and successfully locate events using the location algorithm. For the next step, we conduct another experiment with more sophisticated model. Two-layered physical model is built by joining the two different materials: Plexiglas and Aluminum.

4.3.1 Data Acquisition Procedure

The experimental model was built by assembling two different kinds of materials; the first is aluminum; the second is a Plexiglas block which is placed on top of the aluminum block. This straightforward model is intended to have both elastic and attenuative isotropic materials, well-known velocities, and bent ray paths. The model dimensions are 307.7 x 242.45 x 93.9 mm. The thicknesses of the Plexiglas and aluminum blocks are 93.9 mm and 51.8 mm, respectively. We generally scale the dimensions of the models by a factor of 10,000 to make the ultrasonic measurements (at 1 MHz) look similar to the seismic band at 100 Hz.

Figure 4.19 and Figure 4.20 shows the pictures of the two blocks before joining them together. Since aluminum block is larger than the Plexiglas block, we define the coordinates of Plexiglas on the Aluminum block.

Coupling is fundamental in data acquisition procedures as it directly affects the signal transmission. Poor coupling between Plexiglas and Aluminum blocks bring the issue of weak transmission of ultrasonic signal. To have a good coupling, we heavily use sandpaper to flatten surfaces of both Plexiglas and Aluminum. Further, we use honey as a viscous couplant between the blocks as well as between surface and receivers to enhance signal transmission. Sufficient amount of honey is applied and evenly distributed along the blocks before joining the two.

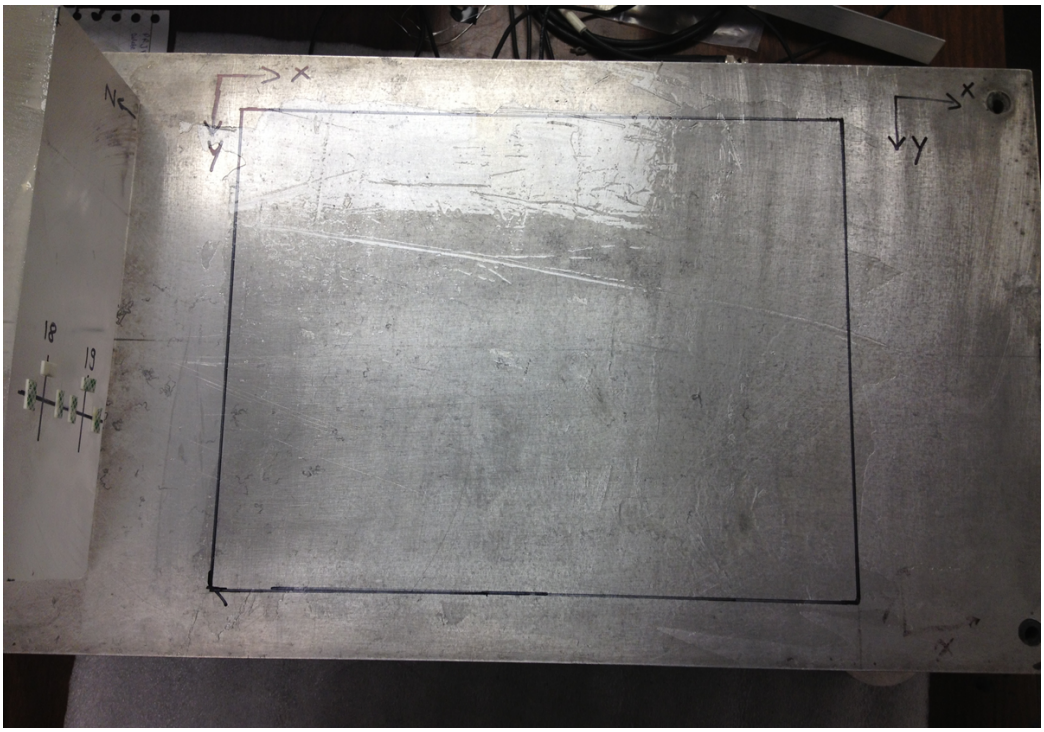

Figure 4.19: Top view of the aluminum block. Sufficient amount of viscous honey is applied.

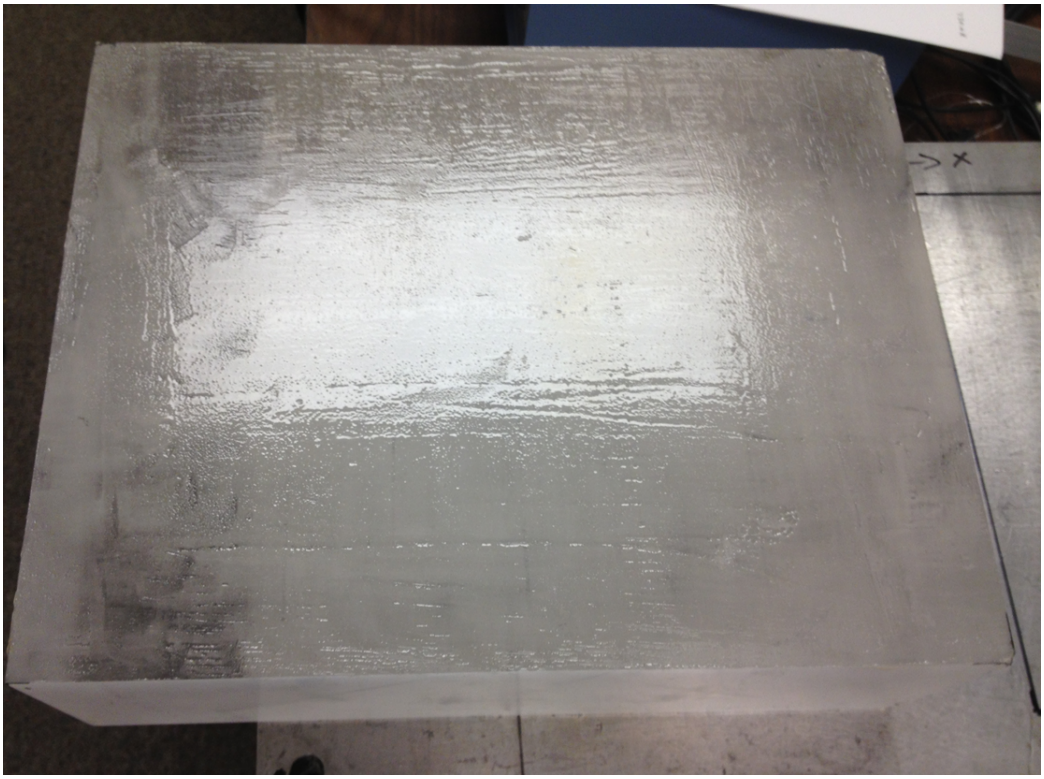

Figure 4.20: Top view of the Plexiglas block. Honey is evenly distributed throughout the block.

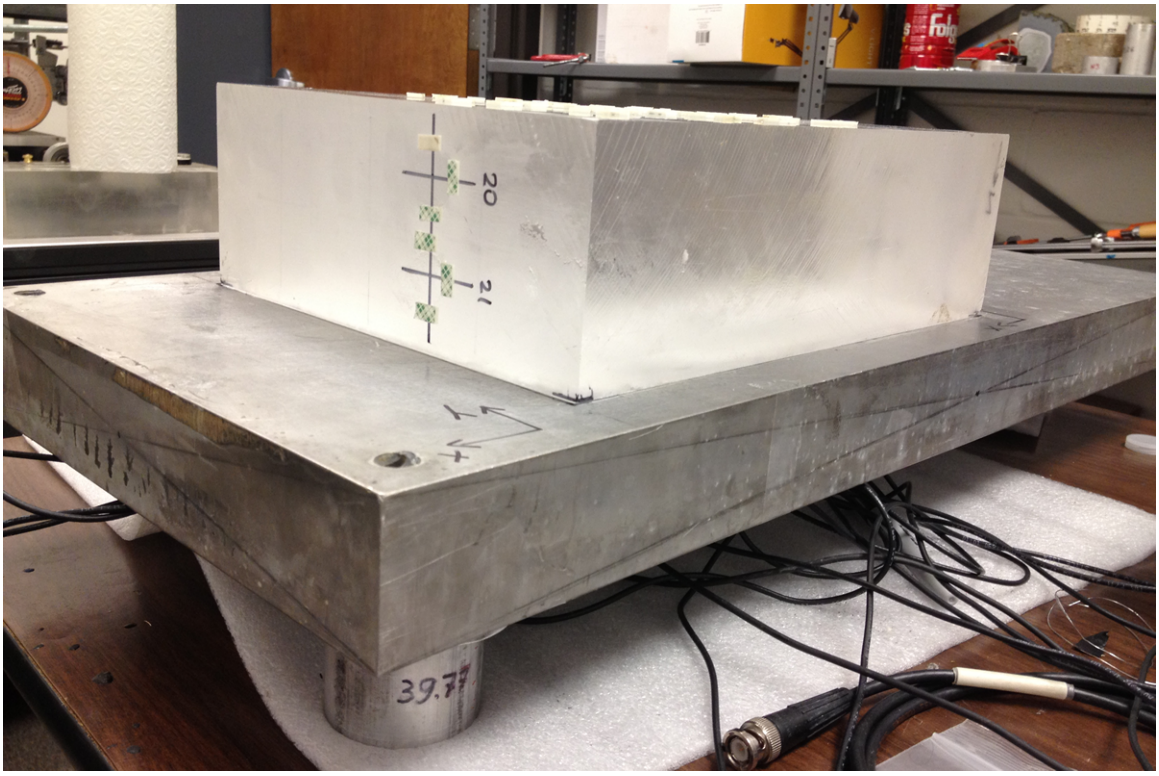

Figure 4.21: Side view of the experimental model; Plexiglas block placed on top of the aluminum block. Receivers are on both surface and well-side of the Plexiglas block. Source is placed underneath the aluminum block.

Figure 4.21 shows the side view of the experimental model. Receivers are placed on Plexiglas block on both surface and well-side. A star-shape receiver geometry is used in this experiment. Totally, 19 cylindrical 3-C receivers are used; 17 receiver positions are on the model's upper surface and 2 of them are positioned at the side of the model. 3-C transducers are placed along x-Axis during the acquisition. The dominant frequency of the transducers is 1 MHz. Table 4.6 summarizes data acquisition parameters.

According to laboratory experiments, the P-wave velocity of aluminum is 6451±5 m/s and velocity of Plexiglas is 2743±5 m/s. The S-wave velocity of aluminum and Plexiglas are 3108±5 m/s and 1382±5 m/s, respectively. Delay time between transducers is 194.81 ns. Figure 4.23 displays the velocity profile of P and S-waves for the Plexiglas and aluminum blocks.

A horizontal (S-wave type) source was positioned at the bottom of the aluminum block at the coordinates of 216.39 x 120.26 x 145.48 mm. Using the horizontal source allows us to observe both P and S-waves at the receivers; however, it generates a weak signal. To overcome this problem, +40 dB preamplifiers were used with every component. Furthermore, all data was recorded using a 64-fold vertical stack. To make an accurate data acquisition and polarization analysis, orientation of the source and receivers was kept the same (parallel to x-axis).

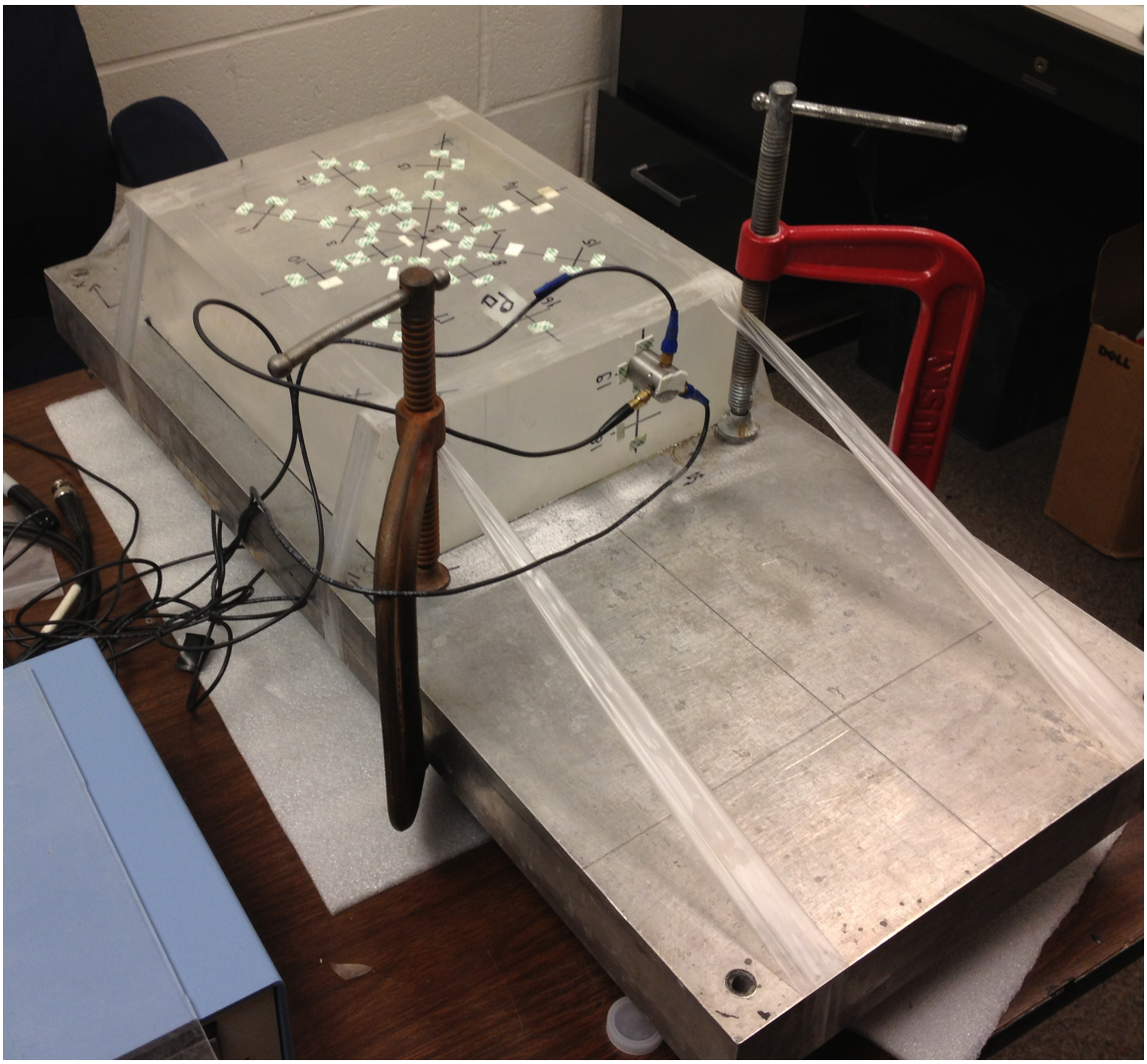

Figure 4.22: Experimental model and instrumental set-up; Plexiglas block placed on top of the aluminum block.

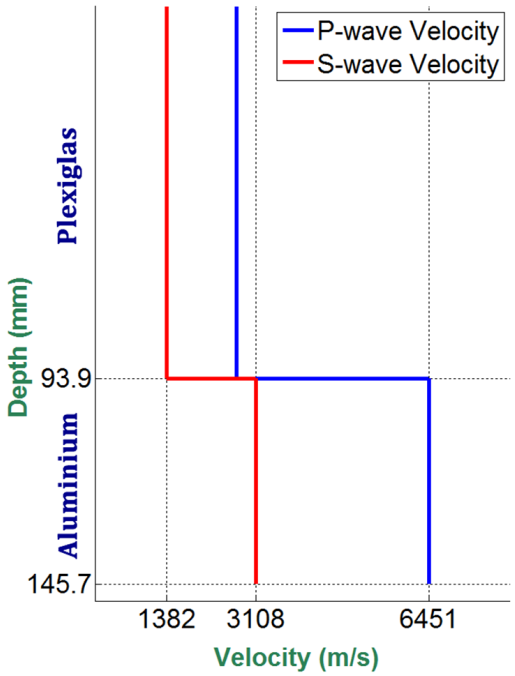

Figure 4.23: Velocity profile of the experimented model for P and S-waves.

Table 4.6: List of data acquisition parameters for the two-layered model experiment.

Acquisition Parameters	**Value**
P-Wave Velocity (Aluminum)	6450 m/s
S-Wave Velocity (Aluminum)	3110 m/s
P-Wave Velocity (Plexiglas)	2740 m/s
S-Wave Velocity (Plexiglas)	1380 m/s
Number of Receivers (Surface)	17
Number of Receivers (Well-Side)	2
Central Frequency of Transducers	1 MHz
Delay Time	194.81 ns
Number of Samples	10k
Total Length of a Recorded Signal	200 μs
Sampling Rate	0.02 μs

The signal was recorded at 19 stations including surface and well-side positions. Figure 4.24 shows a single 3C seismogram at station #4. The seismogram exhibits very clear P and S-wave arrivals; therefore, picking first break has become relatively easy. Furthermore, as we expected, the strongest S-wave amplitude is observed at horizontal sensors; whereas, the strongest P-wave is detected at the vertical sensor.

Star-shape receiver geometry consists of 4 lines, two diagonal, one vertical (parallel to y-Axis), and one horizontal (parallel to x-Axis). Figure 4.25 displays all vertical sensor data.

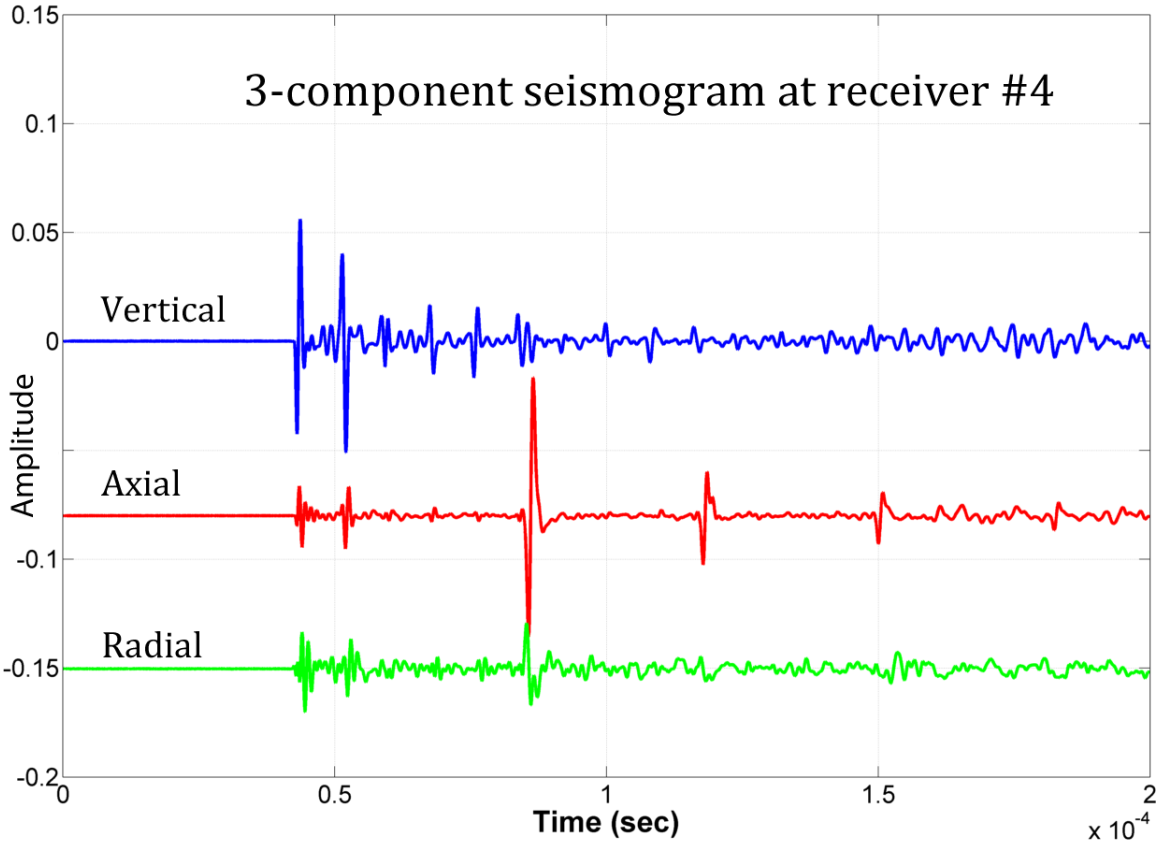

Figure 4.24: Sample three component ultrasonic data at station #4.

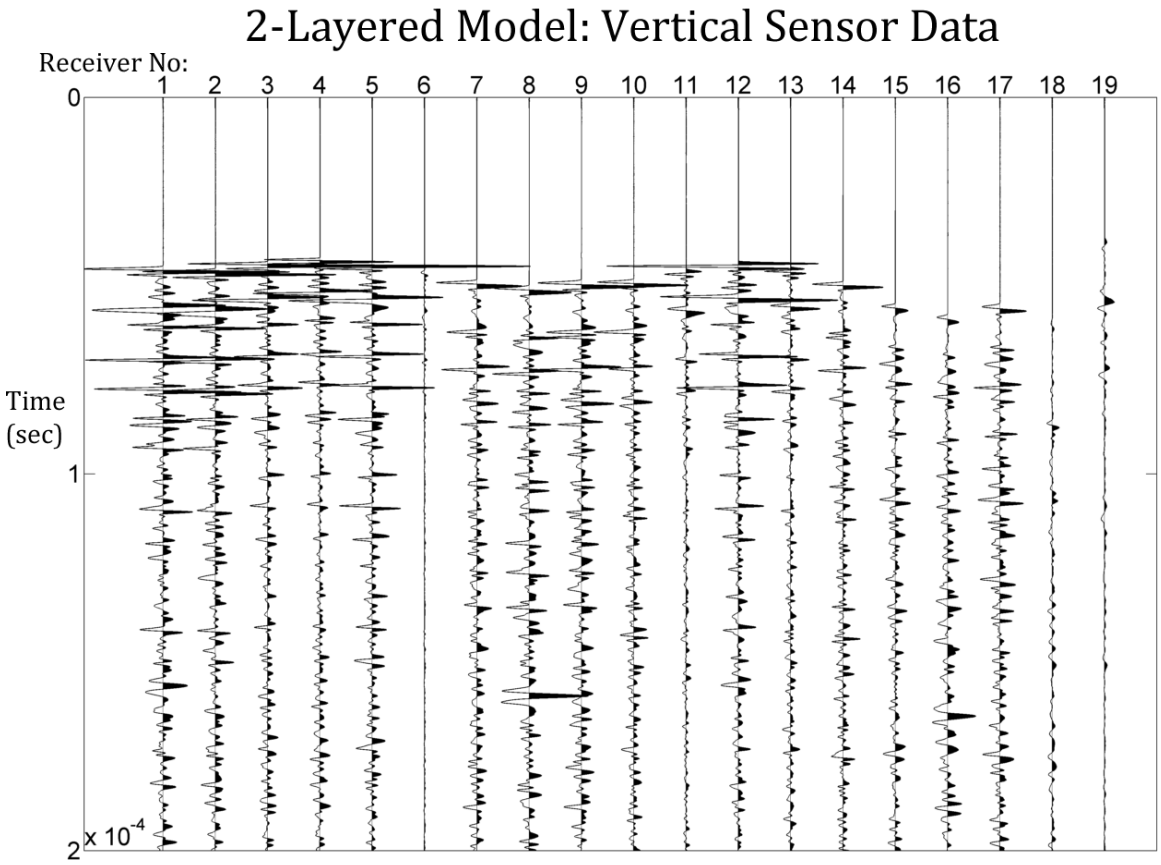

Figure 4.25: All vertical sensor data is displayed. x-Axis is the receiver number, y-Axis is the time in seconds.

4.3.2 Locating Events

After completing the data acquisition process, we, then, proceed to test our location algorithm in two layered medium. For one layered case, we do not need a ray tracing algorithm; nevertheless, in order to compute ray paths and synthetic traveltime accurately, we implement a ray tracing algorithm based on shortest path method.

Figure 4.26 shows the 3D view of the model as well as source and receiver positions. Black start represent the source position, and red stars denote the receiver locations. Red circle corresponds the area of source transducer.

The location algorithm starts with picking first arrivals of P and S-waves with the automated algorithm. After that observed first arrivals are piped to the location

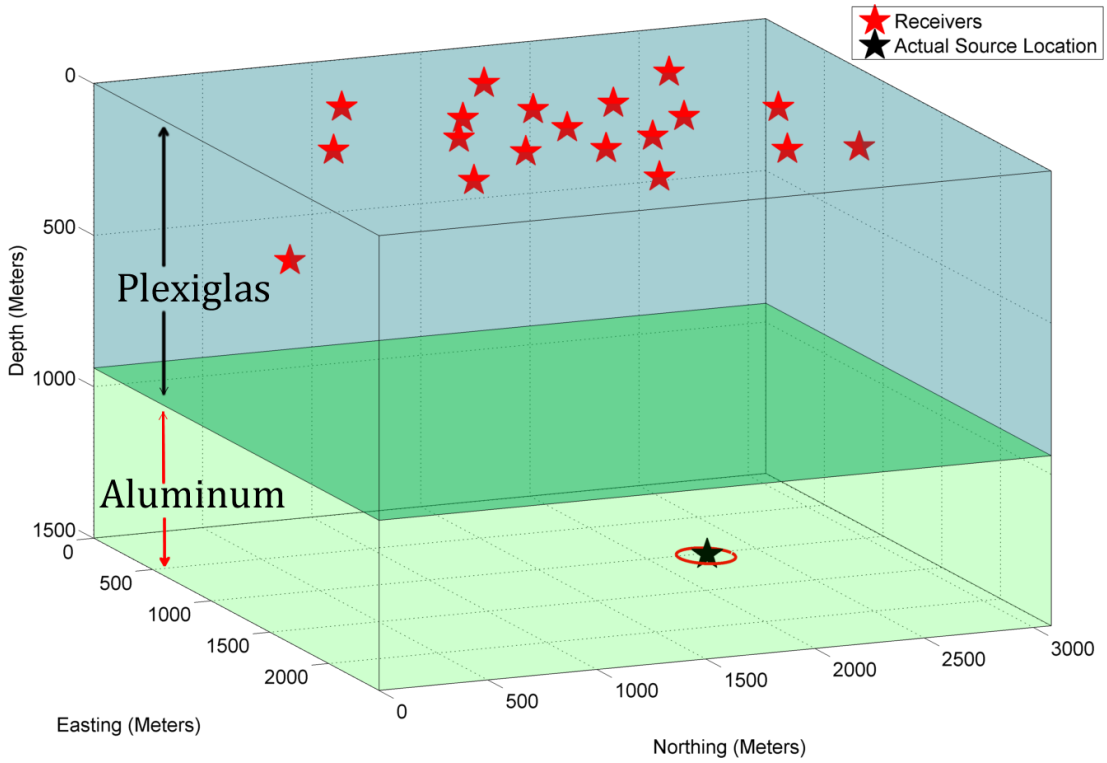

Figure 4.26: 3D view of the 2-layered model showing receiver and source locations. Black stars denote the true source locations, whereas red stars indicates receiver coordinates.

algorithm and it starts to locate events. A single event is located in seven different ways. Table 4.7 and Table 4.8 make comparison between the seven approach.

Table 4.7: Location error comparison using all (surface plus well-side) receivers.

Approach (All receivers)	**Absolute Error (mm)**	**Relative Error (%)**
Using only P-waves		
Traveltime residual	7.13	1.73
Stacked Energy	6.29	1.50
Energy/traveltime ratio	7.13	1.71
Using only S-waves		
Traveltime residual	8.8	2.1
Stacked Energy	4.40	1.05
Energy/traveltime ratio	4.78	1.14
Using P and S-waves		
Traveltime residual	4.61	1.10

Table 4.8: Location error comparison using only surface receivers.

Approach (Only surface)	**Absolute Error (mm)**	**Relative Error (%)**
Using only P-waves		
Traveltime residual	10.07	2.4
Stacked Energy	8.39	2.0
Energy/traveltime ratio	5.45	1.3
Using only S-waves		
Traveltime residual	11.3	2.7
Stacked Energy	5.75	1.37
Energy/traveltime ratio	5.75	1.37
Using P and S-waves		
Traveltime residual	5.87	1.4

Figure 4.27 displays the three event locations obtained by three different approach: Cyan star represents the P & S-waves approach, the blue star denotes the P-wave with energy/traveltime ratio attribute, and the magenta star indicates the approach of S-wave with stacked energy. Combining P and S-waves decreases vertical uncertainty.

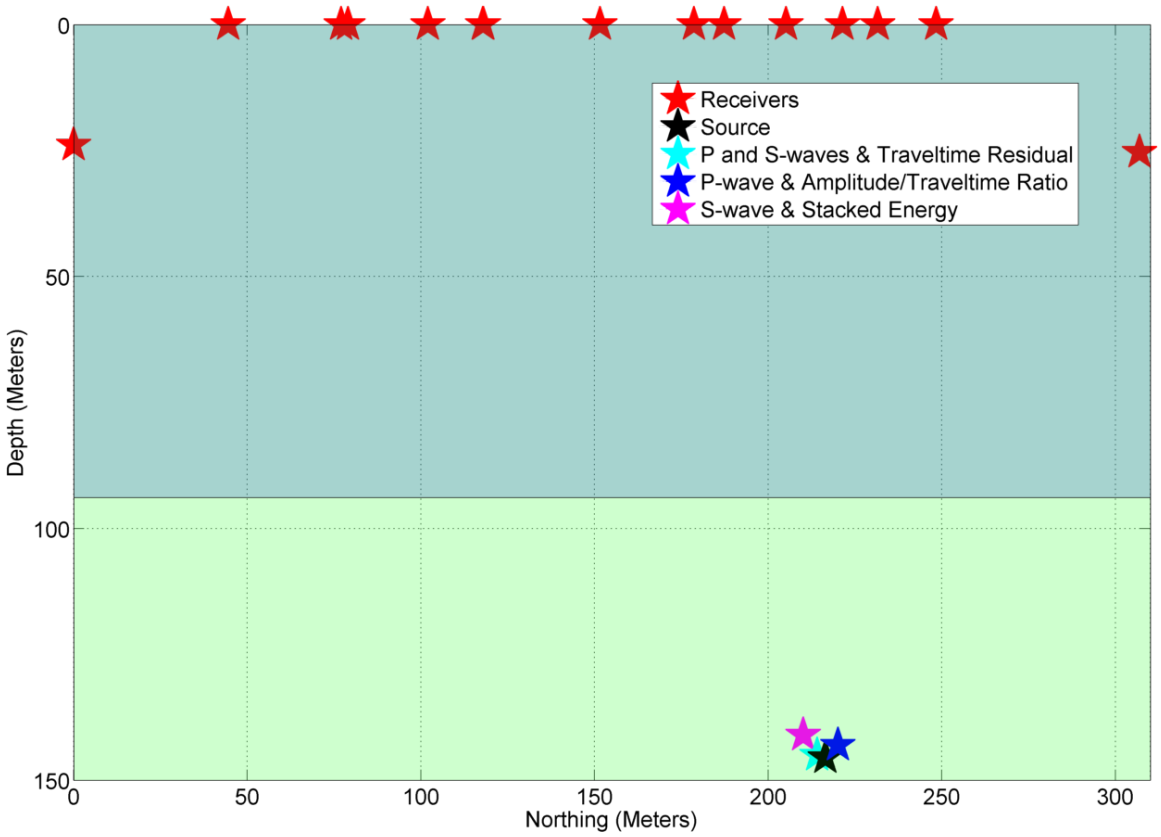

Figure 4.27: Surface plot of normalized probability density function (PDF). Maximum PDF corresponds to the source location.

True source location, calculated event coordinates, absolute error, and relative error for each four data-sets are listed. The absolute error is defined as the distance between true and calculated source location; whereas, the relative error is defined as the ration of the absolute error to the distance between two diagonal corners of the model.

Using only P, only S, and both P and S waves locate event within confidence, less than 3 percent relative error. According to our experiments, the best approach is

combining both P and S waves. Besides, computing energy/traveltime residual ratio and stacked energy provide better accuracy than the traveltime residual approach alone. Another important result is that including well-side receivers decreases relative error for all cases (only P, only S, and P & S-waves).

The most significant improvement is observed on the case using only S-waves. While locating event with traveltime residuals produces 6.39 percent relative error, taking stacked energy approach decreases the relative error to 1.37 percent. This number is further reduced to 1.05 percent relative error when including well-side receiver.

Computing probability density function (PDF) is another efficient way to find source coordinates using the differences between observed and calculated first arrivals (See Chapter 3.2.1). Figure 4.28 illustrates the surface plot of the normalized probability density function. Higher values of PDF are more likely to be the source location. In our case, it clearly pinpoints the source coordinates. Figure 4.29 displays the three different PDF contour slices at $x = 2160$ m, $y = 0$ m, and $z = 1450$ m.

Another attribute that we have been using to locate events is stack energy. Figure 4.30 demonstrates the slices of stacked energy contour map at $x = 2160$ m, $y = 0$ m, and $z = 1450$ m. Again, the location yields maximum stacked energy is assumed to be the found source coordinates.

Figure 4.31 shows the energy/traveltime residual ratio surface plot. This ratio has much clearer image than the stacked energy and distinctly pinpoints the source location. According to Table 4.7 and Table 4.8, energy/traveltime ratio has the least relative error among traveltime residual and stacked energy.

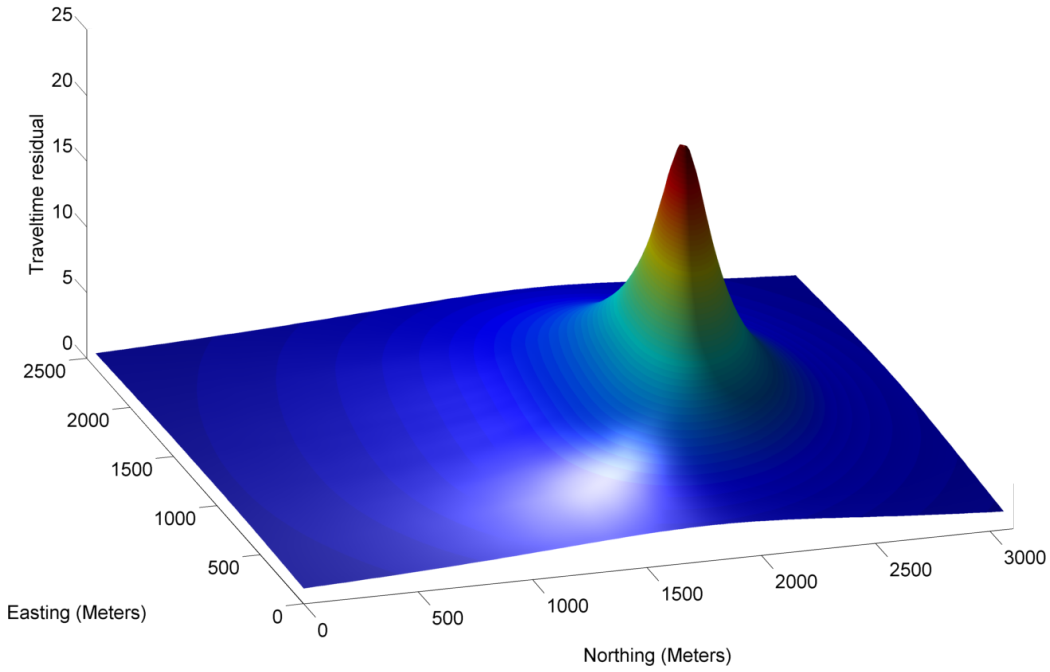

Figure 4.28: Surface plot of normalized probability density function (PDF). Maximum PDF corresponds to the source location.

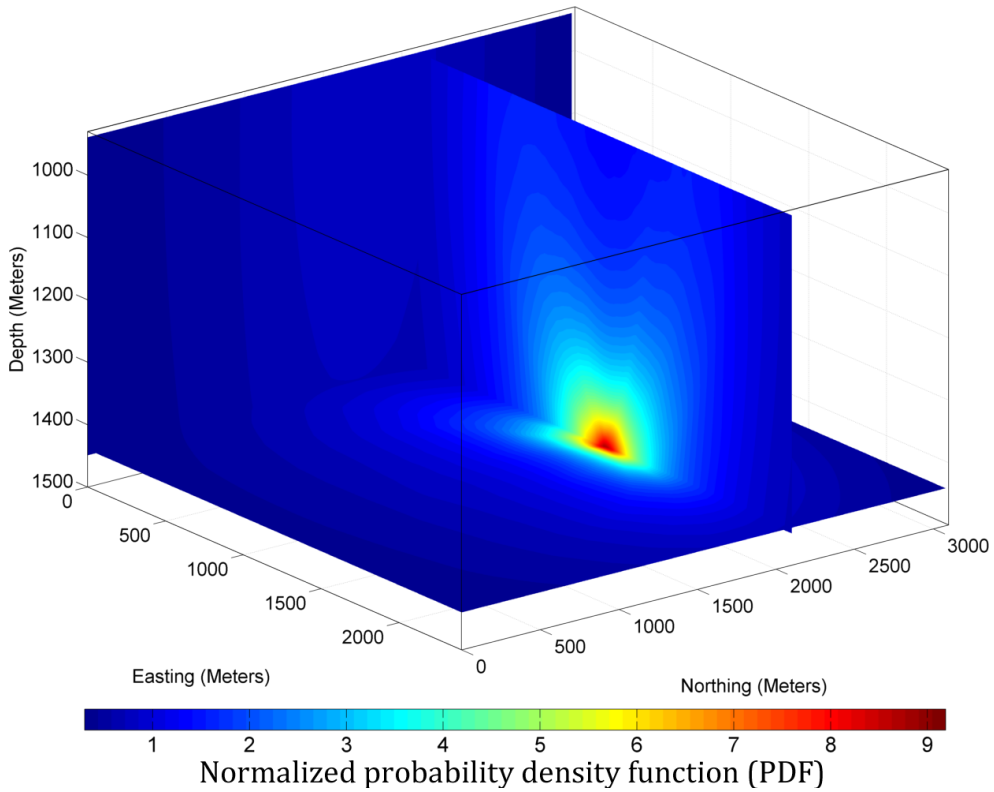

Figure 4.29: Normalized probability density function slices at $x = 2160$ m, $y = 0$ m, and $z = 1450$ m. Higher values are more likely to be the source location.

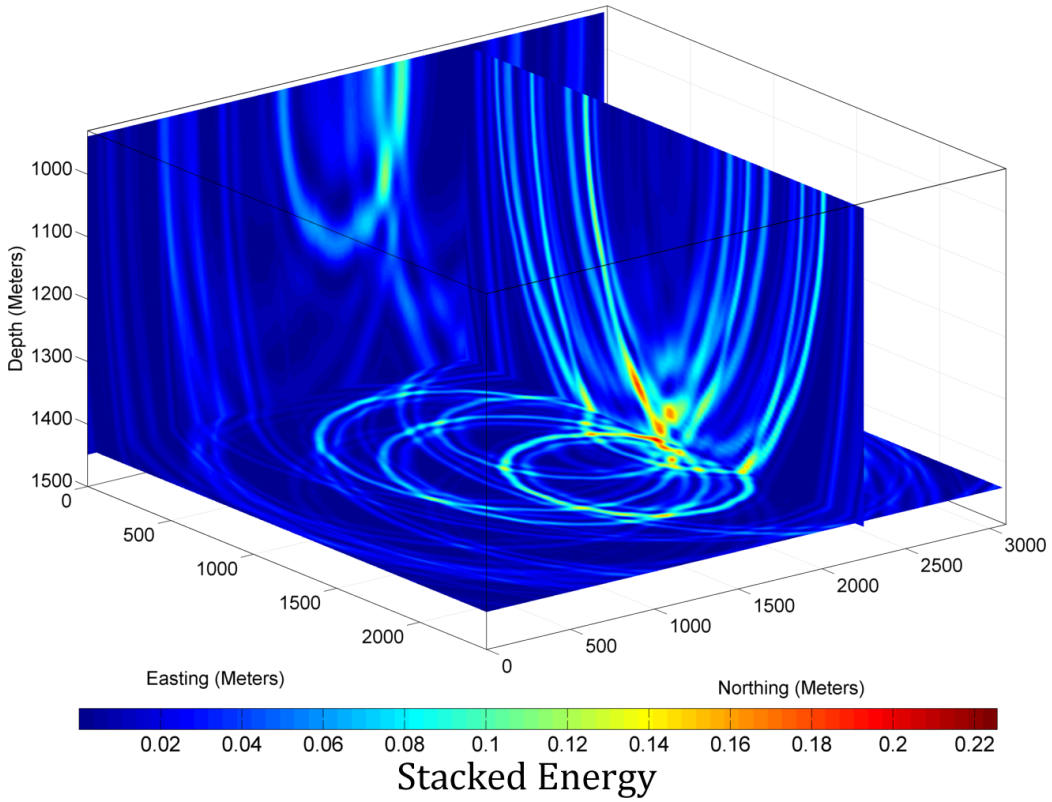

Figure 4.30: Stacked energy contour slices at $x = 2160$ m, $y = 0$ m, and $z = 1450$ m. Maximum stacked energy points the source location.

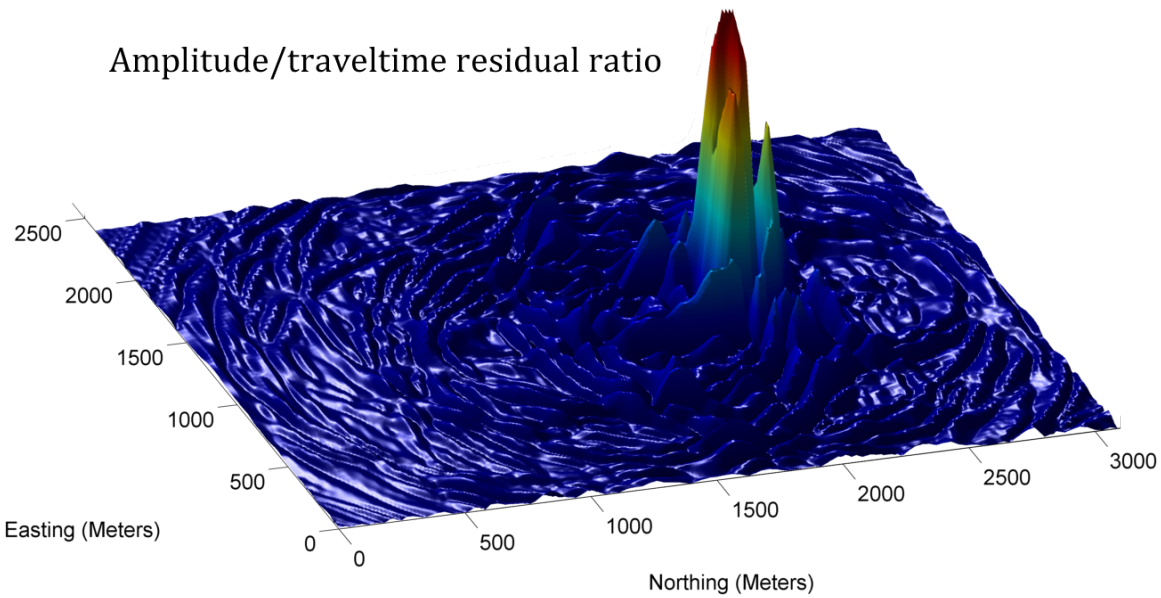

Figure 4.31: Surface plot of the Energy/traveltime residual ratio. Maximum value of this ratio is assumed to be the calculated source location.

4.3.3 Focal Mechanism and Radiation Pattern Determination

The horizontally polarized ultrasonic transducer source we have been using generates both P and S-waves. By analyzing the particle motion of body waves, we can depict the radiation pattern of seismic waves. To this end, first-break maximum amplitudes are picked for both P and S-waves. Vertical sensor data is used to pick amplitudes for P-waves; whereas, S-wave amplitudes are picked on horizontal sensor data.

Figure 4.32 and 4.33 illustrates the first motion contour maps for P and S waves, respectively. In our case, the minimum tension caused by P-waves is occurred at the receiver where is located just above the source location. On the other side, the surface in the Figure 4.32 can be separated into two lobes where P-wave radiates the maximum at its energy; one lobe consists of downward first particle motion, another lobe consists of upward first motion.

The S-wave polarization contour map, Figure 4.33, is different than the P-wave. Unlike P-wave radiation, S-wave radiates with its maximum energy to the location which is just above the source location. S-wave radiation energy decreases as the angle of incidence increases. Particle motion of S-waves converge toward dilatation axis, diverges from compression axis and becomes zero on the null axis (Forouhideh, 2011).

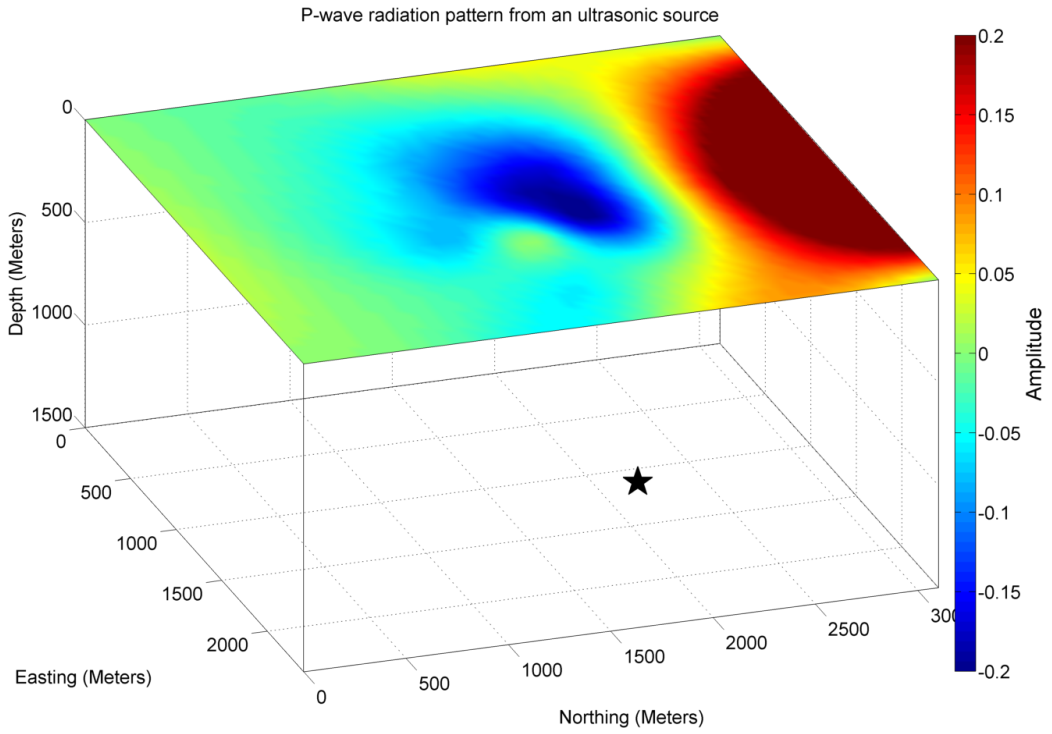

Figure 4.32: P-wave radiation pattern contour plot, generated with the picked first arrival amplitudes of P-waves.

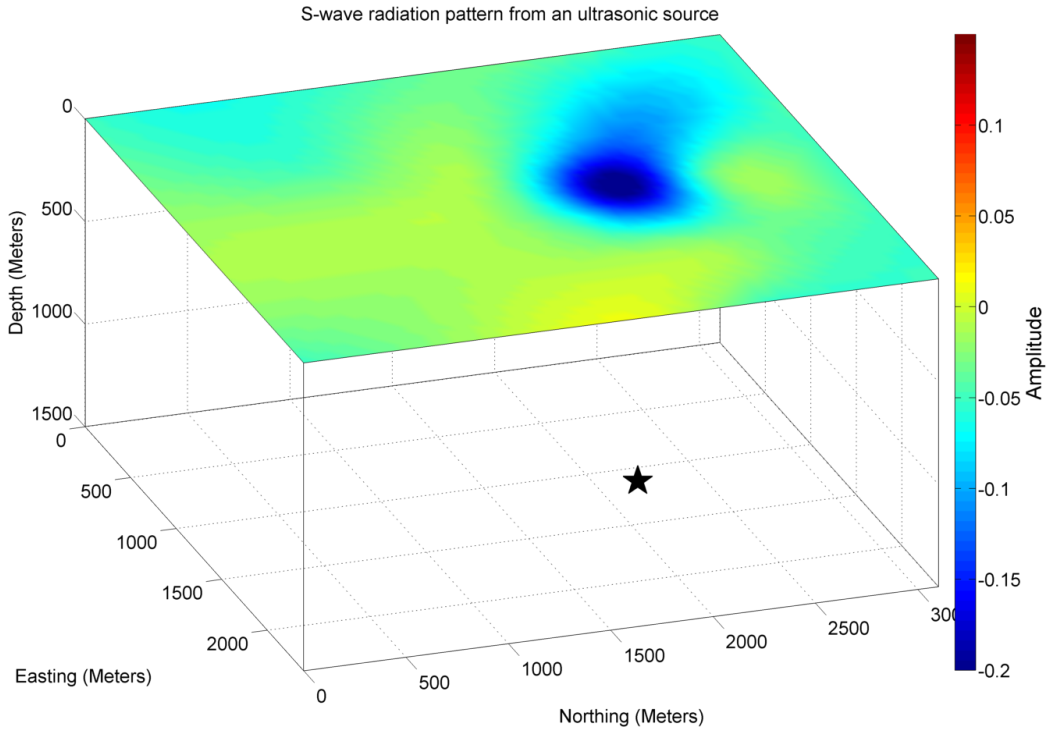

Figure 4.33: S-wave polarization contour plot. A horizontal source is used to generate ultrasonic signal.

After determining radiation patterns of body waves, Focmec (Focal Mechanism Determination) software then is used to characterize source mechanism by calculating strike, dip, and rake. Focmec software requires azimuth, take-off angles, and first motions (dilatational or compressional) of body waves.

The Figure 4.34 demonstrates the found beachball solution, which yields minimum polarity errors among the other found solutions. Strike, dip, and rake is 20°, 90°, and 90°, respectively.

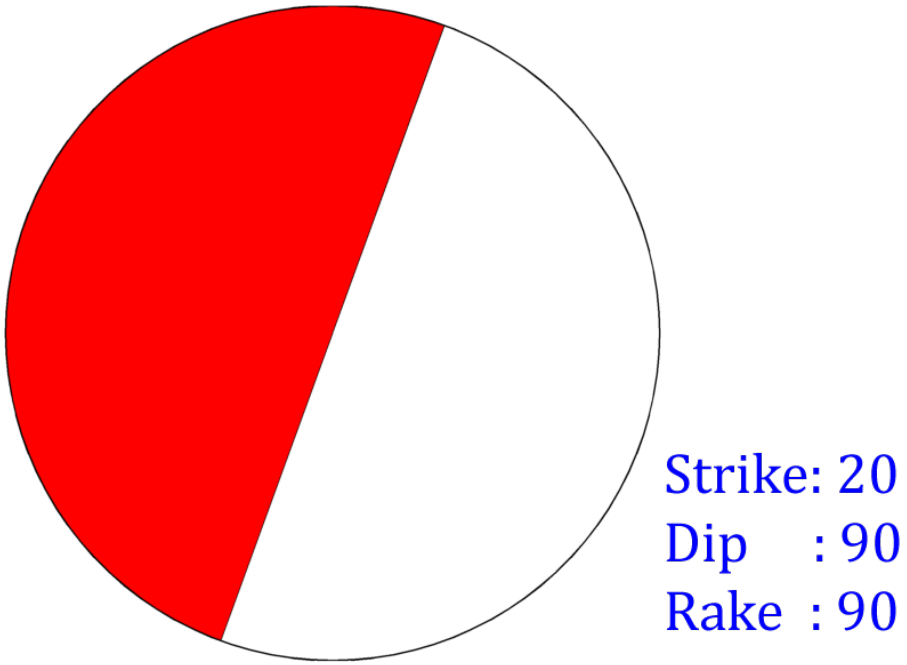

Figure 4.34: Beachball diagram of focal mechanism solution for a horizontal source in two-layered medium. Focmec software, that is based on a grid searching technique, is used to derive strike, dip, and rake.

4.4 SINGLE LAYER PHYSICAL MODELING EXPERIMENT (SANDSTONE)

The last experiment in this research was conducted on a natural sandstone, from Oklahoma, to generate more realistic data. This rock is bigger, thicker and heavier than the other experimental models. Its weight is about 150 kg. The dimensions of the sandstone block are as follows; 57.5 x 43.8 x 17.5 cm.

4.4.1 Data Acquisition Procedure

The third experiment has also conducted at the Allied Geophysical Laboratories (AGL). The same bench-top ultrasonic oscilloscope, preamplifier, and P & S-wave transducers are used to acquire data.

Compared to the condition of sandstone block to the other physical models, it does not have a flat surface or sides. It had too many little bumps that eventually makes it impossible to acquire data on it. To make the surface and sides of the rock flat, we have applied sandpapers heavily. Figure 4.35 shows a picture during this process. Good coupling is the key for acquisition with ultrasonic source and receivers.

Figure 4.35: Both surfaces of the sandstone block is getting flattened using sandpaper.

Figure 4.36 displays the rock after furnishing process is completed on surface. One fundamental objective of this research is to make comparison between different location techniques and receiver geometries such as amplitude versus traveltime, surface versus borehole. Besides surface receivers, we also want to deploy well-side receivers to locate events using variety of approaches. To this end, we determine two "well" locations on the two sides of the rock. Figure 4.36 shows two of the well locations called as "Well A" and "Well B".

Figure 4.37 shows the sandstone block from side view. Even though the coupling on surface of the rock is good after furnishing, further preparation needs to be done in order to acquire data on well-side locations. As it can be seen on Figure 4.36 and 4.37, sides of the rock is not vertically straight, and it is not suitable for acquiring data on the sides of the rock. To make it adequate for positioning the receiver transducers on the rock, sandpaper machine is used to make the flanks of the block vertically straight (Figure 4.38).

Subsequent step in data acquisition process is to deploy source and receiver at various, and known coordinates to determine P and S-wave velocities. According to our laboratory measurements, the P-wave and S-wave velocities of the sandstone block are 3805 and 2510 m/s, respectively. Table 4.9 summarizes all the acquisition parameters for the third experiment.

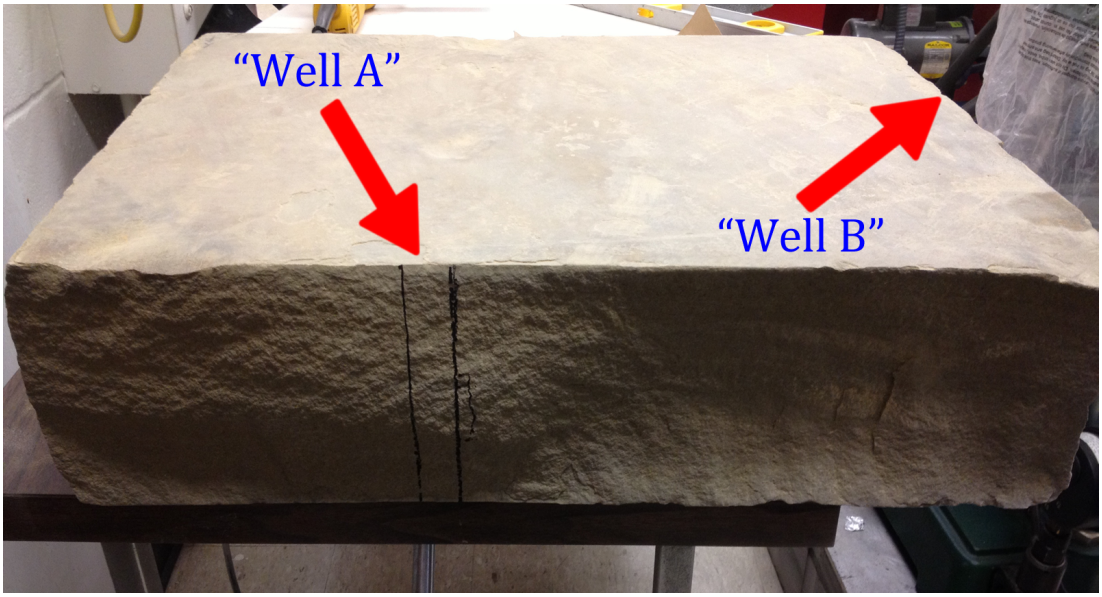

Figure 4.36: Picture of the sandstone block after furnishing surfaces. Two well locations are determined.

Figure 4.37: Side view of the sandstone block. It is not suitable for deploying well-side transducers.

Figure 4.38: A "well" is constructed and aligned vertically. The second well is built at the other side of the rock.

Table 4.9: List of data acquisition parameters for the third experiment with sandstone block.

Acquisition Parameters	**Value**
P-Wave Velocity	3805 m/s
S-Wave Velocity	2510 m/s
Number of Receivers (Surface)	52
Number of Receivers (Well-Side)	8
Central Frequency of Transducers	1 MHz
Delay Time	169.44 ns
Total Length of a Recorded Signal	200 μs
Sampling Rate	0.02 μs
Vertical Stack	64

There are two major changes in this experiment with reference to studies with Plexiglas and aluminum blocks are as follows:

1. We have conduct an experiment with a real sandstone rock rather than man-made physical models, which produces a more realistic data.

2. We have used star-shape receiver geometry in our first two experiments. This time, grid-type receiver geometry is preferred. This allows us to acquire a lot more data than the previous experiments, and once we acquire all the data, it is possible to test different receiver geometries without the need of recording data repeatedly. We can simply enable/disable certain receiver positions to make it star-shape look, for instance.

Totally, sixty-two cylindrical receivers are used; fifty-four receivers are deployed with 6 cm grid interval on the upper surface; whereas, eight receivers are positioned at the two sides of the sandstone block model. Each "well" consists of 4 receiver locations. Horizontal S-wave type ultrasonic source is positioned underneath the block. Microseismic source location coordinates are 30.0 x 19.44 x 17.05 cm.

Figure 4.40 shows the surface view of the sandstone block along with its two sides. To increase transmission strength, sufficient amount of honey is applied on surface and well-side receiver positions. Furthermore, data was acquired with 64-fold vertical stacking to increase signal-to-noise ratio.

Two different data-sets are obtained in this experiment. Both data-sets are acquired at the same receiver-source coordinates; however, only difference is the source polarization. In the first test, or namely "Test A", microseismic source is polarized parallel to x-Axis. In the second test, or "Test B", source location has not changed but the source has turned 90° in such a way that it polarizes parallel to y-Axis.

Recording ultrasonic signal is performed with 3 component high frequency transducer in this experiment. Figure 4.39 shows a picture of the rock along with 3 component transducer used as a receiver. Orientation of source and receiver is kept the same during the data acquisition process.

Another factor that affects signal magnitude and characteristics is the pressure that is applied to transducer while recording. An object with certain weight is placed on top of the transducers to avoid human effect and unfair evaluation of amplitudes.

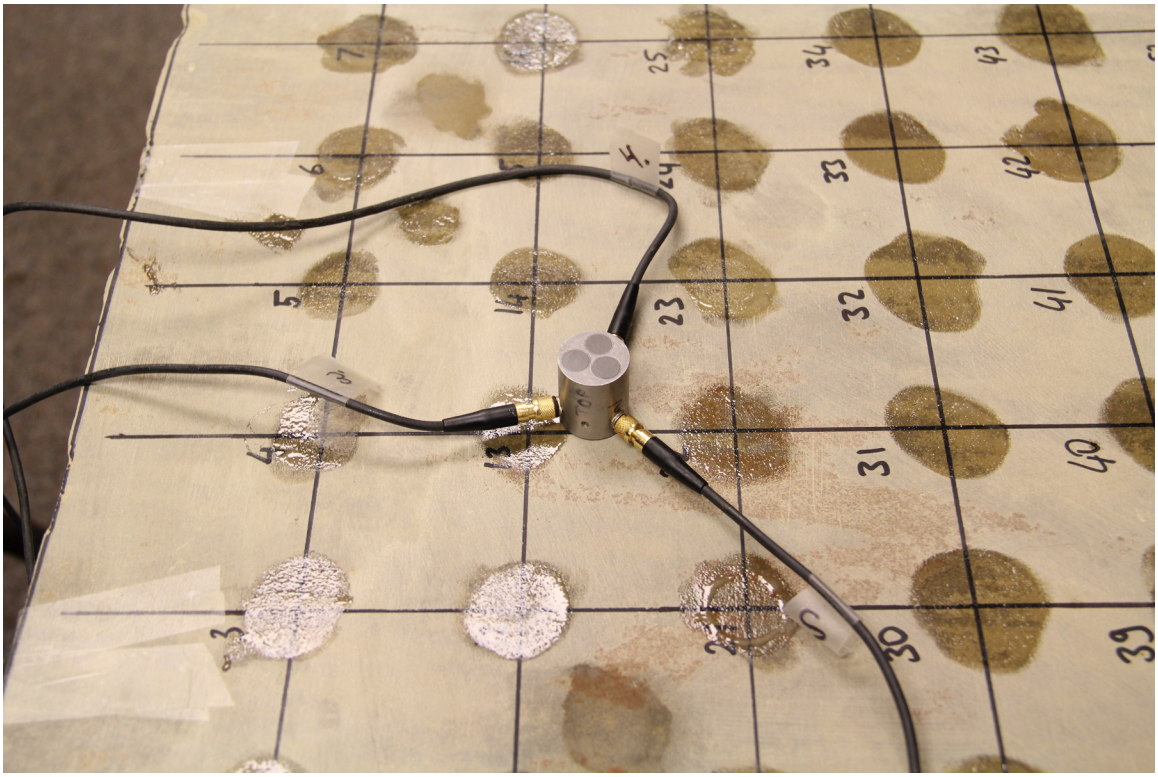

Figure 4.39: 3 component high frequency transducer.

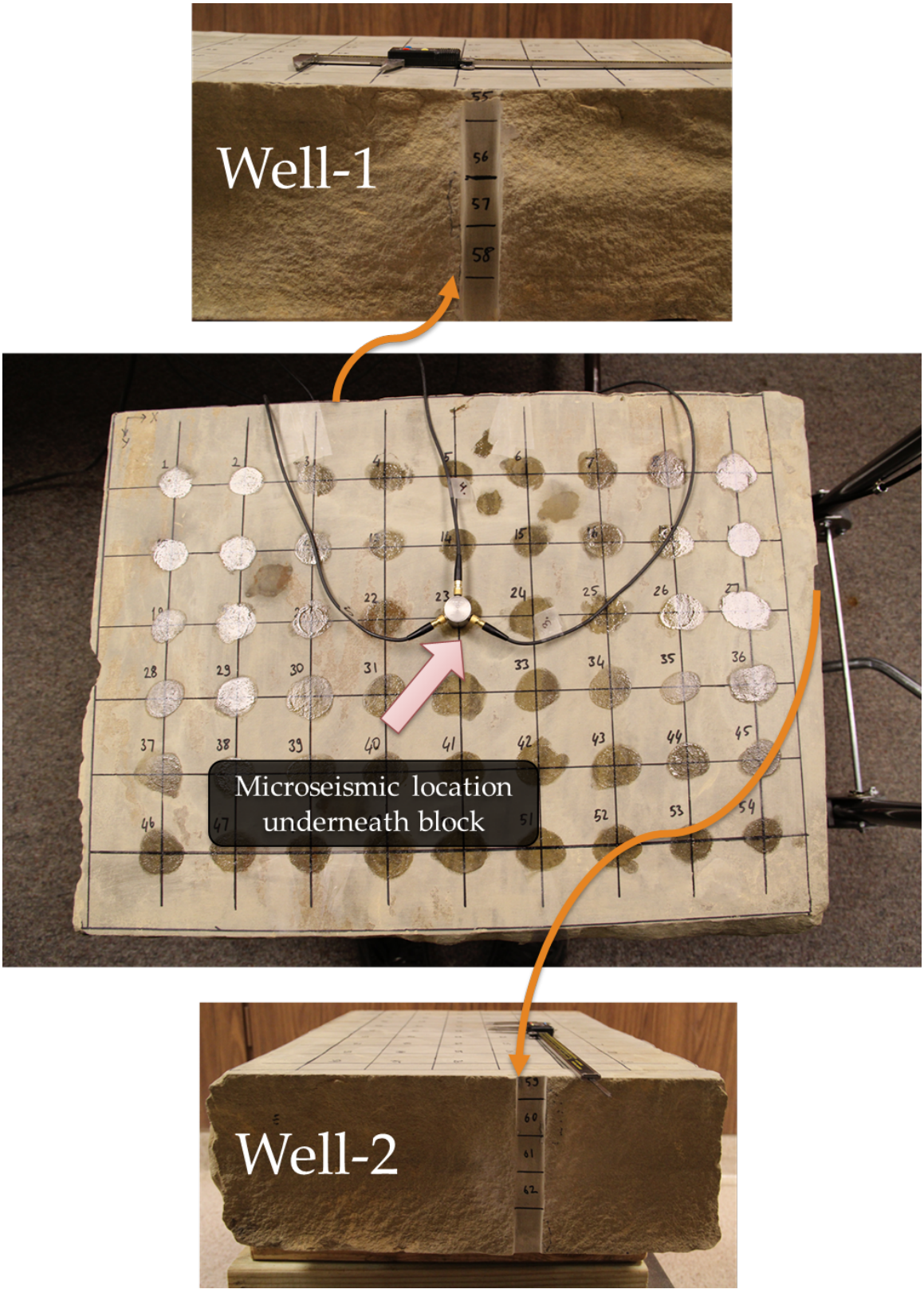

Figure 4.40: Top view of the sandstone block. 54 surface, and 8 well-side receivers are placed.

Figure 4.41 shows a single three component seismogram at station #1. We observe definite first arrivals of P and S-waves. Further, the maximum S-wave amplitude is detected at the horizontal sensor.

Figure 4.42 demonstrates one line of vertical and horizontal sensor data from a horizontal source. Station #28 through #36 are used to generate the figures. Red dots and circles correspond to the first arrival time of P-wave.

As mentioned earlier, we have conducted two different tests; source receiver locations are the same but the source polarization is different. Figure 4.43 displays all surface horizontal sensor data acquired for "Test A", whereas, Figure 4.44 shows surface horizontal sensor data for "Test B".

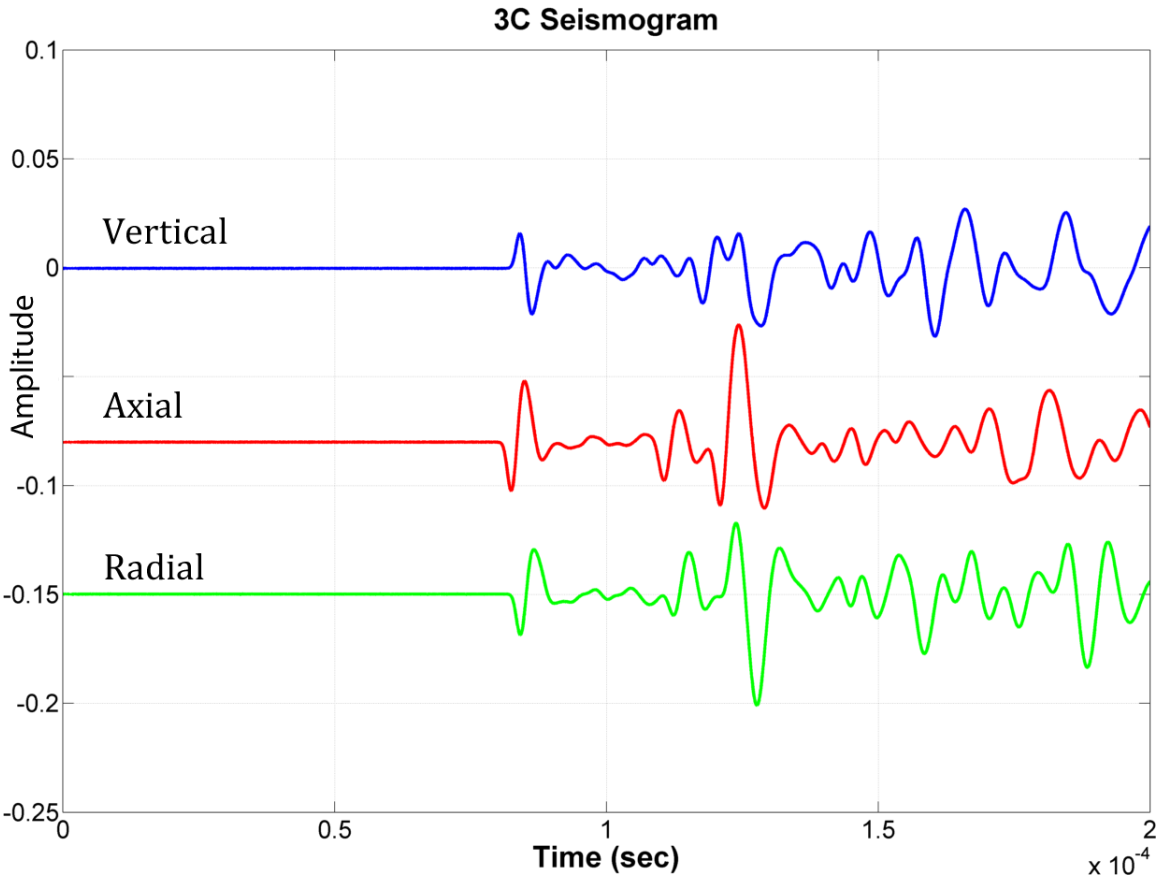

Figure 4.41: Sample three component ultrasonic signal at station #1.

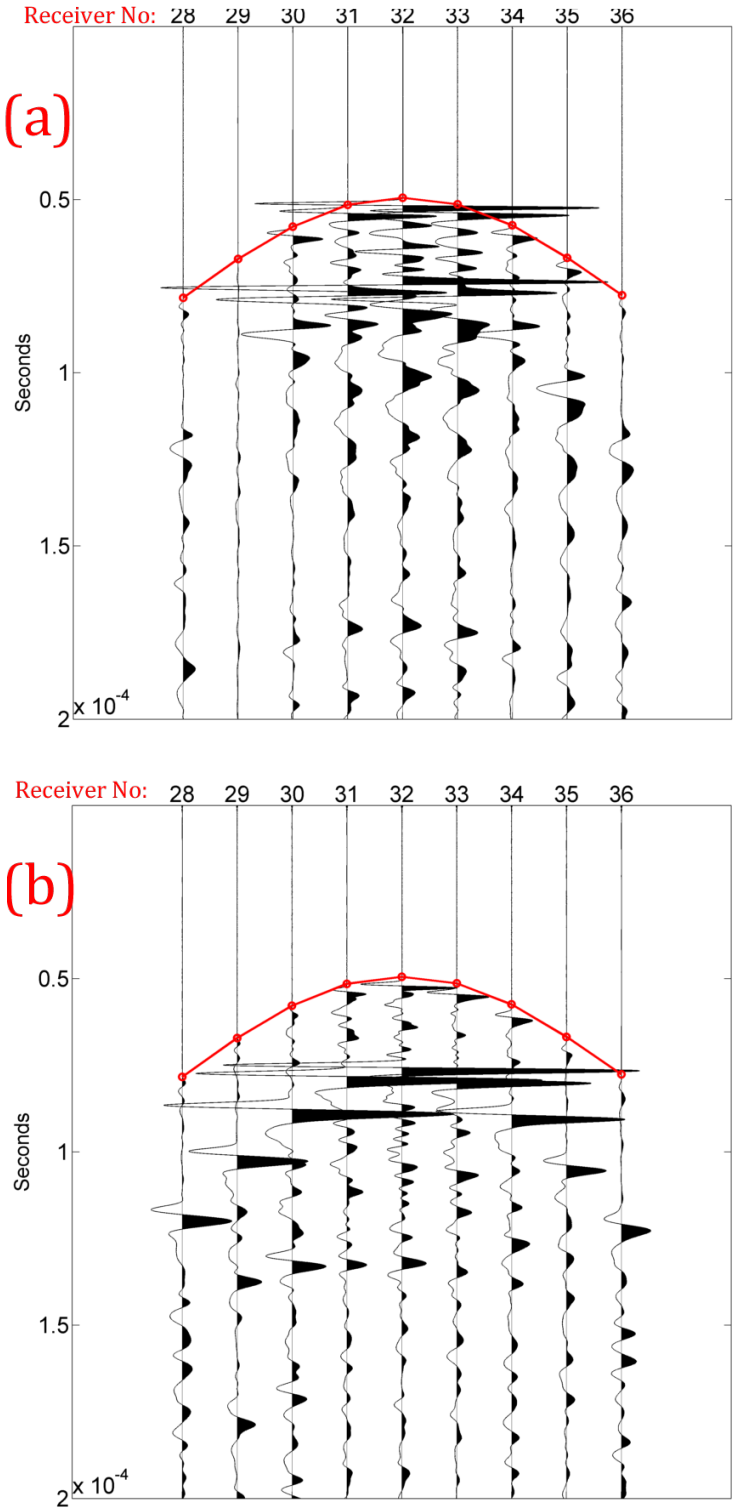

Figure 4.42: One line of stations #28 through #36 are plotted. Sub-figures show (a) vertical sensor data (b) horizontal sensor data.

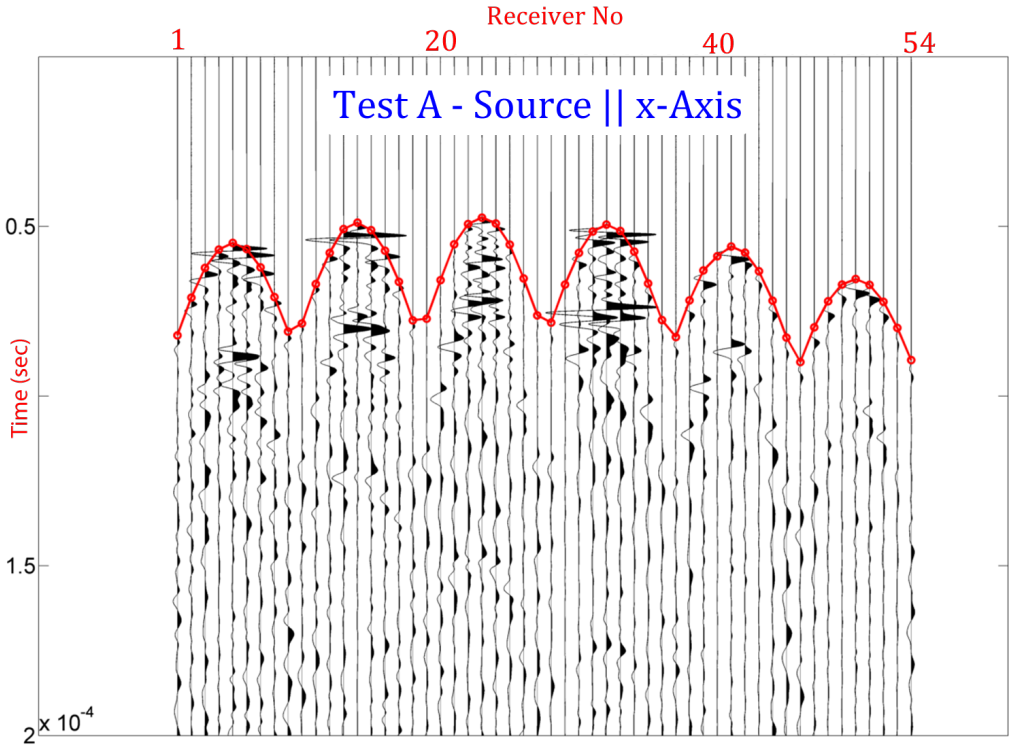

Figure 4.43: Displaying all surface data for "Test A". Red circle corresponds to the first arrival of P-Waves.

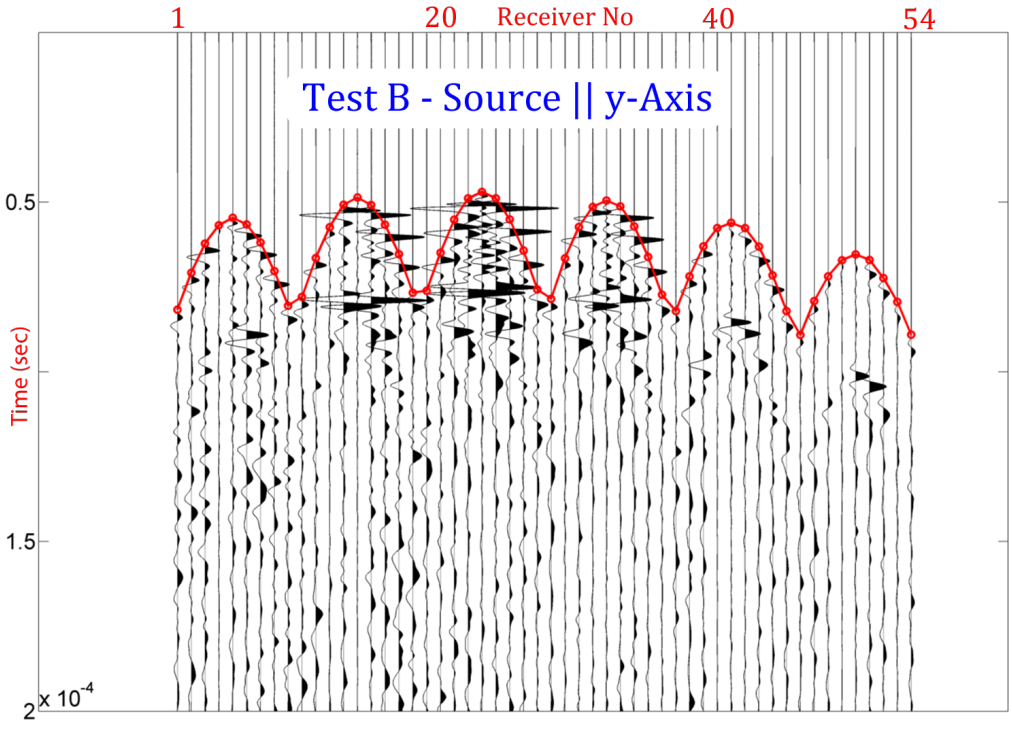

Figure 4.44: Displaying all surface data for "Test B". Red circle denotes the P-wave first breaks.

4.4.2 Locating Events

Location algorithm begins with picking first arrival of P and S-waves for all receivers. After automated picking, slight corrections have made to get more accurate first break times.

Figure 4.45 shows the 3D view of the model as well as source and receiver positions. Black start shows true source position, and red stars indicate the receiver locations.

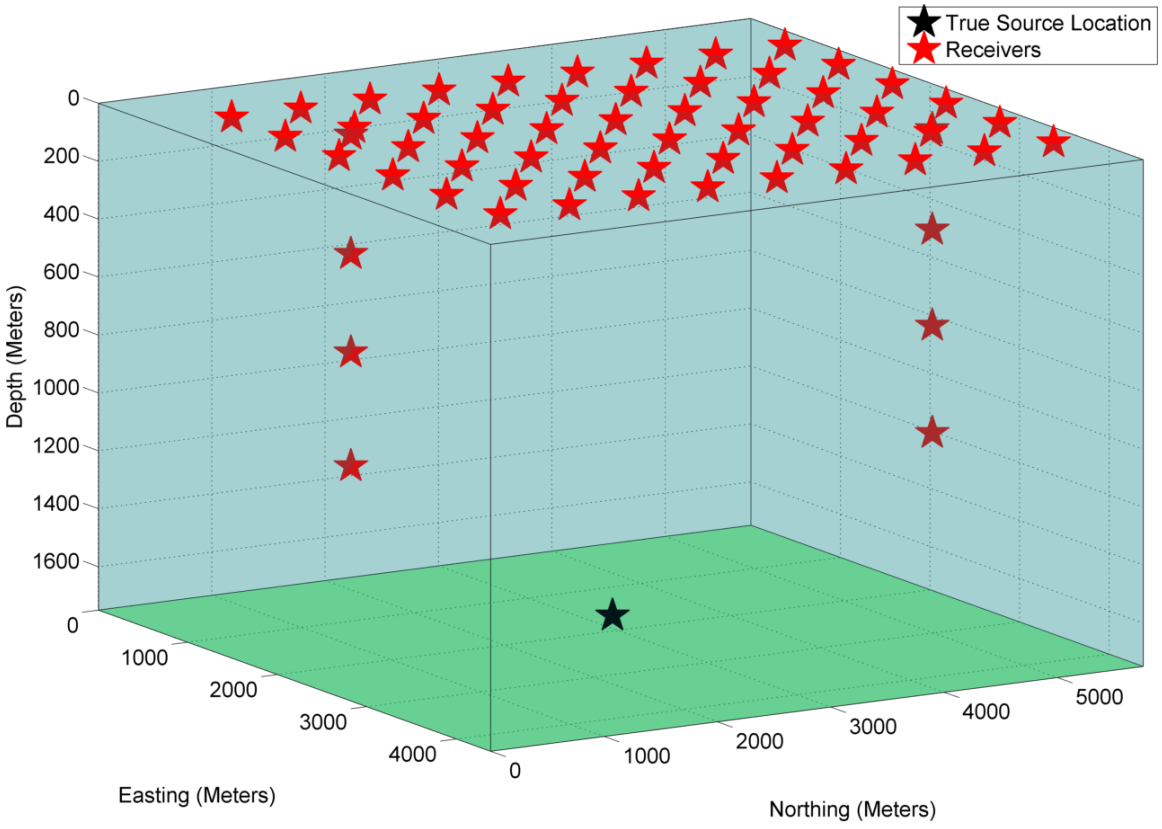

Figure 4.45: 3D View of the sandstone block. Red stars are the receiver locations; black star is the true source location.

Microseismic event coordinates are found in seven different approaches for both using only surface receivers, and all receivers. Summary of these along with relative errors and absolute errors are listed in Table 4.10 and 4.11.

Table 4.10: Experimenting with sandstone block: Location error comparison using all (surface plus well-side) receivers.

Approach (All receivers)	**Absolute Error (mm)**	**Relative Error (%)**
Using only P-waves		
Traveltime residual	11.9	1.6
Stacked Energy	8.1	1.1
Energy/traveltime ratio	5.9	0.8
Using only S-waves		
Traveltime residual	10.41	1.4
Stacked Energy	6.17	0.83
Energy/traveltime ratio	6.69	0.9
Using P and S-waves		
Traveltime residual	4.31	0.58

Table 4.11: Experimenting with sandstone block: Location error comparison using only surface receivers.

Approach (Only surface)	**Absolute Error (mm)**	**Relative Error (%)**
Using only P-waves		
Traveltime residual	14.13	1.9
Stacked Energy	9.52	1.28
Energy/traveltime ratio	8.55	1.15
Using only S-waves		
Traveltime residual	13.39	1.8
Stacked Energy	9.67	1.3
Energy/traveltime ratio	6.99	0.94
Using P and S-waves		
Traveltime residual	5.58	0.75

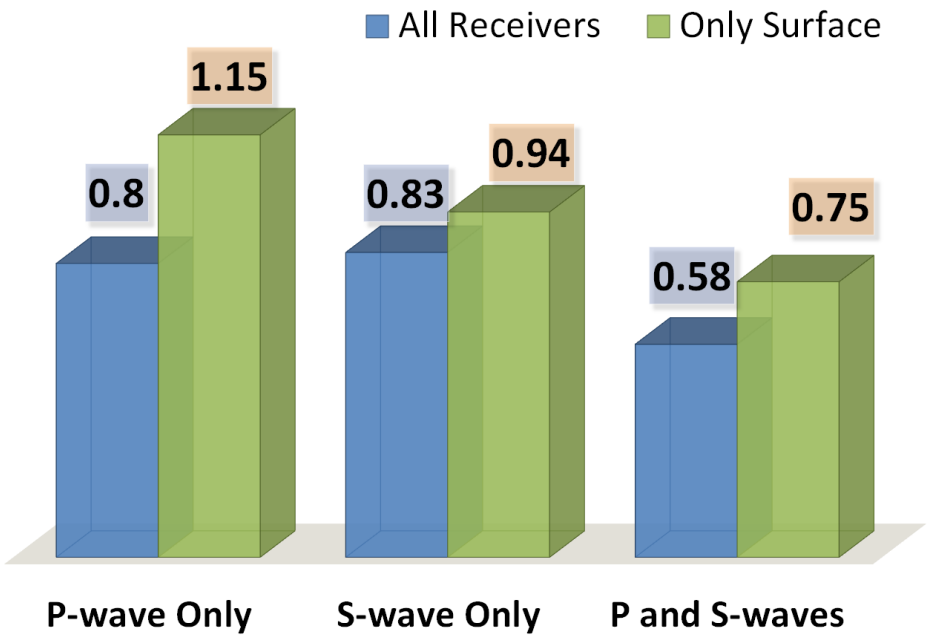

Figure 4.46: Relative location errors (%) for surface vs. all receivers.

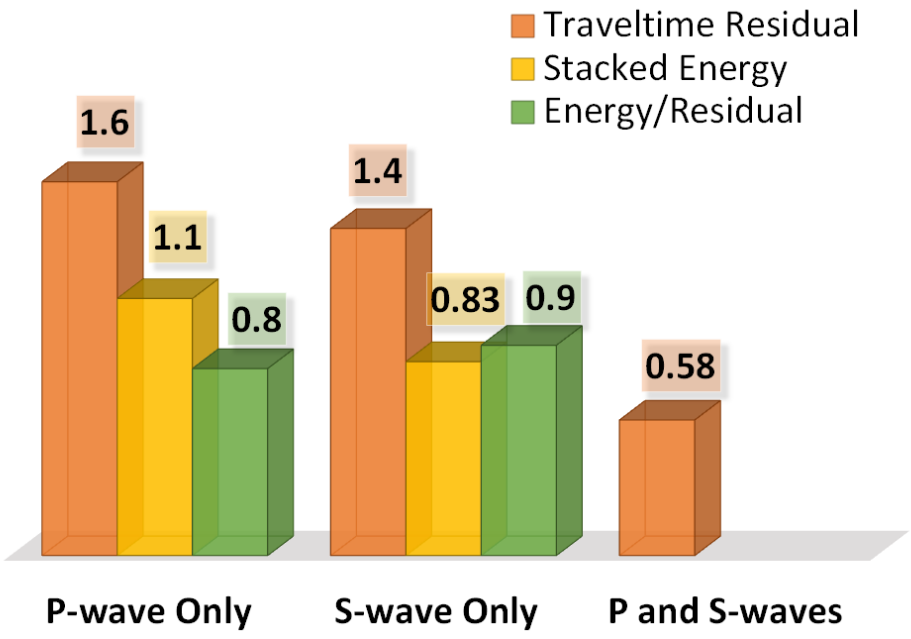

Figure 4.47: Relative location errors (%) for traveltime residual, stacked energy, and energy/residual ratio.

According to the Table 4.10 and 4.11, the most accurate location approach is achieved using stacked energy and energy/traveltime residual ratio. One interesting

result is that locating the event using S-wave has less relative and absolute error than the P-wave case. Further, excluding well-side receivers decreases especially vertical accuracy and resolution as we observe this in all of our experiments.

Figure 4.48 demonstrates the normalized probability density function (PDF) contour map slice at z=1730 meters, while, Figure 4.49 shows the PDF slices at x = 3050 m, y = 1950 m, and z = 1730 m. The location where produces the maximum is considered to be the source location.

Similarly, surface plots and various slices are generated for different attributes. Figure 4.50 and 4.51 displays the surface plot and three slices of the Energy/traveltime residual ratio for P-wave.

For S-wave, stacked energy and energy/traveltime ratio surface plots at slice z = 1730 meters are generated and shown in Figure 4.52 and 4.53. Amplitude ratio contains less noise than the stacked energy. However, both amplitude ratio and stacked energy locate event more accurately for P and S-waves.

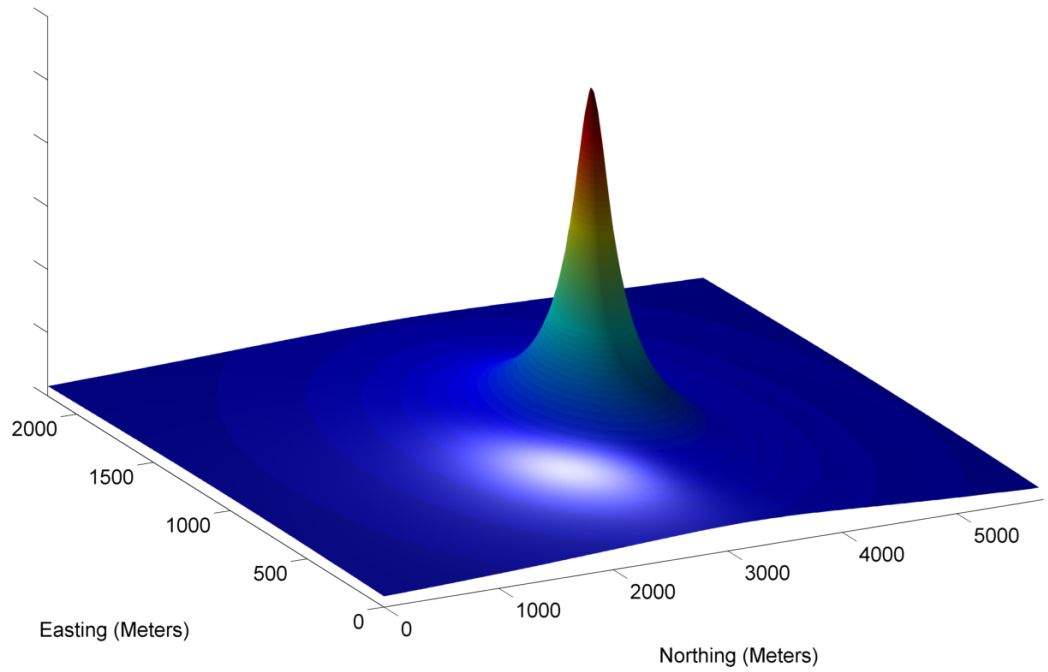

Figure 4.48: P-wave surface plot of normalized probability density function (PDF) slice at z=170 mm. PDF corresponds to the source location.

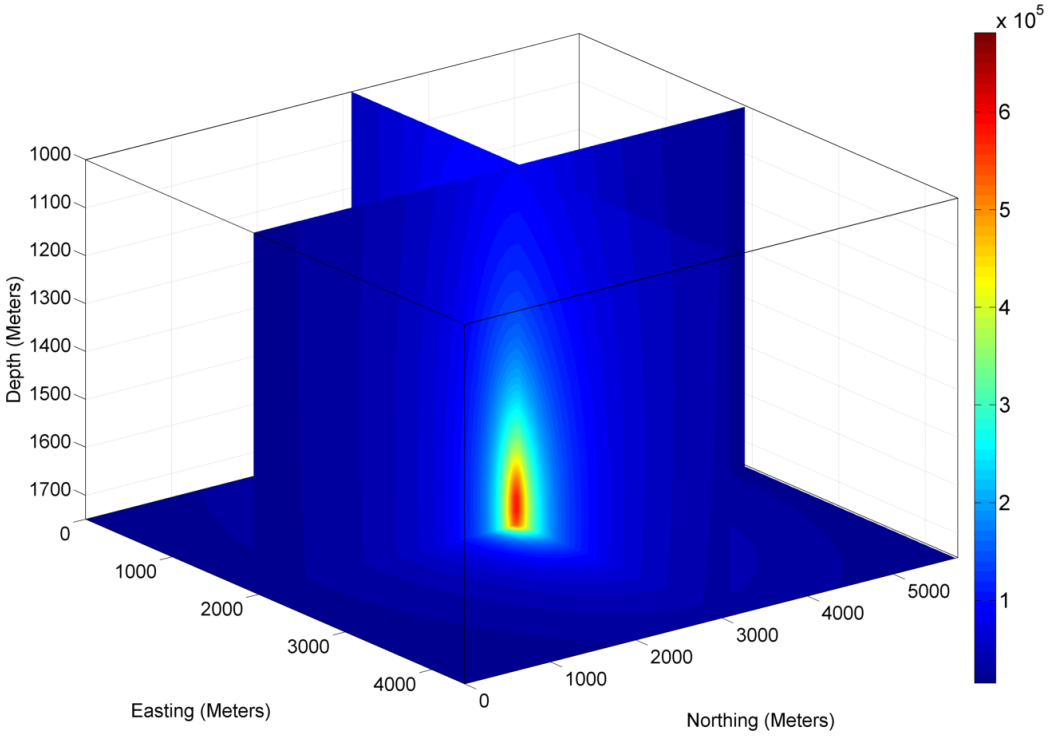

Figure 4.49: Normalized probability density function for P-wave slices at x = 3050 m, y = 1950 m, and z = 1730 m. Higher values are more likely to be the source location.

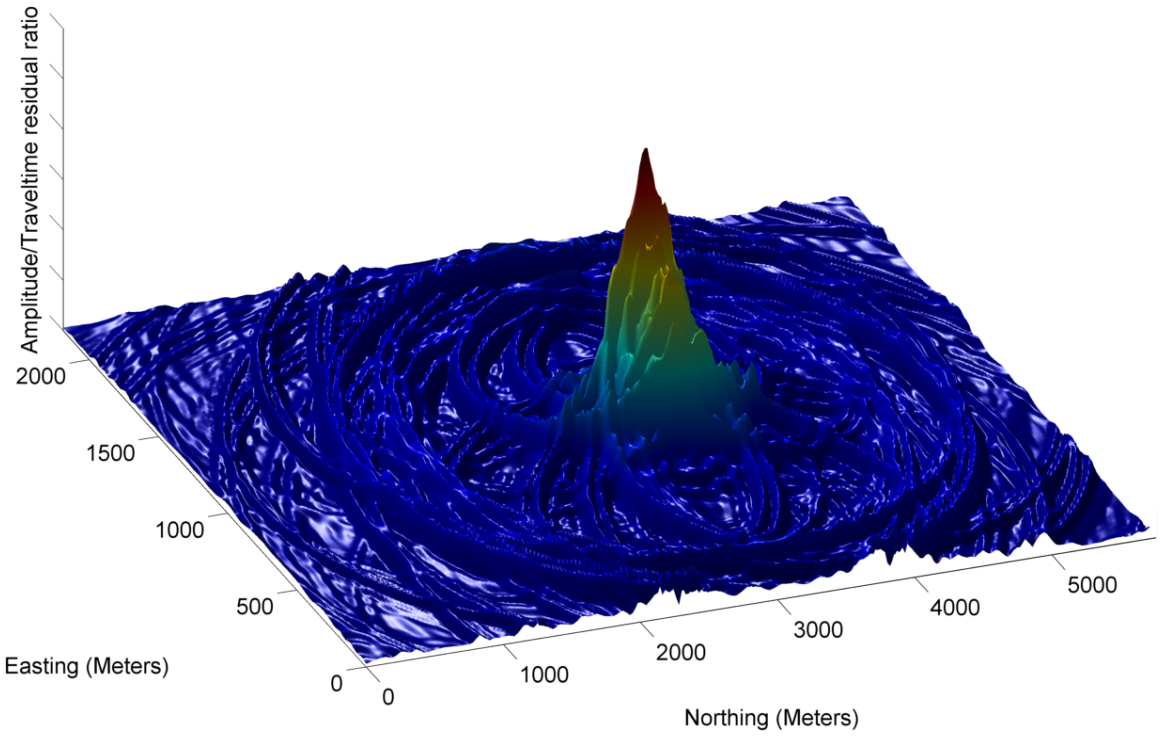

Figure 4.50: Surface plot of the Energy/traveltime residual ratio for P-wave. Maximum value of this ratio is assumed to be the source location.

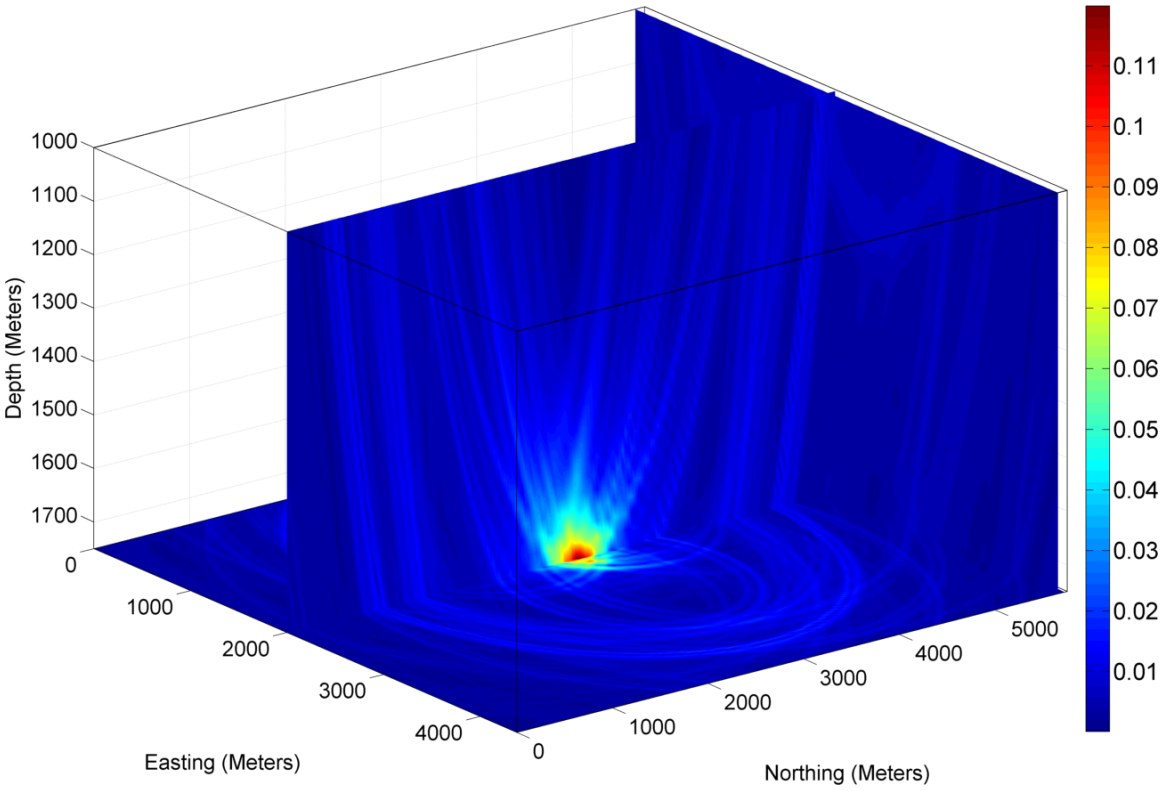

Figure 4.51: P-wave Energy/traveltime residual ratio contour slices at x = 5400 m, y = 1950 m, and z = 1730 m.

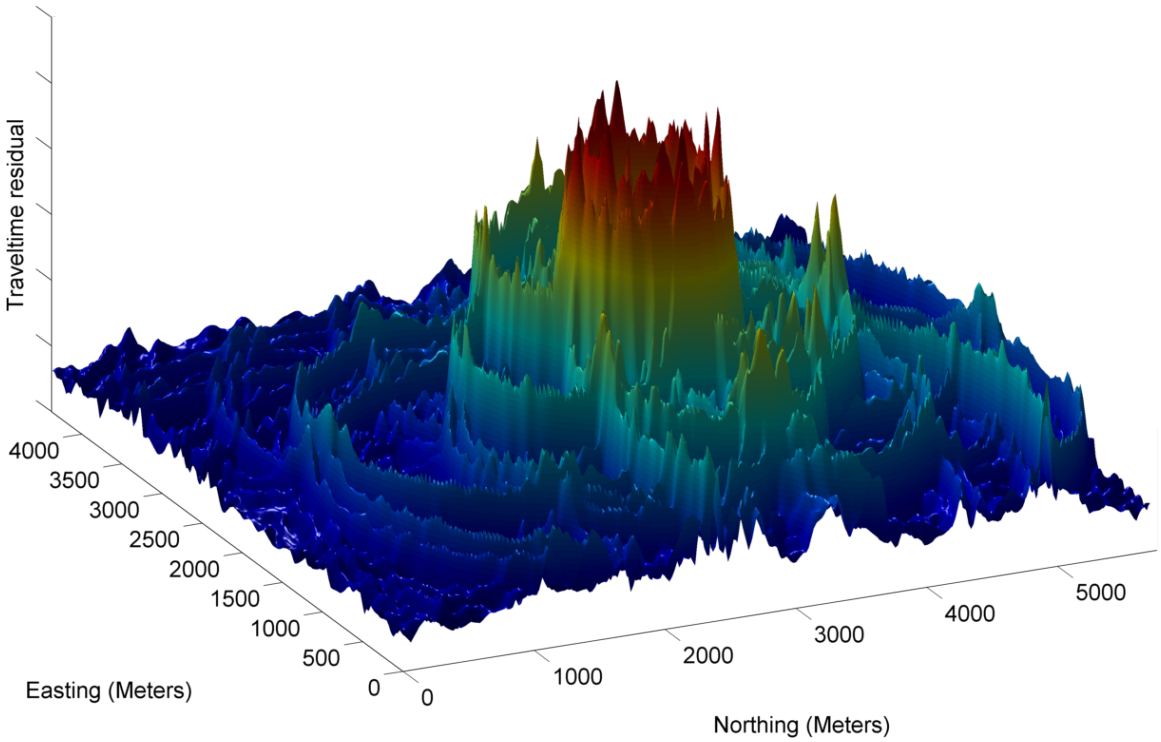

Figure 4.52: Stacked energy surface plot generated for the S-wave slice at z = 1730 meters. Apex of stacked energy is declared as the source location.

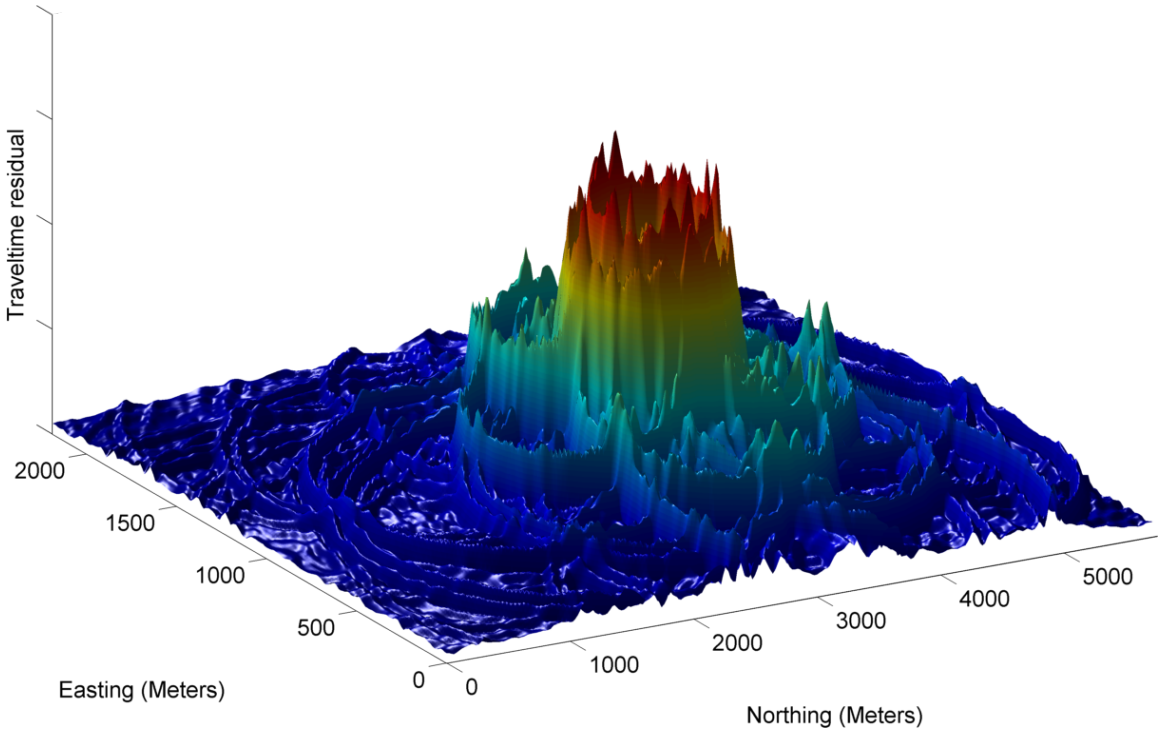

Figure 4.53: Energy/traveltime residual ratio surface plot for the S-wave slice at z = 1730 meters.

4.4.3 Focal Mechanism and Radiation Pattern Determination

The next step after locating events is to characterize source mechanism and determine radiation patterns of P and S-waves. To this end, we have determined first motion polarities of both P an S-waves. As it was mentioned earlier, we have conducted two different test on the same receiver-source configuration. In the Test A, source is placed parallel to x-Axis; whereas, in the Test B, source turned 90 degree to make it parallel to y-Axis.

Figure 4.54 and 4.55 demonstrates the first motion polarities of P-waves for the Test A and Test B, respectively. Red stars denote that the first arrivals are upwards; blue-stars mark stations that first arrivals are downwards. White starts shows that station whose first motion is unclear. In case of Test A, at the epicenter of the source location, there is a clear distinction between P wave first motions along y-Axis. However, when the source orientation is turned, first motion polarities are separated along x-Axis.

After determining polarities of body waves, Focmec (Focal Mechanism Determination) software then is used to characterize source mechanism by calculating strike, dip, and rake. Azimuth, take-off angles, polarities of body waves are inputted to the Focmec. The calculated beachball diagrams through Focmec are shown on Figure 4.54 and 4.55.

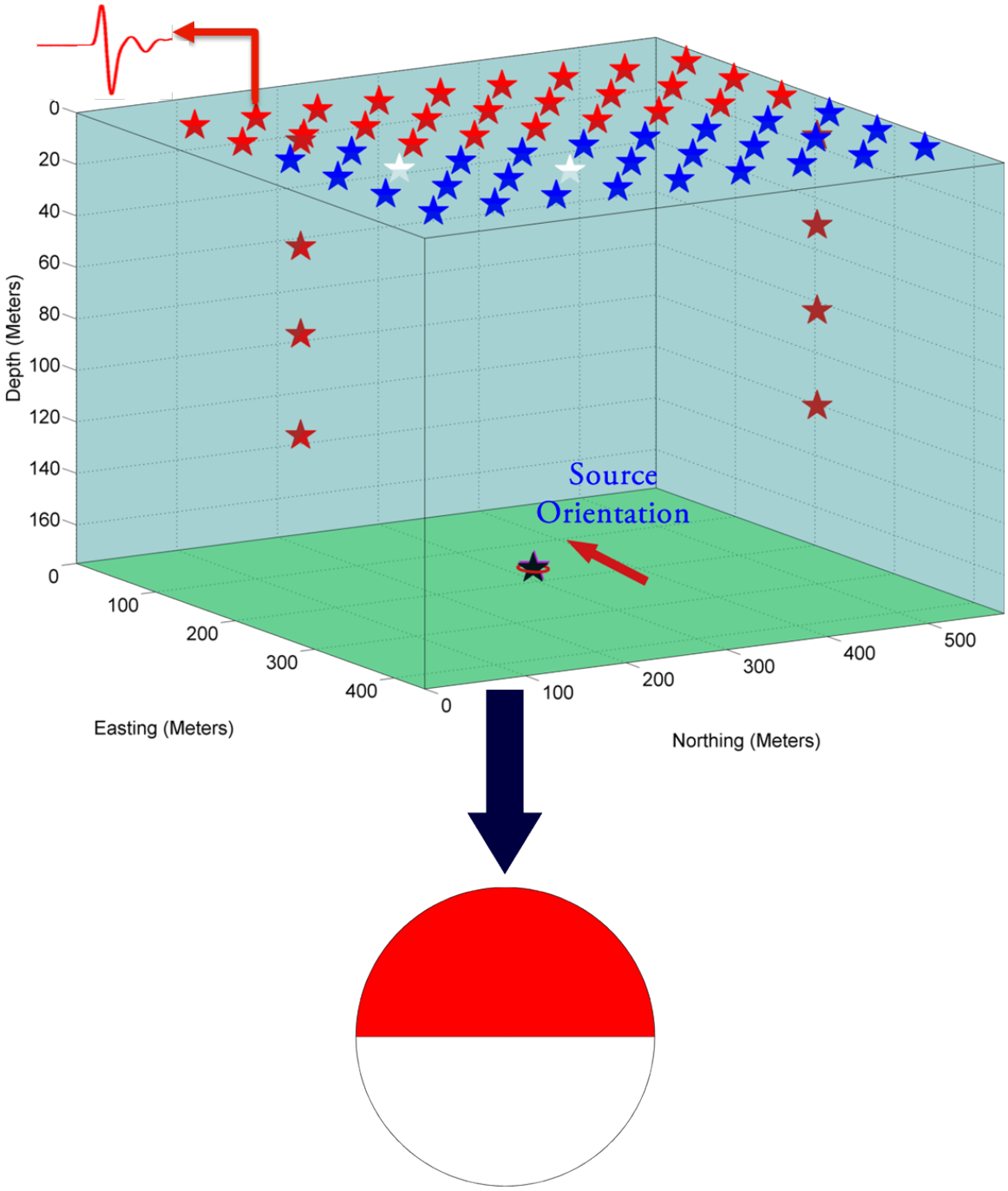

Figure 4.54: Test A: First particle motion of P-waves. Source is parallel to x-Axis. Red and blue stars denotes first motion is up and down, respectively. White stars indicates that the first motion is unclear.

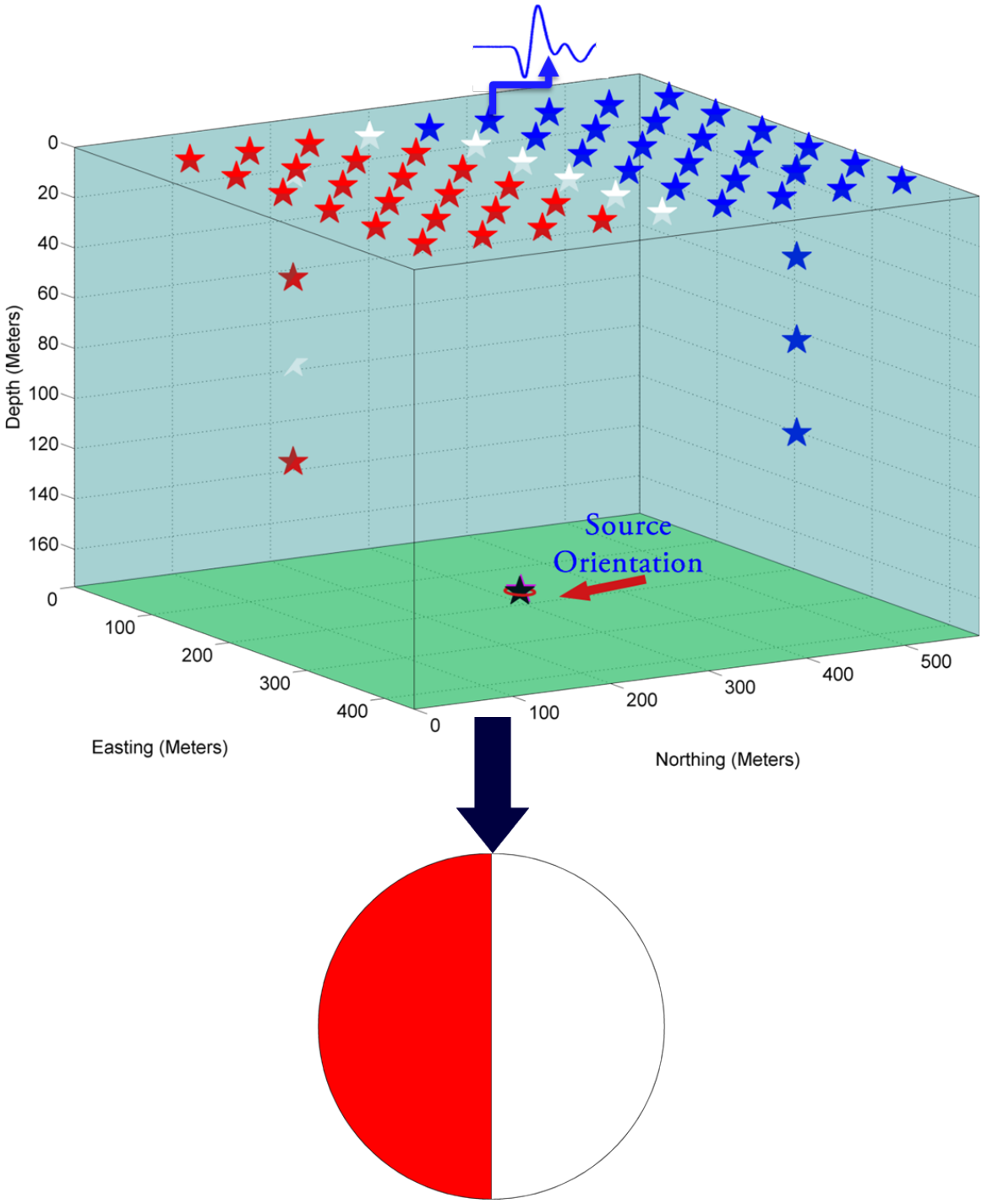

Figure 4.55: Test B: First particle motion of P-waves. Source polarization is turned 90 degree to make it parallel to y-Axis. Upwards first motion is shown with red star; whereas downward first motion is represented with blue stars. White starts denotes station with unclear first breaks.

Figure 4.56 and 4.57 illustrate the P-wave radiation pattern for Test A, source is parallel to x-Axis. For both cases, maximum positive and negative amplitudes are separated at the epicenter of the source. Minimum amplitude (close to zero) is observed along the fault plane which is just above the source location. When the source orientation is turned, radiation pattern of P-wave exhibits similar characteristic but only radiation direction is changed. Surface contour map can be divided into two lobes, where one lobe consists of downward first particle motion, another lobe consists of upward first motion.

Similarly, radiation pattern contour maps are generated using S-wave for both Test A and Test B, shown in Figure 4.58 and 4.59. Red colors denotes high positive; whereas, blue colors corresponds high negative amplitude values. S-wave exhibits different radiation pattern than the P-wave radiation. While P-wave radiates maximum of its energy towards to the epicenter, S-wave radiates to dilatation axis, and almost zero amplitude is observed at the null axis.

Theoretically computed radiation patterns of body waves for a double-couple source are shown in Figure 4.60. Red color denotes P-wave and Blue color represents S-wave radiation pattern.

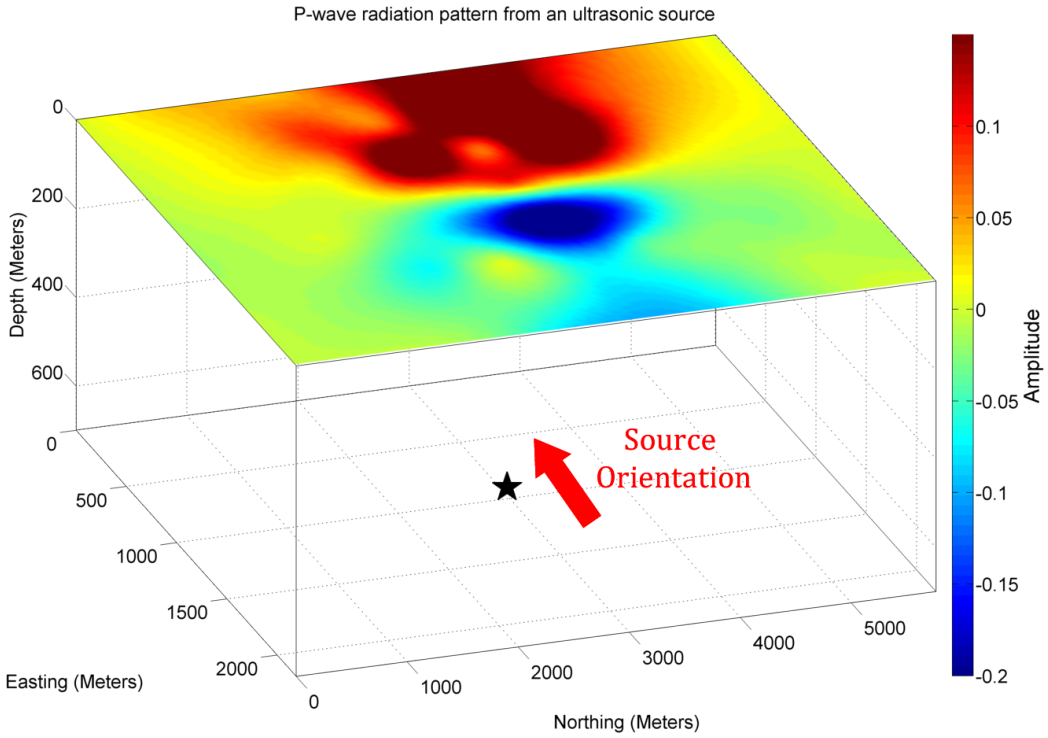

Figure 4.56: Test A: P-wave radiation pattern contour plot. Source parallel to x-Axis. Red denotes positive high and blue shows negative high amplitudes.

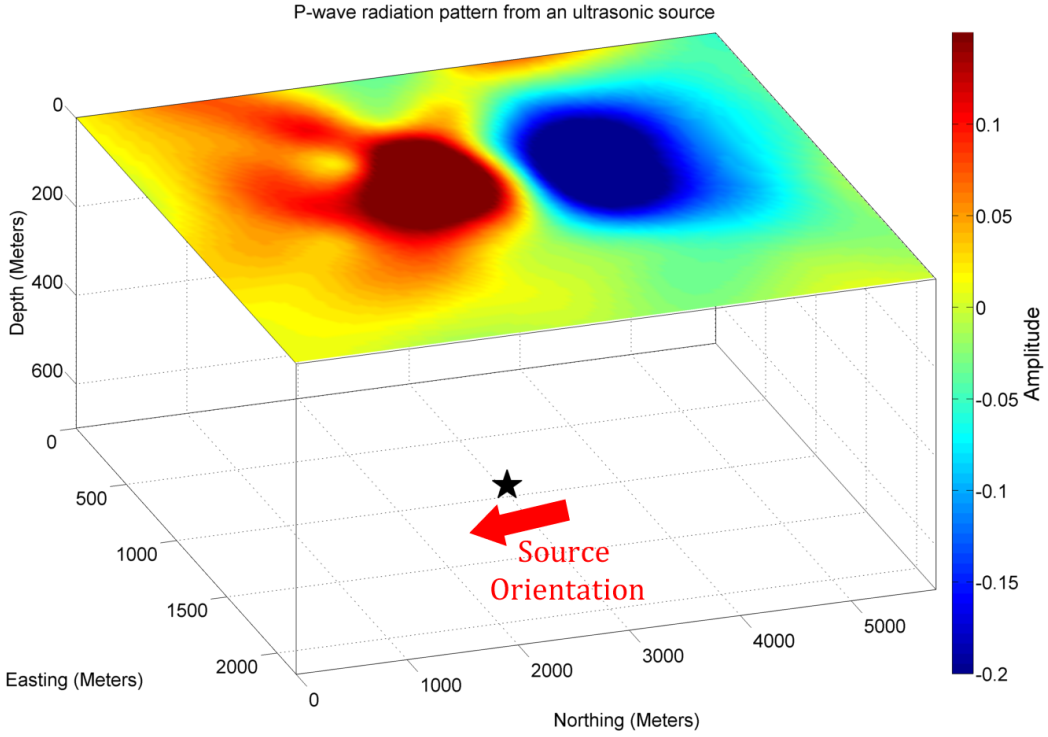

Figure 4.57: Test B: P-wave radiation pattern contour plot. Source parallel to y-Axis.

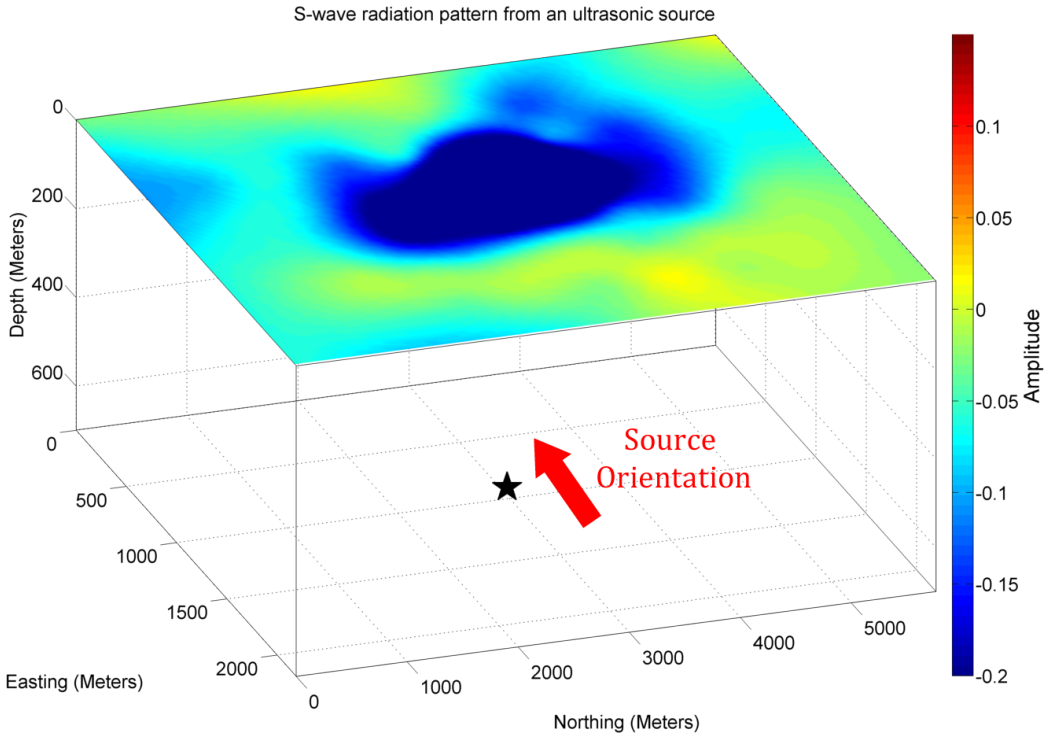

Figure 4.58: Test A: S-wave radiation pattern contour plot. Source parallel to x-Axis.

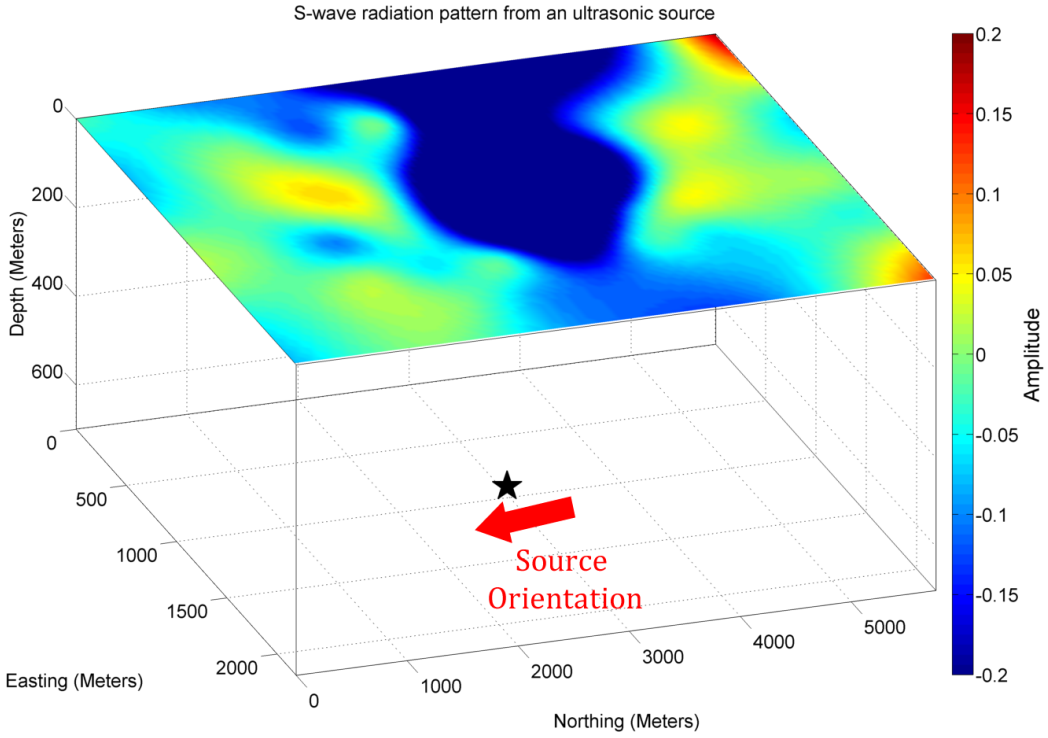

Figure 4.59: Test B: S-wave radiation pattern contour plot. Source parallel to y-Axis.

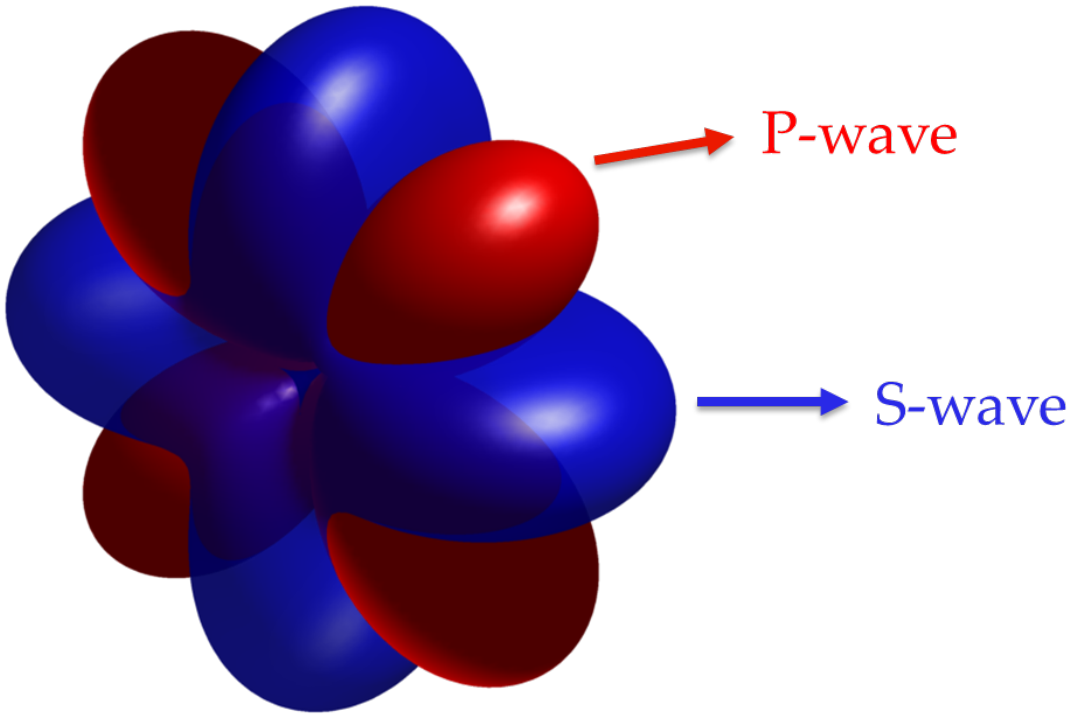

Figure 4.60: Radiation pattern of P and S-waves. Red and blue represents P and S-wave radiation, respectively.

Chapter 5. Conclusions

This study focused on the analyzing and implementing some of the fundamental keys of microseismic monitoring: locating and source characterizing of microseismic events. This was done by implementing a location algorithm and adapting a source mechanism code. The data is used in this research is acquired on both physical models and real rocks.

The major conclusions from this body of work can be summarized as follows:

- **Physical modeling:** To test different ideas and algorithms, we have undertaken novel microseismic experiments and we propose to use more sophisticated models and methods to simulate hydraulic fracturing and create microseismic events. Microseismic events are simulated on both physical models and real rocks using ultrasonic source and 3 component receivers. Microseismic experiments have conducted at the Allied Geophysical Laboratories (AGL) at the University of Houston. Three different models have been experimented throughout in this research. These straightforward models are intended to have both elastic and attenuative isotropic materials, well known velocities, and bent ray paths.

    1. Single layer physical modeling experiment using single layered Plexiglas model.
    2. Two layered model created by joining two different physical models: Aluminum and Plexiglas.
    3. Single layer microseismic experiment using sandstone real rock.

    Working with physical models and real waveforms - and knowing the answer in advance - gives us a chance to test the algorithm's accuracy and reliability. Physical models and natural rocks produce a more realistic data than the synthetic waveforms because of using actual materials. Further, acquiring data on

physical models is faster, easier, and more affordable than acquiring data on field.

- **Implementing algorithms:** We have implemented a location algorithm and adapted a source mechanism algorithm (FOCMEC).

  To locate events, we developed a ray tracing and diffraction stack procedure to undertake locations and their evaluation. The location algorithm is developed in a MATLAB environment and tested on physical modeling data. The location algorithm is based on a grid search technique to find source coordinates. For every possible point source, three attributes (traveltime residual, stacked energy and energy/traveltime ratio) of every potential point source in a grid area area calculated. Then the location can be declared by either choosing the point source that yields a minimum traveltime residual or maximum stacked energy or maximum energy/traveltime ratio.

  Even though using individually all of the three attributes allows us to pinpoint source coordinates with confidence, energy/traveltime ratio has less artifacts and produces clearer image. Traveltime residual attribute is highly dependent on precise picking first arrivals; whereas, migration-type (stacked energy) approach does not require phase arrival picking, which is useful in case of signal-to-noise ratio is low.

  To characterize source mechanism of the simulated microseismic events, Unix-based a source mechanism software, Focmec (Focal Mechanism Determinations) is adapted. First, source codes, originally written in Fortran, are compiled to make it run on 64-bit systems. Then, it is integrated with our location algorithm. Hence, it becomes possible to make simultaneous location and source mechanism inversion. All necessary parameters (azimuths, take-off angles, polarities) are directly piped to the complied version of Focmec. Found solutions

are retrieved and beach-ball diagrams can be generated.

- **Determining radiation patterns:** Another important objective of this research is to have a better understanding of the radiation patterns of simulated microseismic events. We have successfully determined the radiation patterns of body waves in this research.

- **Testing different location techniques:** The location algorithm is developed in such a way that it simultaneously locates a single event with seven different ways, which gives us insight into the accuracy of different location techniques:

  1. Using P waves and traveltime residual method
  2. Using P waves and stacked energy method
  3. Using P waves and energy/traveltime residual ratio
  4. Using S waves and traveltime residual method
  5. Using S waves and stacked energy method
  6. Using S waves and energy/traveltime residual ratio
  7. Using P and S waves and traveltime residual method

  In the light of our experiments, using S-wave alone can also be an effective way to locate events rather than P-wave. Further, combining P and S-waves yields more accurate location results.

- **Testing different acquisition designs:** This research also investigates the effects of survey designs into location accuracy. Should we use surface receivers or borehole or both of them? Should we use grid survey design or star-like shape?

  To be able to find answers for these questions, we have performed location under different scenarios. First, we have located events using only surface receivers,

and then we have included borehole (well-side) receivers to determine location uncertainty. One common result that we have obtained in this research, excluding downhole receivers increase location uncertainty; absolute and relative errors raise.

- **Building variety of GUI's:** Throughout this research, more than 30 scripts are coded; 4 different user-friendly GUI's are built to ease user operations.

- **Accelerating computation speed:** Since grid searching location algorithm requires huge amount of computation, it is desirable to minimize computation cost. For that purpose, we have implemented CPU and GPU computing to increase performance of the location algorithm. According to our benchmark results, while using simultaneously all cores of CPU accelerate computation speed, using GPU together with CPU speeds up computation time significantly. Locating a single microseismic event with 7 different methods takes 11.4 seconds on single core CPU, whereas, this number is decreased to 4.2 seconds using multi-core CPU computing. Further, implementing GPU computing further decreases the total elapsed time to only 1.9 seconds. It is more than %80 increase in terms of computation time compared to single core CPU.

- **First arrival picking:** For location algorithms based on traveltime, it is required to have precise picking of phase arrivals. To this end, we have implemented two different event detection and first arrival picking algorithms: STA/LTA and Modified Energy Ratio.

Chapter 6. Future Work

Microseismic monitoring is a very rich subject with significant room for future investigation. The results shown in this thesis are just preliminary results and more work is needed. To further improve the location and source mechanism algorithm, the following recommendations are made:

1. The proposed location algorithm might also be tested on a fractured physical model, a fluid injection model, and real field data to verify its overall applicability.

2. In contrast to real-world microseismic monitoring, we have known the exact time when the microseismic event is triggered. For location algortihm, the next step is to search for the origin time t_0 in a grid searching fashion.

3. Microseismic moment tensor inversion is a useful tool as it directly links the observed seismograms recorded by monitoring sensors to the seismic source mechanism. Developing or integrating full moment tensor inversion is the next step.

4. Location software should be also be tested using real microseismic datasets to fix possible bugs in the program.

5. Minimizing computation cost is essential. Even though, using GPU computation decreases significantly the elapsed time for locating events, further investigation and research can be done so as to minimize computation time.

References

Aki, K. and Richards, P. G. (1980). *Quantitative seismology: theory and methods*, Vol. 1424. Freeman San Francisco.

Aki, K. and Richards, P. G. (2002). *Quantitative seismology: Theory and methods*. University Science Books.

Allen, R. V. (1978). "Automatic earthquake recognition and timing from single traces." *Bulletin of the Seismological Society of America*, 68, 1521–1532.

Angus, D. A. C. (1999). *Applicability of moment tensor inversions to mine-induced microseismic data.* Queen's University at Kingston.

Bormann, P. and Wielandt, E. (2013). *New Manual of Seismological Observatory Practice 2 (NMSOP2)*, chapter Seismic Signals and Noise, 1–2. Potsdam: Deutsches GeoForschungsZentrum GFZ.

Dai, H. and MacBeth, C. (1995). "Automatic picking of seismic arrivals in local earthquake data using an artificial neural networks." *Geophysical Journal International*, 120, 758–774.

Dingus, C. (2010). "Seismic processing - noise attenuation techniques for relative amplitude processing." *Petroleum Africa*, 36, 47.

Dongarra, J. (2012). "What is gpu computing?

Drew, J., Leslie, H., Armstrong, P., and Michard, G. (2005). "Automated microseismic event detection and location by continuous spatial mapping." *SPE Annual Technical Conference and Exhibition*.

Du, J., Zimmer, U., and Warpinski, N. (2011). "Fault plane solutions from moment tensor inversion for microseismic events using single-well and multi-well data." *CSEG Recorder*, 36(8), 22–28.

Dziewonski, A. and Gilbert, F. (1974). "Temporal variation of the seismic moment tensor and the evidence of precursive compression for two deep earthquakes.

Earle, P. and Shearer, P. (1994). "Characterization of global seismograms using an automatic picking algorithm." *Bulletin of the Seismological Society of America*, 84, 366–376.

Eaton, D. W. (2009). "Resolution of microseismic moment tensors: A synthetic modeling study." *SEG Technical Program Expanded Abstracts 2009*, Society of Exploration Geophysicists, 3569–3573.

Eaton, W. D. (2008). "Microseismic focal mechanisms: A tutorial." *Report no.*, CREWES Research Report.

Economides, M. J. and Nolte, K. G. (2000). *Reservoir Stimulation*. John Wiley & Sons Inc., New York, 3rd edition edition.

Eisner, L. (2013). "Microseismic monitoring in oil or gas reservoir. SEG Continuing Education Course.

Eisner, L., Duncan, P. M., Heigl, W. M., and Keller, W. R. (2009). "Uncertainties in passive seismic monitoring." *The Leading Edge*, 28, 648–655.

Flinn, E. (1965). "Signal analysis using rectilinearity and direction of particle motion." *Proceedings of the IEEE*, 53(12), 1874–1876.

Forouhideh, F. (2011). "Microseismic moment-tensor inversion. Master's thesis, University of Calgary.

Gajewski, D. and Tessmer, E. (2005). "Reverse modelling for seismic event characterization." *Geophysical Journal International*, 163(1), 276–284.

Geiger, L. (1912). "Probability method for the determination of earthquake epicenters from the arrival time only." *Bulletin of St. Louis University*, 8(1), 56–71.

Gilbert, F. (1971). "Excitation of the normal modes of the earth by earthquake sources." *Geophysical Journal International*, 22(2), 223–226.

Granberg, A. (2010). "Hydraulic fracturing of natural gas." *Report no.*, http://www.circleofblue.org/waternews/2010/science-tech/climate/hydraulic-fracturing-infographic/.

Hafez, A. and Kohda, T. (2009). "Accurate p-wave arrival detection via modwt." *International Conference on Computer Engineering & Systems, IEEE, 391-396.*

Han, L. (2010). "Microseismic monitoring and hypocenter location. Master's thesis, University of Calgary.

Holditch, S. A. (2007). "Unconventional gas subgroup of the technology task group of the npc committee on global oil and gas." *Report no.*, National petroleum council.

Jost, M. and Herrmann, R. (1989). "A studentŠs guide to and review of moment tensors." *Seismological Research Letters*, 60(2), 37–57.

Kanamori, H. and Cipar, J. J. (1974). "Focal process of the great chilean earthquake may 22, 1960." *Physics of the Earth and Planetary Interiors*, 9(2), 128–136.

Kanasewich, E. R. (1981). *Time sequence analysis in geophysics.* University of Alberta.

Kendall, M., Maxwell, S. C., Foulger, G., Eisner, L., and Lawrence, Z. (2011). "Microseismicity: Beyond dots in a box." *Geophysics*, 76, 6.

Klein, F. W. (2002). *User's guide to HYPOINVERSE-2000: A Fortran program to solve for earthquake locations and magnitudes*. US Geological Survey.

Lahr, J. (1980). "Hypoellipse." *MULTICS: A computer program for determining local earthquake hypocentral parameters, magnitude and first motion pattern: US Geological Survey Open-file Report*, 80, 59–68.

Lay, T. and Wallace, T. C. (1995). *Modern global seismology*, Vol. 58. Academic Press Inc.

Lee, W. H. K. and Lahr, J. C. (1975). *HYPO71 (revised): a computer program for determining hypocenter, magnitude, and first motion pattern of local earthquakes*. US Department of the Interior, Geological Survey, National Center for Earthquake Research.

Maxwell, S. C. (2012). "Statistical evaluation for comparative microseismic interpretation." *74th EAGE Conference & Exhibition, Extended Abstracts*.

Maxwell, S. C. and Urbancic, T. I. (2001). "The role of passive micro-seismic monitoring in the instrumented oil field." *The Leading Edge*, 20, 636–639.

McMechan, G. A. (1982). "Determination of source parameters by wavefield extrapolation." *Geophysical Journal International*, 71(3), 613–628.

Mendiguren, J. A. (1977). "Inversion of surface wave data in source mechanism studies." *Journal of Geophysical Research*, 82(5), 889–894.

Montalbetti, J. F. and Kanasewich, E. R. (1970). "Enhancement of teleseismic body phases with a polarization filter." *Geophysical Journal of the Royal Astronomical Society*, 21, 119–129.

Moser, T. (1991). "Shortest path calculation of seismic rays." *Geophysics*, 56(1), 59–67.

Munro, K. (2004). "Automatic event detection and picking of p-wave arrivals." *Report no.*, CREWES Research Report.

Nakano, H. (1923). "Notes on the nature of the forces which give rise to the earthquake motions." *Seismol. Bull*, 1, 92–120.

Oye, V. and Roth, M. (2003). "Automated seismic event location for hydrocarbon reservoirs." *Computers & Geosciences*, 29, 851–863.

Press, W. H., Teukolsky, S. A., Vetterling, W. T., and Flannery, B. P. (2007). *Numerical Recipes 3rd Edition: The Art of Scientific Computing*. Cambridge University Press.

Rentsch, S., Buske, S., Lüth, S., and Shapiro, S. (2006). "Fast location of seismicity: A migration-type approach with application to hydraulic-fracturing data." *Geophysics*, 72(1), S33–S40.

Riding, J. B. and Rochelle, C. A. (2009). "Subsurface characterisation and geological monitoring of the co2 injection operation at weyburn, saskatchewan, canada." *Geological Society Special Publications*, 313, 227–256.

Rodriguez, I. V. (2011). "Automatic time-picking of microseismic data combining sta/lta and the stationary discrete wavelet transform." *CSPG CSEG CWLS Convention, Convention Abstracts*.

Romanowicz, B. (1981). "Depth resolution of earthquakes in central asia by moment tensor inversion of long-period rayleigh waves: Effects of phase velocity variations across eurasia and their calibration." *Journal of Geophysical Research: Solid Earth*, 86(B7), 5963–5984.

Saragiotis, C., Alkhalifah, T., and Fomel, S. (2013). "Automatic traveltime picking using instantaneous traveltime." *Geophysics*, 78, T53–T58.

Scott, D. R. and Kanamori, H. (1985). "On the consistency of moment tensor source mechanisms with first-motion data." *Physics of the Earth and planetary interiors*, 37(2), 97–107.

Shearer, P. M. (2009). *Introduction to seismology*. Cambridge University Press.

Sheriff, R. E. (1973). *Encyclopedic dictionary of exploration geophysics*. Society of Exploration Geophysicists Tulsa, OK.

Shi, Z. and Ben-Zion, Y. (2009). "Seismic radiation from tensile and shear point dislocations between similar and dissimilar solids." *Geophysical Journal International*, 179(1), 444–458.

Snoke, J. A. (2003). "Focmec: Focal mechanism determinations." *International Geophysics*, 81, 1629–1630.

Song, F., Kuleli, H. S., Toksöz, M. N., Ay, E., and Zhang, H. (2010). "An improved method for hydrofracture-induced microseismic event detection and phase picking." *Geophysics*, 75.6, A47–A52.

Stein, S. and Wysession, M. (2003). *An introduction to seismology, earthquakes, and earth structure*. Blackwell Publishing.

Strelitz, R. A. (1978). "Moment tensor inversions and source models." *Geophysical Journal International*, 52(2), 359–364.

Urbancic, T. I., Shumila, V., Rutledge, J. T., and Zinno, R. (1999). "Determining hydraulic fracture behavior using microseismicity." *The 37th U.S. Symposium on Rock Mechanics (USRMS)*.

Vidale, J. E. (1986). "Complex polarization analysis of particle motion." *Bulletin of the Seismological Society of America*, 76, 1393–1405.

Wong, J., Han, L., Bancroft, J. C., and Stewart, R. R. (2009). "Automatic time-picking of first arrivals on noisy microseismic data." *Report no.*, CSEG Microseismic Workshop.

Xiantai, G., Zhimin, L., Na, Q., and Weidong, J. (2011). "Adaptive picking of microseismic event arrival using a power spectrum envelope." *Computers & Geosciences*, 37, 158–164.

Appendix A. Ray Tracing Methods

In this research, two different ray tracing algorithms are coded. First one consists of directed grid searching scheme and the second one is based on two-point ray tracing.

Considering the medium is isotropic and homogeneous, the ray paths will be straight lines from source $S(x_s, z_s)$ to the receiver $R(x_r, z_r)$. The coordinates of the intersection point at each layer boundaries is $I(x_i, z_i)$, where i is the i^{th} layer.

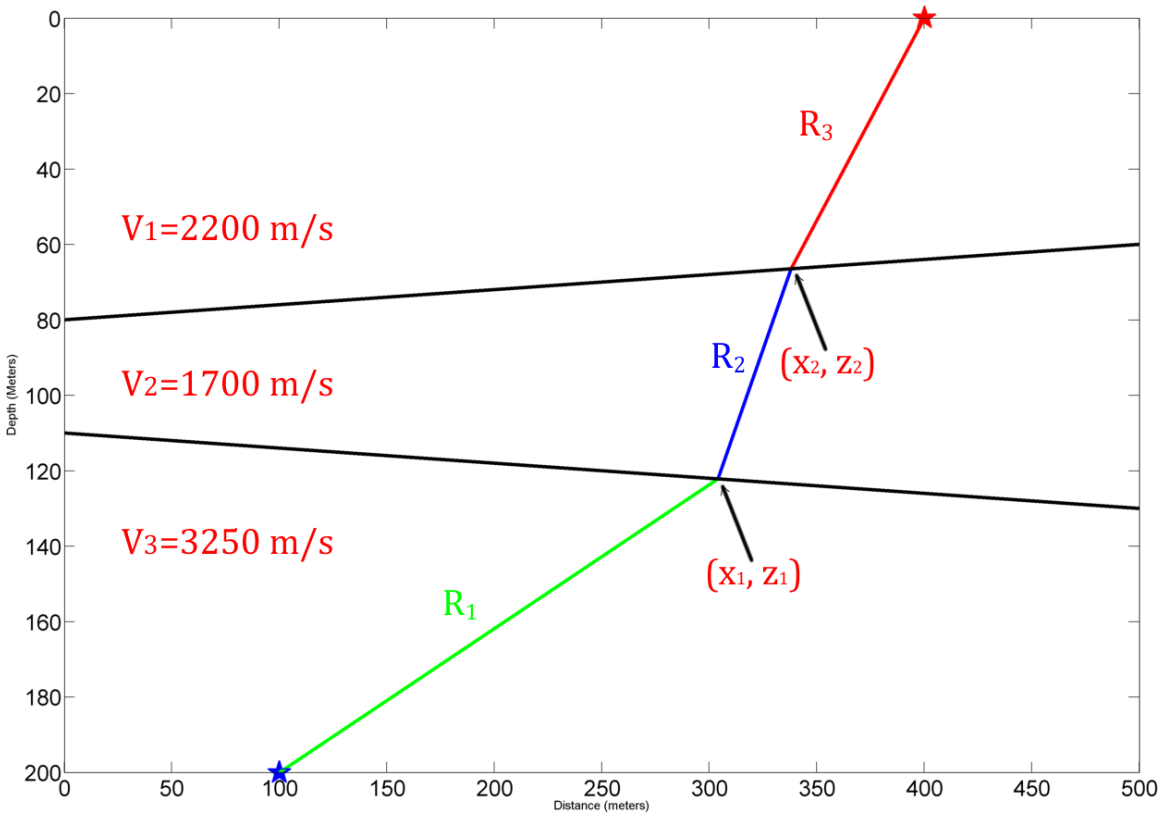

Figure A.1: Schematic of ray tracing in 2D medium with two-point ray tracing.

Figure A.1 shows a 2D layered model and ray paths for given velocity model. R_1, R_2, R_3 are the line segments between source, intersection points, and receiver. Equations A.1, A.2, and A.3 can be used to calculate distance of each line segments.

$$R_1 = \sqrt{(x_s - x_1)^2 + (z_s - z_1)^2} \tag{A.1}$$

$$R_2 = \sqrt{(x_1 - x_2)^2 + (z_1 - z_2)^2} \tag{A.2}$$

$$R_3 = \sqrt{(x_2 - x_r)^2 + (z_2 - z_r)^2} \tag{A.3}$$

Total traveltime for given ray path in Figure A.1 can be calculated as follows:

$$t = R_1 * u_1 + R_1 * u_1 + R_1 * u_1 \tag{A.4}$$

where $u_1, u_2, and u_3$ are the slownesses of each layer.

There are two ways to compute the intersection points $I(x_i, z_i)$.

1. Direct search method

2. Two point ray tracing

The first approach requires computation of all possible ray paths given a grid interval. Then the ray path couples or triplets that yields minimum traveltime can be chosen as the true ray paths.

The second method demands generating 2 equations with 2 unknowns, and then solving for the intersection points. This can be done by taking the derivative of t with respect to x_1 and x_2 and equate to zero because the ray path has minimum traveltime. Equations A.5 and A.6 shows the derivative of t with respect to x_i and x_2.

$$\frac{u_1(x_s - x_1)}{R_1} - \frac{u_2(x_1 - x_2)}{R_2} = 0 \tag{A.5}$$

$$\frac{u_2(x_1 - x_2)}{R_1} - \frac{u_3(x_2 - x_r)}{R_2} = 0 \tag{A.6}$$

Since we have 2 equations with 2 unknowns, the intersection points can be

calculated. Figure A.2 displays the rays traced from a source to 35 receivers.

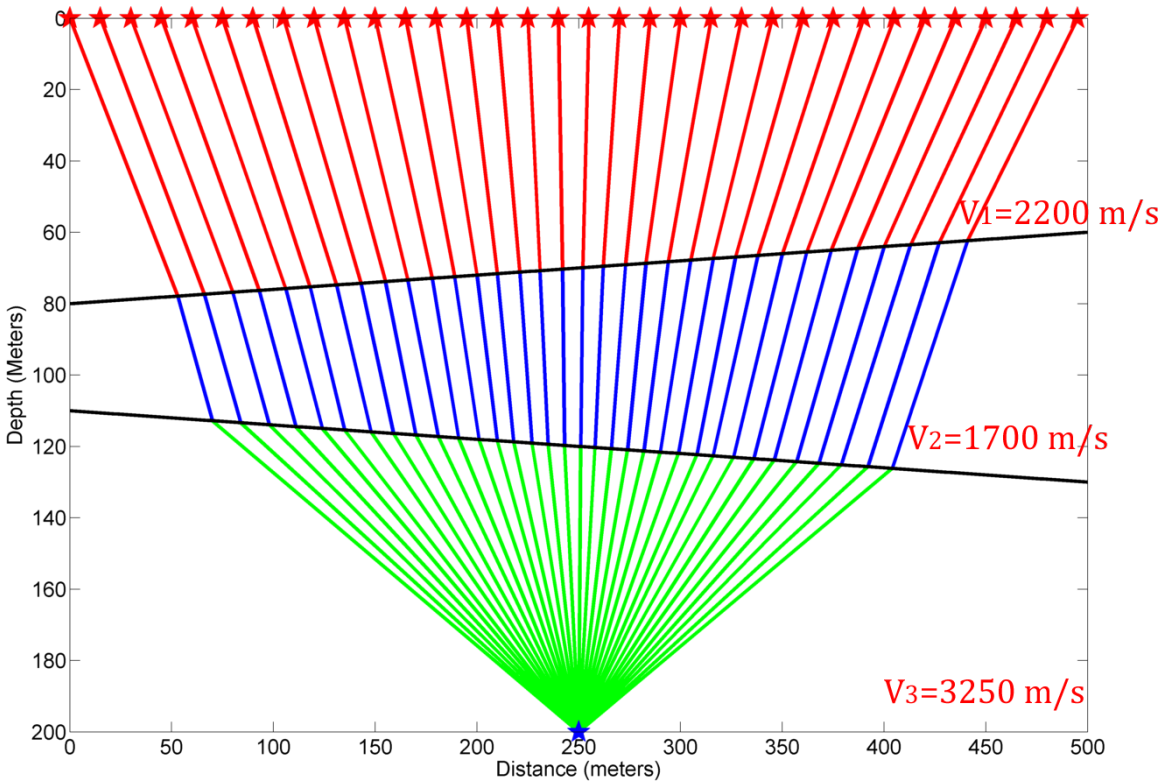

Figure A.2: Rays traced from a source to receivers placed on surface in 2D medium.

We can easily extend this approach into 3D medium by adding y-component to Equations A.1, A.2, and A.3.

Figure A.3 shows ray tracing in two layered medium in 3D. Red stars are receivers, black star is the source location. Velocity of the upper layer and lower layer is 1500 m/s and 3250 m/s, respectively.

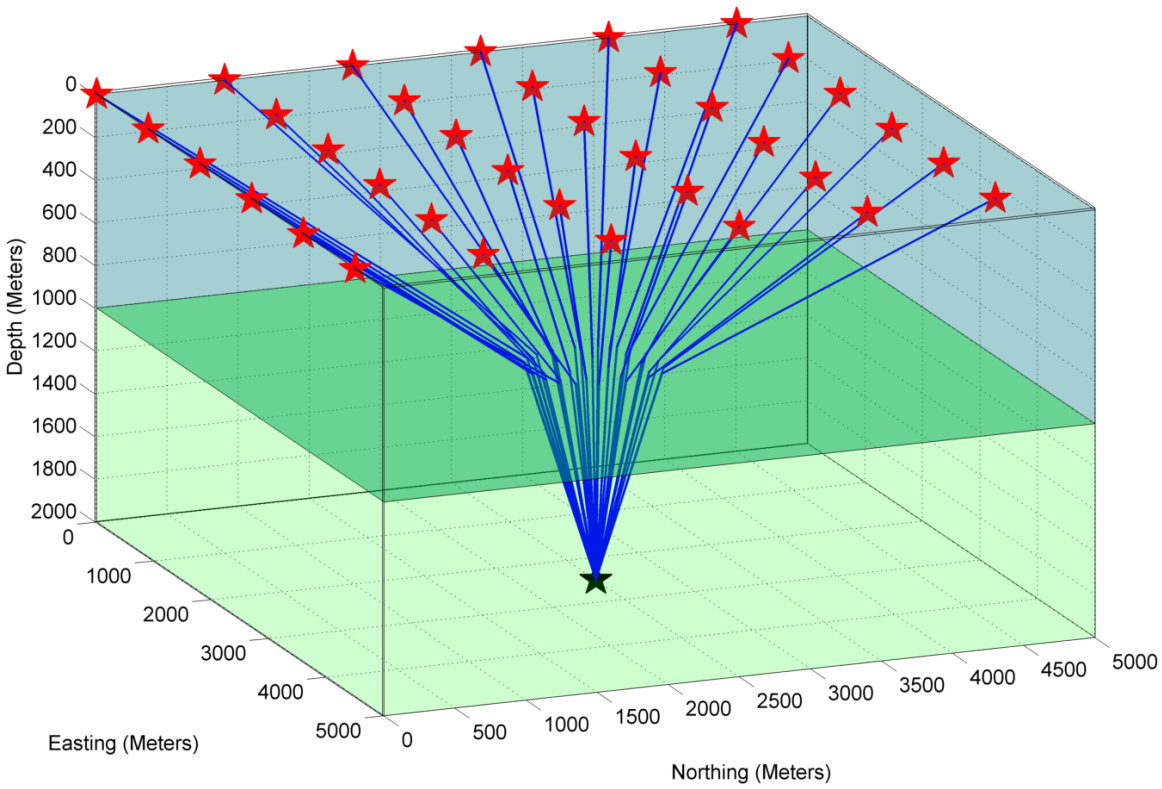

Figure A.3: Ray tracing in 3D media. Black star is the source location, whereas, red stars are the receivers. Velocity of the upper layer is 1500 m/s, and velocity of the lower layer is 3250 m/s.